

Phase Behavior of Single, Binary, and Ternary CH₄-C₂H₆-CO₂
Hydrate Systems

By

Ruyi Zheng

Submitted to the graduate degree program in Chemical & Petroleum Engineering and the
Graduate Faculty of the University of Kansas in partial fulfillment of the requirements for the
degree of Doctor of Philosophy

Chair: Dr. Xiaoli Li

Dr. Shahin Negahban

Dr. Shapour Vossoughi

Dr. Jyun Syung Tsau

Dr. Gibum Kwon

Date Defended: 8 December 2020

The dissertation committee for Ruyi Zheng certifies that this is the approved version of the
following dissertation:

Phase Behavior of Single, Binary, and Ternary CH₄-C₂H₆-CO₂ Hydrate
Systems

Chair: Dr. Xiaoli Li

Date Approved: 8 December 2020

ABSTRACT

Understanding the phase behavior of gas hydrates is critical to flow assurance, geological stability, energy harvest from hydrate reservoirs, and industrial applications such as gas storage and desalination. Systems containing CH_4 , C_2H_6 , and CO_2 are particularly of interest because they are ubiquitous in nature and many industrial applications, and also due to their microscopic properties, e.g., the structure change of the CH_4 - C_2H_6 hydrates and the impact of CO_2 on the variation of hydrate stability.

In this work, a high-pressure PVT experimental apparatus is designed to measure the hydrate phase boundary and to observe the growth behaviors of the hydrate film formed in the water-gas interface. The phase boundary of CH_4 - CO_2 hydrates formed in NaCl solutions is measured to extend the phase boundary database of CH_4 - CO_2 hydrates with pressure up to 61.99 MPa and the temperature to 295.09 K. The roughness of the water-gas interface is greatly increased at the initial stage of hydrate formation and becomes smoother with time because of the thickness growth of the hydrate film. The fine pillars formed at the water-gas interface may be due to the non-equilibrium state of gas and water phases or due to the non-uniform lateral growth of hydrates at the interface.

Three theoretical models with different frameworks are developed to calculate the phase boundary of gas hydrates. The first model employs the original PR EoS for the gas-rich phases and the Henry's law combined with the Poynting correction for the gas solubility in the aqueous phase. In the second model, a single modified PR EoS is applied to calculate the aqueous and gas-rich phase equilibria. In these two models, the effect of electrolytes on the hydrate phase boundary is

determined by employing the Pitzer model. The first two theoretical models are also termed as separate models because different models are used for non-hydrate phases, i.e., gas-rich phase, aqueous phase, and dissolved electrolytes. In the third model, a unified EoS is proposed to account for the non-hydrate phases, i.e., the mPR EoS is used to describe the interactions between water, gas, and uncharged ions, a simplified explicit MSA term for the long-range Coulombic forces, and Born terms for the discharging-charging processes. The vdW-P model is applied in all these three models for the hydrate phase. These developed models are capable of capturing the general trend that the phase boundary pressure of CH₄, C₂H₆, CO₂, and binary CH₄-C₂H₆ and CH₄-CO₂ hydrates increases with the temperature and the NaCl concentration. Also, the phase boundary pressure of the binary CH₄-C₂H₆ and CH₄-CO₂ hydrates increase with the concentration of CH₄ in the feed gas. It is worth noting that the two theoretical models are capable of detecting the sII structure formed by the binary CH₄-C₂H₆ hydrates, which is influenced by various factors, e.g., gas composition, pressure, and temperature. The reliability of the first model is verified by an overall AARD of 5.0% for the 984 data points of CH₄, C₂H₆, CO₂, and binary CH₄-C₂H₆ and CH₄-CO₂ hydrates formed in the bulk pure H₂O phase and NaCl solutions. The data points of the binary CH₄-C₂H₆ and CH₄-CO₂ hydrates formed in the pure water and NaCl solution are employed to quantify the reliability of the second model, with an overall AARD of 5.2% for the 187 data points of the binary CH₄-C₂H₆ and CH₄-CO₂ hydrates. 734 phase boundary data points of pure and binary CH₄, C₂H₆, and CO₂ hydrates formed in single- and mixed-NaCl, KCl, MgCl₂, and CaCl₂ solutions as well as in the pure water are used to evaluate the reliability of the third model, with an overall AARD of these 734 data points predicted by this newly developed model is 3.4%, which proves the capability of the newly developed model in predicting the phase boundary of hydrates in multi-component systems.

The MD simulation is used to explore the structure stability of CH₄-C₂H₆ and CH₄-C₂H₆-CO₂ hydrates. It proves that the sI hydrates formed by CH₄-C₂H₆ mixtures with a CH₄ composition of 20 mol% are more stable than those with a CH₄ composition of 90 mol%. On the contrary, the hydrates formed by CH₄-C₂H₆ mixtures with 90 mol% CH₄ in sII structure are more stable than those with a CH₄ composition of 20 mol%. This is consistent with the theoretical calculation and also the experimental observations.

The impact of CO₂ on the stability of sI structure CH₄-C₂H₆-CO₂ hydrates is investigated using two CO₂ compositions of 20 and 50 mol%. It is observed that the hydrate stability decreases when the CO₂ composition increases. The impact of CO₂ on the motion of gas molecules in the hydrate cages changes with gas composition. For instance, the motion of CH₄ molecules is restricted with the increase in CO₂ concentration when the CH₄ concentration is high. However, the CO₂ has little impact on CH₄ when the CH₄ concentration is low. Also, the CO₂ molecules can move more freely when the CH₄ concentration is low as the concentration of CO₂ is increased. The added CO₂ enhances the free motion of C₂H₆ and this effect becomes less significant when the concentration of C₂H₆ is increased. The fluctuation frequency of the MSD and the rotation angle curves of the water and gas molecules can be explained by the potential energy between water-water and gas-water pairs.

As the pressure increases, the stability of hydrate cages is slightly enhanced in scenarios with a CO₂ concentration of 20 mol%, but the hydrate cages get less stable in scenarios with a CO₂ concentration of 50 mol%. Similarly, the impact of pressure on the motion of gas molecules depends on the gas concentration. At high concentrations, the motion of CH₄ molecules is slightly restricted with the increase in pressure. The pressure effect on CH₄ motion becomes negligible as the concentration of CH₄ decreases. The impact of pressure on the motion of C₂H₆ molecules is

negligible except when the concentration of C_2H_6 is 40 mol%, where C_2H_6 moves more freely. Overall, the impact of pressure on the average rotation angle and MSD of gas molecules in the hydrate cages is less significant than the gas composition. However, the effect of pressure on the interactions between gas molecules is reflected by the amplitude of fluctuations on the rotation angle and MSD curves. For instance, the fluctuation amplitude of both the rotation angle and MSD curves of C_2H_6 molecules get larger as the C_2H_6 concentration decreases. The amplitude of the fluctuation in the rotation angle curves is smaller when the CH_4 concentration is higher, due to the interaction between CH_4 and CO_2 molecules.

ACKNOWLEDGMENT

First and foremost, I express my sincere respect and gratitude to my advisor, Dr. Xiaoli (Laura) Li. I would not have gained such a valuable graduate experience without her. Dr. Li has provided me generous financial support and priceless academic guidance in the past three and a half years of my graduate studies at the University of Kansas. In addition to her professional experience, I also admire her stringent attitude toward work and optimistic view of life.

I want to thank my co-advisor, Dr. Shahin Negahban, who has offered generous financial support as well as invaluable academic suggestions to my research in the past year at the University of Kansas. Besides, I really appreciate his mentorship in industrial vision and open communication as well.

I would like to express my gratitude to Dr. Gibum Kwon from Department of Mechanical Engineering at the University of Kansas for being my committee member. I took the excellent Introduction to Surface and Interface Science course with him. His passionate and professional attitude toward teaching and research inspired me a lot. I also want to thank Dr. Shapour Vossoughi for being in my committee.

I wish to expand my thanks to Tertiary Oil Recovery Program (TORP) for the technical and financial support. Particularly, I want to thank the associate scientist, Dr. Jyun-Syung Tsau and the professional technician, Mr. Scott Ramskill for the technical support to my experiments.

I would like to thank the Chemical & Petroleum Engineering Department for the Graduate Scholarly Presentation Travel Fund, the School of Engineering for the Graduate Student Ambassador (GEA) travel fund, the Graduate Studies at the University of Kansas for the award of

Doctoral Student Research Fund. I also want to express my thanks to the chair of Gordon Research Seminar (GRS) and Gordon Research Conference (GRC) on Natural Gas Hydrate Systems, Dr. Xiaojing Fu and Dr. Tim Collett for the financial support.

I thank the present and past colleagues, Dr. Zhaoqi Fan, Dr. Di Chai, Dr. Gang Yang, Ms. Xuejia Du, Mr. Yuhao Yang, and Ms. Julia Espinoza, for the technical discussions and the enjoyable time we had at the University of Kansas.

Last but not least, I would like to thank my parents, Mrs. Xiaoling Luo and Mr. Chongde Zheng. Particular thanks to my elder brother and my role model, Mr. Jixiang Zheng. I am blessed to have him around when I was growing up.

TABLE OF CONTENTS

ABSTRACT.....	iii
ACKNOWLEDGMENT.....	vii
TABLE OF CONTENTS.....	ix
LIST OF FIGURES	xiii
LIST OF TABLES.....	xviii
NOMENCLATURES	xix
CHAPTER 1 INTRODUCTION	1
1.1 Background.....	1
1.2 Objective of This Study	5
1.3 Outline of This Dissertation.....	6
CHAPTER 2 LITERATURE REVIEW	8
2.1 Determination of Hydrate Phase Boundary	8
2.1.1 Experimental research	8
2.1.2 Theoretical modeling	10
2.2 Hydrate Formation and Structure	13
2.2.1 Observations of hydrate nucleation	18
2.2.2 Hydrate structure and stability	22
2.3 Hydrate Systems Containing CH ₄ , C ₂ H ₆ , and CO ₂	25

2.4 Summary	31
CHAPTER 3 EXPERIMENTAL MEASUREMENTS OF GAS HYDRATE PHASE BEHAVIOR	
.....	33
3.1 Database of Hydrate Phase Boundary	33
3.2 Experimental Measurement	41
3.2.1 Experimental apparatus	42
3.2.2 Experimental materials and procedure	43
3.2.3 Measurement of the hydrate phase boundary	46
3.2.4 Observation of hydrate formation at the interface	47
3.3 Summary	50
CHAPTER 4 DETERMINATION OF THE HYDRATE PHASE BOUNDARY USING SEPARATE MODELS FOR NON-HYDRATE PHASES	
.....	52
4.1 Basic Framework to Determine Hydrate Phase Boundary Pressure	52
4.1.1 Determination of water chemical potential difference in the aqueous phase	55
4.1.2 Determination of water chemical potential in the hydrate phase	56
4.1.3 Reference Properties	58
4.1.4 Kihara parameters	62
4.1.5 Effect of Electrolytes	64
4.2 Separate Models for Aqueous and Gas-rich Phases	65
4.2.1 Mathematical models	65

4.2.2 Simulation results	68
4.3 A Single Modified PR EoS for Aqueous and Gas-rich Phases	79
4.3.1 Mathematical models.....	79
4.3.2 Simulation results	81
4.4 Summary.....	86
CHAPTER 5 DETERMATION OF THE HYDRATE PHASE BOUNDARY USING A UNIFIED EOS FOR THE NON-HYDRATE PHASES	88
5.1 Model Development	88
5.1.1 Unified EoS	88
5.1.2 Model Parameters	94
5.1.3 Calculation Algorithm	98
5.2 Simulation Results.....	100
5.2.1 Phase boundary of CH ₄ hydrates in single-electrolyte solutions.....	100
5.2.2 Phase boundary of CH ₄ hydrate in mixed-electrolyte solutions.....	106
5.2.3 Phase boundary of CH ₄ -CO ₂ and CH ₄ -C ₂ H ₆ hydrates in single-electrolyte solutions	109
5.2.4 Phase boundary of CH ₄ -CO ₂ and CH ₄ -C ₂ H ₆ hydrates in mixed electrolyte solutions	112
5.2.5 Phase boundary of hydrates in pure water.....	114
5.3 Summary.....	116

CHAPTER 6 INSIGHTS INTO THE STABILITY OF CH ₄ -C ₂ H ₆ /CO ₂ HYDRATES USING MOLECULAR DYNAMIC SIMULATION.....	118
6.1 Structure of Hydrate Cages.....	119
6.1.1 sI hydrate structure	119
6.1.2 sII hydrate structure	121
6.2 MD Simulation	121
6.2.1 Potential models.....	121
6.2.2 Simulation procedures	123
6.2.3 Simulation scenarios.....	125
6.3 MD Simulation Results.....	131
6.3.1 Stability of CH ₄ -C ₂ H ₆ hydrates in sI and sII structures.....	131
6.3.2 Stability of CH ₄ -C ₂ H ₆ -CO ₂ hydrates with various gas compositions.....	138
6.3.3 Stability of CH ₄ -C ₂ H ₆ -CO ₂ hydrates at various pressures.....	145
6.4 Summary	155
CHAPTER 7 CONCLUSIONS AND RECOMMENDATIONS FOR FUTURE WORK	158
7.1 Conclusions.....	158
7.2 Recommendations for Future Work	162
REFERENCES	165

LIST OF FIGURES

Fig. 1-1 Schematic structures of gas hydrates (Koh and Sloan, 2007)	2
Fig. 1-2 Schematic diagram of the potential applications of gas hydrates	3
Fig. 1-3 Phase boundary of hydrates in different systems	5
Fig. 2-1 Schematic curve of gas consumption during hydrate formation (Verrett et al., 2012) ...	14
Fig. 2-2 Schematic diagram of free energy change during hydrate formation	15
Fig. 2-3 Morphology of CH ₄ -C ₂ H ₆ hydrate film at various guest composition and degree of subcooling (Li et al., 2014).....	18
Fig. 2-4 Nucleation of the first CH ₄ hydrate cage (Walsh et al., 2009).....	20
Fig. 2-5 Nucleation of the mixed CH ₄ -CO ₂ hydrate cage at different gas compositions	21
Fig. 2-6 Schematic diagram of the structure change of CH ₄ -C ₂ H ₆ hydrates (Ballard and Sloan, 2000)	23
Fig. 2-7 Occupancy preference of CH ₄ molecules in the small and large cages in sI and sII hydrates (Hester and Sloan, 2005)	25
Fig. 2-8 Schematic diagram of structure change of mixed CH ₄ -C ₂ H ₆ -CO ₂ hydrates.....	30
Fig. 3-1 Schematic diagram of experimental apparatus applied in the measurement the phase boundary of gas hydrates	43
Fig. 3-2 Schematic diagram of determining the hydrate phase boundary using the isochoric-pressure search method.....	45
Fig. 3-3 Comparison of the measured phase boundary data of CH ₄ hydrates formed in pure water with the ones collected in the literature	46
Fig. 3-4 Evolution of hydrate formation in the PVT cell.....	49

Fig. 3-5 Evolution of hydrate dissociation in the PVT cell. (a)-(d) are in the time order.	50
Fig. 4-1 Schematic diagrams of the configuration of water and gas molecules in (a) aqueous phase; (b) stable hydrate cages of the sI unit cell; (c) stable hydrate cages of the sII unit cell; (d) unoccupied hydrate cages of the sI unit cell.	52
Fig. 4-2 Flowchart to calculate the hydrate phase boundary using the chemical-potential-difference criterion.	54
Fig. 4-3 Flowchart to select the phase boundary pressure (P_I and P_{II} represent the phase boundary pressure of sI and sII hydrates, respectively).	55
Fig. 4-4 Sensitivity of the calculated phase boundary pressure of CH ₄ hydrates to the reference properties	61
Fig. 4-5 Flowchart to determine the phase boundary of gas hydrates using separate model for aqueous and gas-rich phases	68
Fig. 4-6 Calculated and measured phase boundary of CH ₄ hydrates formed in pure water and NaCl solutions.	70
Fig. 4-7 Calculated and measured phase boundary of C ₂ H ₆ hydrates formed in pure water and NaCl solutions.	72
Fig. 4-8 Calculated and measured phase boundary of CO ₂ hydrates in pure water and NaCl solutions.	73
Fig. 4-9 Calculated and measured phase boundary of CH ₄ -C ₂ H ₆ hydrates in pure water and NaCl solutions.	75
Fig. 4-10 Calculated and measured phase boundary of CH ₄ -CO ₂ hydrates in pure H ₂ O.	77
Fig. 4-11 Calculated and measured phase boundary of CH ₄ -CO ₂ hydrates in NaCl solutions. ...	79

Fig. 4-12 Flowchart to calculate the phase boundary using a single model for the aqueous and gas-rich phases	81
Fig. 4-13 Calculated and measured phase boundary of CH ₄ -C ₂ H ₆ hydrates in pure water and NaCl solutions.....	82
Fig. 4-14 Comparison of the collected phase boundary data (symbols) with the calculated phase boundary (curves) of CH ₄ -CO ₂ hydrates formed in pure water.	84
Fig. 4-15 Comparison of the collected and measured phase boundary data (symbols) with the calculated phase boundary (curves) of CH ₄ -CO ₂ hydrates formed in NaCl solutions.	85
Fig. 5-1 Schematic diagram of the interactions between various components.....	89
Fig. 5-2 Flowchart of the phase boundary calculation using the new model	98
Fig. 5-3 Flowchart of determining the fugacity and water activity using the unified EoS.....	100
Fig. 5-4 Collected and calculated phase boundary of CH ₄ hydrate formed in NaCl solutions (Symbols represent collected data points, curves denote calculated results, numbers are NaCl concentrations in wt%)	103
Fig. 5-5 Collected and calculated phase boundary of CH ₄ hydrate formed in KCl solutions	104
Fig. 5-6 Collected and calculated phase boundary of CH ₄ hydrate formed in MgCl ₂ solutions	105
Fig. 5-7 Collected and calculated phase boundary of CH ₄ hydrate formed in CaCl ₂ solutions .	106
Fig. 5-8 Collected and calculated phase boundary of CH ₄ hydrate formed in mixed NaCl-KCl solutions.....	108
Fig. 5-9 Collected and calculated phase boundary of CH ₄ hydrate formed in the mixed NaCl-CaCl ₂ solutions.....	109
Fig. 5-10 Collected and calculated phase boundary of binary CH ₄ -CO ₂ hydrate formed in NaCl solutions.....	111

Fig. 5-11 Collected and calculated phase boundary of CH ₄ -C ₂ H ₆ and CH ₄ -CO ₂ hydrates formed in NaCl, KCl, and CaCl ₂ solutions	112
Fig. 5-12 Collected and calculated phase boundary of CH ₄ -C ₂ H ₆ and CH ₄ -CO ₂ hydrates formed in mixed-electrolyte solutions.....	114
Fig. 5-13 Collected and calculated phase boundary of CH ₄ -CO ₂ hydrates formed in pure water	115
Fig. 6-1 Configuration of the sI hydrate cages	120
Fig. 6-2 Configuration of the sII hydrate cages	121
Fig. 6-3 Flowchart of the MD simulation employed in this work	125
Fig. 6-4 Cage occupancy of CH ₄ molecules in the small and large cages.....	128
Fig. 6-5 Cage occupancy of C ₂ H ₆ molecules in the small and large cages	129
Fig. 6-6 Cage occupancy of CO ₂ molecules in the small and large cages of sI hydrates	130
Fig. 6-7 Configuration of sI and sII hydrates at the end of simulation of the Scenario #1 (a-sI, b-sII).....	131
Fig. 6-8 MSD of H ₂ O molecules in the sI and sII hydrates of the Scenarios #1 and #3.....	132
Fig. 6-9 MSD of H ₂ O molecules in the sI and sII hydrates of the Scenarios #2 and #4.....	133
Fig. 6-10 Rotation of two random H ₂ O and two CH ₄ molecules in the sI hydrates in Scenario #1	134
Fig. 6-11 Rotational motion of H ₂ O molecules in the sI and sII hydrates of the Scenarios #1 and #3	135
Fig. 6-12 Rotational motion of H ₂ O molecules in the sI and sII hydrates of the Scenarios #2 and #4	136
Fig. 6-13 RDF of O-O in H ₂ O molecules in the sI and sII hydrates of the Scenarios #1 and #3	137

Fig. 6-14 RDF of O-O in H ₂ O molecules in the sI and sII hydrates of the Scenarios #2 and #4	138
Fig. 6-15 Rotation angle (a), MSD (b), and RDF (c) of H ₂ O molecules in Scenarios #5 and #7	139
Fig. 6-16 Rotation angle (a), MSD (b), and RDF (c) of CH ₄ molecules in Scenarios #5 and #7	140
Fig. 6-17 Rotation angle (a), MSD (b), and RDF (c) of C ₂ H ₆ molecules in Scenarios #5 and #7	140
Fig. 6-18 Rotation angle (a), MSD (b), and RDF (c) of CO ₂ molecules in Scenarios #5 and #7	141
Fig. 6-19 Rotation angle (a), MSD (b), and RDF (c) of H ₂ O molecules in Scenarios #9 and #11	142
Fig. 6-20 Rotation angle (a), MSD (b), and RDF (c) of CH ₄ molecules in Scenarios #9 and #11	143
Fig. 6-21 Rotation angle (a), MSD (b), and RDF (c) of C ₂ H ₆ molecules in Scenarios #9 and #11	144
Fig. 6-22 Rotation angle (a), MSD (b), and RDF (c) of CO ₂ molecules in Scenarios #9 and #11	144
Fig. 6-23 Potential energy of between water and gas molecules	145
Fig. 6-24 Rotation angle, MSD, and RDF of H ₂ O molecules in Scenarios #5 (a), #7 (b), #9
 (c), #11 (d)	148
Fig. 6-25 Rotation angle, MSD, and RDF of CH ₄ molecules in Scenarios #5 (a), #7 (b), #9
 (c), #11 (d)	150
Fig. 6-26 Rotation angle, MSD, and RDF of C ₂ H ₆ molecules in Scenarios #5 (a), #7 (b), #9
 (c), #11 (d)	152
Fig. 6-27 Rotation angle, MSD, and RDF of CO ₂ molecules in Scenarios #5 (a), #7 (b), #9
 (c), #11 (d)	154

LIST OF TABLES

Table 2-1 The average gas composition in Gulf of Mexico	26
Table 2-2 Gas size and the gas-cage diameter ratios of sI and sII hydrates	28
Table 3-1 Collected phase boundary data of CH ₄ hydrates	34
Table 3-2 Collected phase boundary data of C ₂ H ₆ hydrates.....	36
Table 3-3 Collected H-A-V three-phase boundary data of CO ₂ hydrates	37
Table 3-4 Collected phase boundary data of binary CH ₄ -C ₂ H ₆ hydrates	38
Table 3-5 Collected phase boundary data of binary CH ₄ -CO ₂ hydrates.....	40
Table 3-6 Experimental scenarios and the measured phase boundary of CH ₄ -CO ₂ hydrates	47
Table 4-1 Summary of reference properties determined in the literature	59
Table 4-2 The optimized Kihara parameters of CH ₄ and CO ₂	63
Table 5-1 The parameters of CH ₄ , C ₂ H ₆ , CO ₂ and H ₂ O	95
Table 5-2 Solvated ion diameter and BIP of water-ion pairs.....	95
Table 5-3 Parameters of uncharged ions.....	97
Table 5-4 Phase boundary of pure CH ₄ hydrates formed in single-electrolyte solutions.....	101
Table 5-5 Phase boundary of pure CH ₄ hydrates formed in mixed electrolyte solutions.....	107
Table 5-6 Phase boundary of binary hydrates formed in single-electrolyte solutions.....	110
Table 5-7 Phase boundary of binary hydrates formed in single-electrolyte solutions.....	113
Table 6-1 Parameters and potential function in the MD simulation.....	122
Table 6-2 Designed scenarios with various gas composition and pressure conditions	126
Table 6-3 The occupancy ratio of various gas components in the small and large cages of sI and sII hydrates.....	127

NOMENCLATURES

List of symbols

A_i, B_i = constants defined in Eq. 4-26

A_R, B_R, C_R = coefficients of the reference hydrate phase boundary in Eq. 4-2

A_ϕ = Debye-Huckel coefficient

a = attractive energy parameter in the PR EoS, J·m³

a_w = water activity

b = molar covolume in the PR EoS, cm³/mol

b_1 = constant in Eq. 4-6, J/mol/K²

B = the London coefficient

\bar{C}_p = molar heat capacity, J/K

C = Langmuir constant, MPa⁻¹

D_r = relative permittivity of electrolyte solution

D_s = relative permittivity of pure water

D_0 = the permittivity of vacuum, F/m

E = maximum attractive potential energy, J

e = electronic charge, esu

f = fugacity, MPa

H = Henry's constant, atm

\bar{H} = molar enthalpy, J/mol

ΔH_d = dissociation enthalpy, J/mol

I = ionic strength, molality

k_B = Boltzmann constant, J/K

k_{ij} = binary interaction parameter between i and j

m = concentration of NaCl in the aqueous phase, molality

N_A = Avogadro number, mol⁻¹

n_e = the number of electrons in the ions

n_g = number of gas species

n_i = moles of ions in the aqueous phase, mol

P = pressure, MPa

R = universal gas constant, J/K/mol

R_i = radius of hydrate cage i , Å

T = temperature, K

ν = stoichiometric numbers of ions

\bar{V} = molar volume, m³/mol

W = potential energy of water-gas interaction, J

x = molar composition

Z = ion charge

z = overall composition in the system

Z_c = compressibility factor

Greek symbols

α = Alpha function in the PR EoS

α_p = polarizability of ions, \AA^3

A^r = change in the Helmholtz free energy, J

$\beta_0, \beta_1, \beta_2$ = electrolyte-specific constants defined in Eq. 4-15

ε_w = dielectric constant of water

μ = Chemical potential, J/mol

\mathcal{V} = number of hydrate cages per water molecule

ρ = density, kg/m^3

θ = hydrate cage occupancy fraction

σ_i^{Born} = the diameter of solvated ion in the Born term, \AA

σ_j = zero potential energy distance of gas species j , \AA

σ_i^{MSA} = the ion diameter in the MSA term, \AA

σ^P = the Pauling diameter of ions, \AA

ϕ_w = fugacity coefficient of water

ψ_i = coordination number of hydrate cage i

ϖ_j = hard-core radius of gas molecule j , \AA

ω = acentric factor

Subscripts and superscripts

H = hydrate phase

A = aqueous phase

c = critical properties, e.g., critical pressure and temperature

r = reduced properties, e.g., reduced temperature

w = water components

π = unoccupied hydrate cage

* = pure

0 = reference condition

Abbreviations

AARD average absolute relative deviation

BIP binary interaction parameter

CPA cubic-plus-association

EoS equation of state

DH Debye-Huckel

DSC differential scanning calorimetry

GC gas chromatograph

GoM Gulf of Mexico

IbTS isobaric temperature search

IcPS isochoric pressure-search

IthPS isothermal pressure search

MD molecular dynamic

MSA mean spherical approximation

MSD	mean square displacement
PR	Peng-Robinson
PSO	particle swarm optimization
PVT	pressure-volume-temperature
RDF	radial distribution function
SAFT	statistical association fluid theory
SDS	sodium dodecyl sulfate
THF	Tetrahydrofuran
vdW-P	van der Waals-Platteeuw

CHAPTER 1 INTRODUCTION

1.1 Background

Gas hydrates are ice-like solid compounds of water and gas molecules. The water molecules connect with each other by hydrogen bonds to form a cage structure and gas molecules will be trapped inside the cages through van der Waals force. Therefore, the water and gas in the hydrate cages are also named as the host and guest molecules, respectively. Based on the configuration of the water molecules, numerous structures of hydrate cages have been identified, e.g., 5^{12} , $5^{12}6^2$, and $5^{12}6^4$, as shown in Fig. 1-1, where the vertices represent water molecules and the edges denote the hydrogen bonds. For example, 5^{12} represents a hydrate cage that is made of 12 faces and each face consists of 5 edges. Gas hydrates are a collection of tons of hydrate cages. These hydrate cages stick together by following a certain pattern. A number of patterns, i.e., basic structures of gas hydrates have been identified according to the cage types and the number of different cages in a unit structure. The most two common structures for simple natural gas hydrates are structure-I (sI) and structure-II (sII), as demonstrated in Fig. 1-1. It is illustrated that a unit sI hydrate is made of two small cages (5^{12}) and six large cages ($5^{12}6^2$) and that of sII hydrate is composed of sixteen small cages and eight large cages ($5^{12}6^4$). In general, small molecules of CH_4 and CO_2 tend to form sI hydrates whereas large ones, e.g., C_3H_8 will form sII hydrates.

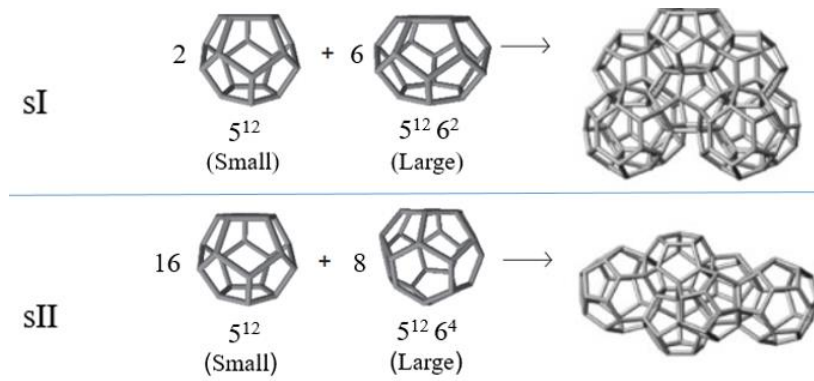


Fig. 1-1 Schematic structures of gas hydrates (Koh and Sloan, 2007)

Gas hydrates were initially regarded as a problem in flow assurance because they would block the pipelines for natural gas transport or the wellbores (Hammerschmidt, 1934). A few decades ago, natural gas hydrates were found widely distributed in nature, e.g., in the permafrost areas and under the seafloor. It was estimated that the hydrocarbons trapped in natural gas hydrate reservoirs were more than twice of those in other fossil fuels (Burshears et al., 1986). Numerous efforts have been made to understand the mechanisms and feasibility of gas production from hydrate reservoirs using various approaches, e.g., experiments in the lab (Li et al., 2015a; 2015b; 2016a; Yousif et al., 1990), mathematical calculations (Li et al., 2016b; Zheng et al., 2015; 2017), and numerical simulation (Li et al., 2017; 2020; Sun et al., 2005; Zheng et al., 2018a; 2018b). A number of in-situ field-scale tests have been carried out to explore the possibility of commercial exploitation of gas hydrate reservoirs, e.g., Alaska of the USA, Qilian Mountain of China, Nankai Trough of Japan, and the first commercial production at Messoyakha (Anderson et al., 2014; Colwell et al., 2004; Makogon et al., 2013; Zhao et al., 2013). However, unexpected hydrate dissociation in the underground, e.g., under the seafloor may induce geological hazards. The cementation effect of hydrates on the porous media is important for the geological stability (Zheng et al., 2019).

Recently, gas hydrates have found themselves an important role in industrial applications, e.g., gas separation, storage, transportation, and desalination (Babu et al., 2018; Cai et al., 2019; Gambelli et al., 2019; Inkong et al., 2019; Kastanidis et al., 2019; Xu et al., 2018). Hydrate-based technologies might be more efficient than conventional methods. For instance, over 160 m³ natural gas can be stored in a unit volume of hydrates at relatively moderate pressure and temperature conditions. When the temperature is below the freezing point, the gas hydrates will be more stable owing to the self-preservation effect (Chong et al., 2016). Hydrate-based desalination takes advantage of the fact that the ions cannot enter the hydrate cages. Therefore, by forming hydrates with seawater first and then dissociating the separated solid hydrates, relatively fresh water can be obtained. The significance of gas hydrate research is summarized in Fig. 1-2.

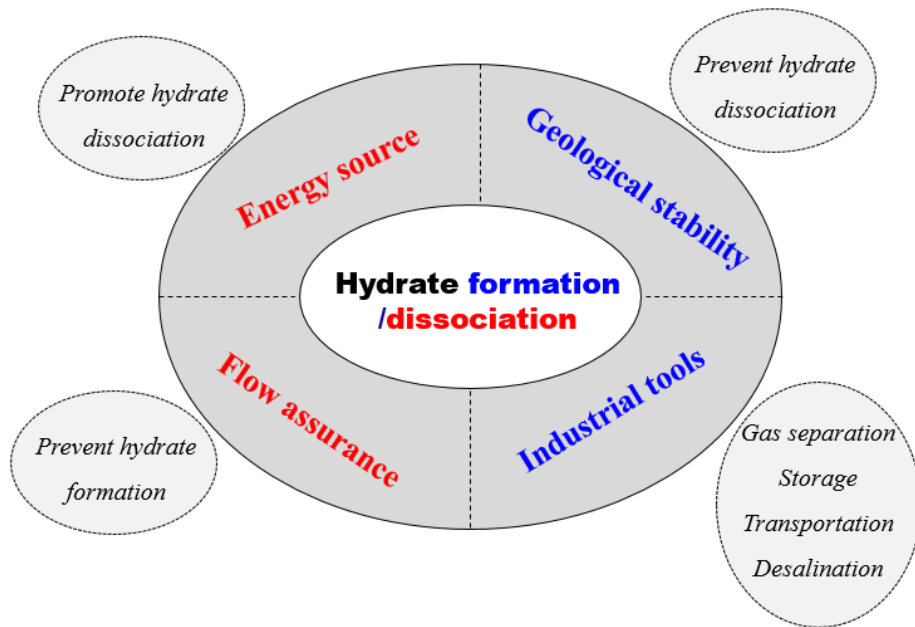


Fig. 1-2 Schematic diagram of the potential applications of gas hydrates

Gas hydrates tend to be stable at high-pressure and low-temperature conditions and will be dissociated when the pressure is reduced or the temperature is elevated. The incipient hydrate formation condition is termed as the phase boundary of gas hydrates. The phase boundary of CH₄ hydrates formed in pure water is illustrated as the black dots in Fig. 1-3, which divides the phase diagram of the system into two zones, i.e., the hydrate-present zone above the curve and the hydrate-absent zone below the phase boundary curve. Phase boundary is the foundation to understand the formation and dissociation behaviors of a hydrate system. The phase boundary of gas hydrates is influenced by numerous factors, e.g., gas species, composition of the gas mixture, and the chemical additives in the aqueous phase. As demonstrated in Fig. 1-3, the phase boundary pressure decreases when C₂H₆ or CO₂ is added into the CH₄-H₂O system, whereas it increases as the chemical additive, i.e., NaCl is added. The elevation of phase boundary pressure by adding the chemical additives is termed as the inhibition effect and the chemical additives in this scenario are called inhibitors. Some other chemical additives, e.g., sodium dodecyl sulfate (SDS) and Tetrahydrofuran (THF) can reduce either the kinetics or the phase boundary pressure of hydrate formation and therefore, are named promoters. Inhibitors are widely applied in flow assurance to prevent hydrate accumulation in the pipelines and effective promoters of hydrates are being explored in hydrate-based technologies, e.g., desalination, gas separation and storage.

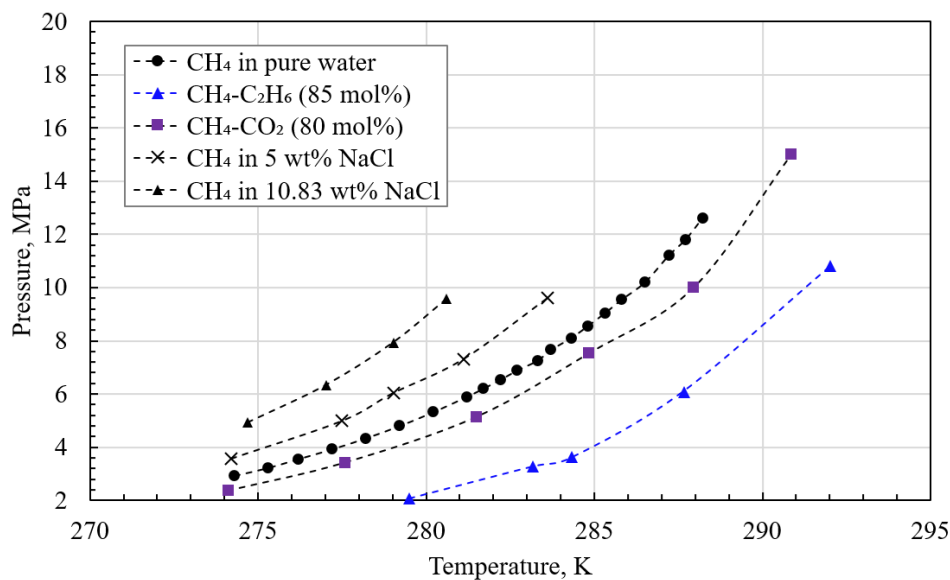


Fig. 1-3 Phase boundary of hydrates in different systems

(The data points in this figure can be found in the database in Chapter 3)

1.2 Objective of This Study

The objective of this study is to elucidate the phase behavior, i.e., the phase boundary, stability and growth behavior of CH₄-C₂H₆-CO₂ hydrates using experimental measurement, theoretical modeling, and molecular dynamic (MD) simulation methods. The specific goals include:

i) To establish a comprehensive database of the measured phase boundary of the single and binary CH₄, C₂H₆, and CO₂ hydrates formed in pure water and NaCl solutions covering a wide range of pressure and temperature conditions, including the corresponding experimental approaches. This database will not only provide a benchmark to validate the experimental apparatus and the experimental procedures adopted in this work, but also serves as a tool to cross-verify the collected data from various sources and further verify the reliability of the theoretical models developed in this work.

ii) To measure the phase boundary of the binary CH₄-CO₂ hydrates formed in pure water and NaCl solutions by employing the high-pressure PVT cell. These data points fill the blank of CH₄-CO₂ hydrates formed in NaCl solutions at the high-pressure conditions.

iii) To analyze the impact of parameters, e.g., reference properties on the determination of hydrate phase boundary and develop new theoretical phase boundary models by using a different set of reference properties. Three theoretical models are developed in this work to predict the phase boundary of gas hydrates. The first model is a standard one using the original Peng-Robinson (i.e., PR) equation of state (i.e., EoS) and the Henry's law respectively for the gas-rich phase(s) and the aqueous phase. In the second model, a single modified PR EoS is developed to calculate the aqueous and gas-rich phases. In these two models, the effect of electrolyte on the hydrate phase boundary is quantified by employing the Pitzer model. In the third model, a unified EoS is proposed to account for the non-hydrate phases, i.e., the aqueous phase, the gas-rich phase, and the dissolved electrolytes.

iv) To explore the mechanisms behind the structure change of the CH₄-C₂H₆ hydrates with gas composition using the MD simulation. The effect of CO₂ and pressure on the hydrate structure stability is also elucidated.

1.3 Outline of This Dissertation

This dissertation consists of seven chapters. Chapter 1 describes the background and objectives of this research. Chapter 2 provides a literature review regarding the determination of hydrate phase boundary using experimental approaches and the theoretical models; hydrate nucleation and growth process using MD simulation, experiments, and mathematical models; hydrate stability

and structure change with gas composition and pressure conditions; previous research the CH₄-C₂H₆ hydrates and motivations to the study of CH₄-C₂H₆-CO₂ hydrates formed in pure water and saline water systems. In Chapter 3, a comprehensive database of measured phase boundary of CH₄, C₂H₆, CO₂, CH₄-C₂H₆, CH₄-CO₂ hydrates is established. The phase boundary of CH₄-CO₂ hydrates formed in NaCl solutions at high-pressure conditions is measured by using the designed experimental apparatus in this work to fill the blank of the database. The growth behavior of hydrates formed at the interface of gas-bulk water and water-gas bubble is also observed and recorded. In Chapter 4, the basic framework of determining the hydrate phase boundary is introduced. Two theoretical models using separate models for the non-hydrate components, i.e., gas, water, and electrolytes. The impact of reference properties is evaluated by using sensitivity analysis. A new set of reference properties are used in all the theoretical models developed in this research. The Kihara parameters of CH₄, C₂H₆, and CO₂ are optimized by employing the particle swarm optimization approach. A unified EoS is developed in Chapter 5 so that all the non-hydrate components can be considered in the unified EoS. The performance of this model is evaluated by comparing with the collected phase boundary data points of pure and binary CH₄, C₂H₆, and CO₂ hydrates formed in single and mixed NaCl, KCl, CaCl₂, and MgCl₂ solutions. In Chapter 6, the stability of CH₄-C₂H₆ and CH₄-C₂H₆-CO₂ hydrates at various gas composition and pressure conditions are investigated by using MD simulation. The cage occupancy in all the designed scenarios are calculated using the developed theoretical model. The rotational and translational motion of gas molecules and cage water is analyzed in detail to examine the stability of hydrate cages and the interactions between gas and water and between different gas molecules. In Chapter 7, the conclusions of this work and the recommendations for the further work is summarized.

CHAPTER 2 LITERATURE REVIEW

Various research topics have been developed on gas hydrates, e.g., hydrate formation and dissociation behaviors, and physical properties (Braeuer et al., 2015; Ji et al., 2019; Khurana et al., 2017; Majid et al., 2017; Li et al., 2016a; 2016b; 2017; Zheng et al., 2015). The phase boundary of gas hydrates refers to the pressure and temperature conditions of the incipient hydrate formation, which can be influenced by many factors, e.g., gas composition, components in the aqueous phase, and the confinement (Cai et al., 2020; Chen et al., 2017; Li et al., 2015a; 2015b; Song et al., 2016). The confinement, e.g., porous media will increase the phase boundary pressure due to the presence of capillary effect (Østergaard et al., 2002; Uchida et al., 2004). This work focuses on the phase boundary of hydrates formed in the bulk phase, where the impact of the capillary pressure is negligible (Zheng et al., 2020b). This is because the phase boundary of hydrate in porous media is greatly influenced by the properties of the porous media, e.g., pore size distribution, which makes it hard to evaluate the reliability of measured data from various sources. Also, the phase boundary of hydrates in porous media can be determined by combining the phase boundary of hydrates in the bulk phase with an additional term, e.g., capillary pressure (Goel, 2006).

2.1 Determination of Hydrate Phase Boundary

2.1.1 Experimental research

Quantities of experimental studies have been carried out on the phase boundary of gas hydrates formed in various hydrate-forming systems in the bulk phase over the past decades by many researchers. For example, Adisasmito et al. (1991) measured the phase boundary of hydrates

formed by pure gas components with pure water. The impacts of impurities in the gas phase (Dholabhai and Bishnoi, 1994; Legoix et al., 2017; McLeod and Campbell, 1961), as well as inhibitors and promoters in the aqueous phase on the phase boundary of gas hydrates, have been quantified (Belandria et al., 2012; Fan et al., 2001; Kang et al., 1998; Porz et al., 2009; Ricaurte et al., 2012; Sun et al., 2001). Apart from the phase boundary of gas hydrates, the interfacial phenomenon is also significant for the analysis of the phase behavior of gas hydrate systems because hydrate formation mainly occurs at the water-gas interface. Various experimental systems have been established to investigate the interfacial phenomenon during hydrate formation, and can be roughly divided into two categories, i.e., dynamic system (Yu et al., 2020) and static system (Sun et al., 2007). It has been found that the hydrate formation at the water-gas interface is greatly influenced by the size and shape of the gas bubble, NaCl concentration, and the driving force of hydrate formation (Li et al., 2015a).

Various experimental apparatus and approaches have been utilized by different researchers (Khan et al., 2016; Shahnazar and Hasan, 2014). The pressure-volume-temperature (PVT) cell is a common device to measure the phase boundary of gas hydrates using isochoric pressure-search (IcPS), isobaric temperature search (IbTS), and isothermal pressure search (IthPS) approaches. These experimental methods have different advantages and limitations. For example, the phase boundary dissociation method is only applicable for systems with a unit degree of freedom. The reliability of the measured experimental data can be affected by the experimental approaches. For instance, the phase boundary conditions are commonly determined visually in the IbTS and IthPS methods, i.e., to visually catch the pressure and temperature at which the last visible hydrate particle disappears in the PVT cell or the Cailletet equipment (De Roo et al., 1983). Therefore, the accuracy of the visual determination approach is restricted by the experience of the observers and

the IcPS method is more reliable. New techniques, e.g., DSC, Raman, and light beams may improve the reliability of the measured data (Cha et al., 2016; Jager and Sloan, 2001; Kharrat and Dalmazzone, 2003; Maekawa, 2001; Zhong et al., 2019). Also, the measurement procedures, e.g., the temperature elevation rate during the heating process, have a significant impact on the accuracy of the measured experimental data. One example is the graphic method that is commonly used in the IcPS approach, in which the phase boundary is determined by a sharp change in the slope of the pressure-temperature curve in the heating process. Errors may be introduced if the rate of temperature elevation is too large during the heating process (Tohidi et al., 2000), even though the graphic method is thermodynamically sound (Zheng et al., 2020c).

2.1.2 Theoretical modeling

Numerous efforts have been made to reproduce and predict the phase boundary of gas hydrates. A typical thermodynamic model of hydrate phase boundary bears three functions, i.e., *i*) able to handle the hydrate phase, *ii*) capable of describing the chemical additive-free non-hydrate phases, and *iii*) able to quantify the effect of chemical additives in the aqueous phase. Various approaches have been developed for the hydrate phase, such as empirical approaches of specific gravity and K-value method (Katz, 1945; Wilcox et al., 1941), and thermodynamic models (Parrish and Prausnitz, 1972; van der Waals and Platteeuw, 1958). The most popular model is the van der Waals-Platteeuw (vdW-P) model, which assumes that the gas molecules do not distort the hydrate cages, hydrate cages are perfectly spherical, gas molecules can freely rotate within the cavities, and the partition of gas molecules into the hydrate cages resembles Langmuir adsorption (van der Waals and Platteeuw, 1958). These assumptions are valid for simple gas molecules in ordinary conditions. Xu et al. (2011) revealed through a first-principle calculation that the distortion of

hydrate cages was negligible for small molecules, e.g., CH₄ and C₂H₆. However, they may not be valid at some other conditions, e.g., high pressure and large molecules. More sophisticated models have been proposed for complicated systems over the years. Examples include the removal of the assumptions in the vdW-P model, e.g., the gas molecules do not distort the hydrate cage (Ballard and Sloan, 2002; Klauda and Sandler, 2003; Zele et al., 1999), gas molecules can freely rotate within the cavities (John et al., 1985), the hydrate cages are perfectly spherical (Sparks et al., 1999), and the Langmuir adsorption assumption (Chen and Guo, 1996). Furthermore, different modeling frameworks have been tested for the chemical additive-free non-hydrate phases, i.e., gas-rich phase and additive-free aqueous phase. The first example is to employ combined models, e.g., a cubic equation of state (EoS) combined with Henry's law and a cubic EoS combined with mixing rules (Munck et al., 1988; Osfouri et al., 2015; Yang et al., 1997). Another example is to apply a single EoS, e.g., modified Peng-Robinson (PR) EoS or cubic-plus-association (CPA) EoS (Aasen et al., 2017; Li and Yang, 2013; Meragawi et al., 2016). The latter approach is advantageous in thermodynamic consistency but is more complex than the former one (Jager et al., 2003). Moreover, cutting-edge research techniques, e.g., ab initio quantum mechanical calculation is well-accepted to determine parameters in the thermodynamic models (Anderson, 2005; Cao, 2002; Velaga and Anderson, 2013).

Apart from gas and water components, the electrolytes dissolved in the reservoir fluids also have a significant impact on the phase boundary of gas hydrates by competing for water molecules with gas (Englezos and Bishnoi, 1988). The electrostatic forces generated by the dissolved electrolytes make the modeling work more challenging. Different models have been developed to account for the effect of the dissolved electrolytes on the phase boundary of gas hydrates. For instance, Zheng et al. (2020b) developed a model to predict the hydrate phase boundary by

combining a modified PR EoS and the Pitzer activity model. Zuo and Guo (1991) combined the Patel-Teja (PT) EoS with a Debye-Huckel (DH) term and Kurihara's mixing rule to calculate the phase equilibrium of electrolyte solutions at high-temperature conditions. Later, Liao et al. (1999) applied this model in predicting the phase boundary of gas hydrates by replacing the Kurihara's mixing rule with a classical one and applying ion-water binary interaction parameters (BIP). Masoudi et al. (2003) modified Zuo and Guo's model by eliminating the DH term and employing the non-density dependent (NDD) mixing rule. In general, the combined models are advantageous in simplicity, and the single, or unified models outweigh the combined models in the consistency of the thermodynamic foundation. Søreide and Whitson (1992) took into account the effect of electrolytes by using the modified Alpha function and binary interaction parameters. A combination of EoS with an electrostatic term approach has been explored and produces satisfactory results in specific conditions (Zuo and Stenby, 1997). Unified electrolyte-EoS models, which explicitly consider the interactions among gas, water, and dissolved ions by summing up the contributions of various interactions to the Helmholtz free energy are gaining increasing attention (Selam et al., 2018). Numerous unified models have been proposed to quantify the impact of various components on the change of system free energy (Fürst and Renon, 1993), e.g., electrolyte-statistical association fluid theory (e-SAFT) models (Selam et al., 2018) and electrolyte-CPA (e-CPA) models (Courtial et al., 2014). Also, activity models, e.g., the Pitzer model have been widely applied which proves to be reliable up to the electrolyte concentration of six molalities (Pitzer and Mayorga, 1973). In the Pitzer model, the ions are regarded as hard spheres and a continuous solvent assumption is made, which is not suitable for high concentrated electrolyte solutions where the short-range interactions, e.g., the repulsive interactions between ions of like sign and the ion-water interactions are strong. In a sense, the Pitzer model is a semi-

empirical collection of functions and terms keeping a balance between the simplicity in the calculation and the accuracy in reproducing the experimental data. In general, the Pitzer model applied in this work is capable of representing the effect of electrolytes on water activity up to the concentration of 6 molalities. Efforts have been made to extend the Pitzer model into higher concentrated electrolyte solutions, e.g., by combining with a short-range water activity coefficient model, which involves a large number of adjustable parameters.

2.2 Hydrate Formation and Structure

The hydrate formation process has been divided into two stages, i.e., hydrate nucleation and hydrate growth (Bishnoi and Natarajan, 1996). A schematic plot of gas consumption during hydrate formation is presented in Fig. 2-1. In the nucleation stage, i.e., section (a) in Fig. 2-1 the gas and water molecules organize into stable critical nuclei under the effect of hydrophobic hydration which induces a significant decrease in entropy of the solution. In the hydrate growth stage, i.e., section (b) in Fig. 2-1 the gas consumption rate increases rapidly due to the high rate of hydrate formation.

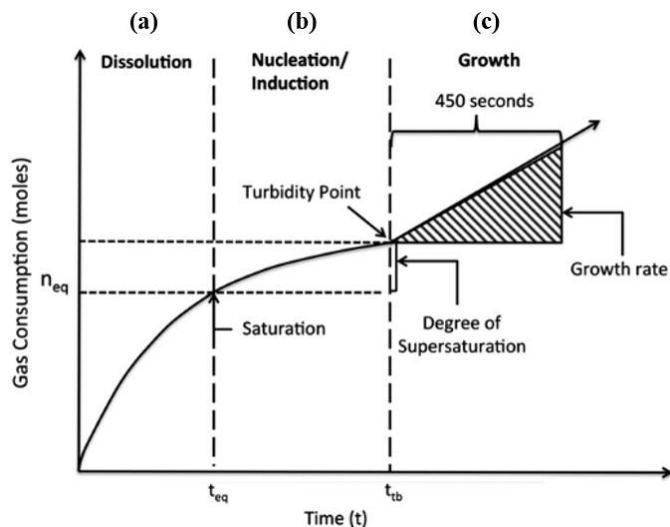


Fig. 2-1 Schematic curve of gas consumption during hydrate formation (Verrett et al., 2012)

The critical nuclei serve as a boundary to distinguish the hydrate nucleation and growth stages. Quantitatively, the critical nucleus is defined as the hydrate crystal having the same probability of dissociation and nucleation, i.e., 50% respectively (Guo et al., 2011; Zhang et al., 2016). Physically, the amorphous nuclei or crystalline nuclei of hydrates will be formed at low-temperature and high-pressure conditions in the water-guest mixture because the newly formed hydrate nuclei are more stable than the original water-guest system at the given conditions (Barnes and Sum, 2013). However, an energy penalty is needed to form the interface between the new hydrate phase and the original phases of the water-guest mixture. In the early stage, i.e., when the size of hydrate nuclei is smaller than that of the critical nuclei, the effect of this energy penalty is dominant and the formed hydrate nuclei are more likely to be dissociated. Above the size of critical nuclei, the impact of free energy decrease induced by the formation of the hydrate phase is dominant, which promotes hydrate growth at a relatively high rate (Debenedetti and Sarupria,

2009). The schematic diagram of free energy variation during hydrate formation is illustrated in Fig. 2-2.

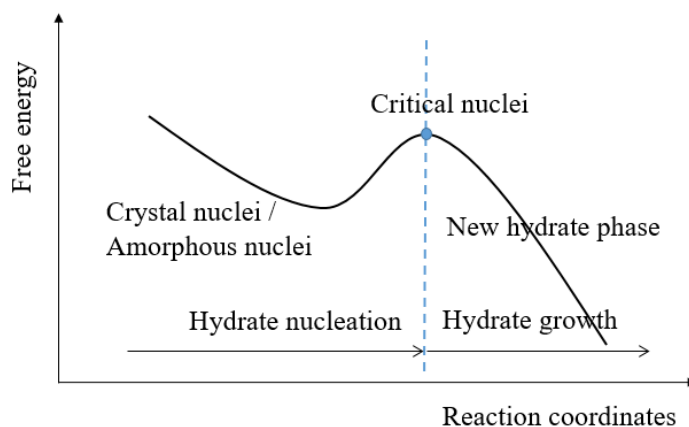


Fig. 2-2 Schematic diagram of free energy change during hydrate formation

Observations of hydrate surface morphology can extend our knowledge on hydrate formation kinetics and are also significant for the study of interfacial properties. For example, the roughness of the hydrate surface has a great impact on the crystal-crystal cohesive force (Aman et al., 2012). The morphology of hydrate particles may change the dissociation behavior, e.g., it was found the dissociation rate of the dendritic particle is slower (Wang et al., 2020). Freer et al. (2001) asserted that single crystals tended to form at low driving-force, which was proceeded by a step mechanism; while at high driving force, facets disappeared and the hydrate film became roughened due to the continuous mechanism. Various shapes of hydrate crystals have been observed, e.g., triangle, polygons, and sword-like shape, as presented in Fig. 2-3 (Li et al., 2014), where we can see the variation of hydrate surface morphology with the degree of subcooling, guest species, and the guest composition. Ohmura et al. (2005) found that the morphology of CH₄ hydrate crystals formed at

the interface of vapor and gas-saturated water phases changes from columnar to polygonal to dendritic with the increase in pressure. It was observed that the size of individual hydrate crystals on the hydrate film decreased with the increase of CH₄ composition in CH₄-C₂H₆-C₃H₈ (Saito et al., 2011). It was indicated that the morphology of the hydrate surface was in favor of mass or heat transfer which in turn contributed to the further growth of the hydrate film (Li et al., 2014). Aman and Koh (2016) suggested that asserted that the change of hydrate film morphology is to maximize the crystal surface area to volume ratio to release the heat from hydrate formation. Researchers have tried to classify the morphology of hydrate film based on the degree of subcooling (Sakemoto et al., 2010; Saito et al., 2011; Tanaka et al., 2009). The additives in the aqueous phase, e.g., hydrate inhibitors also influence the morphology of hydrate surface by changing the wettability of the water-gas interface (Aman et al., 2010). In addition, the morphology of hydrate surface is greatly influenced by the location of hydrate formation. For instance, it was found that the maximum hydrate particle size in the bulk liquid is larger than that in the gas-water interface, but the average particle size in the bulk liquid is smaller than that at the interface, which is due to the larger shear force caused by stirring in the bulk liquid phase (Wang et al., 2020). Servio and Englezos (2003) demonstrated the hydrate film formed at the gas-water droplet interface has higher roughness.

The morphology of hydrate surface is determined by the lateral and thickness growth of the hydrate film, which is further a function of subcooling, supersaturation, gas composition, and chemical additives in the aqueous solutions (Liu et al., 2018; Sun et al., 2018). The lateral growth rate of hydrate film changes with the gas components, e.g., the lateral growth rate of CH₄-C₃H₈ mixed hydrates is smaller than that of pure hydrates at the same driving force; In turn, the thickness of hydrate film of the mixed hydrates is larger than that of the pure hydrates due to the limitation

of mass transfer (Peng et al., 2007). Kishimoto et al. (2012) found that the morphology of single cyclopentane hydrate crystals is not influenced by the concentration of NaCl, but the lateral growth rate of the hydrate film decreased with the addition of NaCl. The lateral hydrate film growth rate changes with gas species, e.g., the rate of CO₂ hydrates formed at the gas-water droplet interface is higher than that of CH₄, C₂H₆, and C₃H₈ at the same degree of subcooling (Tanaka et al., 2009). Li et al. (2014) measured the lateral and thickness growth of pure and mixed CH₄-C₂H₆ hydrate film formed at the interface of the gas bubble and the surrounding water and found that the lateral growth rate is higher for pure than the mixed hydrates and the initial thickness of hydrate film is smaller for the pure hydrate. By observing the measured lateral hydrate film growth rate of different gas molecules, Saito et al. (2010) concluded that the lateral growth of hydrate film is more mass-transfer limited than heat-transfer. Various mass-transfer-rate-limiting models of the thickness growth of hydrate film have been established, e.g., diffuse layer models, permeable micro-perforated plate model (e.g., guest permeable and water permeable), and sedimented particle aggregate layer model, based on different assumptions of mass transfer (Mori, 1998). Peng et al. (2007) used the convective heat-transfer model to calculate the lateral hydrate film growth rate which fitted well with the measured ones formed at the interface of the gas bubble and the surrounding water. In their model, the thickness growth rate of the hydrate film was assumed inversely proportional to the degree of subcooling. Freer et al. (2001) established a model combining kinetics and heat transfer. Sugaya and Mori (1996) proposed three controlling mechanisms of hydrate film growth at the interface, i.e., water-gas interaction at the interface, diffusive transport of water and gas across the interface, diffusive transfer of heat released by hydrate formation.

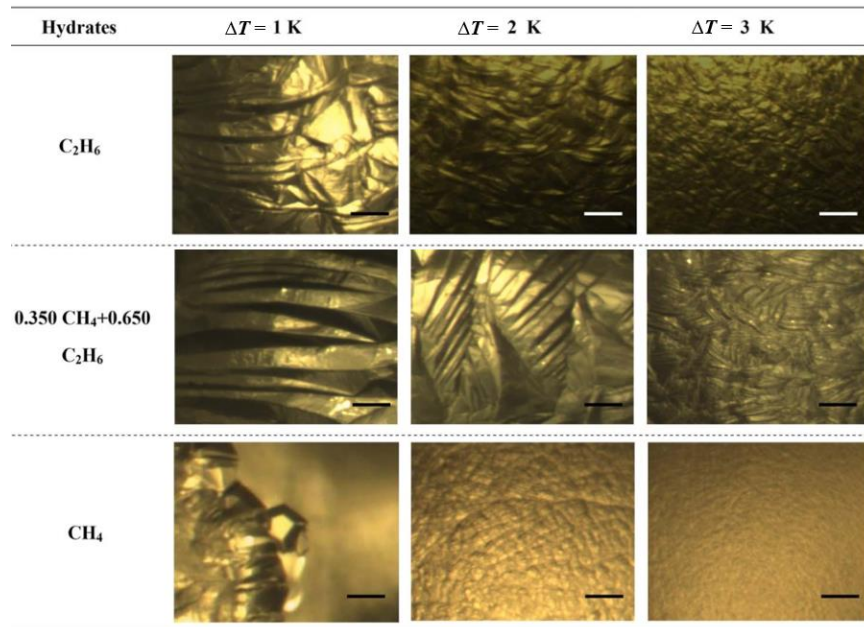


Fig. 2-3 Morphology of CH_4 - C_2H_6 hydrate film at various guest composition and degree of subcooling (Li et al., 2014)

2.2.1 Observations of hydrate nucleation

Hydrate nucleation is triggered by the subcooling (i.e., $\Delta T = T_e - T_s$, where T_e and T_s denote the equilibrium temperature and the temperature of the system, respectively) or the supersaturation and is a stochastic process, which has been reflected by the extended induction time. Numerous hypotheses have been proposed for the hydrate nucleation, e.g., local structuring, labile clusters, cage adsorption, and blob mechanism hypothesis (Lehmkuhler et al., 2009; Liu, 2017; Radhakrishnan and Trout, 2002). The cage adsorption hypothesis is more promising according to the MD simulation. For instance, it was found that the dissolved CH_4 molecules tend to be adsorbed to the hydrate cage, and by evaluating hydrogen bonds it was concluded that the adsorbed CH_4 will enhance the connectivity of water molecules in the hydrate cage (Guo et al., 2007).

The stochastic nature of hydrate nucleation makes it challenging to fully understand this process. Due to the small dimensions along the pathway hydrate nucleation occurs (i.e., nanometer-scale) and the short timescale (i.e., typically in microseconds), it is difficult to observe the hydrate nucleation process through experiments (Aman and Koh, 2016). With the development of molecular dynamic (MD) simulation, several insights into the hydrate nucleation process have been provided in recent decades. One representative process of hydrate nucleation is presented in Fig. 2-4 (Walsh et al., 2009), which highlights the ordering of CH₄ guest and water molecules during the formation of the first hydrate cage. The first observation to note is the adsorption force of the water rings and the partial water cages to the CH₄ guest molecules. In Fig. 2-4(A), one water ring made of five water molecules adsorbs two orange CH₄ molecules on opposite sides of this water ring. When the first hydrate cage is formed, 11 CH₄ molecules are adsorbed on the water faces of the hydrate cage, as shown in Fig. 2-4(D). It should be noted that the first cage formed in this MD simulation is a 5¹² one, which is consistent with the molecular-level experimental observations (Schicks and Luzi-Helbing, 2013). These adsorbed CH₄ molecules become more ordered around the hydrate cage with time going by, as illustrated in Fig. 2-4(E). In separate research, Guo et al. (2007; 2009) not only observed the adsorption of CH₄ molecules on the hydrate cage but also found that the adsorbed guest molecules can enhance the stability of the hydrate cage. Guo et al. attributed the enhanced stability of the hydrate cage to the decreased hydrogen bond between water forming the cage and the water molecules in the surrounding aqueous phase. Another observation is the dissociation of the incomplete hydrate cage by comparing the Fig. 2-4(B) and Fig. 2-4(C). This fluctuation may be one source of the stochastic nature of the hydrate nucleation process. One more observation is that the water rings in the hydrate cage open and break

before the formation of new hydrate cages with the absorbed CH₄ molecules, as demonstrated in Fig. 2-4(F).

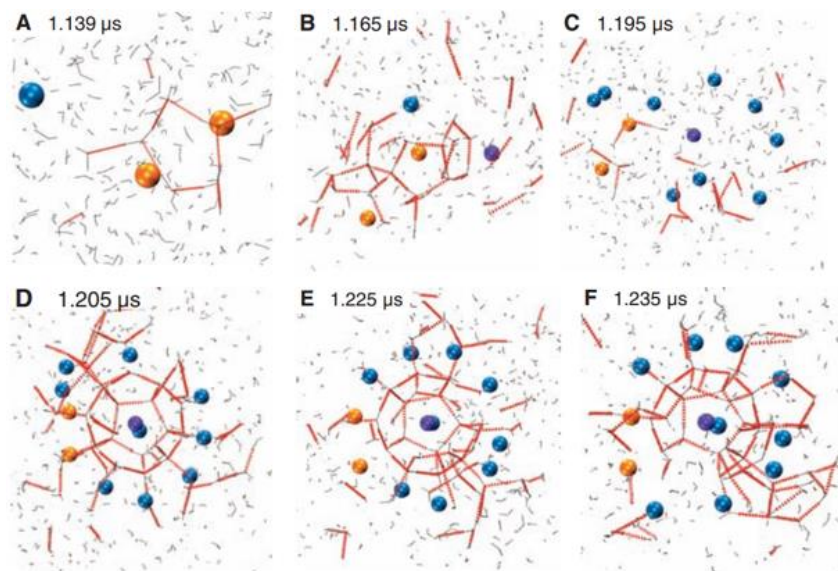


Fig. 2-4 Nucleation of the first CH₄ hydrate cage (Walsh et al., 2009)

(Water: gray lines; Methane: blue spheres; Hydrogen bonds: red lines; Violet sphere: the first methane molecule to become permanently enclathrated; Two orange sphere: the first absorbed CH₄ molecules)

The nucleation of mixed CH₄-CO₂ hydrates has been investigated, as presented in Fig. 2-5 (He et al., 2016). Similar to the nucleation of pure CH₄ hydrate, the adsorption of guest molecules to the water rings occurs in Fig. 2-5(A). Also, the first complete hydrate cage formed in a mixed CH₄-CO₂ system is a 5¹² one occupied by CH₄, as shown in Fig. 2-5(B) through Fig. 2-5(D). It is evaluated that the 5¹² cage structure has the smallest deviation from the hydrogen bond network of water (He et al., 2016), i.e., the lowest entropy penalty (Liu, 2017). The adsorption ratio, i.e.,

the ratio of guests adsorbed on the cage faces changes with the guest composition. For example, the adsorption ratio of CH₄-to-CO₂ is 7:4 when the CH₄ concentration in the mixed guests is 50%, i.e., Fig. 2-5(B) and when it decreases to 25%, i.e., Fig. 2-5(C), the adsorption ratio becomes 5:5. The fluctuation, i.e., the dissociation of incomplete cages and the opening and break of the hydrate cage before the formation of new cages are observed as well in the mixed hydrate nucleation. It is worth noting that some other types of hydrate cages than those illustrated in Fig. 1-1 have been detected by a various researcher in the nucleation stage, e.g., 5¹²6³, 4¹⁵10⁶2, 4¹⁵10⁶3, and 4¹⁵10⁶4 not only for mixed but also for pure gas hydrates (He et al., 2016; Vatamanu and Kusalik, 2006; Wilson et al., 2016). These hydrate cages are metastable but might be kinetically preferred during hydrate nucleation. For example, the 4¹⁵10⁶2 hydrate cages have been found formed in the early stage and more common than other cages during C₂H₆ hydrate nucleation, but gradually change into other thermodynamically preferred cages, e.g., 5¹²6² (Wilson et al., 2016). Therefore, the observation of the hydrate nucleation process is greatly sensitive to the time scale applied in the MD simulation.

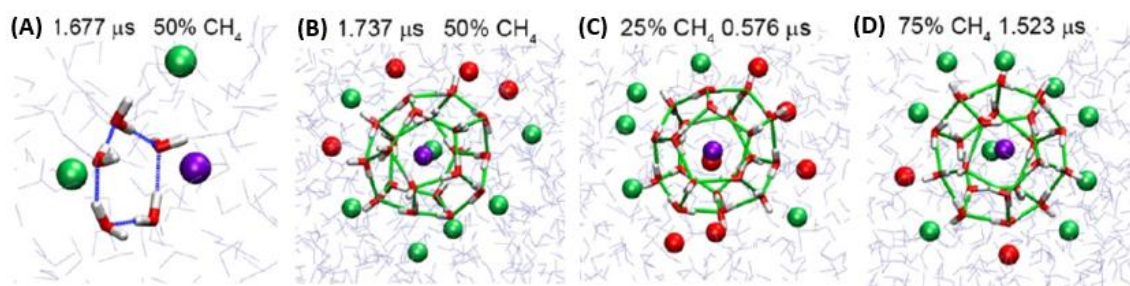


Fig. 2-5 Nucleation of the mixed CH₄-CO₂ hydrate cage at different gas compositions

(Free water: gray lines; CH₄: blue spheres; CO₂: red sphere; Violet sphere: the central CH₄ molecule to form the first hydrate cage; Water molecules forming cages around the central CH₄ molecule are shown as red and white rods)

2.2.2 Hydrate structure and stability

The specific structure formed at a given condition is a comprehensive result of the kinetic and thermodynamic stability of hydrate cages. The impact of the kinetics of hydrate formation on the hydrate structure mainly dominant in the nucleation stage and the initial stage of hydrate growth. As aforementioned, various hydrate structures can be formed, depending on the gas species, gas composition, pressure, and temperature conditions. Many experimental efforts have been made to identify the structure of gas hydrates, e.g., Raman spectroscopy (Schicks and Ripmeester, 2004), NMR spectroscopy (Pietrass et al., 1995), and X-ray diffraction (Chou et al., 2000). For instance, Chou et al. (2000) observed the sII structure of CH₄ hydrates when the pressure was elevated up to 100 MPa, which was also indicated in the experimental phase boundary data measured by Dyadin et al. (1997). The coexistence of sI and sII CH₄ hydrates at moderate pressure and temperature conditions were also indicated in the Raman spectra experiments (Schicks and Ripmeester, 2004). An intermediate phase was indicated during xenon hydrate formation (Pietrass et al., 1995). The sII structure was also detected in the CO₂ hydrates (Fleyfel and Devlin, 1991; Staykova et al., 2003). De Menezes et al. (2019) investigated the hydrates formed in CH₄-C₃H₈-H₂O systems using HP- μ DSC and a PVT cell and observed the coexistence of sI and sII hydrates. It is noted that there are different conclusions in the hydrate structure change. For instance, Hirai et al. (2000) reported that no structure change of the CH₄ hydrates was observed in the X-ray experiment when the pressure ranged from 200 to 5500 MPa. Fleyfel and Sloan (1991) suggested that no structure change was observed in the CH₄-C₂H₆ hydrates because the pressure-temperature curves shared the same slope in their work. Molecular dynamic (MD) simulation is also a powerful tool in hydrate structure research. Walsh et al. (2009) detected sI-sII coexistence for CH₄ hydrates in a microsecond time scale MD simulation. Moon et al. (2003) observed the simultaneous

formation of sI and sII hydrates during nucleation, in which the sII structure was inferred from the observations that the small cages, i.e., 5^{12} were face-sharing connected. Furthermore, the hydrate structures have also been investigated using the thermodynamic models. Ballard and Sloan (2000) demonstrated the structure change of the $\text{CH}_4\text{-C}_2\text{H}_6$ hydrates at various pressure and gas composition conditions by employing a theoretical model, as shown in Fig. 2-6.

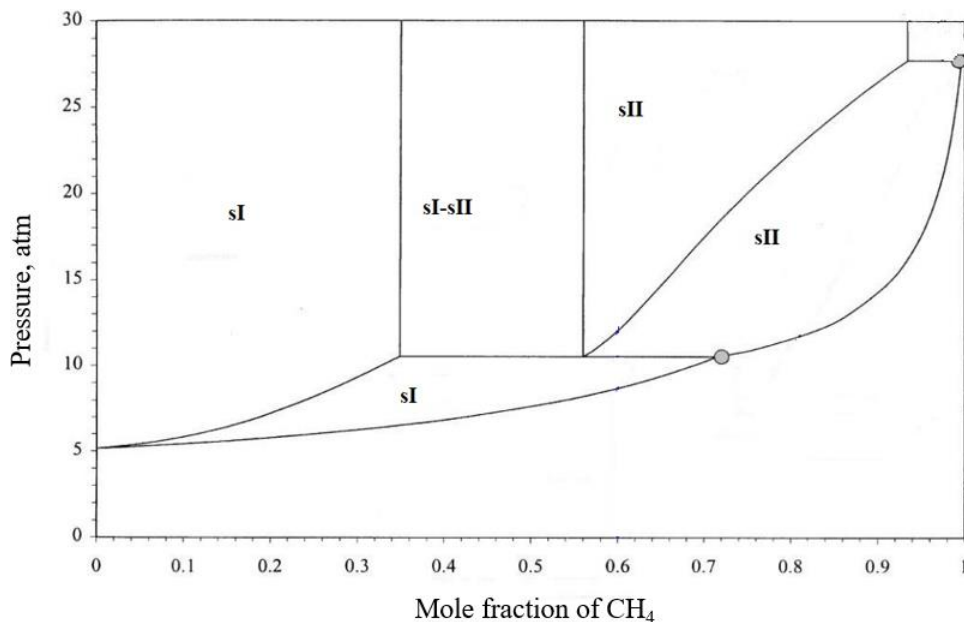


Fig. 2-6 Schematic diagram of the structure change of $\text{CH}_4\text{-C}_2\text{H}_6$ hydrates (Ballard and Sloan, 2000)

The stability of gas hydrates is crucial to the hydrate structure, which is inferable from the preference of gas occupancy in various hydrate cages. Hester and Sloan (2005) quantified the cage occupancy of gas molecules in the small and large cages of sI and sII hydrates using the Langmuir constant, as shown in Fig. 2-7. According to the Langmuir adsorption described in Eq. 4-8, larger Langmuir constant results in a higher fraction of gas molecules in the hydrate cages. Therefore,

CH₄ hydrates are more stable in sI structure. Experiments and MD simulation also have been widely used to evaluate the stability of gas hydrates. Chialvo et al. (2002) compared the structure stability of the sI CH₄ hydrates with various cage occupancy using MD simulation and concluded that the configuration energy decreased monotonically with cage occupancy. The stability of the hydrate structure is influenced not only by the overall cage occupancy but also by the occupancy of small and large cages. For example, the stability of sI CO₂ hydrates increases with the overall cage occupancy and it is more stable to occupy the large cages compared with the small ones (Liu et al., 2012). Martos-Villa et al. (2013) calculated the binding energy of sI CH₄ hydrates with various occupancy modes in small and large cages, it was found the binding energy increased with increasing occupancy in the large cages. Also, the binding energy of single CH₄ in small cages was found higher than that in the large cage, while that of CO₂ was higher in the large cages than in the small ones. Liu et al. (2016) designed various full cage occupancy for pure and mixed CH₄-CO₂ hydrates and analyzed the change in the interaction energy to evaluate the stability and fitness of CH₄ and CO₂ molecules in small and large cages in sI hydrates. By analyzing the potential energy and the mean square displacement (MSD) of atoms in the water cage, Qi and Zhang (2011) indicated that the stability of CH₄-CO₂ mixed hydrate with CO₂ occupancy of 75% is higher than that with 85% occupancy. Based on NMR study of mixed sI CH₄-C₂H₆ hydrates, it was found that the dissociation rate of C₂H₆ in the large cage is higher than CH₄ in the small cage (Dec et al., 2007). The authors also examined the faster dissociation behavior of C₂H₆ in large cages by combining with the thermodynamic models and suggested that the less stable behavior of C₂H₆ in large cages was due to the empty small cages. In an MD simulation of the sI CH₄-C₂H₆ hydrates, one peak in the RDF curve of C₂H₆-C₂H₆ pair was found equal to the average length between the

large cage of sI hydrates, i.e., $5^{12}6^2$, which indicated the stability of the hydrate structure at the simulation conditions and no cage distortion was observed (Erfan-Niya et al., 2011).

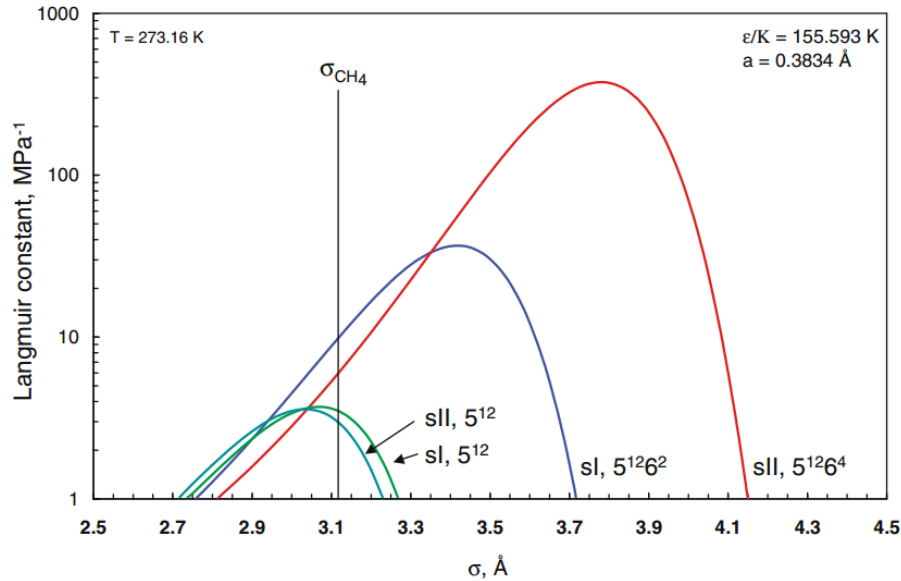


Fig. 2-7 Occupancy preference of CH_4 molecules in the small and large cages in sI and sII hydrates (Hester and Sloan, 2005)

2.3 Hydrate Systems Containing CH_4 , C_2H_6 , and CO_2

Systems containing CH_4 , C_2H_6 , and CO_2 are of great interest since CH_4 and C_2H_6 are the two most concentrated species in the natural gases (Kvenvolden, 1995). For example, the average composition of CH_4 and C_2H_6 in the natural gases is above 96 mol% in the Gulf of Mexico (GoM) and Alaska North Slope (Collett et al., 1988; Sassen et al., 1998). The mean gas composition at different locations of GoM is as shown in Table 2-1. The average gas composition of the vent gas: 93.15% CH_4 , 3.73% C_2H_6 , 1.96% C_3H_8 , 0.35% $i\text{-C}_4\text{H}_{10}$, 0.53% $n\text{-C}_4\text{H}_{10}$, 0.25% $i\text{-C}_5\text{H}_{12}$, 0.03% $n\text{-C}_5\text{H}_{12}$.

Table 2-1 The average gas composition in Gulf of Mexico

Location	Gas type	CH ₄	C ₂ H ₆	C ₃ H ₈	i- C ₄ H ₁₀	n- C ₄ H ₁₀	i- C ₅ H ₁₂	n- C ₅ H ₁₂	CO ₂	References
Green Canyon	Vent gas	93.42	4.22	1.22	0.24	0.64	0.36	0	0	Sassen and MacDonald, 1997
	Hydrate	61.30	10.48	9.70	2.25	5.50	10.63	0	0	
	Vent gas	93.15	3.45	2.45	0.30	0.45	0.20	0	0	Sassen et al., 1998
	Hydrate	76.78	10.00	9.85	1.85	1.18	0.35	0	0	
	Hydrate	69.03	5.97	17.13	4.03	0.82	0	0	2.97	Brooks et al., 1986
	Vent gas	93.13	3.58	2.07	0.37	0.53	0.23	0.12	0	Sassen et al., 2001a
	Hydrate	76.17	9.86	10.25	1.96	1.36	0.28	0.05	0	
	Sediment	87.70	7.20	3.30	0.50	0.90	0.20	0.20	0	Sassen et al., 2001b
	Vent gas	93.20	3.70	2.10	0.50	0.50	0.20	0	0	
	Hydrate	77.50	9.50	9.70	1.80	1.20	0.50	0	0	Sassen et al., 1999
Sediment	71.93	14.27	3.82	2.15	2.22	5.29	0.33	0		
Mississippi Canyon	Hydrate	75.18	7.53	11.20	5.45	0.50	0.15	0.10	0	Sassen et al., 2001a

CO₂ naturally exists in natural gas reservoirs and the gas hydrate reservoirs (Adisasmito and Sloan, 1992; Jia et al., 2019a; 2019b; van Denderen et al., 2009). It has been estimated that the composition of CO₂ in natural gas hydrate reservoirs is 0.1-4.6 mol% (Seo et al., 2000). The concentration of CO₂ in natural gases is being increased with enhanced oil recovery by CO₂ injection (Fan and Guo, 1999; Jia et al., 2018; Zhang et al., 2019), with the production of gas hydrates by CO₂ exchange and with CO₂ sequestration (Boswell et al., 2016). When the aforementioned CO₂-contained natural gases, with a majority of CH₄ and C₂H₆, are produced through wellbore or during wellbore drilling, gas hydrates may be formed, resulting in severe flow

assurance issues. Furthermore, CO₂ sequestration and hydrate production using CO₂ exchange are significant to alleviate global warming.

Another motivation to select CH₄/C₂H₆/CO₂ gas mixture as the targeted gas system is from the microscopic perspective. In consistence with the size ratio analysis in Table 2-2, CH₄, C₂H₆, and CO₂ have been proved as sI hydrate formers (Hester and Sloan, 2005; Ripmeester, 2000; Sloan and Koh, 2007), i.e., only sI hydrates will be formed by the three pure gases with H₂O along the hydrate phase boundary. However, surprising complexity will be introduced when these simple sI hydrate formers are mixed with each other due to the preference of various gas species in the different hydrate cages. For instance, by using full occupancy mode in the MD simulation, i.e., all the cages in the sI hydrates are occupied either by CO₂ or CH₄ molecules, Geng et al. (2009) concluded that at their simulation conditions, CO₂ molecules were more stable in the large cages in the sI hydrates and CH₄ molecules preferred the small cages, which was confirmed by the MD simulation work of Nohra et al. (2012). Experimentally, it was observed that CO₂ molecules can enter both the small and large hydrate cages (Fleyfel and Sloan, 1991). Hence, CO₂ will compete with C₂H₆ molecules for the large cages and under some conditions, it also competes with the CH₄ molecules for the small cages. Phase boundary data is a useful tool to reveal the mechanisms behind hydrate structure transition in systems containing CH₄ and C₂H₆, as well as the role of competing effect between C₂H₆ and CO₂ molecules. Gas molecules cannot enter the hydrate cage if the gas-to-hydrate cage diameter ratio, γ , is significantly larger than 1, whereas it requires a lower temperature to stabilize the hydrate structure if γ is too small (Adisasmito and Sloan, 1992). Overall, hydrates are more stable when γ is less and closer to 1 (Becke et al., 1992).

Table 2-2 Gas size and the gas-cage diameter ratios of sI and sII hydrates

Gas species	Gas diameter, Å	Gas-cage diameter ratio, γ			
		sI structure		sII structure	
		Small cage	Large cage	Small cage	Large cage
CH ₄	4.4	0.88	0.76	0.89	0.67
C ₂ H ₆	5.5	1.10	0.95	1.12	0.84
CO ₂	5.1	1.02	0.89	1.04	0.78

Moreover, sII hydrates have been found formed in systems containing CH₄-C₂H₆ gas mixture, even though CH₄ and C₂H₆ are both sI hydrate formers. By attributing two peaks in the Raman spectra of C-C stretching-vibration mode of C₂H₆ hydrates to C₂H₆ molecules in the large cage of sI and sII respectively, Uchida et al. (2002) detected the structure change of CH₄-C₂H₆ hydrates formed with ice particles. Only sI hydrates were formed when the vapor composition of C₂H₆ was below 2 mol% and above 22 mol%. However, sII hydrates were detected when the vapor C₂H₆ composition was between 2 and 12 mol%. By forming CH₄-C₂H₆ hydrates with water, Subramanian et al. (2000a) also observed the hydrate structure change when the vapor composition of C₂H₆ was between 25 and 27.8 mol% by using Raman and NMR spectroscopic measurements. The authors also detected a lower point for the structure change, i.e., 0.6-0.8 mol% of C₂H₆ in the vapor phase of the CH₄-C₂H₆ mixture (Subramanian et al., 2000b). It is noted that the determined guest composition where hydrate structure has changed is close but not exactly the same in these two research groups (Uchida et al., 2002; Subramanian et al., 2000a; 2000b). This is mainly attributed to the different experimental conditions, e.g., pressure and temperature. It is also noted that the pressure and temperature conditions applied in these measurements were well inside the phase boundary of gas hydrates. Ballard and Sloan (2000) shed light on the structure change of mixed CH₄-C₂H₆ hydrates at the incipient hydrate formation conditions through thermodynamic

modeling, which indicated that upper and lower structure change point varied with pressure and temperature. In addition, the coexistence of sI and sII hydrates was detected when the composition of C₂H₆ ranged from 12 to 22 mol% by Uchida et al. (2002). However, it had been presented that the coexistence of sI and sII hydrates of CH₄-C₂H₆ hydrates was metastable and would transform into either sI or sII structure depending on the guest composition (Ohno et al., 2009; Takeya et al., 2003). Efforts have been made to explore the mechanisms behind the structure change of mixed CH₄-C₂H₆ hydrates by using thermodynamic calculation (Adamova et al., 2010; Hendriks et al., 1996; Hester and Sloan, 2005; Uchida et al., 2002). Adamova et al. (2010) explored the sI and sII structure change of CH₄-C₂H₆ hydrates using molecular modeling. Uchida et al. (2002) indicated that the structure change was driven by two competing factors, i.e., the occupancy preference of guests in hydrate cages and the cage number ratio in different hydrate structures. For instance, C₂H₆ is thermodynamically more stable in 5¹²6⁴, i.e., the large cage in sII structure than in 5¹²6², i.e., the large cage in sI structure. On the other hand, the ratio of large cages in sI is greater than that of the large cage in sII, as illustrated in Fig. 1-1. Therefore, sI structure is preferred when the composition of C₂H₆ is high. However, this conclusion is based on a rough thermodynamic analysis of interactions between the hydrate cage and the specific guest molecules, which does not consider the impact of other guest molecules, e.g., the interactions between guest-guest molecules, and is not on a molecular level base. Besides, even though no structure change of mixed CH₄-CO₂ or C₂H₆-CO₂ hydrates has been reported, the appearance of CO₂ could impact the hydrate structure formed by CH₄-C₂H₆-CO₂ mixtures. This is because CO₂ molecules can not only enter the large cage of either sI or sII hydrates but also the smaller ones and therefore, will compete with CH₄ and C₂H₆ molecules for the small and large hydrate cages. This, for one thing, might change the cage occupancy due to the interactions of guest molecules and for another thing may also influence the

hydrate structure change. The aforementioned impacts of CO₂ on the formation of mixed CH₄-C₂H₆-CO₂ hydrates, as illustrated with the grey line in Fig. 2-8, are still unknown. In Fig. 2-8, the triangle is used to represent the composition of this system. The vertices and edges represent the pure gas component and binary gas mixture, respectively, and each point inside this triangle represents a ternary gas mixture. For example, the points along the edge of CH₄-C₂H₆ denote the binary CH₄-C₂H₆ gas mixture, and the composition of C₂H₆ increases as the point moves from left to right along this edge.

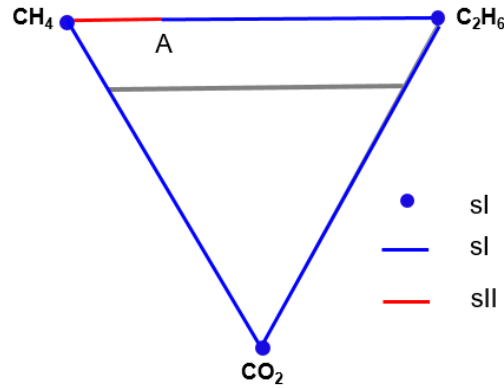


Fig. 2-8 Schematic diagram of structure change of mixed CH₄-C₂H₆-CO₂ hydrates

The sodium chloride (NaCl) is the most concentrated electrolyte in the seawater and reservoir fluids (Castellini et al., 2006; Fu and Aharon, 1998). It is believed that anions have a greater effect than cations on the phase boundary of gas hydrates, and the impact is elevated with a decrease in ion diameters (Cha et al., 2016). Hence, NaCl has been chosen to represent the impact of electrolytes on the phase boundary of gas hydrates by numerous researchers. The phase boundary of pure or binary CH₄, C₂H₆, and CO₂ hydrates formed in NaCl solutions is crucial for not only the flow assurance and energy recovery but also CO₂ sequestration. When the captured CH₄-CO₂

gas mixture, e.g., from biogas and coal-bed methane is sequestered in deep water or depleted fossil fuel reservoirs (White et al., 2005; Zatsepina and Pooladi-Darvish, 2012), it is important to understand the hydrate phase behavior at various CH₄, C₂H₆, and CO₂ composition and concentration of NaCl solutions.

2.4 Summary

A comprehensive literature review is carried out covering the experimental and theoretical modeling approaches in determining the phase boundary of gas hydrates formed in the bulk phase, experimental observations and MD simulation results of hydrate nucleation and growth behaviors, hydrate systems containing CH₄, C₂H₆, and CO₂ gas species. The reliability and shortcomings of various experimental devices and methods, e.g., IcPS, IbTS, and IthPS, are compared. Different frameworks of theoretical models for hydrate systems, e.g., combined models and single EoS models and various models accounting for the effect of electrolytes are summarized. The morphology of the surface of hydrate film formed at the water-gas interface is decided by the degrees of subcooling, supersaturation, gas composition, and chemical additives in the aqueous phase. The structure of gas hydrates is influenced by numerous factors, e.g., gas composition and pressure. A structure change of the CH₄-C₂H₆ hydrates has been observed in experiments and thermodynamic models. However, the mechanisms of CH₄-C₂H₆ hydrate structure change is unknown. Also, the structure stability of CH₄-C₂H₆-CO₂ hydrates is not clear. By examining the investigations of the hydrate formation process using MD simulation, it was found that two routines might be eligible to explore the mechanisms driving the structure change of mixed CH₄-C₂H₆ hydrates with the guest composition. The first routine is through simulating the nucleation process, i.e., starting from a mixture of guest and water molecules in the vapor and liquid phases

and run the simulation to figure out the final structure of the formed hydrates. The second routine is to evaluate the stability of the sI structure and the sII structure respectively of the mixed CH₄-C₂H₆ hydrates. The observation of nucleation results depends on the time scale of the simulation because the nucleation process is controlled by both kinetic and thermodynamic preferences of the guests in various hydrate cages. However, the structure change of interest in this work occurs in a relatively large time scale, e.g., lab observation and hydrates formed in nature. Therefore, the second routine is recommended.

CHAPTER 3 EXPERIMENTAL MEASUREMENTS OF GAS HYDRATE PHASE BEHAVIOR

3.1 Database of Hydrate Phase Boundary

A comprehensive database is critical not only for cross-verification of experimental data from different sources but also for reliable parameter regression in the modeling work. In this section, we have established a comprehensive database of the measured phase boundary of CH₄, C₂H₆, CO₂, and binary CH₄-C₂H₆ and CH₄-CO₂ hydrates formed in pure H₂O and NaCl solutions, which is an extension of the experimental data summarized by Sloan and Koh (2007). Experimental approaches applied in various research groups are also summarized in the new database, which is important to preliminarily evaluate the reliability of the experimental data. A total of 1036 measured equilibrium phase boundary data points for pure CH₄, C₂H₆, CO₂, and binary CH₄-C₂H₆, CH₄-CO₂ hydrate systems published in the period of 1946 to 2020 have been collected. Tables Table 3-1 through Table 3-5 list the equilibrium pressures and temperatures, measurement methods, water salinity, and the number of data points for gas hydrates formed by CH₄, C₂H₆, CO₂, and CH₄-C₂H₆, CH₄-CO₂ mixture, respectively.

The first group of experimental phase boundary data of CH₄ hydrates was provided by Deaton and Frost (1946), who systematically measured the phase boundary of CH₄ hydrates at moderate pressures. Researchers also measured the phase boundary of CH₄ hydrates at high-pressure conditions (Dyadin et al., 1997; Kobayashi and Katz, 1949; Marshall et al., 1964; Nakano et al., 1999). For example, Dyadin et al. (1997) investigated the phase behavior of CH₄ hydrates at pressures up to 1000 MPa and indicated a structure change of CH₄ hydrates at pressures higher

than 620 MPa. The phase boundary data of CH₄ hydrates formed in high concentrated NaCl solutions, up to 30 wt%, were supplemented by Hu et al. (2017). In this work, only the measured phase boundary data points of CH₄ hydrates with a temperature lower than 300 K and NaCl concentration smaller than 6 molalities, i.e., 25.98 wt% are collected and presented in Table 3-1, with the purpose of parameter regression and validation of the developed model in Chapter 4. A total of 383 data points have been collected in Table 3-1, in which 213 points are for the CH₄ hydrates formed in pure H₂O, and the other 170 data points are for those formed in NaCl solutions.

Table 3-1 Collected phase boundary data of CH₄ hydrates

<i>P</i> , MPa	<i>T</i> , K	Methods	NaCl, wt%	Data points	References
2.68-10.57	273.4-286.4	PBD		11	Adisasmito et al., 1991
2.69-10.04	273.3-286.0	IthPS (visual)		9	De Roo et al., 1983
2.77-9.78	273.7-285.9	IthPS (visual)		13	Deaton and Frost, 1946
20.19-50.45	291.9-298.7	IcPS (Raman)		9	Jager and Sloan, 2001
2.65-28.57	273.2-294.3	IcPS (visual)		8	Jhaveri and Robinson, 1965
2.92-9.54	274.3-285.8	IcPS (graphic)		17	Kamari et al., 2017
5.36-7.07	280.0-282.7	IcPS (graphic) & PBD		3	Kastanidis et al., 2016
5.73-7.68	281.2-284.0	IbTS (DSC)		3	Kharrat and Dalmazzone, 2003
2.90-12.60	274.2-288.2	IcPS (light)		30	Maekawa, 2001
15.93-43.78	290.2-298.2	IcPS (graphic)	0	7	Marshall et al., 1964
9.62-48.68	285.7-298.7	IcPS (visual)		8	McLeod and Campbell, 1961
2.96-8.96	274.2-285.2	IcPS (visual)		12	Mei et al., 1996
3.06-47.86	274.6-298.3	IcPS (graphic)		11	Mohammadi et al., 2005
2.92-9.54	274.3-285.8	PBD		17	Nakamura et al., 2003
2.77-28.02	273.6-294.0	IthPS (visual)		13	Ross and Toczykin, 1992
5.55-15.29	280.2-288.7	IcPS (graphic)		9	Sabil et al., 2014
5.00-25.00	279.5-293.0	IbTS (visual)		6	Sadeq et al., 2017
2.60-5.00	273.2-279.6	IcPS (visual)		3	Seo et al., 2001

3.50-6.50	276.3-282.1	IthPS (visual)		3	Servio and Englezos, 2002
2.87-6.10	275.4-281.2	PBD		6	Thakore and Holder, 1987
3.02-16.96	275.2-290.7	IcPS (visual)		7	Verma, 1974
3.53-9.38	276.3-285.6	IcPS (graphic)		8	Ward et al., 2014
3.42-22.50	274.5-291.1	IcPS (graphic)		6	Atik et al., 2009
2.75-5.36	272.7-279.4	IthPS (visual)	3	6	Dholabhai et al., 1991
4.00-7.90	276.4-283.1	IcPS (light)		7	Maekawa, 2001
7.00-20.00	281.3-290.1	IcPS (DSC)		5	Lafond et al., 2012
3.31-15.89	275.0-288.9	IcPS (light)	3.5	13	Maekawa et al., 1995
3.58-9.60	274.2-283.6	IcPS (graphic)	5	5	Mohammadi et al., 2008
3.97-10.02	275.1-283.7	IcPS (graphic)	5.44	5	Cha et al., 2016
6.60-67.81	280.7-299.1	IcPS (Raman)	6.22	11	Jager and Sloan, 2001
3.07-18.08	269.7-286.4	IcPS (light)	10	19	Maekawa et al., 1995
4.92-11.42	274.7-282.0	IcPS (graphic)	10.83	5	Cha et al., 2016
7.51-71.56	279.2-296.0	IcPS (Raman)	10.85	11	Jager and Sloan, 2001
2.69-7.55	268.3-278.0	IthPS (visual)	11.76	6	De Roo et al., 1983
4.50-7.57	272.7-277.7	IbTS (DSC)	11.89	3	Kharrat and Dalmazzone, 2003
28.80-79.4	288.0-296.0	IcPS (graphic)	12	2	Hu et al., 2017
3.93-26.50	269.5-285.1	IcPS (graphic)	15	3	Haghighi et al, 2009
4.23-8.57	269.2-277.7	IbTS (DSC)		3	De Roo et al., 1983
2.39-8.57	263.4-275.1	IthPS (visual)	17.13	5	Kharrat and Dalmazzone, 2003
7.92-70.56	274.4-291.0	IcPS (Raman)	17.17	10	Jager and Sloan, 2001
5.02-15.38	268.6-277.3	IcPS (graphic)		3	Haghighi et al, 2009
5.90-17.35	268.5-278.7	IcPS (light)	20	14	Maekawa et al., 1995
2.94-11.00	261.8-272.8	IthPS (visual)	21.52	7	De Roo et al., 1983
7.85-71.30	270.7-285.8	IcPS (Raman)	22.07	10	Jager and Sloan, 2001
28.20-186.00	277.0-293.0	IcPS (graphic)	23	6	Hu et al., 2017
4.78-9.55	263.0-268.6	IthPS (visual)	24.12	5	De Roo et al., 1983

Note: DSC- differential scanning calorimetry; PBD- phase boundary dissociation; IcPS- Isochoric pressure search; IthPS- Isothermal pressure search; IbTS- Isobaric temperature search.

Different from the CH₄ hydrates, the phase boundary of C₂H₆ hydrates is characterized by an upper quadruple point, which separates the hydrate-aqueous-vapor (i.e., H-A-V) three-phase

boundary from that of hydrate-aqueous-liquid C₂H₆ (i.e., H-A-L_{C₂H₆}). A total of 179 data points have been collected in Table 3-2, in which 118 points are for the C₂H₆ hydrates formed in pure H₂O, and the other 61 data points are for those formed in the NaCl solutions. These data points cover a temperature range from 265.4 to 296.5 K and the NaCl concentration of 3.1 to 20 wt%. The methods adopted to determine the phase boundary conditions are also summarized.

Table 3-2 Collected phase boundary data of C₂H₆ hydrates

<i>P</i> , MPa	<i>T</i> , K	Methods	NaCl, wt%	Data points	Reference
0.85-3.08	277.8-287.2	-		10	Avlonitis, 1988*
0.51-2.73	273.7-286.5	IthPS (visual)		20	Deaton and Frost, 1946
0.81-1.55	277.6-282.5	PBD		3	Galloway et al., 1970
0.95-3.36	278.8-288.2	IcPS (visual)		7	Holder and Hand, 1982
0.78-2.62	277.5-286.5	IcPS (visual)		7	Holder and Grigoriou, 1980
0.59-3.17	274.6-287.3	IcPS (light)		20	Maekawa and Imai, 2000
19.48-67.52	290.4-296.5	-		19	Nakano et al., 1998a*
3.33-20.34	288.0-290.6	IcPS (visual)		8	Ng and Robinson, 1985
0.55-6.84	273.4-288.4	-		18	Roberts et al., 1940*
0.60-32.52	273.9-292.0	IthPS (visual)		6	Ross et al., 1992
0.73-3.07	275.2-286.2	IcPS (light)	3.1	17	Maekawa and Imai, 2000
0.54-2.90	272.2-284.7	IcPS (graphic)	5	7	Mohammadi et al., 2008
0.88-2.17	273.7-280.4	IcPS (graphic)	10	5	Tohidi et al., 1997
0.70-2.88	271.6-282.1	IcPS (light)		13	Maekawa and Imai, 2000
1.08-2.15	272.7-277.1	IcPS (graphic)	15	3	Tohidi et al., 1997
1.21-2.48	268.9-274.2	IcPS (light)		7	Maekawa and Imai, 2000
0.69-1.52	266.3-271.5	IcPS (graphic)	20	4	Tohidi et al., 1993
0.74-1.83	265.4-271.9	IthPS (visual)		5	Englezos et al., 1991

Note: PBD- phase boundary dissociation; IcPS- Isochoric pressure search; IthPS- Isothermal pressure search.

* The original copy is not available, data are transferred from elsewhere (Sloan and Koh, 2007).

Similar to the phase boundary of C₂H₆ hydrates, the phase boundary of CO₂ hydrates is also featured by an upper quadruple point. However, the determined upper quadruple points of CO₂ hydrates in pure H₂O are diverse (Chapoy et al., 2011; Kastanidis et al., 2016; Mohammadi et al., 2005; Nakano et al., 1998; Ng and Robinson, 1985). In this work, only the measured phase boundary data of CO₂ hydrates with temperature below 282 K, i.e., H-A-V three-phase boundary data points are collected and tabulated in Table 3-3. The NaCl solution concentrations range from 3 wt% to 20 wt%. As can be seen in Table 3-3, a total of 187 data points have been collected for the phase boundary of CO₂ hydrates, 158 of which are for CO₂ hydrates formed in pure H₂O, and the rest 29 data points are for those formed in NaCl solutions.

Table 3-3 Collected H-A-V three-phase boundary data of CO₂ hydrates

<i>P</i> , MPa	<i>T</i> , K	Methods	NaCl, wt%	Data points	Reference
1.42-3.51	274.3-281.5	PBD		7	Adisasmito et al., 1991
1.32-3.71	273.7-281.9	IthPS (visual)		17	Deaton and Frost, 1946
1.50-2.78	274.7-279.7	IthPS (visual)		10	Fan and Guo, 1999
1.50-2.78	274.7-279.7	IthPS (visual)		3	Fan et al., 2000
2.04-3.69	277.2-281.9	IcPS (graphic)		4	Kamari et al., 2017
2.33-3.97	278.6-282.0	IcPS (graphic) & PBD		7	Kastanidis et al., 2016
1.05-3.69	271.8-282.0	Differential	0	33	Larson, 1955
1.82-3.69	276.5-282.0	IcPS (visual)	0	8	Mooijer-van den Heuvel et al., 2001
1.35-3.83	274.0-281.8	IcPS (graphic)		7	Ohgaki et al., 1993
1.38-3.84	273.9-282.0	-		6	Robinson and Mehta, 1971
1.10-3.38	272.7-281.5	IcPS (graphic)		11	Sabil et al., 2014
1.50-3.50	274.8-281.5	IcPS (visual)		4	Seo et al., 2001
2.04-3.69	277.2-281.9	IcPS (visual)		4	Unruh and Katz, 1949
1.22-3.68	273.1-281.8	-		37	Vlahakis et al., 1972 ^a
1.30-2.96	272.2-278.9	IthPS (visual)	3	4	Dholabhai et al., 1993

1.37-3.73	271.8-280.2	IcPS (graphic)	5	4	Mohammadi et al., 2008
1.66-3.62	273.6-279.7	Differential	5.53	4	Larson, 1955
1.16-3.16	268.0-276.1	IthPS (visual)	10	5	Dholabhai et al., 1993
1.86-3.23	263.2-276.1	IcPS (graphic)		4	Tohidi et al., 1997
1.21-3.24	265.4-273.0	IthPS (visual)	15	4	Dholabhai et al., 1993
1.52-3.12	263.2-268.8	IcPS (graphic)	20	4	Tohidi et al., 1997

Note: PBD- phase boundary dissociation; IcPS- Isochoric pressure search; IthPS- Isothermal pressure search.

^a The original copy is not available, data are transferred from elsewhere (Sloan and Koh, 2007);

‘-’ denotes that the information is unavailable.

The collected data points of the binary CH₄-C₂H₆ hydrates formed in pure H₂O and NaCl solutions are demonstrated in Table 3-4, with the composition of CH₄ in the feed CH₄-C₂H₆ gas mixture ranging from 1.6 mol% to 98.8 mol% and the NaCl concentration up to 23 wt%. A total of 185 data points have been collected in Table 3-4, in which 150 are for the binary CH₄-C₂H₆ hydrates formed in pure H₂O and 35 data points are for those formed in the NaCl solutions. The phase boundary pressure and temperature cover a range of 0.95-172.8 MPa and 274.8-314.2 K, respectively for the hydrates formed in pure H₂O. For those formed in the NaCl solutions, the measured phase boundary pressure and temperature are ranged from 4.00 to 179.00 MPa and 276.0 to 314.5 K, respectively.

Table 3-4 Collected phase boundary data of binary CH₄-C₂H₆ hydrates

CH ₄ , mol% ^a	<i>P</i> , MPa	<i>T</i> , K	Methods	NaCl, wt%	Data points	Reference
98.8	2.86-5.09	274.8-280.4	IthPS (visual)		3	Deaton and Frost, 1946
97.8	2.37-6.09	274.8-283.2	IthPS (visual)	0	5	Deaton and Frost, 1946
97.1	2.16-4.03	274.8-283.2	IthPS (visual)		3	Deaton and Frost, 1946

95	1.84-4.77	274.8-283.2	IthPS (visual)		5	Deaton and Frost, 1946
94.6	6.93-68.43	284.9-302.0	IcPS (visual)		8	McLeod and Campbell, 1961
90.4	1.52-3.97	274.8-283.2	IthPS (visual)		4	Deaton and Frost, 1946
85	2.08-10.80	279.5-292.0	IcPS (graphic)		6	Becke et al., 1992
80.9	6.90-68.57	284.9-304.1	IcPS (visual)		8	McLeod and Campbell, 1961
74.7	33.7-172.8	299.1-314.2	IcPS (graphic)		5	Hu et al., 2018
56.4	0.95-2.43	274.8-283.2	IthPS (visual)		4	Deaton and Frost, 1946
27.51	2.76-11.28	280.4-288.0	IcPS (graphic)		5	Sabil et al., 2014
17.7	1.42-3.00	281.6-287.0	IcPS (visual)		5	Holder and Grigoriou, 1980
4.7	0.99-2.99	279.4-287.6	IcPS (visual)		6	Holder and Grigoriou, 1980
1.6	1.81-3.08	283.9-287.8	IcPS(visual)		4	Holder and Grigoriou, 1980
47.5-91.3 [*]	1.25-7.13	279.0-290.3	IcPS (light)		27	Maekawa, 1998
90.2-98.9 [*]	1.70-11.10	275.4-289.6	IcPS (light)		52	Maekawa, 2001
74.7	34.30-176.70	282.3-314.5	IcPS (graphic)	12	6	Hu et al., 2018
74.7	33.20-179.00	292.4-307.4	IcPS (graphic)	23	5	Hu et al., 2018
90.2-97.9 [*]	4.00-10.00	276.0-288.0	IcPS (light)	3	24	Maekawa, 2001

Note: IcPS- Isochoric pressure search; IthPS- Isothermal pressure search.

^a The composition denotes the mole fraction of CH₄ in the feed gas mixture.

^{*} indicates that the unit of composition is in volume fraction.

The collected data points of binary CH₄-CO₂ hydrates formed in pure H₂O and NaCl solutions are listed in Table 3-5. The composition of CH₄ in the feed CH₄-CO₂ gas mixture ranges from 3.48 mol% to 92 mol%, aiming at various potential applications of CH₄-CO₂ hydrates, e.g., CO₂ sequestration and gas storage. The phase boundary pressure and temperature cover a range of 1.10-25.00 MPa and 262.0-295.1 K, respectively, and the concentration of NaCl ranges from 5 wt% to

20 wt%. As demonstrated in Table 3-5, a total of 158 data points have been collected for the measured phase boundary of CH₄-CO₂ hydrates, in which 124 points are for those formed in pure H₂O, and 34 points belong to those formed in NaCl solutions. Most data points of the binary CH₄-CO₂ hydrates formed in NaCl solutions focused on low-pressure conditions, i.e., below 10 MPa (Dholabhai and Bishnoi, 1994; Fan and Guo, 1999). High-pressure data of this system have been supplemented recently by Zheng et al. (2020) with pressure up to 61.99 MPa.

Table 3-5 Collected phase boundary data of binary CH₄-CO₂ hydrates

CH ₄ , mol% ^a	<i>P</i> , MPa	<i>T</i> , K	Methods	NaCl, wt%	Data points	Reference
92	3.83-8.40	277.8-285.1	PBD		4	Adisasmito et al., 1991
90	5.00-25.00	280.6-293.4	IbT (visual)		6	Sadeq et al., 2017
87	3.24-10.90	276.9-287.4	PBD		5	Adisasmito et al., 1991
84	5.00-25.00	281.5-293.5	IbT (visual)		6	Sadeq et al., 2017
	2.36-7.47	275.1-285.3	IthPS (visual)		6	Beltrán and Servio, 2008
	5.00-25.00	282.1-294.0	IbTS (visual)		6	Sadeq et al., 2017
80	2.36-7.53	274.1-284.8	IthPS (visual)		4	Dholabhai and Bishnoi, 1994
	2.00-5.00	273.6-281.5	IcPS (visual)		4	Seo et al., 2001
	2.30-3.40	274.0-278.3	IthPS (visual)		4	Servio et al., 1999
74.49	2.63-3.46	274.3-277.3	IcPS (graphic)	0	5	Kastanidis et al., 2017
73.6	5.29-11.62	284.2-289.2	IcPS (graphic)		3	Belandria et al., 2010
70	2.19-6.56	275.4-285.3	IthPS (visual)		6	Beltrán and Servio, 2008
61	5.43-9.78	283.1-287.4	PBD		3	Adisasmito et al., 1991
60	2.05-5.88	275.3-284.7	IthPS (visual)		5	Beltrán and Servio, 2008
59.71	2.03-5.17	275.5-283.4	IcPS (graphic)		4	Mohammadi et al., 2013
51.0	5.82-12.41	284.8-289.9	IcPS (graphic)		2	Belandria et al., 2010
	1.92-5.63	275.2-284.7	IthPS (visual)		6	Beltrán and Servio, 2008
50	1.78-5.07	273.5-283.1	IthPS (visual)		14	Servio et al., 1999
40	1.50-3.50	273.6-280.2	IcPS (visual)		4	Seo et al., 2001
32	2.58-4.12	278.2-282.0	PBD		3	Adisasmito et al., 1991

29.9	3.25-5.32	281.4-284.7	IcPS (graphic)	3		Partoon et al., 2016
27.51	2.76-11.28	280.4-287.9	IcPS (graphic)	5		Sabil et al., 2014
27.0	3.16-13.06	280.6-289.1	IcPS (graphic)	3		Belandria et al., 2010
5.9	1.82-5.81	276.0-284.2	IcPS (graphic)	4		Chapoy et al., 2014
3.48	1.10-4.80	273.5-282.3	IthPS (visual)	9		Fan and Guo, 1999
	2.30-6.98	271.6-282.0		5	4	
80	2.03-6.56	268.5-279.0	IthPS (visual)	10	4	Dholabhai and Bishnoi, 1994
	1.86-7.31	264.8-277.2		15	5	
	2.12-9.15	261.9-274.3		20	4	
29	13.51-61.99	287.0-295.1	IcPS (graphic)	5.0	5	Zheng et al., 2020a ^b
21	10.26-51.98	286.1-292.4	IcPS (graphic)	3.5	5	
5.02	1.24-3.75	267.9-277.4	IthPS (visual)	9.45	7	Fan and Guo, 1999

Note: PBD- phase boundary dissociation; IcPS- Isochoric pressure search; IthPS- Isothermal pressure search; IbTS- Isobaric temperature search.

^a The composition denotes the mole fraction of CH₄ in the feed gas mixture.

^b These data points are measured in this work, which will be introduced in Section 3.2.

3.2 Experimental Measurement

Before one of our recent works (Zheng et al., 2020a), only two groups of phase boundary data points are available for CH₄-CO₂ hydrates formed in NaCl solutions based on the established database, with the pressure lower than 10 MPa. However, the pressure could be over 20 MPa in the real application. For example, gas hydrates have been detected at the water depth of 2400 m in the Gulf of Mexico with the deepest bottom simulating reflector (BSR) at around 600 m below the seafloor (Kastner et al., 2008; Milkov and Sassen, 2003; Shedd et al., 2012). It is necessary to supplement the experimental phase boundary database of CH₄-CO₂ hydrates formed in NaCl solutions at high-pressure and high-temperature conditions due to the fact some interesting phenomena may occur at these conditions, e.g., the deformation of hydrate cage at high pressure

and the pairing between ions at high temperature. In this section, a high-pressure experimental apparatus system is established to investigate the phase boundary and the interfacial phenomenon, i.e., hydrate formation at the water-gas interface and to measure the phase boundary of CH₄-CO₂ hydrates formed in NaCl solutions at high-pressure and high-temperature conditions.

3.2.1 Experimental apparatus

A schematic diagram of the experimental apparatus designed to measure the phase boundary and morphology of gas hydrates is illustrated in Fig. 3-1. The central component is a PVT cell where hydrate formation and dissociation take place. The wetting parts of the PVT cell are made of stainless steel coated with anticorrosive Hastelloy. It is equipped with a sapphire window through which the view inside the cell can be observed and recorded by using a CCD digital video camera. The maximum pressure of the PVT cell can sustain is 70 MPa and the temperature can range from -10 to 200 °C. The volume of the PVT cell is changeable between 5 and 300 ml by moving a motor-driven piston. A magnetic stirrer is mounted on the top of the piston for agitation. The PVT cell can be rotated between 0° and 135° so that the optimal observation angle can be utilized. The temperature inside the PVT cell is regulated with an external silicon oil bath. The capacity of the external bath is -20 to 200 °C with a resolution of 0.01 °C. The pressure and temperature inside the cell are measured by using the pressure and temperature transducers and recorded continuously with a Falcon data acquisition system. The accuracy of the pressure and temperature transducers are ±0.35% F.S. and ±0.01 °C, respectively. An Agilent 490 Micro gas chromatograph (GC) is equipped to measure the guest composition of the guest mixture prepared in the transfer cylinder. A Platinum DV-200N vacuum pump with a capacity of 200 L/min is employed to degas the experimental device.

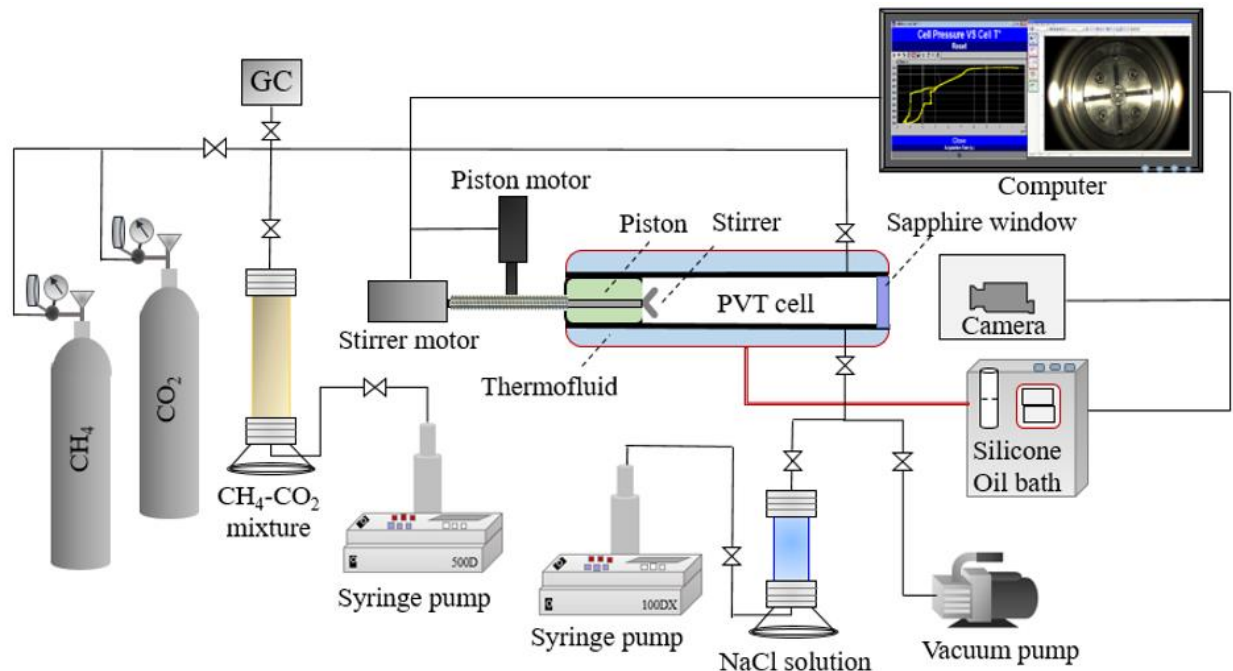


Fig. 3-1 Schematic diagram of experimental apparatus applied in the measurement the phase boundary of gas hydrates

3.2.2 Experimental materials and procedure

The CH₄, C₂H₆, and CO₂ gases with a purity of 99.99 mol% are supplied by Matheson Tri-Gas and stored in three gas tanks, respectively. Deionized water with a resistivity of 18 MΩ·cm (measured with YSI 3200 Conductivity Instrument) is prepared in the lab with Milli-Q Direct water purification system. Sodium Chloride (NaCl) with a purity of 99.5 wt% provided by Fisher Scientific Company is used.

The experimental procedures are as described below.

1) Prepare the guest mixture (take the binary gas mixture of CH₄-CO₂ for example):

a. Vacuum the PVT cell using the vacuum pump for 30 min;

b. Transfer the pure CH₄ from the CH₄ gas cylinder to the PVT cell until a specified pressure is reached;

c. Calculate the moles of CH₄ that has been injected into the PVT cell by employing the PR EoS as described in Chapter 4, and estimate the final pressure using the PR EoS after the CO₂ injection;

d. Transfer the pure CO₂ from the CO₂ gas cylinder to the PVT cell, until the estimated final pressure is obtained;

e. Measure the bubble point of the prepared gas mixture to confirm the composition;

f. Further confirm the composition of gas composition using the Micro GC.

2) Prepare the aqueous solution:

The NaCl solution with a specific concentration is prepared and stored in the cleaned transfer cylinder.

3) Loading the aqueous solution:

a. Vacuum the tubing that connects the PVT cell and the transfer cylinder;

b. Inject the prepared NaCl solution into the PVT cell by employing the syringe pump.

4) Measure the equilibrium phase boundary of the mixed hydrates formed in the NaCl solution:

The isochoric pressure-search method (Zheng et al., 2020a) is applied to obtain the equilibrium pressure and temperature, as shown in Fig. 3-2. In the isochoric pressure-search method, the phase boundary of gas hydrates is determined with the intersection of the pressure-temperature (P-T) curves, which involves two processes, i.e., hydrate formation (see the blue

curves A-E-B-C in Fig. 3-2) and hydrate dissociation (see the red curves C-D-E-A in Fig. 3-2). Along the red curves, the temperature in the PVT cell is decreased stepwise at a rate of 5 K/h (Tohidi et al., 2000), until a small amount of hydrates is formed in the cell. In this stage, the pressure decline is initially induced by gas dissolution and then by hydrate formation, i.e., hydrate nucleation and crystal growth. When some amount of hydrates are formed, the temperature of the PVT cell is increased to dissociate the hydrates. The temperature is increased fast stepwise initially with a rate of 0.5 K/h. When approaching the phase boundary temperature, the temperature in the PVT cell is increased at a rate of 0.1 K/h (Atik et al., 2010), until a sharp change in the slope of the P-T curve is observed, which is cross-verified by the disappearance of hydrates in the PVT cell from the video camera. During the experiments, the pressure and temperature are regulated by moving the piston and through the external bath respectively. The magnetic stirrer is turned on to agitate the fluids until equilibrium.

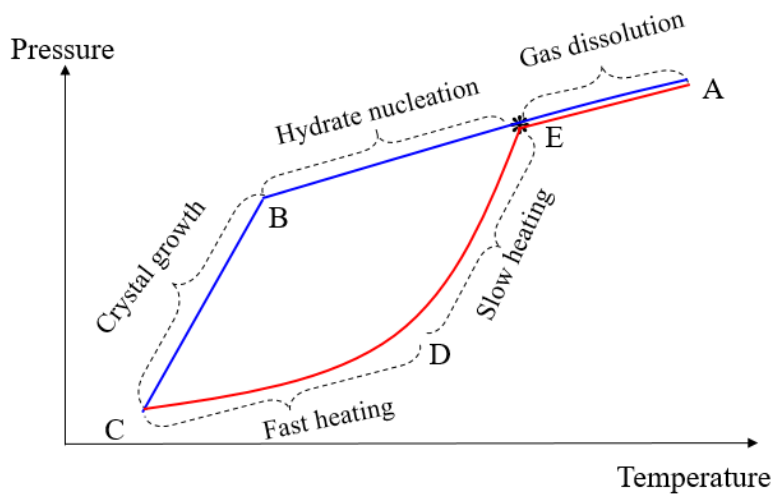


Fig. 3-2 Schematic diagram of determining the hydrate phase boundary using the isochoric-pressure search method

5) *Observe the morphology of hydrates formed in the PVT cell:*

The morphology of the CH₄-CO₂ hydrates formed at the water-gas interface and its variation with time will be observed.

3.2.3 Measurement of the hydrate phase boundary

Verification of the experimental device

To verify the reliability of the experimental apparatus and the procedures adopted in this work for quantitative measurements, the phase boundary of CH₄ hydrates in pure water is measured and compared with 213 experimental data points from the collected database in Section 3.1, as shown in Fig. 3-3. It is illustrated that measured data by using the experimental device in this work and the isochoric pressure-search method are consistent with those in the collected database. The phase boundary pressure increases linearly with temperature in this semi-log plot, indicating that there is no structure change of the CH₄ hydrates in this temperature range.

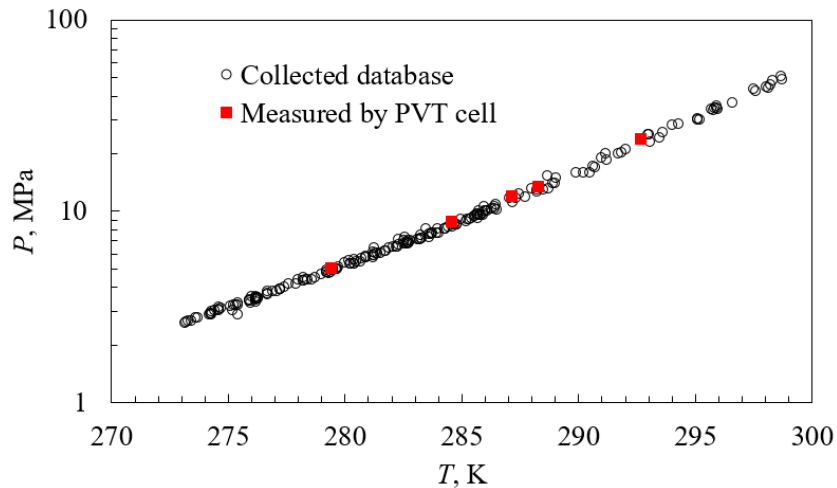


Fig. 3-3 Comparison of the measured phase boundary data of CH₄ hydrates formed in pure water with the ones collected in the literature

Measured phase boundary of CH₄-CO₂ hydrates in NaCl solutions

The measured phase boundary data of the mixed CH₄-CO₂ hydrates are listed in Table 3-6. The temperature of Mix-1 ranges from 286.05 to 292.35 K and the measure phase boundary pressure is up to 51.98 MPa. As for Mix-2, the temperature is ranged from 287.04 to 295.09 K, with the pressure as large as 61.99 MPa. These data points have filled the blank of the database of CH₄-CO₂ hydrate phase boundary in NaCl solutions at high-pressure and high-temperature conditions.

Table 3-6 Experimental scenarios and the measured phase boundary of CH₄-CO₂ hydrates

Gas mixture	CH ₄ , mol%	CO ₂ , mol%	NaCl, wt%	<i>T</i> , K	<i>P</i> , MPa
Mix-1	21	79	3.5	286.05	10.26
				288.66	22.03
				290.20	33.73
				291.95	46.05
				292.35	51.98
Mix-2	29	71	5.0	287.04	13.51
				289.11	21.60
				291.05	31.21
				292.74	44.64
				295.09	61.99

3.2.4 Observation of hydrate formation at the interface

It is known that hydrate formation tends to occur at the water-gas interface, but the observations of the interfacial phenomena in the PVT cell are scarce. In this work, the hydrate formation and dissociation in the PVT cell are observed through the sapphire window and the video camera

(Zheng et al., 2020a). The evolution of hydrate formation at the water-gas interfaces have been illustrated in Fig. 3-4. It can be seen that the roughness of the water-gas interfaces increases due to hydrate growth in Fig. 3-4a and Fig. 3-4b. Two hypotheses are proposed to explain the fine pillars formed at the planar gas-water interface (i.e., Fig. 3-4a) and the bubble-water interface (i.e., Fig. 3-4b) as illustrated by the white arrows in Fig. 3-4a and Fig. 3-4b. The first hypothesis is that the fine pillars are formed owing to the non-equilibrium state of gas and water phases (Fu et al., 2018), and the second hypothesis attributes these fine pillars to the non-uniform lateral growth of hydrates at the interface. Hydrate formation is controlled by various mechanisms, e.g., mass transfer, heat transfer, and kinetic rate of hydrate formation (Zheng et al., 2015, 2018a, 2018b). Given the size of the PVT cell and the two-fold temperature controlling system, the heat transfer mechanism is negligible in this work. When the mass transfer rate, e.g., gas dissolution from the gas phase to water induced by the non-equilibrium condition is lower than the kinetic rate of hydrate formation, the pillars at the water-gas interfaces will be formed. The non-uniform lateral growth of gas hydrates at the interfaces can also lead to the formation of pillars. The growth of hydrate film at the water-gas interface tends to deform the geometry of the interface, e.g., gas escapes from the gas bubbles due to the change of interfacial tension as gas hydrates are formed. However, when the kinetic rate of hydrate growth is larger than the rate of gas transfer and, in the meanwhile, if the driving force for gas transfer is not high enough to overcome the restraint of the hydrate film, the fine pillars will be formed at the surface of the gas bubble. To investigate the interfacial phenomena with a larger mass transfer rate, a perturbation, i.e., stirring is applied in the PVT cell, as shown in Fig. 3-4c. It is demonstrated that a portion of gas bubbles have been broken into pieces which promoted hydrate growth due to the larger surface for hydrate formation. It is interesting to notice that the roughness of the water-gas interface becomes smaller as time goes

by, which can be clearly observed by comparing the bubble marked by the white arrow in Fig. 3-4c and Fig. 3-4d. The reduced roughness at the water-gas interface is induced by the thickness growth of the hydrate film (Sun et al., 2007).

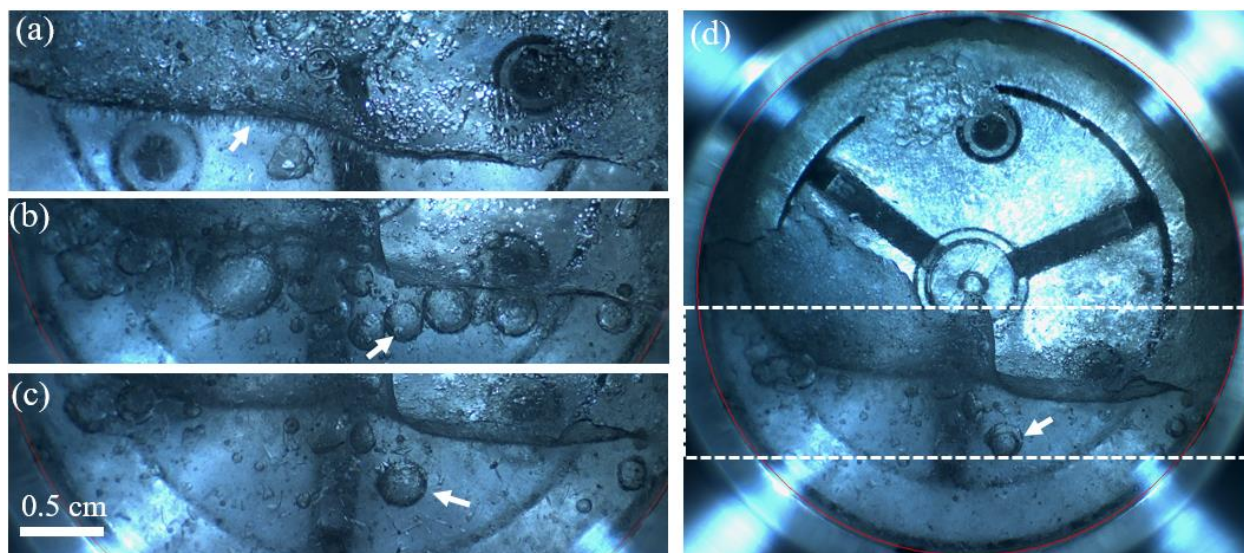


Fig. 3-4 Evolution of hydrate formation in the PVT cell.

(a) Hydrate formation at the bulk gas-liquid phase interface; (b) Hydrate formation at the bubble-liquid phase interface; (c) Hydrate distribution after perturbation; (d) Final view of hydrate formation process. Note that (a)-(d) are in the time order. (d) demonstrates the full view of the PVT cell, and view location in (a), (b), and (c) is denoted with the white rectangle in (d).

The evolution of hydrate dissociation in the PVT cell is presented in Fig. 3-5. It is worth noting that the gas hydrates formed in the PVT cell are not consolidated due to the short duration. Therefore, no specific location of hydrate dissociation is observed. During hydrate dissociation, gas is released from the solid hydrate phase and accumulates from small gas bubbles into larger

ones. The surface of bubbles is smooth and their shapes are restricted by the occurrence of hydrate and liquid phases.

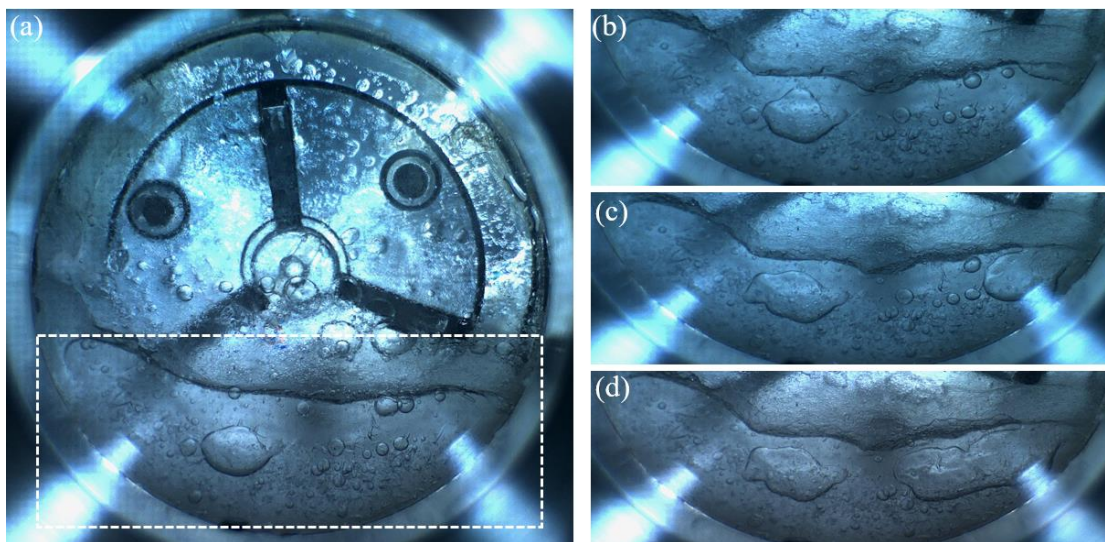


Fig. 3-5 Evolution of hydrate dissociation in the PVT cell. (a)-(d) are in the time order.

3.3 Summary

In this section, a database of the measured phase boundary of CH_4 , C_2H_6 , CO_2 , and binary CH_4 - C_2H_6 and CH_4 - CO_2 hydrates formed in pure H_2O and NaCl solutions has been established, which not only supplements the newly published experimental data to the existing database but also adds the experimental approaches.

In order to fill the blank in the database of CH_4 - CO_2 hydrates formed in the NaCl solutions at high-pressure and high-temperature conditions, a high-pressure PVT equipment is designed. In this section, the phase behavior of CH_4 - CO_2 hydrates formed in NaCl solution is investigated by using the PVT cell. The phase boundary of the CH_4 - CO_2 hydrates is measured by using the

isochoric pressure-search method in the high-pressure and high-temperature regions. The measured phase boundary data points of CH₄-CO₂ hydrates formed in NaCl solutions extend the phase boundary pressure up to 61.99 MPa and the temperature to 295.09 K. These data points are important for the study of interactions between water, gas, and ions in high-pressure and high-temperature regions.

Hydrate formation at the water-gas interface is also observed. The roughness of the water-gas interface is greatly increased at the initial stage of hydrate formation in the PVT cell. Two hypotheses have been proposed to explain the fine pillars formed at the water-gas interface, i.e., the non-equilibrium state of gas and water phases and the non-uniform lateral growth of hydrates at the interface. During hydrate formation, the water-gas interface becomes smoother with time, due to the thickness growth of the hydrate film.

CHAPTER 4 DETERMINATION OF THE HYDRATE PHASE BOUNDARY USING SEPARATE MODELS FOR NON-HYDRATE PHASES

4.1 Basic Framework to Determine Hydrate Phase Boundary Pressure

In a gas-hydrate system, two phases may occur in the aqueous solutions, i.e., aqueous phase and sI or sII hydrate phase, as shown in Fig. 4-1 (Zheng et al., 2020b). Each molecule in the system keeps rotating, vibrating, and translating. At the equilibrium state, the rate of one specific component, e.g., gas and water entering a phase is equal to that departing from that phase. At the equilibrium phase boundary conditions, the gas and water molecules are in a dynamic equilibrium state. Some water molecules organize to form new hydrate cages and at the same time, some other water molecules break away from the hydrate cages and enter the aqueous phase. The rate of these two processes are identical at the equilibrium state.

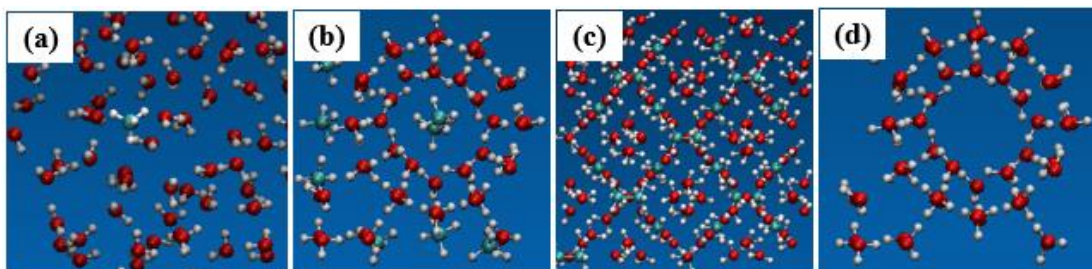


Fig. 4-1 Schematic diagrams of the configuration of water and gas molecules in (a) aqueous phase; (b) stable hydrate cages of the sI unit cell; (c) stable hydrate cages of the sII unit cell; (d) unoccupied hydrate cages of the sI unit cell.

(The red, white, and green balls represent oxygen, hydrogen, and carbon atoms, respectively)

In the theoretical models of this work, the chemical potential difference of water components, i.e., $\Delta\mu_w$ is used to quantify the driving force of the water molecules' motion. Therefore, the criterion of hydrate phase boundary is the equality of $\Delta\mu_w$ between various phases, e.g., hydrate phase and aqueous phase. In this work, the water chemical potential in the unoccupied hydrate cage used as a reference to determine the chemical potential difference of water molecules, as can be seen in Fig. 4-1. Hence, the criterion of equilibrium condition at the hydrate phase boundary can be summarized in Eq. 4-1 (Holder et al., 1988).

$$\Delta\mu_w^H = \mu_w^\pi - \mu_w^H = \mu_w^\pi - \mu_w^A = \Delta\mu_w^A \quad (4-1)$$

where μ_w^π , μ_w^H , and μ_w^A denote the water chemical potential in the unoccupied hydrate cage, the stable hydrate, and the aqueous phases, respectively; $\Delta\mu_w^H$ is the water chemical potential difference between the unoccupied hydrate cage and the stable hydrate phase; $\Delta\mu_w^A$ represents the water chemical potential difference between the unoccupied hydrate cage and the aqueous phase.

A typical flowchart to calculate the phase boundary of gas hydrates by using the chemical-potential-difference criterion is demonstrated in Fig. 4-2. When the composition and temperature of the system of interest is specified, this calculation algorithm starts from an initial guess of the phase boundary pressure. In this work, the reference hydrate phase boundary proposed by Parrish and Prausnitz (1972) serves as the initial guess of the phase boundary pressure, as shown in Eq. 4-2. Then a flash calculation is performed on the non-hydrate phases, e.g., gas-rich vapor phase and gas-rich liquid phase to obtain the required parameters for the calculation of water chemical potential difference. The details of this step will be discussed in the following sections. If the difference of the calculated water chemical potential difference of hydrate phase and aqueous phase are within the specified number, e.g., 10^{-6} , the algorithm is ended. Otherwise, the pressure

will be updated using bisection method or Newton-Raphson method and the abovementioned steps are to be repeated.

$$\ln(P) = A_R + B_R / T + C_R \ln T \quad (4-2)$$

where P and T are in atm and K, respectively. Coefficients A_R , B_R , and C_R are hydrate structure-specific constant, i.e., $A_R = -1212.2$, $B_R = 44344.0$, $C_R = 187.719$ for sI hydrates, and $A_R = -1023.14$, $B_R = 34984.3$, $C_R = 159.923$ for sII hydrates.

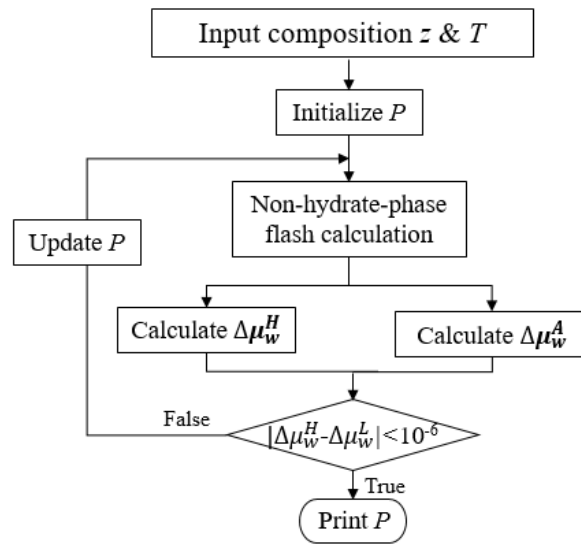


Fig. 4-2 Flowchart to calculate the hydrate phase boundary using the chemical-potential-difference criterion

As aforementioned, sI or sII hydrates will be formed by the light natural gas components. In the thermodynamic modeling, it is necessary to determine the phase boundary pressure of both sI and sII hydrates and choose the smaller one as the phase boundary pressure. The flowchart of this process is illustrated in Fig. 4-3.

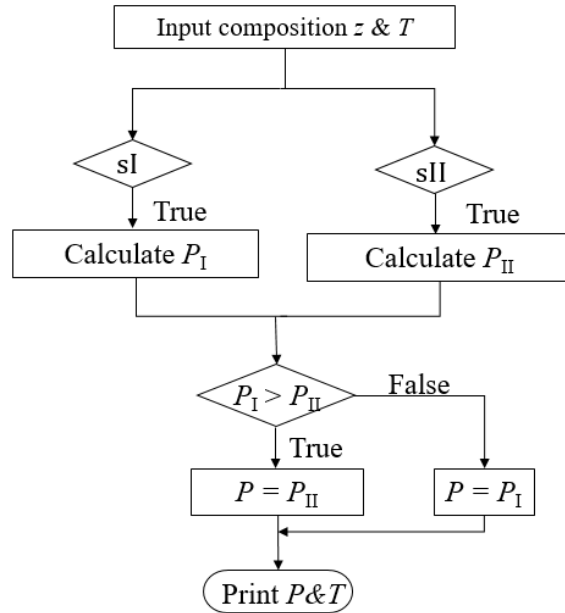


Fig. 4-3 Flowchart to select the phase boundary pressure (P_I and P_{II} represent the phase boundary pressure of sI and sII hydrates, respectively)

4.1.1 Determination of water chemical potential difference in the aqueous phase

The water chemical potential difference in the aqueous phase, i.e., $\Delta\mu_w^A$ is calculated using a classical thermodynamic model (Englezos and Bishnoi, 1988):

$$\Delta\mu_w^A = \Delta\mu_w^{A*} - RT \ln a_w \quad (4-3)$$

where a_w is the water activity in the aqueous phase; $\Delta\mu_w^{A*}$ is the water chemical potential difference in the pure water phase, which is a function of pressure and temperature, quantified by Eq. 4-4 (Holder et al., 1980; Munck et al., 1988):

$$\frac{\Delta\mu_w^{A*}}{RT} = \frac{\Delta\mu_{w0}^{A*}}{RT_0} - \int_{T_0}^T \frac{\Delta\bar{H}_w}{RT^2} dT + \int_{P_0}^P \frac{\Delta\bar{V}_w}{RT} dP \quad (4-4)$$

where the subscript 0 means the reference condition, i.e., $T_0 = 273.15$ K and $P_0 = 0$ Pa; $\Delta\bar{V}_w$ denotes the molar volume difference of water between the unoccupied hydrate cage and the pure water phase, which was determined by Stackelberg and Müller (1951) using X-ray crystallography; $\Delta\bar{H}_w$ represents the molar enthalpy difference between water in the unoccupied hydrate cage and that in the pure water phase. In this work, $\Delta\bar{V}_w$ is assumed independent on of pressure and temperature (Munck et al., 1988) and $\Delta\bar{H}_w$ varies with temperature, described using Eq. 4-5:

$$\Delta\bar{H}_w = \Delta\bar{H}_{w0} + \int_{T_0}^T \Delta\bar{C}_{Pw} dT \quad (4-5)$$

where $\Delta\bar{H}_{w0}$ denotes the molar water enthalpy difference at the reference condition; $\Delta\bar{C}_{Pw}$ is the molar heat capacity difference of water in the unoccupied hydrate cage and the pure water phase, which is a function of temperature:

$$\Delta\bar{C}_{Pw} = \Delta\bar{C}_{Pw0} + b_1 (T - T_0) \quad (4-6)$$

where $\Delta\bar{C}_{Pw0} = 38.12$ J/mol/K and $b_1 = 0.14$ J/mol/K², determined using experimental data (Parrish and Prausnitz, 1972).

4.1.2 Determination of water chemical potential in the hydrate phase

The water chemical potential difference in the hydrate phase is determined by using the vdw-P model (van der Waals and Platteeuw, 1958), as illustrated in Eq. 4-7. The vdw-P model assumes that the hydrate phase is an ideal solid solution (Ballard and Sloan, 2002).

$$\Delta\mu_w^H = -RT \sum_{i=1}^2 \left[v_i \cdot \ln \left(1 - \sum_{j=1}^{n_g} \theta_{ij} \right) \right] \quad (4-7)$$

where v_i denotes the number of small ($i = 1$) and large ($i = 2$) hydrate cages per water molecule in the hydrate phase. It was determined that $v_1 = 1/23$, $v_2 = 3/23$ for the unit sI hydrates, and $v_1 = 2/17$, $v_2 = 1/17$ for the unit sII hydrates. n_g represents the total number of gas species in the system of interest; θ_{ij} denotes the fraction of i -type cage occupied by gas species j , which is calculated by assuming that the process of gas entering the hydrate cage is similar to the Langmuir adsorption:

$$\theta_{ij} = \frac{C_{ij} f_j}{1 + \sum_k C_{ik} f_k} \quad (4-8)$$

where f_j is the gas fugacity, which is determined by flash calculation using EoS that will be introduced in the following sections; C_{ij} is the Langmuir constant, representing the driving force for the occupancy of gas molecules in the hydrate cages:

$$C_{ij} = \frac{4\pi}{k_B T} \int_0^{R_i - \varpi_j} \exp \left[\frac{-W(r)}{k_B T} \right] r^2 dr \quad (4-9)$$

where k_B is Boltzmann constant; R_i and ϖ_j denote the radius of the hydrate cage i and the hard-core radius of gas molecule j , respectively. $R_1 = 3.975 \text{ \AA}$ and $R_2 = 4.30 \text{ \AA}$ are used for the small and large cages of sI hydrates respectively, and $R_1 = 3.91 \text{ \AA}$ and $R_2 = 4.73 \text{ \AA}$ are for those of sII hydrates (Parrish and Prausnitz, 1972). $W(r)$ is the potential energy due to the interaction of gas with water molecules forming the hydrate cages (Holder et al., 1988). Kihara potential functions applied to determine $W(r)$ (McKoy and Sinanoğlu, 1963; Parrish and Prausnitz, 1972):

$$W(r)_{ij} = 2\psi_i E_j \left[\frac{\sigma_j^{12}}{R_i^{11} r} \left(\delta_{ij}^{10} + \frac{\varpi_j}{R_i} \delta_{ij}^{11} \right) - \frac{\sigma_j^6}{R_i^5 r} \left(\delta_{ij}^4 + \frac{\varpi_j}{R_i} \delta_{ij}^5 \right) \right] \quad (4-10)$$

$$\delta_{ij}^N = \frac{1}{N} \left[\left(1 - \frac{\varpi_j}{R_i} - \frac{r}{R_i} \right)^{-N} - \left(1 - \frac{\varpi_j}{R_i} + \frac{r}{R_i} \right)^{-N} \right] \quad (4-11)$$

where E_j is the maximum attractive potential energy of gas species j ; σ_j is the zero potential energy distance of gas species j ; ψ_i is the coordination number of small and large hydrate cages, i.e., the number of water molecules in each cage. $\psi_1 = 20$, $\psi_2 = 24$ for sI hydrates and $\psi_1 = 20$, $\psi_2 = 28$ for sII hydrates are adopted in this work (Parrish and Prausnitz, 1972).

4.1.3 Reference Properties

Reference properties, i.e., the properties at the reference conditions are important parameters for the calculation of $\Delta\mu_w^A$, e.g., $\Delta\mu_{w0}^{A*}$ and $\Delta\bar{H}_{w0}$ in Eqs. 4-4 and 4-5. The reference properties determined by various researchers has been summarized in Table 4-1. It can be seen that there is a discrepancy on these reference properties with different sources. Given the fact that the unoccupied hydrate cage is not stable, it is unrealistic to measure the reference properties directly. Hence, the experimental data, e.g., hydrate phase boundary and hydrate composition have been employed in various ways to decide the reference properties indirectly, which results into the disagreement as shown in Table 4-1. For example, Parrish and Prausnitz (1972) evaluated the reference properties of sI and sII hydrates using a trial-and-error algorithm. Dharmawardhana et al. (1980) calculated the reference properties by using the experimental data of cyclopropane hydrate composition. The reference properties of sI hydrates were obtained by forcing satisfactory of the criterion in Eq. 4-1. Later, Holder et al. (1984) revisited the experimental data measured by

Dharmawardhana et al. (1980) and achieved a new set of reference properties by employing a sounder approach, i.e., linear regression.

Table 4-1 Summary of reference properties determined in the literature

$\Delta\mu_{w0}^{A*}$, J/mol		$\Delta\bar{H}_{w0}$, J/mol ^a		References
sI	sII	sI	sII	
1256	795	-5258	-5174	Child, 1964
1264	883	-4858	-5201	Parrish and Prausnitz, 1972
1297	937	-4622	-4986	Dharmawardhana et al., 1980
1235	-	-4327	-	Holder et al., 1980
1155	-	-5627	-6008	Holder and Hand, 1982
1299.4	-	-4150	-	Holder et al., 1984
1120	931	-4297	-4611	John et al., 1985
1287	1068	-5080	-5247	Handa and Tse, 1986
1236	-	-4308	-	Cao, 2002
Gas specific				Lee and Holder, 2002
1203	1077	-4839	-4715	Anderson, 2005
1206	-	-4751	-	Velaga and Anderson, 2013

^a Molar enthalpy difference of -6011 J/mol between ice and liquid water is applied (Holder et al., 1980).

Preliminary assessments of the sensitivity of the reference properties by previous researchers (Cao et al., 2002; Mehta and Sloan, 1994) suggest that the phase boundary pressure of gas hydrates is more sensitive to $\Delta\mu_{w0}^{A*}$ than $\Delta\bar{H}_{w0}$. In this work, a straightforward algorithm is proposed to quantitatively evaluate the sensitivity of hydrate phase boundary pressures to these two reference properties. The reference properties obtained by Parrish and Prausnitz (1972) are used as the Base case for comparison. The difference between the reference properties determined by other

researchers in Table 4-1 and the Base case is evaluated by using a variation parameter defined in Eq. 4-12 (take the variation of $\Delta\mu_{w0}^{A*}$ for instance):

$$Variation = \frac{\Delta\mu_{w0}^{A*} - \Delta\mu_{w0,PP}^{A*}}{\Delta\mu_{w0,PP}^{A*}} \times 100\% \quad (4-12)$$

where $\Delta\mu_{w0}^{A*}$ is the water chemical potential difference of pure H₂O evaluated by other researchers, and $\Delta\mu_{w0,PP}^{A*}$ is the one determined by Parrish and Prausnitz (1972), i.e., 1264 J/mol for sI hydrates.

The average absolute relative deviation (AARD) defined in Eq. 4-13 is applied to quantify the sensitivity of the reference properties.

$$AARD = \frac{1}{N_p} \sum_{j=1}^{N_p} \left| \frac{P_{cal}^j - P_{exp}^j}{P_{exp}^j} \right| \times 100\% \quad (4-13)$$

where P_{exp}^j represents the measured phase boundary pressure at the specified j^{th} temperature; P_{cal}^j denotes the calculated phase boundary pressure using various reference properties; N_p is the number of experimental data points.

The deviations of the CH₄ hydrate phase boundary pressure using different variations of the reference properties are illustrated in Fig. 4-1. It is shown that the calculated phase boundary pressure of gas hydrates can be deviated by as large as 40% when different $\Delta\mu_{w0}^{A*}$ determined by various researchers are employed. Overall, the phase boundary pressure is strongly sensitive to $\Delta\mu_{w0}^{A*}$, and weakly sensitive to $\Delta\bar{H}_{w0}$. Therefore, it is crucial to select appropriate reference properties, particularly $\Delta\mu_{w0}^{A*}$.

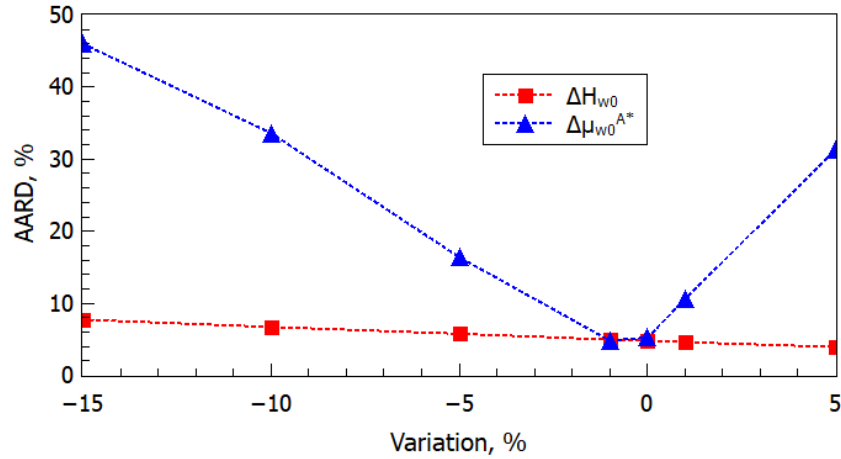


Fig. 4-4 Sensitivity of the calculated phase boundary pressure of CH₄ hydrates to the reference properties

With closer observation, the approaches applied to determine the reference properties can be classified into two categories, i.e., simultaneous approach and stepwise approach (Zheng et al., 2020b). In the simultaneous approach, the reference properties and Kihara parameters (see Section 4.1.4) are determined simultaneously by forcing the equality of measured and calculated phase boundary of gas hydrates (Holder and Hand, 1982; Holder et al., 1980; Parrish and Prausnitz, 1972). In the stepwise approach, the Kihara parameters are evaluated with experimental data of hydrate compositions (Dharmawardhana et al., 1980; Holder et al., 1984) or with ab initio quantum mechanical calculation (Anderson, 2005; Cao, 2002; Velaga and Anderson, 2013). Then the reference properties are determined with the phase boundary data of gas hydrates. Physically, the simultaneous approach attributes the uncertainties, e.g., errors in the measured experimental data randomly to parameters in the models of $\Delta\mu_w^A$ and $\Delta\mu_w^H$. While in the stepwise approach, especially in the cases where the Kihara parameters are determined by the ab initio calculation, the experimental uncertainties in the measured phase boundary of gas hydrates are automatically

attributed to the reference properties. It is believed that the treatment of experimental uncertainties in the latter approach is more physically reasonable, particularly for CH₄-CO₂ hydrates where the non-ideality of the hydrate phase is negligible at moderate conditions (McKoy and Sinanoğlu, 1963). Therefore, the reference properties evaluated by Anderson (2005) are selected in this work (see Table 4-1).

4.1.4 Kihara parameters

Kihara parameters ϖ_j , σ_j , and E_j need to be decided for the gas species of interest when the reference properties are settled (Zheng et al., 2020b). The particle swarm optimization (PSO) algorithm (Clerc and Kennedy, 2002) is adopted to optimize these six parameters by fitting against the experimental data of phase boundary of pure and binary CH₄, C₂H₆, and CO₂ hydrates formed in pure water (Avlonitis, 1994). The upper and lower searching range limits are 0.25-0.40 Å, 2.5-3.7 Å, 147-158 K for ϖ , σ , and E/k_B of CH₄, are 0.50-0.60 Å, 3.0-4.0 Å, 160-180 K for ϖ , σ and E/k_B of C₂H₆, and 0.65-0.77 Å, 2.5-3.5 Å, 165-175 K for those of CO₂, based on the optimization results of previous researchers (Avlonitis, 1994; Clarke and Bishnoi, 2003; Lee et al., 2016; Parrish and Prausnitz, 1972). The implicit least squares objective function proposed by Clarke and Bishnoi (2003) is used in this work, making the computation less expensive (Zheng et al., 2020b):

$$\text{Objective function} = \sum_{i=1}^{N_p} \left(\frac{\Delta\mu_{w,i}^A - \Delta\mu_{w,i}^H}{RT_i} \right)^2 \quad (4-14)$$

where $\Delta\mu_{w,i}^A$ and $\Delta\mu_{w,i}^H$ are calculated with Eqs. 4-3 and 4-7, respectively; N_p is the number of experimental data points selected for optimization; i denotes the i^{th} data points used in the optimization.

In this work, 146 out of 1092 data points in Table 3-1 through Table 3-5 in Chapter 3 are selected for the optimization of the six Kihara parameters simultaneously, including 75 points for CH₄ hydrates formed in pure H₂O, 13 data points for C₂H₆ hydrates formed in pure H₂O, 48 points for CO₂ hydrates formed in pure H₂O, 4 data points for CH₄-C₂H₆ hydrates formed in pure H₂O and 6 points for binary CH₄-CO₂ hydrates formed in pure H₂O. The phase boundary temperatures of CH₄ hydrates are collected below 300 K, because it is not reasonable to assume constant hydrate cage parameters above 300 K (Ballard and Sloan, 2002; Parrish and Prausnitz, 1972). As for CO₂ hydrates, the H-A-V three-phase boundary data are more reliable and therefore chosen for regression. It is noted that the data points of pure CH₄ and CO₂ hydrates for optimization are selected randomly after removing the ones with obvious deviation. For the binary CH₄-CO₂ hydrates, the ones with a CH₄ composition of 70 mol% is used for regression. The optimized Kihara parameters of CH₄, C₂H₆, and CO₂ are presented in Table 4-2.

Table 4-2 The optimized Kihara parameters of CH₄, C₂H₆, and CO₂

Kihara parameters	ω , Å	σ , Å	E/k_B , K
CH ₄	0.309	3.136	157.11
C ₂ H ₆	0.435	3.472	178.28
CO ₂	0.709	2.981	165.20

4.1.5 Effect of Electrolytes

As aforementioned, the presence of electrolytes in the aqueous phase will change the water activity, which further plays a role in the phase boundary of gas hydrates. In the separate models proposed in this section, the Pitzer model (Pitzer and Mayorga, 1973; Zha et al., 2012) is employed to quantify the effect of electrolytes, i.e., NaCl in this work on water activity, denoted as $a_{w,NaCl}$.

$$\ln(a_{w,NaCl}) = -\frac{18vm}{1000} \left[1 + Z_{Na^+} Z_{Cl^-} \left(-\frac{A_\phi I^{0.5}}{1+1.2I^{0.5}} \right) + m(\beta_0 + \beta_1 \cdot \exp(-2I^{0.5})) + m^2 \beta_2 \right] \quad (4-15)$$

where m represents the concentration of NaCl in the aqueous phase, in molality; Z_{Na^+} and Z_{Cl^-} are the charge of ions Na^+ and Cl^- ; $\nu = \nu_{Na^+} + \nu_{Cl^-}$; ν_{Na^+} and ν_{Cl^-} are the stoichiometric numbers of ions in NaCl; β_0 , β_1 , and β_2 are electrolyte-specific constants, which are 0.0765, 0.2664, and 0.00127 respectively for NaCl (Pitzer and Mayorga, 1973); I is the ionic strength, determined by Eq. 4-16; A_ϕ denotes the Debye-Huckel coefficient, as shown in Eq. 4-17.

$$I = \frac{1}{2} \left(z_{Na^+}^2 \cdot m \cdot \nu_{Na^+} + z_{Cl^-}^2 \cdot m \cdot \nu_{Cl^-} \right) \quad (4-16)$$

$$A_\phi = \frac{1}{3} \sqrt{\frac{2\pi N_A \rho_w}{1000}} \left(\frac{e^2}{\epsilon_w k_B T} \right)^{3/2} \quad (4-17)$$

where N_A is the Avogadro number; k_B denotes the Boltzmann constant; ρ_w represents water density; e is the electronic charge, 4.8029×10^{-10} esu; ϵ_w is the water dielectric constant evaluated with Eq. 4-18 (Englezos, 1992).

$$\epsilon_w = 305.7 \exp \left[-\exp(-12.741 + 0.01875T) - T/219 \right] \quad (4-18)$$

4.2 Separate Models for Aqueous and Gas-rich Phases

4.2.1 Mathematical models

In this section, a modeling framework using separate models for the aqueous phase and the gas-rich phase is described, i.e., the Peng-Robinson (PR) EoS for the gas-rich phase and Henry's law combined with the Poynting correction for the gas solubility in the aqueous phase. The effect of NaCl on the hydrate phase boundary is considered using the Pitzer model described in Section 4.1.5.

The PR EoS is described in the following equations (Peng and Robinson, 1976):

$$P = \frac{RT}{\bar{V} - b} - \frac{a(T)}{\bar{V}(\bar{V} + b) + b(\bar{V} - b)} \quad (4-19)$$

$$a(T) = 0.457235 \frac{R^2 T_c^2}{P_c} \cdot \alpha(T) \quad (4-20)$$

$$b = 0.07780 \frac{RT_c}{P_c} \quad (4-21)$$

where \bar{V} and b denote the molar volume and the covolume, respectively; T_c and P_c are the critical temperature and pressure. The universal alpha function $\alpha(T)$ is applied for the gas species, as illustrated in the following equation (Zheng et al., 2020a).

$$\alpha(T) = \left[1 + \left(0.37464 + 1.54226\omega - 0.26992\omega^2 \right) (1 - T_r) \right]^2 \quad (4-22)$$

where ω is the acentric factor; T_r is the reduced temperature, e.g., $T_r = T / T_c$.

For gas mixtures, van der Waals mixing rule is employed:

$$a = \sum_i \sum_j x_i x_j (1 - k_{ij}) \sqrt{a_i} \sqrt{a_j} \quad (4-23)$$

$$b = \sum_i x_j b_i \quad (4-24)$$

where x_i denotes the molar composition; k_{ij} is the binary interaction parameter (BIP). In this section, the BIP for the CH₄-C₂H₆ and CH₄-CO₂ pairs are 0 and 0.13, respectively.

The aqueous phase can be regarded as ideal solution when only CH₄, C₂H₆, and CO₂ are present due to the relatively low solubility, and $a_{w,g} = x_w$, i.e., water composition in the aqueous phase for the ideal solution. Henry's law combined with Poynting correction is employed to determine x_w (Holder et al., 1988):

$$x_w = 1 - \sum_{i=1}^{n_g} \frac{f_i}{H_i \exp\left[\frac{P\bar{V}_i}{RT}\right]} \quad (4-25)$$

where n_g is the number of gas species dissolved in the aqueous phase; \bar{V}_i denotes the partial molar volume of gas species i in the water phase given by Holder et al. (1988); f_i represents the gas fugacity determined with PR EoS; H_i is the Henry's constant, calculated with Eq. 4-26 (Holder et al., 1988):

$$H_i = \exp(A_i + B_i/T) \quad (4-26)$$

where H and T are in atm and K, respectively; A_i and B_i are gas specific constants, e.g., $A_i = 15.826277$, $B_i = -1559.0631$ for CH₄, $A_i = 18.400368$, $B_i = -2410.4807$ for C₂H₆, and $A_i = 14.283146$, $B_i = -2050.3269$ for CO₂.

The water activity in the aqueous solution can be determined using the following equation:

$$a_w = x_w \cdot a_{w,NaCl} \quad (4-27)$$

where x_w is the composition of water in the aqueous phase, described in Eq. 4-25; $a_{w,NaCl}$ considers the effect of NaCl on the water activity, which can be calculated by employing Eq. 4-15.

By combining with the equations listed in Section 4.1, this model can be used to calculate the phase boundary pressure of gas hydrates. The procedure of the calculation algorithm is illustrated in the flowchart in Fig. 4-5 (Zheng et al., 2020b). The parameters, e.g., gas composition and temperature of interest are prepared in the input file. Then an initial guess of pressure is achieved by using the phase boundary of the reference hydrates. A flash calculation with PR EoS is implemented for the input gas species to obtain the fugacity of the gas at the equilibrium conditions. The water chemical potential difference of the hydrate phase, i.e., $\Delta\mu_w^H$ is calculated with the vdW-P model and the achieved fugacity. The fugacity is also used with Henry's law to determine the composition of the aqueous phase, which is further employed to calculate the water chemical potential difference of the aqueous phase, i.e., $\Delta\mu_w^A$. The impact of NaCl on water activity is calculated by using the Pitzer model (Pitzer and Mayorga, 1973). The pressure is updated until the difference between the calculated $\Delta\mu_w^H$ and $\Delta\mu_w^A$ is within a certain error, e.g., 10^{-6} . Note that this procedure is employed to calculate the phase boundary pressure of both sI and sII hydrates, and the smaller one is the phase boundary pressure at the specified temperature.

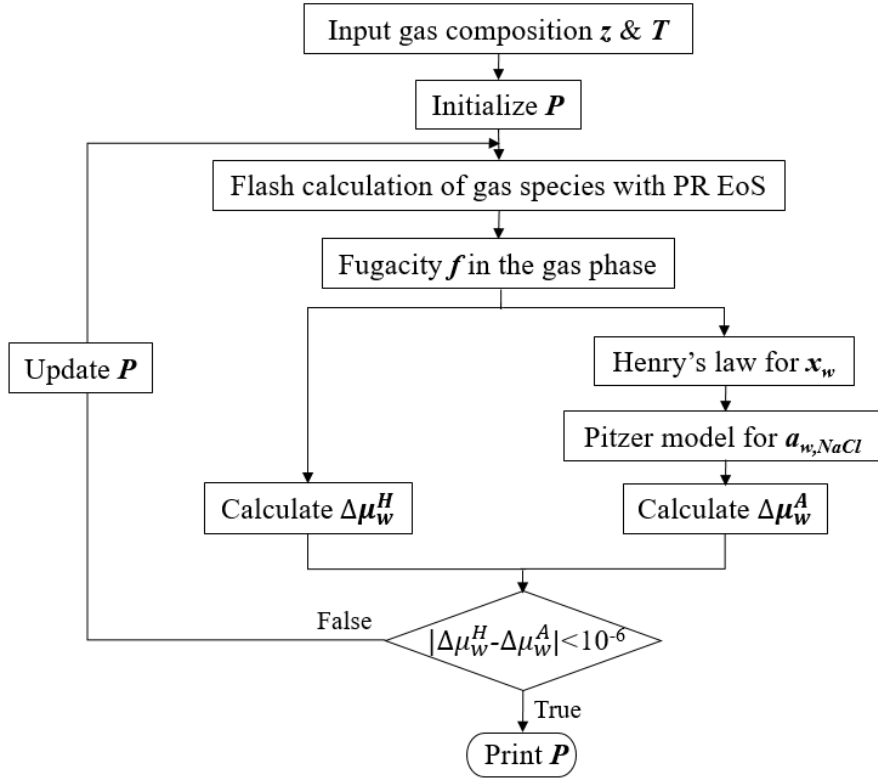


Fig. 4-5 Flowchart to determine the phase boundary of gas hydrates using separate model for aqueous and gas-rich phases

4.2.2 Simulation results

To verify the reliability of the developed model, the phase boundary data collected in the literature and measured in this work in Chapter 3 will be applied to compare with the calculated results. The AARD defined in Eq. 4-13 is applied to evaluate the difference between the measured phase boundary pressure and those calculated using the proposed model (Zheng et al., 2020a). The program is coded by using MATLAB platform.

CH₄ hydrates

The measured phase boundary data of CH₄ hydrates formed in pure H₂O and various concentrated NaCl solutions are illustrated in Fig. 4-6, along with the calculated results. It can be seen that the phase boundary pressure increases with the temperature for all cases. Also, the phase boundary pressure increases with the concentration of NaCl solutions, owing to the stronger interaction between the charged ions and the dipoles of water molecules at the higher concentration of NaCl solutions. The consequence of the strong interaction is that fewer water molecules are available for the hydrate formation. In general, the developed model can accurately reproduce the 383 data points, in which only 75 data points are included in the optimization process. The deviations between the calculated and the measured phase boundary pressure are calculated with Eq. 4-13. The AARD of the total 383 data points is 4.63%, indicating the developed model is capable of predicting the equilibrium phase boundary of CH₄ hydrate formed in both pure and saline water. The largest deviation is found for 20 wt% resulting in an AARD of 18.01%. It is noted that the collected phase boundary data points are scattered for the case of 20 wt% NaCl solution. Also, there is a distinct disagreement in the collected two groups of measured phase boundary data points for 20 wt% case (Haghighi et al, 2009; Maekawa et al., 1995). Overall, the calculated results by using the developed model demonstrate a higher deviation from the measured phase boundary pressure at larger concentrations of NaCl solutions. This is because the interactions between the dissolved gas and ions are not explicitly included in this work. The effect of NaCl on the phase boundary of hydrates is simply expressed with the Pitzer model, which has intrinsic limitations at high electrolyte concentrations (Rowland et al., 2015). However, the AARDs of most cases are small. For example, the AARDs of the cases with 0, 3, 5, 10, and 15 wt% NaCl concentrations are 1.93, 2.59, 0.96, 3.73, and 1.97%, respectively.

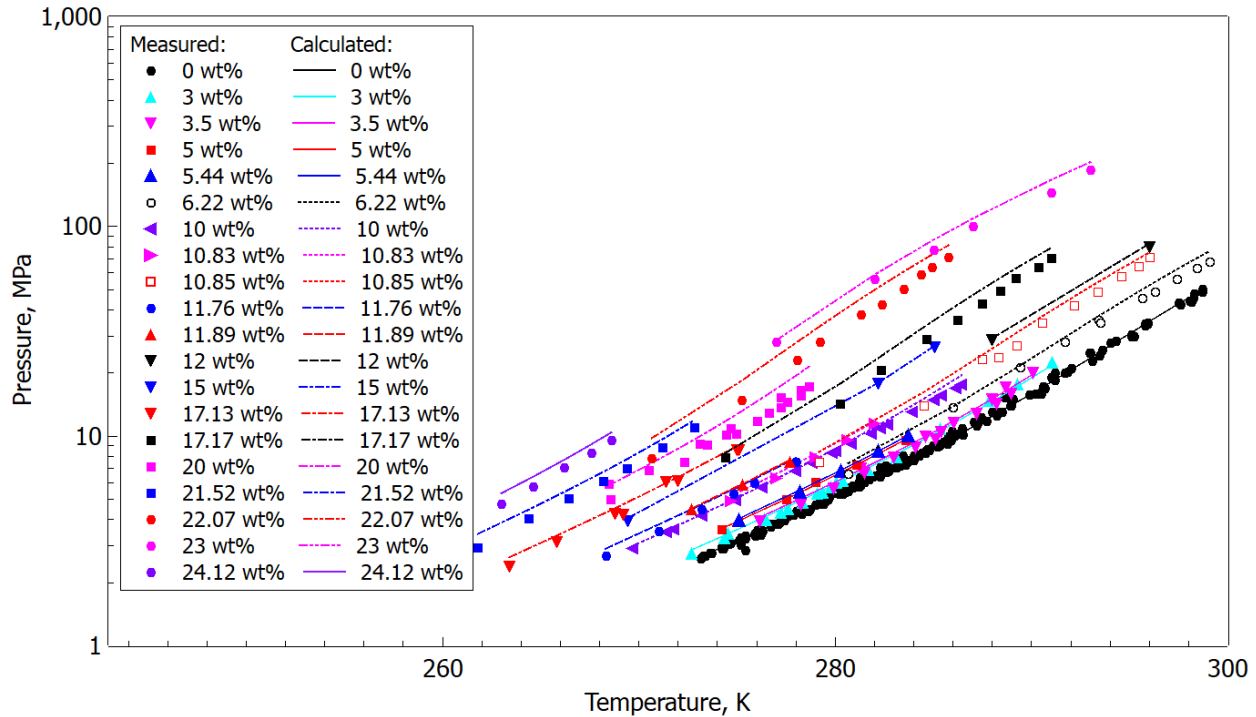


Fig. 4-6 Calculated and measured phase boundary of CH₄ hydrates formed in pure water and NaCl solutions.

References: ● (Adisasmito et al., 1991; De Roo et al., 1983; Deaton and Frost, 1946; Jager and Sloan, 2001; Jhaveri and Robinson, 1965; Kamari et al., 2017; Kastanidis et al., 2016; Kharrat and Dalmazzone, 2003; Maekawa, 2001; Marshall et al., 1964; McLeod and Campbell, 1961; Mei et al., 1996; Mohammadi et al., 2005; Nakamura et al., 2003; Ross and Toczylkin, 1992; Sabil et al., 2014; Sadeq et al., 2017; Seo et al., 2001; Servio and Englezos, 2002; Thakore and Holder, 1987; Verma, 1974; Ward et al., 2014); ▲ (Atik et al., 2009; Dholabhai et al., 1991; Maekawa, 2001); ▼ (Lafond et al., 2012; Maekawa et al., 1995); ■ (Mohammadi et al., 2008); ▲ (Cha et al., 2016); ○ (Jager and Sloan, 2001); ◀ (Maekawa et al., 1995); ▶ (Cha et al., 2016); □ (Jager and Sloan, 2001); ● (De Roo et al., 1983); ▲ (Kharrat and Dalmazzone, 2003); ▼ (Hu et al., 2017); ▼ (Haghighi et al, 2009); ▼ (De Roo et al., 1983; Kharrat and Dalmazzone, 2003); ■ (Jager and Sloan, 2001); ■ (Haghighi et al, 2009; Maekawa et al., 1995); ■ (De Roo et al., 1983); ● (Jager and Sloan, 2001); ● (Hu et al., 2017); ● (De Roo et al., 1983). Note that the percentage in the legend denotes the weight fraction of NaCl in the aqueous solution. The symbols represent the measured data points and the lines are for the calculated ones.

C₂H₆ hydrates

The measured and calculated phase boundary of C₂H₆ hydrates formed in the pure water and the NaCl solution is demonstrated in Fig. 4-7. It is observed that the phase boundary pressure of the C₂H₆ hydrates also increases with the concentration of NaCl solution. An upper quadruple point exists in the phase boundary curve of C₂H₆ hydrates when the temperature is around 288 K and this upper quadruple point is also captured using the proposed theoretical model. The deviation of the calculated phase boundary pressure from the measured ones is evaluated using Eq. 4-13. The deviation of the C₂H₆ hydrates formed in pure water is relatively large, with the AARD of 8.0% for the 118 data points in the pure water. The large deviation may result from the fact that the collected data points at the high-pressure conditions are scarce and lack of cross-verification. The AARDs of the phase boundary pressure of C₂H₆ hydrates formed in the NaCl solutions range from 2.5 to 4.7% when the NaCl concentration is between 3.1 and 20 wt%. The overall AARD of these 61 phase boundary data points is 3.9%. The deviations of the calculated results from the measured ones are acceptable because only 13 out of 179 data points were used for optimization in Section 4.1.4.

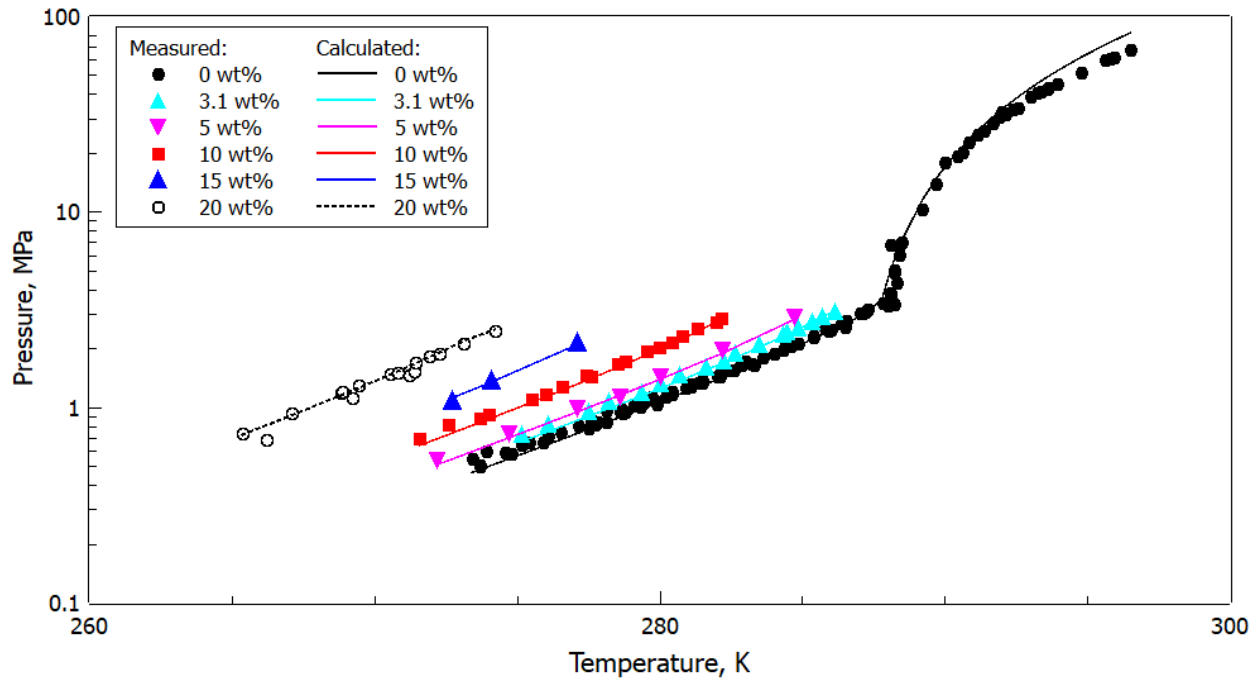


Fig. 4-7 Calculated and measured phase boundary of C_2H_6 hydrates formed in pure water and NaCl solutions.

References: ● (Deaton and Frost, 1946; Galloway et al., 1970; Holder and Grigoriou, 1980; Holder and Hand, 1982; Maekawa and Imai, 2000; Nakano et al., 1998; Ross et al., 1992); ▲ (Maekawa and Imai, 2000); ▼ (Mohammadi et al., 2008); ■ (Maekawa and Imai, 2000; Tohidi et al., 1997); ▲ (Tohidi et al., 1997); ○ (Englezos et al., 1991; Maekawa and Imai, 2000; Tohidi et al., 1993). Note that the percentage in the legend denotes the weight fraction of NaCl in the aqueous solution. The symbols represent the measured data points and the lines are for the calculated ones.

CO₂ hydrates

The measured and calculated phase boundary of CO_2 hydrates formed in pure H_2O and NaCl solutions are presented in Fig. 4-8. Similar to those of CH_4 and C_2H_6 hydrates, the phase boundary pressure of CO_2 hydrates increases with the temperature and the concentration of NaCl solutions. The phase boundary pressure increases from 1.66 to 2.47 MPa when the NaCl solution increases from 10 to 15 wt% at the temperature of 271 K. The lowest AARD is 1.08% for the case of 15

wt% NaCl solution, and the highest one is 3.71% for the case of 5.53 wt% NaCl solution. Overall, the calculated phase boundary pressure of CO₂ hydrates by using the developed model is satisfactory with an AARD of 2.79% for the total 187 points. Although only 48 data points of CO₂ hydrates in pure H₂O are included in the parameter optimization process, the model demonstrates good predictability when NaCl is present.

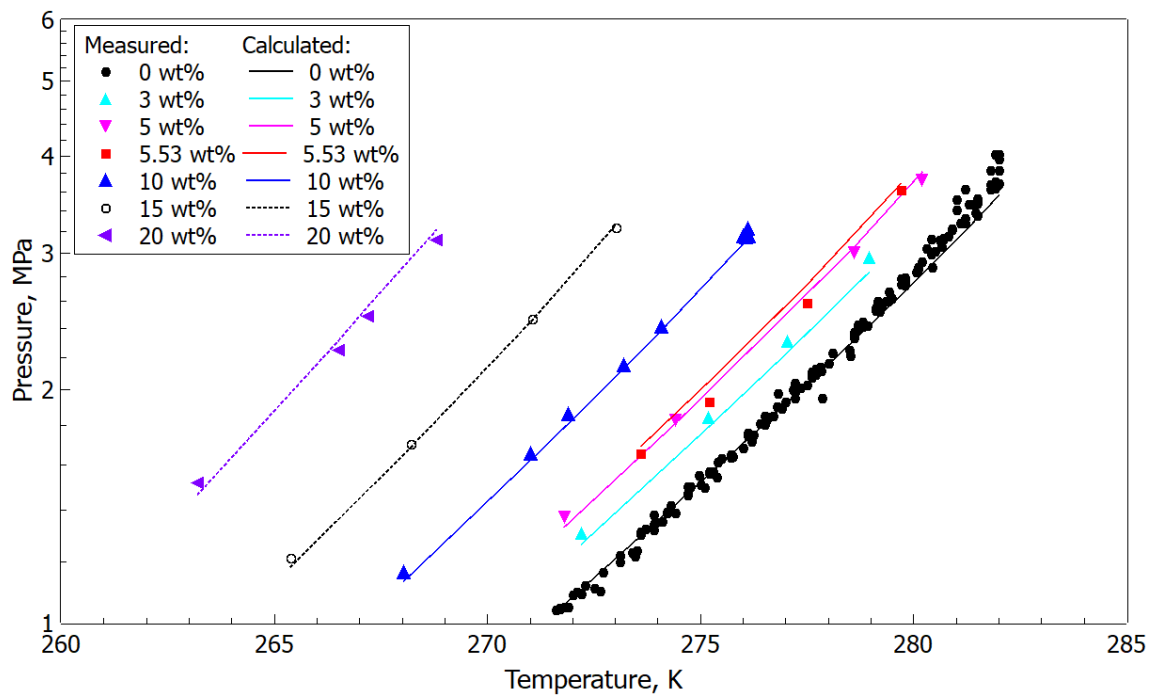


Fig. 4-8 Calculated and measured phase boundary of CO₂ hydrates in pure water and NaCl solutions.

References: ● (Adisasmito et al., 1991; Deaton and Frost, 1946; Fan and Guo, 1999; Fan et al., 2000; Kamari et al., 2017; Kastanidis et al., 2016; Larson, 1955; Mooijer-van den Heuvel et al., 2001; Ohgaki et al., 1993; Robinson and Mehta, 1971; Sabil et al., 2014; Seo et al., 2001; Unruh and Katz, 1949; Vlahakis et al., 1972); ▲ (Dholabhai et al., 1993); ▼ (Mohammadi et al., 2008); ■ (Larson, 1955); ▲ (Dholabhai et al., 1993; Tohidi et al., 1997); ○ (Dholabhai et al., 1993); ◀ (Tohidi et al., 1997). Note that the percentage in the legend denotes the weight fraction of NaCl in the aqueous solution. The symbols represent the measured data points and the lines are for the calculated ones.

CH₄-C₂H₆ hydrates in pure H₂O and NaCl solutions

The calculated and measure phase boundary curves of the binary CH₄-C₂H₆ hydrates formed in pure water and NaCl solutions are presented in Fig. 4-9. Overall, the phase boundary pressure of the CH₄-C₂H₆ hydrates decreases as the concentration of CH₄ becomes smaller. Also, the phase boundary pressure increases with the addition of NaCl in the aqueous solution by comparing the phase boundary curves with the CH₄ composition of 74.7 mol%. It is noted that the measured data points of the case with a CH₄ composition of 27.51 mol% is less reliable. Because the measured phase boundary pressure of this case is larger than that of case with a higher CH₄ composition, e.g., 56.4 and 85 mol%, which is contrary to the general trend that the phase boundary pressure increases with the rise in CH₄ concentration in the CH₄-C₂H₆ mixture. Hence, this group of data points are not included to validate the developed theoretical model. The overall AARD of the 77 data points in the Fig. 4-9 is 6.9%. As aforementioned, the mixture of CH₄-C₂H₆ might form sII structure hydrates even though both CH₄ and C₂H₆ are sI formers. According to the theoretical model proposed in this section, it is found that only sI hydrate structure is formed when the CH₄ composition is 98.8 mol% and when its composition is below 74.7 mol%. When the composition of CH₄ is between 97.8 and 74.7 mol%, sII structure is detected. For instance, only sII structure hydrates are formed for the data points with CH₄ concentration of 97.1, 95, 90.4, and 80.9 mol%. It is worth noting that the hydrate structure is also influenced by the pressure and temperature, which is observed when the CH₄ concentration is 97.8, 94.6, 85, and 74.7 mol%.

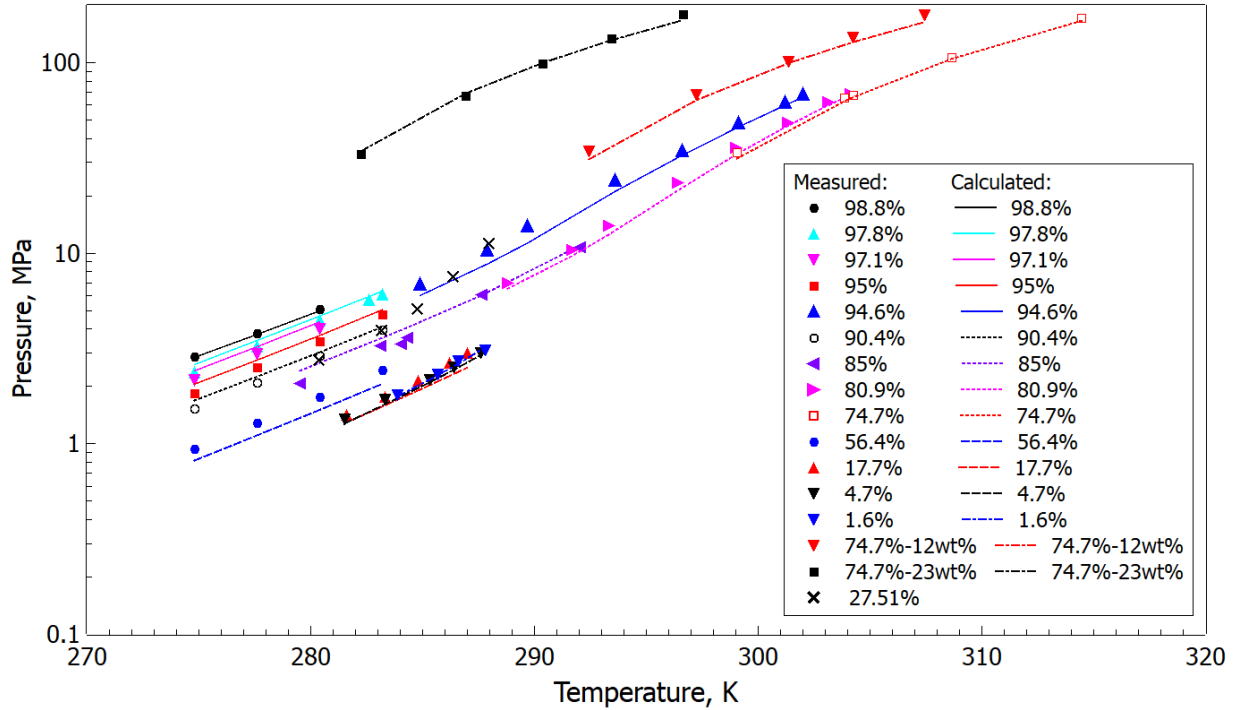


Fig. 4-9 Calculated and measured phase boundary of CH₄-C₂H₆ hydrates in pure water and NaCl solutions.

References: ●, ▲, ▼, ■, ●, and ○ (Deaton and Frost, 1946); ▲ and ► (McLeod and Campbell, 1961); ◀ (Becke, 1992); □, ▼, and ■ (Hu et al., 2018); ▲, ▼, and ▼ (Holder and Grigoriou, 1980); × (Sabil et al., 2014). Note that the percentage in the legend represents the mole fraction of CH₄ in the feed gas mixture. ‘74.7%-12wt%’ and ‘74.7%-23wt%’ denote that the CH₄ composition in the gas mixture is 74.7 mol% and the NaCl concentration is 12 and 23 wt%, respectively. The symbols represent the measured data points and the lines are for the calculated ones.

CH₄-CO₂ hydrates in pure H₂O

The measured and calculated phase boundary of binary CH₄-CO₂ hydrates formed in pure H₂O with various gas compositions are demonstrated in Fig. 4-10. The phase boundary curves of the binary CH₄-CO₂ hydrates are characterized by a convergence trend at the high-temperature

range (Adisasmito et al., 1991; Sadeq et al., 2017; Seo et al., 2001). This convergence trend may be explained qualitatively with the Clausius-Clapeyron equation:

$$\frac{d(\ln P)}{dT} = \frac{\Delta H_d}{Z_c RT^2} \quad (4-28)$$

where ΔH_d is the dissociation enthalpy of gas hydrates; Z_c represents the compressibility factor. Both ΔH_d and Z_c are dependent on temperature T . It has been found that ΔH_d of CO₂ hydrates is generally larger than that of CH₄ hydrates (Kang et al., 2001). Also, CO₂ is more compressible than CH₄. Therefore, the slope of phase boundary curves of the binary CH₄-CO₂ hydrates in the semi-logarithm pressure-temperature plot increases with the concentration of CO₂ in the gas mixture, resulting in a convergence trend at the high-temperature range in Fig. 4-10. This trend was also observed in the calculated phase boundary of binary CH₄-CO₂ hydrates formed in NaCl solutions.

In addition, the phase boundary pressure of the binary hydrates declines with increasing CO₂ compositions in the feed gas mixture. This is because the diameter of the CO₂ molecule is similar to that of the large cages in sI hydrates so that CO₂ molecules form hydrates more readily than CH₄ at the same conditions (Becke et al., 1992). Compared with the measured phase boundary data of pure gas, those of gas mixture tend to have larger discrepancies. Because more errors might be introduced in determining composition the of gas mixture. For instance, the measured phase boundary pressure of CH₄-CO₂ hydrates with a CH₄ composition of 74.49 mol% in the feed gas mixture, denoted with the inverted red triangle in Fig. 4-10 is even higher than that with a CH₄ composition of 80 mol%. This goes against the abovementioned trend. In spite of the discrepancies among data with various sources, the overall AARD of these 124 points is 5.86%, which is acceptable given only 6 of the 124 data points have been used for optimization. The deviations are

relatively large when the concentration of CH₄ in the feed gas mixture is low, partially due to the fact that cross-verification is unavailable for the data reported in these composition ranges. For the data with cross-verification, e.g., with CH₄ composition in the feed gas mixture of 80, 70, and 60 mol%, the AARDs are 3.87, 3.63, and 1.77%. Specifically, the AARDs of the cases with NaCl concentration of 12 and 23 wt% are 5.9% and 3.2%, which proves the accuracy of the proposed model.

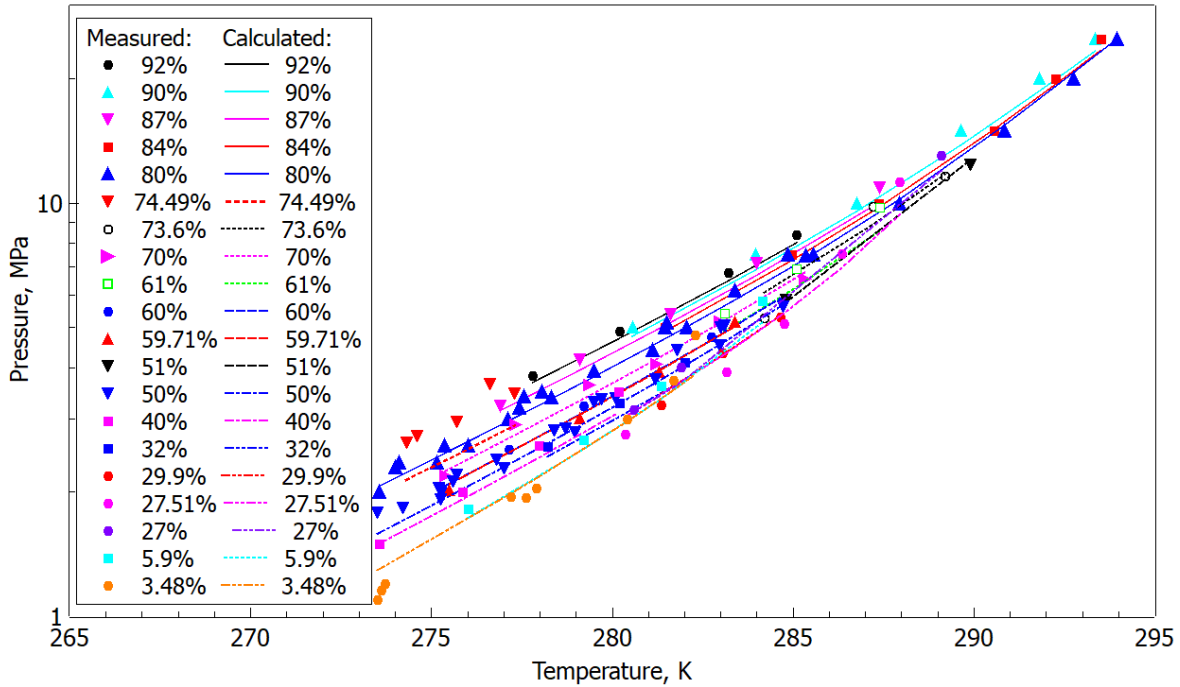


Fig. 4-10 Calculated and measured phase boundary of CH₄-CO₂ hydrates in pure H₂O.

Reference: ● (Adisasmito et al., 1991); ▲ (Sadeq et al., 2017); ▼ (Adisasmito et al., 1991); ■ (Sadeq et al., 2017); ▲ (Beltrán and Servio, 2008; Sadeq et al., 2017; Dholabhai & Bishnoi et al., 1994; Seo et al., 2001; Servio et al., 1999); ▼ (Kastanidis et al., 2017); ○ (Belandria et al., 2010); ▶ (Beltrán and Servio, 2008); □ (Adisasmito et al., 1991); ● (Beltrán and Servio, 2008); ▲ (Mohammadi et al., 2013); ▼ (Belandria et al., 2010); ▼ (Beltrán and Servio, 2008; Servio et al., 1999); ■ (Seo et al., 2001); ■ (Adisasmito et al., 1991); ● (Partoon et al., 2016); ● (Sabil et al., 2014); ● (Belandria et al., 2010); ■ (Chapoy et al., 2014); ● (Fan and

Guo, 1999). Note that the percentage in the legend represents the mole fraction of CH₄ in the feed gas mixture. The symbols represent the measured data points and the lines are for the calculated ones.

CH₄-CO₂ hydrates in NaCl solutions

The impact of NaCl on the phase boundary of the binary CH₄-CO₂ hydrates is presented in Fig. 4-11. It can be seen that the phase boundary pressure of the binary CH₄-CO₂ hydrates increases with the concentrations of NaCl solutions, similar to that of pure CH₄ and CO₂ hydrates. The deviations of the collected 34 phase boundary data points are evaluated by using Eq. 4-13. The largest AARD is 9.08% in the case with CH₄ composition of 80 mol% and NaCl concentration of 5 wt%. One possible cause of the relatively large deviation is the simplified treatment of water activity. As described in Section 3, the effect of dissolved gas and NaCl on the phase boundary of gas hydrates were represented by Henry's law and the Pitzer model separately, which neglects the interactions between gas and dissolved ions. Hence, models explicitly taking into account the interactions among gas, water, and ions are recommended to more accurately predict the phase boundary of hydrates formed in systems containing gas mixture and electrolytes. It is worth noting that the AARD of the 34 data points is 5.94%, which proves the reliability of the developed model since none of these data points have been employed in the optimization.

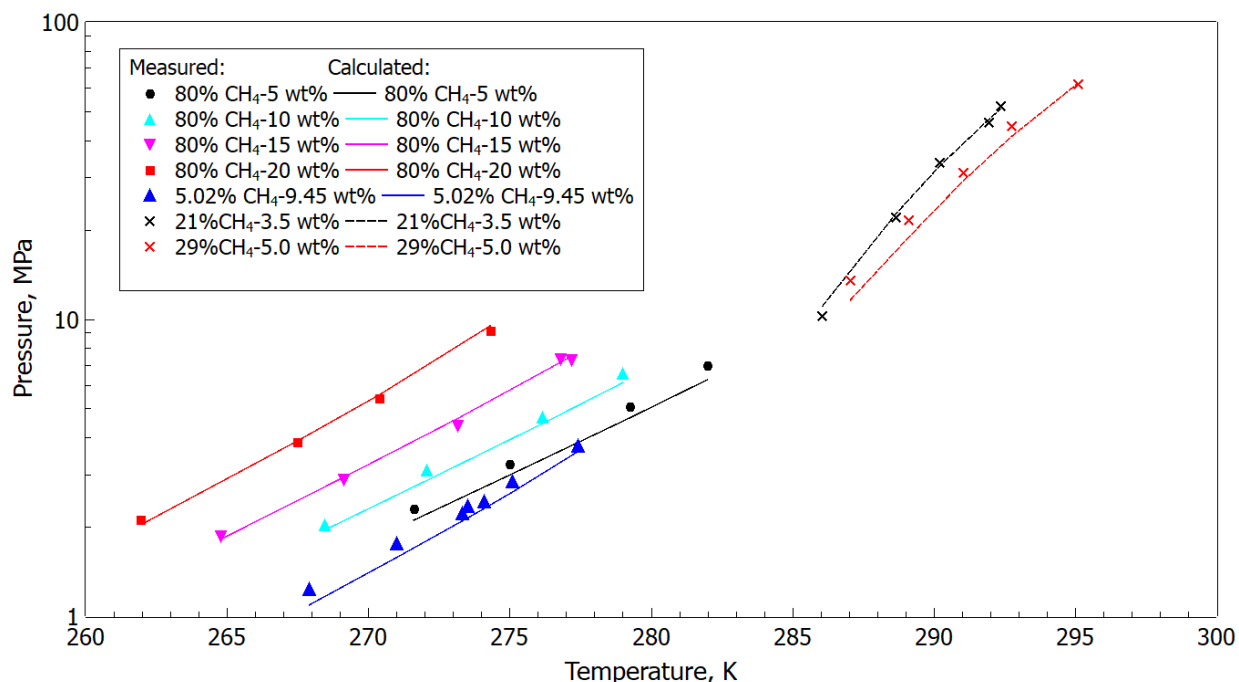


Fig. 4-11 Calculated and measured phase boundary of CH₄-CO₂ hydrates in NaCl solutions.

References: ●, ▲, ▼, ■ (Dholabhai and Bishnoi, 1994); ▲ (Fan and Guo, 1999); ×, × (Zheng et al., 2020). Note that the percentage before CH₄ denotes the mole percent of CH₄ in the feeding gas mixture and that after CH₄ represents the mass fraction of NaCl in the aqueous phase, in wt%. The symbols represent the measured data points and the lines are for the calculated ones.

4.3 A Single Modified PR EoS for Aqueous and Gas-rich Phases

4.3.1 Mathematical models

In this section, a modeling framework using a single model for the aqueous phase and the gas-rich phase is described, i.e., a modified Peng-Robinson (mPR) EoS. The effect of NaCl on the hydrate phase boundary is determined using the Pitzer model. The modified PR EoS proposed by Li and Yang (2013) is applied in this work due to its high capability for the polar molecule of water. Such a modified PR EoS incorporates a new alpha function for water and asymmetric binary interaction

parameters (BIP) for water-gas pairs so that the fluid phase can be considered by using a single EoS (Zheng et al., 2020a).

Alpha function of water is illustrated in the following equation:

$$\alpha_w(T) = \left[1.00095 + 0.39222(1 - T_{rw}) - 0.07294(1 - T_{rw}^{-1}) + 0.00706(1 - T_{rw}^{-2}) \right]^2 \quad (4-29)$$

where T_{rw} is the reduced water temperature, i.e., $T_{rw} = T / T_{cw}$. The alpha function in Eq. 4-22 is applied for the gas components.

The asymmetric BIP is used for water-gas pairs. In the gas-rich phase, the BIP between CH₄-H₂O, C₂H₆-H₂O, and CO₂-H₂O equal 0.485, 0.492, and 0.1896, respectively (Søreide and Whitson, 1992). While in the aqueous phase, the following correlations are proposed (Li and Yang, 2013; Søreide and Whitson, 1992):

$$k_{HC,H_2O}^A = -1.1120 - 1.7369\omega^{-0.1} + (1.1001 + 0.8360\omega)T_r - (0.15742 + 1.0988\omega)T_r^2 \quad (4-30)$$

$$k_{CO_2,H_2O}^A = -1.104324 + 2.040527T_r - 1.417707T_r^2 + 0.379003T_r^3 \quad (4-31)$$

where k_{HC,H_2O}^A and k_{CO_2,H_2O}^A represent the BIP between water and hydrocarbon component and that between water and CO₂ in the aqueous phase, respectively.

The flowchart of the phase boundary calculation by using the modified PR EoS is illustrated in Fig. 4-12. First, the gas composition, water salinity, and temperature of interest are provided. Then the gas fugacity and water composition in the aqueous phase are calculated by using the modified PR EoS with the initial guess of pressure. The effect of NaCl on water activity is evaluated by using the Pitzer model. The pressure is updated until the difference between $\Delta\mu_w^H$ and $\Delta\mu_w^A$, which are respectively determined by using the vdW-P model and the Holder's

framework (Holder et al., 1980), is within a certain error. Note that the correlation of the reference hydrate phase boundary (Parrish and Prausnitz, 1972) provides a good guess of the initial pressure. This flowchart will be implemented twice to calculate the phase boundary pressure of sI and sII hydrates respectively, and the smaller one is selected as the phase boundary pressure under the specific temperature and composition conditions.

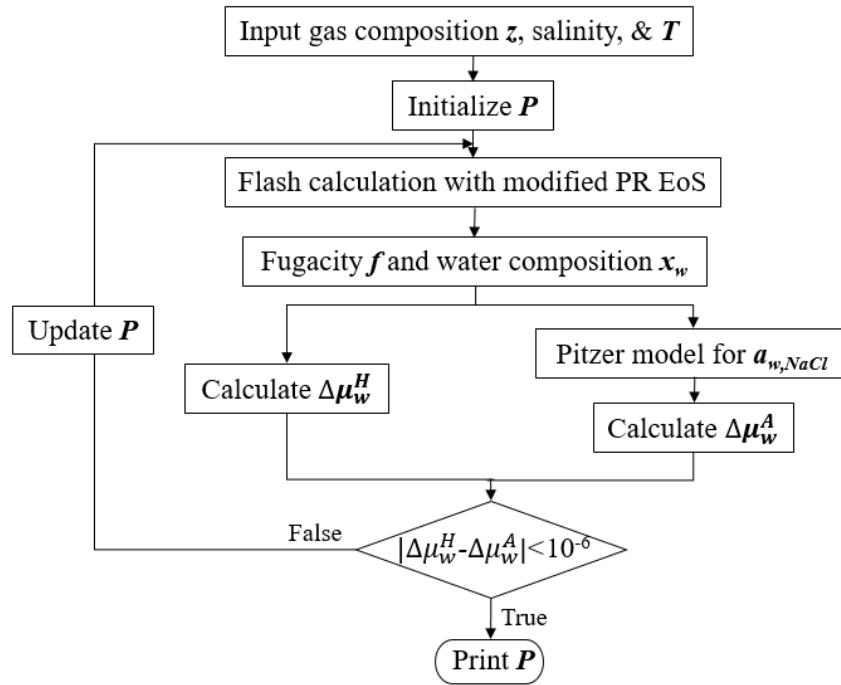


Fig. 4-12 Flowchart to calculate the phase boundary using a single model for the aqueous and gas-rich phases

4.3.2 Simulation results

The collected and measured phase boundary database of binary CH₄-C₂H₆ and CH₄-CO₂ hydrates established in Chapter 3 is adopted to evaluate the reliability of the proposed theoretical model using a modified PR EoS for the aqueous and gas-rich phases.

Phase boundary of CH₄-C₂H₆ hydrates in pure water and NaCl solutions

The calculated phase boundary of the binary CH₄-C₂H₆ hydrates formed in the pure water and the NaCl solutions are compared with the measured ones, as illustrated in Fig. 4-13. It can be seen that the theoretical model developed in this section can well capture the effect of gas composition and NaCl concentration on the hydrate phase boundary. It is worth noting that this model is also capable of capturing the effect of gas composition, pressure, and temperature on the structure change of CH₄-C₂H₆ hydrates. Quantitatively, the overall AARD of these data points determined by using Eq. 4-13 is 6.8%, close to the model developed in Section 4.2. For instance, the AARDs are 2.1, 2.2, and 8.3% respectively for the scenarios of the binary CH₄-C₂H₆ hydrates with a CH₄ composition of 74.7 mol% formed in the pure water, in 12 wt% and 23 wt% NaCl solutions.

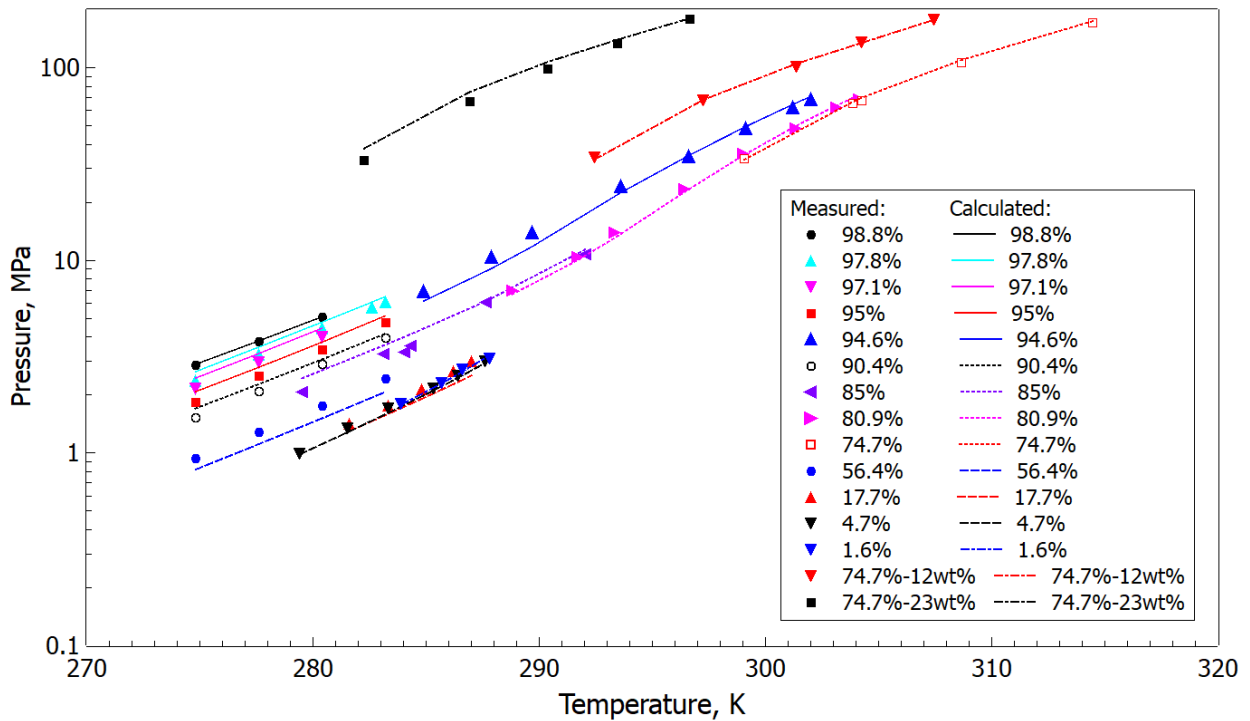


Fig. 4-13 Calculated and measured phase boundary of CH₄-C₂H₆ hydrates in pure water and NaCl solutions.

References: ●, ▲, ▼, ■, ●, and ○ (Deaton and Frost, 1946); ▲ and ► (McLeod and Campbell, 1961); ◀ (Becke, 1992); □, ▼, and ■ (Hu et al., 2018); ▲, ▼, and ▼ (Holder and Grigoriou, 1980); × (Sabil et al., 2014). Note that the percentage in the legend represents the mole fraction of CH₄ in the feed gas mixture. ‘74.7%-12wt%’ and ‘74.7%-23wt%’ denote that the CH₄ composition in the gas mixture is 74.7 mol% and the NaCl concentration is 12 and 23 wt%, respectively. The symbols represent the measured data points and the lines are for the calculated ones.

Phase boundary of CH₄-CO₂ hydrates in pure water

A total of 86 collected phase boundary data points of CH₄-CO₂ hydrates formed in the pure water are used in this section to validate the theoretical model proposed in this section. The CH₄ concentration in the feed gas mixture ranging from 27 to 92 mol%, with pressure and temperature up to 25 MPa and 294 K, respectively, as demonstrated in Fig. 4-14. The collected data points are denoted with symbols and the calculated results are represented with curves. It is shown that the phase boundary pressure decreases with the concentration of CO₂ in the feed gas mixture, due to the larger diameter of CO₂ than that of CH₄. Similar to that of pure CH₄ hydrates, the phase boundary curve of individual CH₄-CO₂ hydrates is linear in the semi-log curve, but the slope of the phase boundary curves changes with the gas composition, resulting in a convergence trend of the phase boundary curves at the high-temperature region. This convergence trend can be explained with the Clausius-Clapeyron equation (Zheng et al., 2020b). It can be observed that the calculated phase boundary by using the proposed theoretical model is close to the measured ones, with an overall AARD of 3.7%. The relatively large deviations of 4.2% and 4.9% are from scenarios with CH₄ concentration of 50 mol% and 80 mol%, respectively. One cause of the relatively large deviation of these two cases is that the measured data for these cases are more scattered. The AARD of the rest cases is below 4.0%.

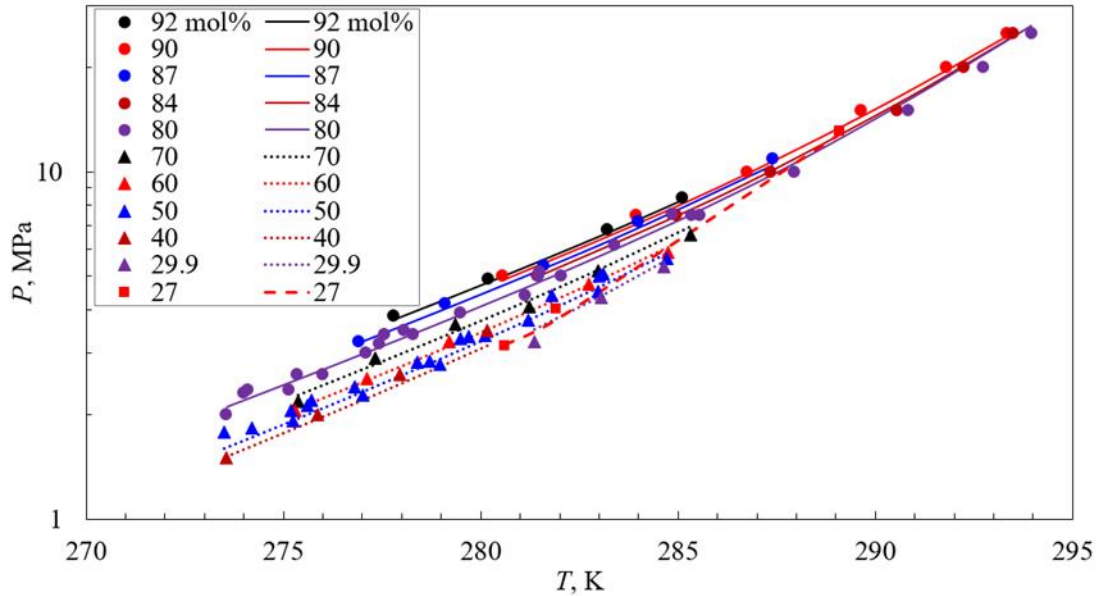


Fig. 4-14 Comparison of the collected phase boundary data (symbols) with the calculated phase boundary (curves) of CH₄-CO₂ hydrates formed in pure water.

Reference: ● and ● (Adisasmito et al., 1991); ● and ● (Sadeq et al., 2017); ● (Beltrán and Servio, 2008; Sadeq et al., 2017; Dholabhai and Bishnoi, 1994; Seo et al., 2001; Servio et al., 1999); ▲ and ▲ (Beltrán and Servio, 2008); ▲ (Beltrán and Servio, 2008; Servio et al., 1999); ▲ (Seo et al., 2001); ▲ (Partoon et al., 2016); ■ (Belandria et al., 2010). Note that the percentage in the legend represents the mole fraction of CH₄ in the feed gas mixture. The symbols represent the measured data points and the lines are for the calculated ones.

Phase boundary of CH₄-CO₂ hydrates in NaCl solutions

In this section, the reliability of the newly developed model will be further evaluated by using the collected database of CH₄-CO₂ hydrates formed in NaCl solutions. As aforementioned, only two groups of measured phase boundary data of CH₄-CO₂ hydrates formed in NaCl solutions are available in the literature (Dholabhai and Bishnoi, 1994; Fan and Guo, 1999), as presented in Fig. 4-15, where the filled circles and the triangle symbols represent the collected data and the curves denote the phase boundary conditions calculated with the newly developed model. It is

demonstrated that the phase boundary pressure of CH₄-CO₂ hydrates increases with the NaCl concentrations, owing to the influence of ions on the water activity. The deviations of the calculated phase boundary pressure from the collected database are evaluated by using Eq. 4-13. The overall AARD 24 data points is 5.3%, which is acceptable since none of these data points have been used for parameter optimization. This proves the reliability of the newly developed model in predicting the phase boundary of CH₄-CO₂ hydrates formed in NaCl solutions.

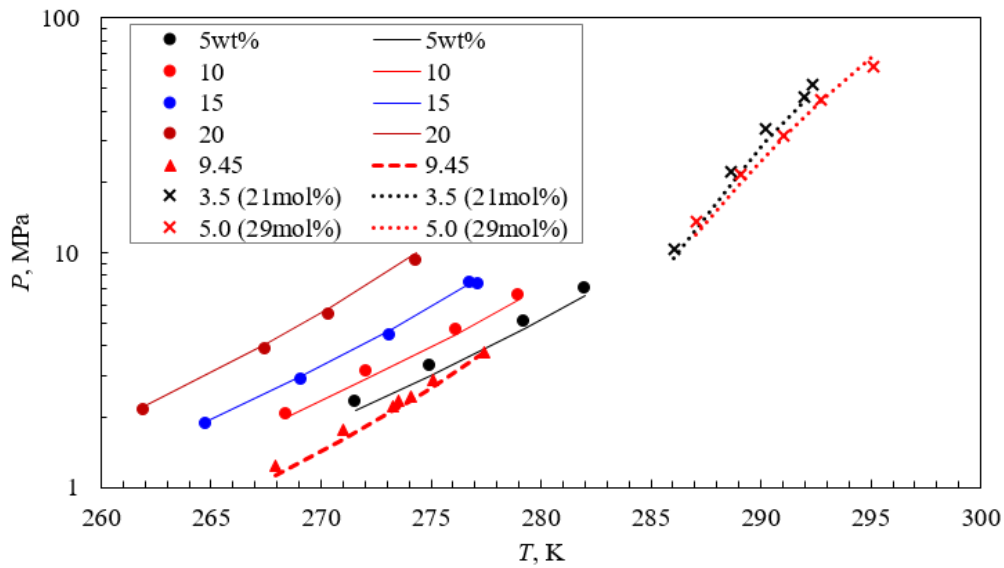


Fig. 4-15 Comparison of the collected and measured phase boundary data (symbols) with the calculated phase boundary (curves) of CH₄-CO₂ hydrates formed in NaCl solutions.

Reference: ●, ●, ●, and ● (Dholabhai and Bishnoi, 1994); ▲ (Fan and Guo, 1999); × and × (Zheng et al., 2020a). Note that the percentage in the legend represents the mass fraction of NaCl in the solutions. The CH₄ concentration in the feed gas mixtures are 80 mol% and 5.02 mol% respectively for the collected data denoted with the filled circles and the triangle, and those for the black and red crosses are 21 and 29 mol%, respectively.

It is interesting to see the phase boundary denoted by the black and red crosses in Fig. 4-15 is in contrast to the observations that the phase boundary pressure of CH₄-CO₂ hydrates increases

with CH₄ concentration as well as the salinity of NaCl solutions. This is due to the high concentration of CO₂ measured in this work, i.e., 79 and 71 mol% respectively, in which case the upper quadruple point (i.e., hydrate-vapor-water-liquid gas four-phase coexistence point) is easily satisfied (Zheng et al., 2020a). It was estimated that the upper quadruple point is around 8 MPa for the CH₄-CO₂ mixture containing 78 mol% CO₂ (Bi et al., 2013). The high-pressure condition, i.e., above 10 MPa is of interest for the data points denoted with the black and red crosses. When the pressure is above the upper quadruple point of the CH₄-CO₂ mixture, the phase boundary pressure is higher for mixture with a larger concentration of CO₂. This is supported by the phase boundary curve of CH₄-CO₂ hydrates containing 27 mol% CH₄ in the feed gas mixture in Fig. 4-14, where we can see its phase boundary pressure is higher than that of CH₄-CO₂ hydrates containing 80 mol% CH₄ in the feed gas mixture when the pressure is higher than 10 MPa. The AARDs are 8.9% and 6.2% for the scenarios represented by the black and red crosses respectively. This is acceptable since an ideal solid solution of hydrate model is applied in this work. Also, none of these data points have been used in parameter regression. These data points have filled the blank of experimental phase boundary data at high-pressure and high-temperature conditions, which is significant to investigate the interactions between gas, water, and ions.

4.4 Summary

In this section, two theoretical models have been established, both of which adopt separate models for the non-hydrate phases. In the first model, the PR EoS for the gas-rich phase and the Henry's law combined with the Poynting correction for the gas solubility in the aqueous phase. The effect of NaCl on the hydrate phase boundary is considered using the Pitzer model. In the second model, a single mPR EoS is applied for both aqueous and gas-rich phases and the Pitzer model is used to

account for the impact of NaCl on water activity in the aqueous phase. In both of the two models, a new set of reference properties are applied and the Kihara parameters of CH₄, C₂H₆, and CO₂ are optimized by fitting against the measured phase boundary data points of hydrates formed in pure water.

The database developed in this section is used to quantify the reliability of the two developed models. It is found that the two models can capture the general trend that the phase boundary pressure of CH₄, C₂H₆, CO₂, and binary CH₄-C₂H₆ and CH₄-CO₂ hydrates increases with the temperature and the concentration of NaCl solutions. Also, the phase boundary pressure of the binary CH₄-C₂H₆ and CH₄-CO₂ hydrates increases with the concentration of CH₄ in the feed gas. The overall AARD of the 984 data points using the first theoretical model is 5.0%. The data points of the binary CH₄-C₂H₆ and CH₄-CO₂ hydrates formed in the pure water and NaCl solution are employed to evaluate the reliability of the second model. The overall AARD of the 187 data points of the binary hydrates is 5.2%. It is worth noting that the two theoretical models are capable of detecting the sII structure formed by the binary CH₄-C₂H₆ hydrates. The structure of the binary CH₄-C₂H₆ hydrates is influenced not only by the gas composition, but the temperature and pressure as well. Also, the reliability of the two groups of data points of CH₄-CO₂ hydrates measured in Section 3.2 has been verified with the calculated results by using these two theoretical models. For example, the AARD of the data points of the cases with a NaCl concentration of 3.5 and 5.0 wt% are 8.9% and 6.2%, respectively.

CHAPTER 5 DETERMINATION OF THE HYDRATE PHASE BOUNDARY USING A UNIFIED EOS FOR THE NON-HYDRATE PHASES

A unified EoS is developed in this chapter to quantify the effect of the dissolved gas and electrolyte on water activity in the aqueous phase. The performance of this model will be tested by comparing with the phase boundary of pure and binary CH₄, C₂H₆, and CO₂ hydrates formed in single and mixed NaCl, KCl, MgCl₂, and CaCl₂ solutions. These electrolytes are the most concentrated ones in the seawater and the reservoir fluids. Also, NaCl and KCl are the representatives of 1-1 type electrolytes and MgCl₂ and CaCl₂ are those of 2-1 type ones (Zheng et al., 2020c).

5.1 Model Development

5.1.1 Unified EoS

As demonstrated in Fig. 5-1, in addition to the van der Waals forces between gas molecules, a system containing natural gas, water, and ions involves various other interactions, e.g., the hydrogen bonds between water molecules, ionic solvation between water and ions, hydrophobic hydration between water and gas molecules, and Coulombic forces between cation and anion. In this work, a unified EoS is developed to represent the influences of different interactions on the thermodynamic properties, e.g., water activity and fugacity. In this new unified EoS, a modified PR EoS is employed to quantify the interactions between water, natural gas, and uncharged ions. As for the charged ions, a simplified explicit mean spherical approximation (MSA) term and a Born term are used to describe the Coulombic force and discharging-charging processes, respectively. Two assumptions are made in the development of this model. First, the interactions

between gas and ions can be ignored due to the low solubility of natural gas. The second one is that the ion-pairing effect is negligible. This is because the ion-pairing is significant at high-temperature conditions (Kontogeorgis et al., 2018). The electrolytes of interest, i.e., NaCl, KCl, MgCl₂, and CaCl₂, can be regarded as fully ionized at hydrate formation conditions.

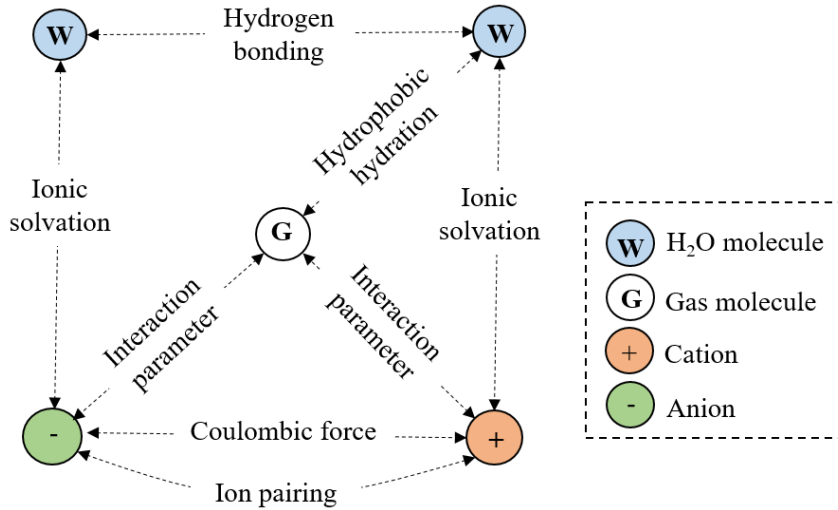


Fig. 5-1 Schematic diagram of the interactions between various components

The unified EoS is established by summing up the contributions of the aforementioned interactions to the Helmholtz free energy. Similar to the work of Ahmed et al. (2018), the first step is to turn the ions into uncharged ones and the energy change is determined by using the Born term, as described in Eq. 5-1.

$$\frac{A_{Born,dis}^r}{RT} = -\frac{e^2 N_A}{4\pi D_0 RT} \sum_i \frac{n_i Z_i^2}{\sigma_i^{Born}} \quad (5-1)$$

where e denotes the elementary charge, 1.60×10^{-19} C; N_A is the Avogadro number, 6.0232×10^{23} mol⁻¹; D_0 represents the permittivity of vacuum, 8.854×10^{-12} F/m; n_i and Z_i are the moles and

charges of ions respectively in the aqueous phase; σ_i^{Bom} denotes the diameter of solvated ion, which includes the effect of ionic solvation (Inchekel et al., 2008).

The next step is to include the effect of the repulsive and attractive interactions between gas, water, and uncharged ions by using a modified PR EoS (Li and Yang, 2013). Their contributions to the Helmholtz free energy are quantified with the following equations:

$$\frac{A_{mPR}^r}{nRT} = -\ln\left(\frac{\bar{V}-b}{\bar{V}}\right) - \frac{a(T)}{2\sqrt{2}bRT} \ln\left(\frac{\bar{V}+(1+\sqrt{2})b}{\bar{V}+(1-\sqrt{2})b}\right) \quad (5-2)$$

$$a(T) = a^0 \cdot \alpha(T) = 0.457235 \frac{R^2 T_c^2}{P_c} \cdot \alpha(T) \quad (5-3)$$

$$b = 0.07780 \frac{RT_c}{P_c} \quad (5-4)$$

The new alpha function of water described in Section 4.3.1 is applied. Similarly, the asymmetric BIP for water-gas pairs in the aqueous phase is employed. In this model, the BIP of gas-gas and gas-ion pairs are assumed 0.

The third step of developing the unified EoS is to charge the ions. The corresponding change in the Helmholtz free energy is described by the Born term as shown in Eq. 5-5 (Inchekel et al., 2008).

$$\frac{A_{Born, ch}^r}{RT} = \frac{e^2 N_A}{4\pi D_0 D_r RT} \sum_i \frac{n_i Z_i^2}{\sigma_i^{Bom}} \quad (5-5)$$

where D_r denotes the relative dielectric constant.

In the last step, a simplified explicit MSA term (Haghtalab and Mazloumi, 2010; Lin et al., 2007) is used to quantify the contribution of Coulombic force to the Helmholtz free energy, as shown in the following equations:

$$\frac{A_{MSA}^r}{RT} = -\frac{2\Gamma^3 V}{3\pi N_A} \left(1 + \frac{3}{2} \sigma^{MSA} \Gamma \right) \quad (5-6)$$

$$\Gamma = \frac{1}{2\sigma^{MSA}} \left(\sqrt{1 + 2\sigma^{MSA} \kappa} - 1 \right) \quad (5-7)$$

$$\sigma^{MSA} = \frac{\sum n_i Z_i^2 \sigma_i^{MSA}}{\sum n_i Z_i^2} \quad (5-8)$$

$$\kappa^2 = \frac{e^2 N_A^2}{D_0 D_r RT V} \sum n_i Z_i^2 \quad (5-9)$$

where σ_i^{MSA} denotes the ion diameter in the MSA term.

Therefore, the total residual Helmholtz free energy of a system containing gas, water, and electrolytes can be expressed as:

$$A^r = A_{mPR}^r + A_{Born}^r + A_{MSA}^r \quad (5-10)$$

where $A_{Born}^r = A_{Born,dis}^r + A_{Born,ch}^r$.

The pressure and fugacity coefficients may be calculated with Eqs. 5-11 and 5-12, respectively:

$$P = \frac{RT}{\bar{V}} - \left(\frac{\partial A_{mPR}^r}{\partial V} \right)_T - \left(\frac{\partial A_{Born}^r}{\partial V} \right)_T - \left(\frac{\partial A_{MSA}^r}{\partial V} \right)_T \quad (5-11)$$

$$\ln \phi_i = \frac{1}{RT} \left[\left(\frac{\partial A_{mPR}^r}{\partial n_i} \right) + \left(\frac{\partial A_{Born}^r}{\partial n_i} \right) + \left(\frac{\partial A_{MSA}^r}{\partial n_i} \right) \right]_{T,V,n_{j \neq i}} - \ln Z_c \quad (5-12)$$

where Z_c denotes the compressibility factor.

Derivation of pressure

In this work, it is assumed that the relative dielectric constant D_r is dependent on the molar volume.

$$P = \frac{RT}{\bar{V}} - \left(\frac{\partial \bar{A}_{mPR}^r}{\partial \bar{V}} \right)_T - \left(\frac{\partial A_{Born}^r}{\partial V} \right)_T - \left(\frac{\partial A_{MSA}^r}{\partial V} \right)_T \quad (5-13)$$

$$\begin{aligned} \frac{RT}{\bar{V}} - \left(\frac{\partial \bar{A}_{mPR}^r}{\partial \bar{V}} \right)_T &= \frac{RT}{\bar{V}} - RT \frac{\partial}{\partial \bar{V}} \left(-\ln \left(\frac{\bar{V}-b}{\bar{V}} \right) - \frac{a(T)}{2\sqrt{2}bRT} \ln \left(\frac{\bar{V}+(1+\sqrt{2})b}{\bar{V}+(1-\sqrt{2})b} \right) \right) \\ &= \frac{RT}{\bar{V}-b} - \frac{a(T)}{\bar{V}(\bar{V}+b)+b(\bar{V}-b)} \end{aligned} \quad (5-14)$$

$$\begin{aligned} \left(\frac{\partial A_{Born}^r}{\partial V} \right)_T &= \frac{\partial}{\partial V} \left(-\frac{e^2 N_{Av}}{4\pi D_0} \left(1 - \frac{1}{D_r} \right) \sum_i \frac{n_i Z_i^2}{\sigma_i^{Born}} \right) \\ &= -\frac{e^2 N_{Av}}{4\pi D_0 D_r^2} \cdot \frac{\partial D_r}{\partial V} \cdot \sum_i \frac{n_i Z_i^2}{\sigma_i^{Born}} \end{aligned} \quad (5-15)$$

where,

$$\frac{\partial D_r}{\partial V} = \frac{1}{1 + \sum_i \zeta x_i} \cdot \left(-\frac{n_w M_w}{\rho_0 V^2} \right) \cdot (F_1(T) + F_2(T) + F_3(T) + F_4(T)) \quad (5-16)$$

$$\begin{aligned} \left(\frac{\partial A_{MSA}^r}{\partial V} \right)_T &= RT \cdot \frac{\partial}{\partial V} \left(-\frac{2\Gamma^3 V}{3\pi N_A} \left(1 + \frac{3}{2} \sigma^{MSA} \Gamma \right) \right) \\ &= -\frac{2\Gamma^3 RT}{3\pi N_A} \left(1 + \frac{3}{2} \sigma^{MSA} \Gamma \right) - \frac{2RTV}{\pi N_A} \cdot (1 + 2\sigma^{MSA} \Gamma) \cdot \Gamma^2 \cdot \frac{\partial \Gamma}{\partial V} \end{aligned} \quad (5-17)$$

where,

$$\frac{\partial \Gamma}{\partial V} = \frac{1}{2\sqrt{1+2\sigma^{MSA}\Gamma}} \frac{\partial \kappa}{\partial V} \quad (5-18)$$

and

$$\frac{\partial \kappa}{\partial V} = \frac{1}{2\kappa} \frac{e^2 N_A^2}{D_0 RT} \cdot \sum n_i Z_i^2 \cdot \frac{\partial}{\partial V} \left(\frac{1}{D_r V} \right) \quad (5-19)$$

Derivation of fugacity coefficient

$$\ln \phi_i = \frac{1}{RT} \left[\left(\frac{\partial A_{mPR}^r}{\partial n_i} \right) + \left(\frac{\partial A_{Born}^r}{\partial n_i} \right) + \left(\frac{\partial A_{MSA}^r}{\partial n_i} \right) \right]_{T,V,n_{j \neq i}} - \ln Z_c \quad (5-20)$$

$$\begin{aligned} \frac{1}{RT} \left(\frac{\partial A_{mPR}^r}{\partial n_i} \right) - \ln Z_c &= -\ln(Z_c - B) + \frac{b_i}{b} (Z_c - 1) \\ &\quad - \frac{A}{2\sqrt{2}B} \left(\frac{2\sum_j x_j a_{ij}}{a} - \frac{b_i}{b} \right) \ln \left[\frac{Z_c + (1+\sqrt{2})B}{Z_c + (1-\sqrt{2})B} \right] \end{aligned} \quad (5-21)$$

where, $B = bP/(RT)$, $A = aP/(RT)^2$, and $a_{ij} = \sqrt{a_i a_j} (1 - k_{ij})$.

$$\begin{aligned} \frac{\partial A_{Born}^r}{\partial n_i} &= \frac{\partial}{\partial n_i} \left(-\frac{e^2 N_{Av}}{4\pi D_0} \left(1 - \frac{1}{D_r} \right) \sum_j \frac{n_j Z_j^2}{\sigma_j^{Born}} \right)_T \\ &= -\frac{e^2 N_{Av}}{4\pi D_0} \cdot \left(\frac{1}{D_r^2} \cdot \frac{\partial D_r}{\partial x_i} \cdot \sum_j \frac{x_j Z_j^2}{\sigma_j^{Born}} + \left(1 - \frac{1}{D_r} \right) \cdot \frac{Z_i^2}{\sigma_i^{Born}} \right) \end{aligned} \quad (5-22)$$

where,

$$\frac{\partial D_r}{\partial x_i} = \frac{1}{1 + \sum_j^{ions} \zeta x_j} \cdot \frac{M_w}{\rho_0 V} \cdot (F_1(T) + F_2(T) + F_3(T) + F_4(T)), \text{ for water} \quad (5-23)$$

$$\frac{\partial D_r}{\partial x_i} = \frac{-D_s}{\left(1 + \sum_j^{\text{ions}} \zeta x_j\right)^2} \cdot \zeta, \text{ for ions} \quad (5-24)$$

$$\begin{aligned} \frac{\partial A_{MSA}^r}{\partial n_i} &= RT \cdot \frac{\partial}{\partial n_i} \left(-\frac{2\Gamma^3 V}{3\pi N_A} \left(1 + \frac{3}{2} \sigma^{MSA} \Gamma \right) \right)_T \\ &= -\frac{2RT\bar{V}}{\pi N_A} \cdot (1 + 2\sigma^{MSA} \Gamma) \cdot \frac{\partial \Gamma}{\partial n_i} \end{aligned} \quad (5-25)$$

where,

$$\frac{\partial \Gamma}{\partial n_i} = \frac{1}{2\sqrt{1 + 2\sigma^{MSA} \Gamma}} \frac{\partial \kappa}{\partial n_i} \quad (5-26)$$

and

$$\frac{\partial \kappa}{\partial n_i} = \frac{1}{2\kappa} \frac{e^2 N_A^2}{D_0 RT V D_r^2} \cdot \left(D_r Z_i^2 - \frac{\partial D_r}{\partial n_i} \cdot \sum n_j Z_j^2 \right) \quad (5-27)$$

The fugacity and water activity can be determined by using Eqs. 5-28 and 5-29, respectively.

$$f_i = x_i \phi_i P \quad (5-28)$$

$$a_w = x_w \frac{\phi_w}{\phi_w^\infty} \quad (5-29)$$

where ϕ_w^∞ denotes the fugacity coefficient of water in the infinite dilute solution at the same pressure and temperature conditions.

5.1.2 Model Parameters

Two categories of parameters are still unsettled in the proposed unified EoS at this point, i.e., the non-ion-associated parameters and the ion-associated parameters. The non-ion-associated

parameters are T_c , P_c and ω of CH₄, C₂H₆, CO₂, and H₂O in Eqs. 5-3 and 5-4. These parameters have been well tabulated in the literature (Sandler, 2017) and are summaries in Table 5-1.

Table 5-1 The parameters of CH₄, C₂H₆, CO₂ and H₂O

Molecules	T_c , K	P_c , MPa	ω
CH ₄	190.6	4.60	0.008
C ₂ H ₆	305.4	4.88	0.098
CO ₂	304.2	7.38	0.225
H ₂ O	647.3	22.05	0.344

The ion-associated parameters that are to be determined include σ_i^{Bom} in Eqs. 5-1 and 5-5, σ_i^{MSA} in Eq. 5-8, BIP of water-uncharged ion pairs, i.e., k_{H_2O-ion} in Eq. 5-5, D_r in Eqs. 5-5 and 5-9, and parameters of a_i and b_i of uncharged ions in Eqs. 4-23 and 4-24. In this work, σ_i^{Bom} proposed by Maribo-Mogensen (2014) is used, which were determined by calculating the ionization energy and electron affinity with the Born term, as listed in Table 5-2. σ_i^{MSA} equal to σ_i^{Bom} is applied. The BIP of k_{H_2O-ion} determined by Inchekel et al. (2008) are adopted, as demonstrated in Table 5-2.

Table 5-2 Solvated ion diameter and BIP of water-ion pairs

Ions	σ^{Bom} , Å ^a	K_{H_2O-ion} ^b
Na ⁺	2.8	-0.439
K ⁺	3.4	0.087
Mg ²⁺	2.54	0.114
Ca ²⁺	3.2	-0.287
Cl ⁻	3.98	-0.356

^a Maribo-Mogensen, 2014; ^b Inchekel et al., 2008

The Simonin model (Courtial et al., 2014) is used to calculate the relative dielectric constant:

$$D_r = \frac{D_s}{1 + \sum_i^{\text{ions}} \zeta x_i} \quad (5-30)$$

where ζ is a tunable parameter, set to 5.08 in this work; D_s is the relative permittivity of pure water, determined by employing the Schmidt correlation:

$$D_s = 1 + F_1(T)\rho^* + F_2(T)\rho^{*2} + F_3(T)\rho^{*3} + F_4(T)\rho^{*4} \quad (5-31)$$

$$F_1(T) = \frac{7.62571}{T^*} \quad (5-32)$$

$$F_2(T) = \frac{244.003}{T^*} - 140.569 + 27.7841T^* \quad (5-33)$$

$$F_3(T) = \frac{-96.2805}{T^*} + 41.7909T^* - 10.2099T^{*2} \quad (5-34)$$

$$F_4(T) = \frac{-45.2059}{T^{*2}} + \frac{84.6395}{T^*} - 35.8644 \quad (5-35)$$

$$\rho^* = \frac{n_w M_w}{\rho_0 V} \quad (5-36)$$

where ρ^* and T^* denote the reduced density and temperature, respectively, with $T^* = T/298.15$ and $\rho_0 = 1000 \text{ kg/m}^3$; n_w and M_w are the moles and molar weight of water.

As to the uncharged ions, parameter a^0 , b , and T_c have been found obeying the following correlations (Wu and Prausnitz, 1998):

$$a^0 = 0.2536 \cdot B \cdot 10^{73} / \bar{V}_c - 0.0074 \quad (5-37)$$

$$b = 0.2891 \cdot \bar{V}_c - 1.7073 \quad (5-38)$$

$$T_c = 25.819 \times 10^{47} \cdot B / (k_B \cdot \bar{V}_c^2) - 3.4127 \quad (5-39)$$

$$\bar{V}_c = \sqrt{(0.0756 \cdot B \cdot 10^{79} + 0.3108) / (\varepsilon^{ion} / k_B \cdot 6 \times 10^6)} \quad (5-40)$$

where \bar{V}_c denotes the critical molar volume; ε^{ion} is the Lennard-Jones energy parameter, determined by using Eq. 5-41; B represents the London coefficient, calculated with Eq. 5-42.

$$\varepsilon^{ion} / k_B = 356 \cdot (\alpha^P)^{1.5} \frac{n_e^{0.5}}{(\sigma^P / 2)^6} \quad (5-41)$$

$$B = 4 \cdot \varepsilon^{ion} \cdot (\sigma^P)^6 \quad (5-42)$$

where n_e denotes the number of electrons in the ions; α^P and σ^P are the polarizability and the Pauling diameter of ions, as shown in Table 5-3. It is noted that the unit of σ^P in Eq. 5-41 is Å and that in Eq. 5-42 is meter. The results of parameter a^0 , b , and T_c of ions are illustrated in Table 5-3. The parameter a of ions can be calculated using $a = a^0 \cdot \alpha(T)$, where $\alpha(T)$ is determined by employing Eq. 4-22 with ω being 0.

Table 5-3 Parameters of uncharged ions

Ions	$\sigma^P, \text{Å}^a$	$\alpha_p, \text{Å}^3^b$	n_e	$b, \text{cm}^3/\text{mol}$	$a^0, \text{J} \cdot \text{m}^3$	T_c, K
Na ⁺	1.92	0.21	10	5.824	0.0299	102.10
K ⁺	2.66	0.87	18	13.308	0.2040	296.89
Mg ²⁺	1.30	0.12	10	1.421	0.0316	260.84
Ca ²⁺	2.12	0.53	18	6.590	0.1119	303.18
Cl ⁻	3.62	3.02	18	34.726	0.5561	326.49

^a (Zuo and Guo, 1991); ^b (Jin and Donohue, 1988)

5.1.3 Calculation Algorithm

The calculation procedure of hydrate phase boundary pressure is demonstrated in Fig. 5-2. The first step is to specify gas, water, and electrolyte concentrations in the system, as well as other parameters and conditions, e.g., temperature. An initial guess of the hydrate phase boundary pressure is obtained by using the reference hydrate approach proposed by Parrish and Prausnitz (1972). The flash calculation is implemented by employing the newly proposed unified EoS to determine the fugacity and the water activity at the equilibrium conditions. The pressure is updated until the difference between the calculated $\Delta\mu_w^H$ and $\Delta\mu_w^A$ is within a certain error, e.g., 10^{-6} . This procedure is performed twice: one is for the phase boundary pressure of sI hydrates and the other one is for that of sII hydrates. The smaller pressure can be assigned as the phase boundary pressure (P) at the specified temperature.

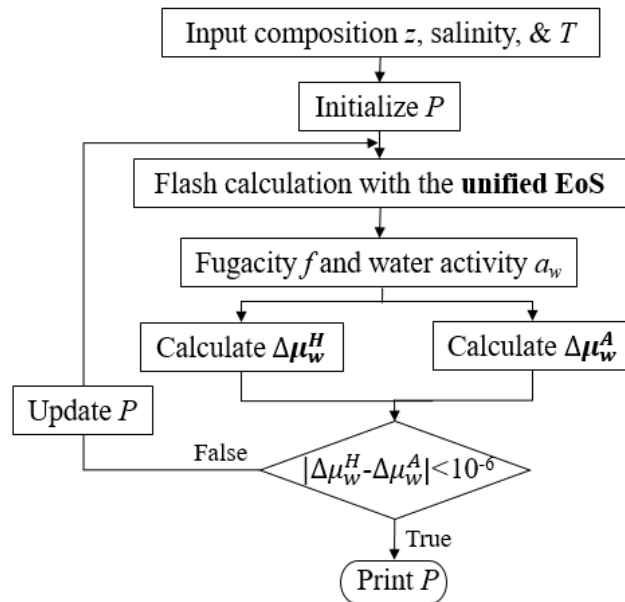


Fig. 5-2 Flowchart of the phase boundary calculation using the new model

As demonstrated in Fig. 5-2, the unified EoS will be applied to determine the thermodynamic quantities of fugacity and water activity at the equilibrium conditions. The flowchart of this algorithm is presented in Fig. 5-3. A successive implementation of stability tests and flash calculations is able to handle multiphase scenarios up to three non-hydrate phases. In a system containing gas, water, and electrolytes above the freezing point, the possible non-hydrate phases that may occur are aqueous phase, gas-rich vapor phase, and gas-rich liquid phase. It is assumed that ions only show up in the aqueous phase. The first step of this algorithm is to specify the parameters of the system, e.g., temperature T and overall composition z . Then a stability test is implemented. The trial phase of this step is the aqueous phase composed of 99.9 mol% H₂O and other non-ion components evenly share the rest 0.1 mol% (Mortezazadeh and Rasaei, 2017). Next, a 2-phase flash calculation is carried out using the K -value obtained from the stability test at the previous step. The compositions of the aqueous and the gas-rich phases, i.e., x and h can be determined by the 2-phase flash calculation algorithm. Then the stability test will be performed again to check whether the gas-rich phase is stable in a single phase. The K -value in this step is obtained by employing the Wilson equation (Whitson and Brulé, 2000). If the gas-rich phase is not stable in one single phase, a 3-phase flash calculation will be implemented. In this work, the stability test follows Michelsen's algorithm, which has been elucidated clearly elsewhere (Whitson and Brulé, 2000). The 2-phase and 3-phase flash calculations are based on Rachford-Rice equations (Haugen et al., 2011; Li and Firoozabadi; Moortgat et al., 2012; Nazari et al., 2019; Qiu et al., 2014).

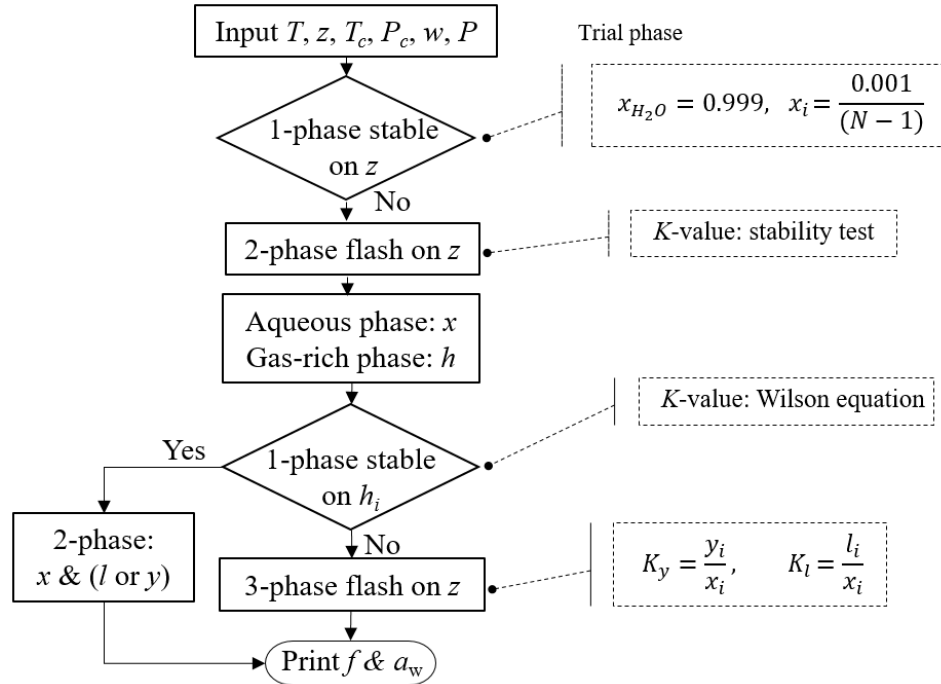


Fig. 5-3 Flowchart of determining the fugacity and water activity using the unified EoS

5.2 Simulation Results

5.2.1 Phase boundary of CH₄ hydrates in single-electrolyte solutions

The newly developed model is applied in calculating the phase boundary of pure CH₄ hydrates formed in single NaCl, KCl, MgCl₂, or CaCl₂ aqueous solution. A total of 276 measured data points have been collected in this section, as tabulated in Table 5-4. The temperature of the collected data extends from 261.8 to 296.0 K, with the concentration of electrolytes range of 3-24.12 wt% for NaCl, 5-15 wt% for KCl, 1-15 wt% for MgCl₂, and 5-19.8 wt% for CaCl₂. The phase boundary curves of these scenarios are illustrated in Fig. 5-4 through Fig. 5-7.

Table 5-4 Phase boundary of pure CH₄ hydrates formed in single-electrolyte solutions

Electrolytes	C _{ele} , wt%	No. of Data	T range, K	AARD, %	Data source
NaCl	3	19	277.7-291.1	3.0	Atik et al., 2009; Dholabhai et al., 1991; Maekawa, 2001
	3.5	18	275.0-290.1	5.4	Lafond et al., 2012; Maekawa et al., 1995
	5	5	274.2-283.6	1.6	Mohammadi et al., 2008
	5.44	5	275.1-283.7	2.6	Cha et al., 2016
	10	19	269.7-286.4	3.0	Maekawa et al., 1995
	10.83	5	274.7-282.0	2.6	Cha et al., 2016
	10.85	11	279.2-296.0	7.1	Jager and Sloan, 2001
	11.76	6	268.3-278.0	5.12	De Roo et al., 1983
	11.89	3	272.7-277.7	0.34	Kharrat and Dalmazzone, 2003
	12	2	288.0-296.0	2.5	Hu et al., 2017
	15	3	269.5-285.1	2.8	Haghighi et al, 2009
	17.13	8	263.4-275.1	2.4	De Roo et al., 1983; Kharrat and Dalmazzone, 2003
	17.17	10	274.4-291.0	3.06	Jager and Sloan, 2001
	20	17	268.5-278.7	4.9	Haghighi et al, 2009; Maekawa et al., 1995
	21.52	7	261.8-272.8	4.2	De Roo et al., 1983
22.07	10	270.7-285.8	4.0	Jager and Sloan, 2001	
24.12	5	263.0-268.6	4.9	De Roo et al., 1983	
KCl	5	6	271.6-283.2	0.9	Mohammadi et al., 2008
	6.83	7	275.5-284.2	3.4	Cha et al., 2016
	10	7	270.1-281.5	2.0	Mohammadi et al., 2008
	13.41	8	275.1-282.3	4.6	Cha et al., 2016
	15	3	276.5-285.0	5.9	Haghighi et al, 2009
MgCl ₂	1	5	280.8-292.2	0.6	Atik et al., 2006

	3	6	272.9-286.4	0.8	Kang et al., 1998
	5	11	273.3-290.0	1.4	Atik et al., 2006; Mohammadi et al., 2009
	6	5	271.3-284.1	1.0	Kang et al., 1998
	10	21	272.4-287.4	4.1	Atik et al., 2006; Haghghi et al, 2009; Kang et al., 1998; Mohammadi et al., 2009
	15	9	270.4-280.2	11.7	Atik et al., 2006; Kang et al., 1998
	5	11	272.0-284.4	1.7	Kharrat and Dalmazzone, 2003; Mohammadi et al., 2008
	10.2	4	278.4-282.3	1.3	Kharrat and Dalmazzone, 2003
CaCl ₂	14.5	4	273.5-278.8	2.4	Kharrat and Dalmazzone, 2003
	15	6	268.0-277.4	6.9	Mohammadi et al., 2008
	17.1	6	265.4-282.2	12.1	Atik et al., 2006
	19.8	4	270.1-273.5	6.8	Kharrat and Dalmazzone, 2003

Note: C_{ele} denotes the concentration of electrolytes.

The measured and calculated phase boundary of CH₄ hydrates formed in NaCl solutions are presented in Fig. 5-4. It can be seen that the phase boundary pressure increases with the concentration of NaCl and this trend has been well captured by the newly developed thermodynamic model. The AARD of most scenarios are below 5% even at the high NaCl concentration of 24.12 wt%. A total of 153 data points of CH₄ hydrates formed in NaCl solutions have been used for comparison in this work and the overall AARD of these data points is 2.8%, which suggests that the new model is accurate to predict the phase boundary of pure CH₄ hydrates formed in NaCl solutions with electrolyte concentration up to 24.12 wt%.

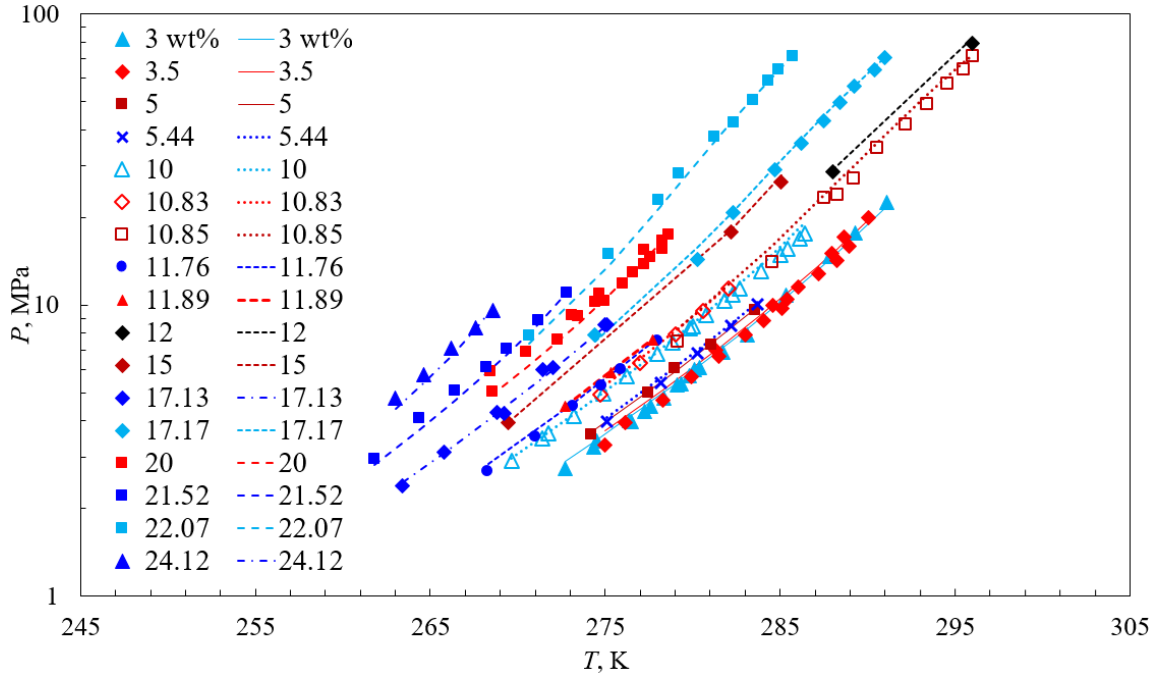


Fig. 5-4 Collected and calculated phase boundary of CH₄ hydrate formed in NaCl solutions (Symbols represent collected data points, curves denote calculated results, numbers are NaCl concentrations in wt%)

The calculated phase boundary of CH₄ hydrates formed in KCl solutions is compared with the measured ones in Fig. 5-5. The effect of KCl on the hydrate phase boundary is similar to that of NaCl, i.e., elevating the phase boundary pressure. The AARDs for KCl concentrations of 5, 6.83, 10, and 13.41 wt% are 0.9, 3.4, 2.0, and 4.6%, respectively. The AARDs are relatively high for the scenarios with the KCl concentration of 6.83 and 13.41 wt%. This might be because Cha et al. (2016) measured these data points with two methods, i.e., isochoric pressure-search method and differential scanning calorimetry. All the data points measured using these two approaches have been included in this work for comparison, which may induce error due to the different accuracy of various measuring approaches (Zheng et al., 2020a). The overall AARD of these 31 data points are 3.1% despite the possible inaccuracies in the collected data points, which proves that this new

model is reliable in predicting the phase boundary of CH₄ hydrates formed in KCl solutions with KCl concentration up to 15 wt%.

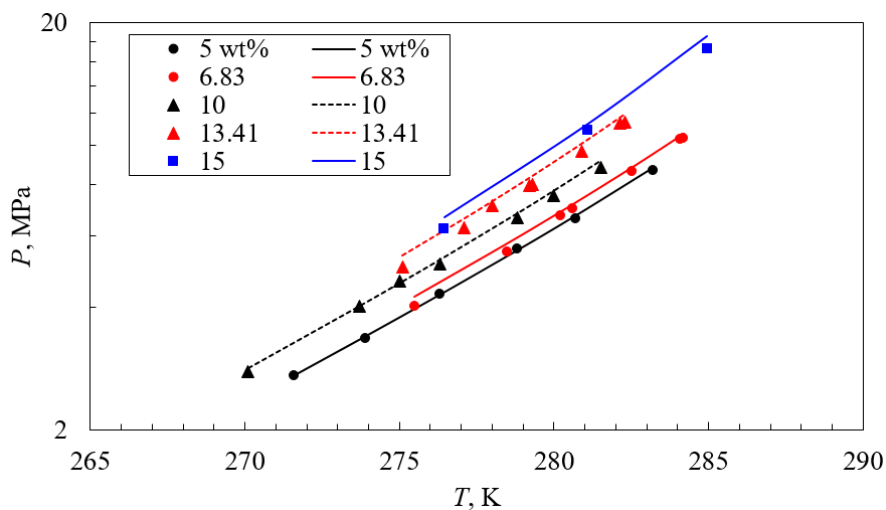


Fig. 5-5 Collected and calculated phase boundary of CH₄ hydrate formed in KCl solutions (Symbols represent collected data points, curves denote calculated results, numbers are KCl concentrations in wt%)

The phase boundary of CH₄ hydrates in MgCl₂ solution is demonstrated in Fig. 5-6. It can be seen that the phase boundary pressure also increases with the concentration of MgCl₂. The AARD is smaller for the scenarios with lower concentration of MgCl₂. For instance, the AARD is smaller than 2% when the concentration of MgCl₂ is lower than 6 wt% and jumps to 11.7% when the concentration increases to 15 wt%. The large deviation may result from two aspects. For one thing, the measured data points are scattered at high concentrations of MgCl₂ as shown in Fig. 5-6. For another thing, it is noted that all the ion-associated parameters applied in this work are selected from the literature without regression. Parameters from different sources, e.g., those in Table 5-2

and Table 5-3 may induce some inconsistency. In spite of this, the overall AARD of these 57 data points is 3.8%, which proves that the framework applied in this work is reliable. And the prediction results for hydrates formed in MgCl_2 solutions can be further improved by better selection or regression of the ion-associated parameters.

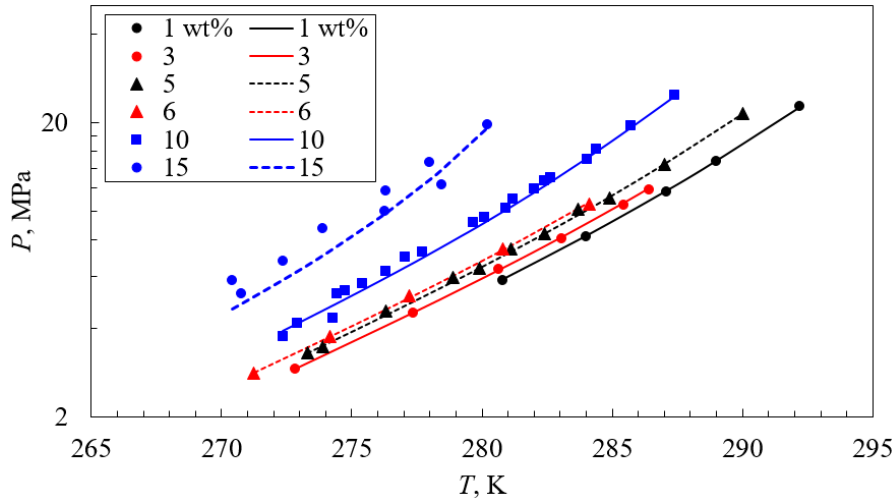


Fig. 5-6 Collected and calculated phase boundary of CH_4 hydrate formed in MgCl_2 solutions (Symbols represent collected data points, curves denote calculated results, numbers are MgCl_2 concentrations in wt%)

The measured and calculated phase boundary of CH_4 hydrates formed in CaCl_2 solutions are compared in Fig. 5-7, denoted with symbols and curves respectively. The hydrate phase boundary pressure also rises with CaCl_2 concentrations. Similar to those of MgCl_2 solutions, the AARD of hydrate phase boundary pressure is larger at higher CaCl_2 concentrations. For example, the AARD are smaller than 3% when the concentration of CaCl_2 is lower than 15 wt% and larger than 6% when the concentration is above 15 wt%. The overall AARD of these 35 data points is 5.0%.

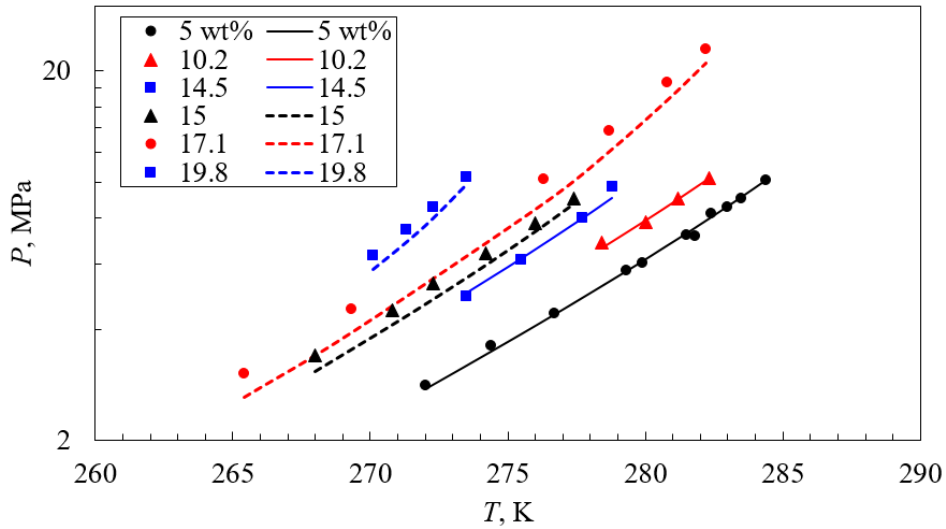


Fig. 5-7 Collected and calculated phase boundary of CH₄ hydrate formed in CaCl₂ solutions

(Symbols represent collected data points, curves denote calculated results, numbers are CaCl₂ concentrations in wt%)

5.2.2 Phase boundary of CH₄ hydrate in mixed-electrolyte solutions

The performance of the new model in predicting the phase boundary of pure CH₄ hydrates formed in mixed electrolyte solutions are investigated in this section. A total of 55 measured phase boundary data points have been used, i.e., 31 data points of hydrates formed in mixed NaCl-KCl solutions and the rest 24 points of hydrates formed in mixed NaCl-CaCl₂ solutions, as shown in Table 5-5. The temperature of these collected data ranges from 264.4 to 281.8 K, with the mass concentration range of 6-23 wt% and 6-16 wt% respectively for the mixed NaCl-KCl and NaCl-CaCl₂ solutions. The deviations of calculated phase boundary pressure from the measured one have been evaluated using Eq. 4-13, with the AARD listed in Table 5-5.

Table 5-5 Phase boundary of pure CH₄ hydrates formed in mixed electrolyte solutions

Electrolytes	C_{ele} , wt%	No. of Data	T range, K	AARD, %	Data source
NaCl-KCl	[3, 3]	7	271.4-279.2	4.8	Dholabhai et al., 1991
	[5, 5]	7	270.3-281.5	5.4	
	[5, 10]	4	267.5-279.0	6.5	
	[5, 15]	4	266.3-276.2	5.2	
	[10, 12]	5	264.6-274.2	1.8	
	[15, 8]	4	264.4-272.1	0.9	
NaCl-CaCl ₂	[3, 3]	4	270.4-281.8	1.3	Dholabhai et al., 1991
	[6, 3]	4	271.3-280.1	1.4	
	[10, 3]	4	269.4-277.3	0.9	
	[10, 6]	4	266.0-274.3	0.4	
	[3, 10]	4	268.8-277.7	0.8	
	[6, 10]	4	268.6-277.1	1.8	

Note: C_{ele} denotes the concentration of electrolytes.

The measured and calculated phase boundary of CH₄ hydrates formed in mixed NaCl-KCl solutions are demonstrated in Fig. 5-8. It is shown that the phase boundary pressure increases with an elevation in the concentration of both NaCl and KCl, which is consistent with the effect of single-electrolyte solutions. The overall AARD of these 31 data points is 4.2%, which means the performance of the new model in predicting the hydrate phase boundary formed in mixed NaCl-KCl solutions is satisfactory.

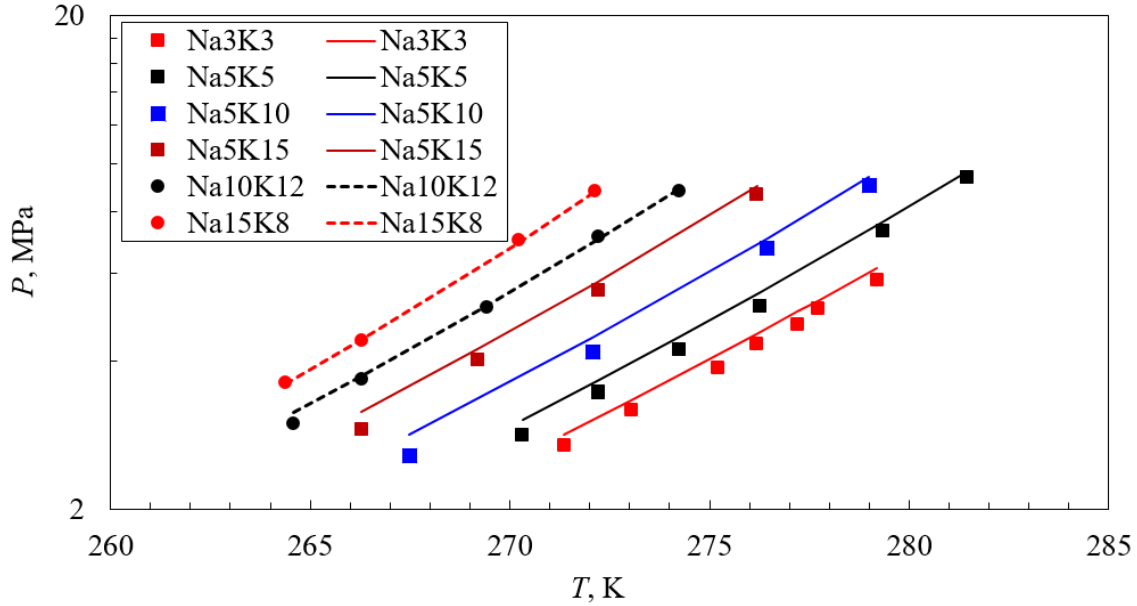


Fig. 5-8 Collected and calculated phase boundary of CH₄ hydrate formed in mixed NaCl-KCl solutions

(Symbols and curves represent the collected data points and the calculated results respectively; Na3K3 means the concentration of NaCl and KCl are both 3 wt%)

The phase boundary of CH₄ hydrates formed in NaCl-CaCl₂ solutions are presented in Fig. 5-9, where we can see the difference between the calculated results and the measured data points is quite narrow. The AARD of all these 6 scenarios are smaller than 2% and the overall AARD is 1.1%. It is demonstrated in Fig. 5-9 that the hydrate phase boundary curves are very close but not identical when the total mass concentration of NaCl plus CaCl₂ is the same, e.g., Na3Ca10 and Na10Ca3. This is because the molar mass and the ion charges are different for these two electrolytes.

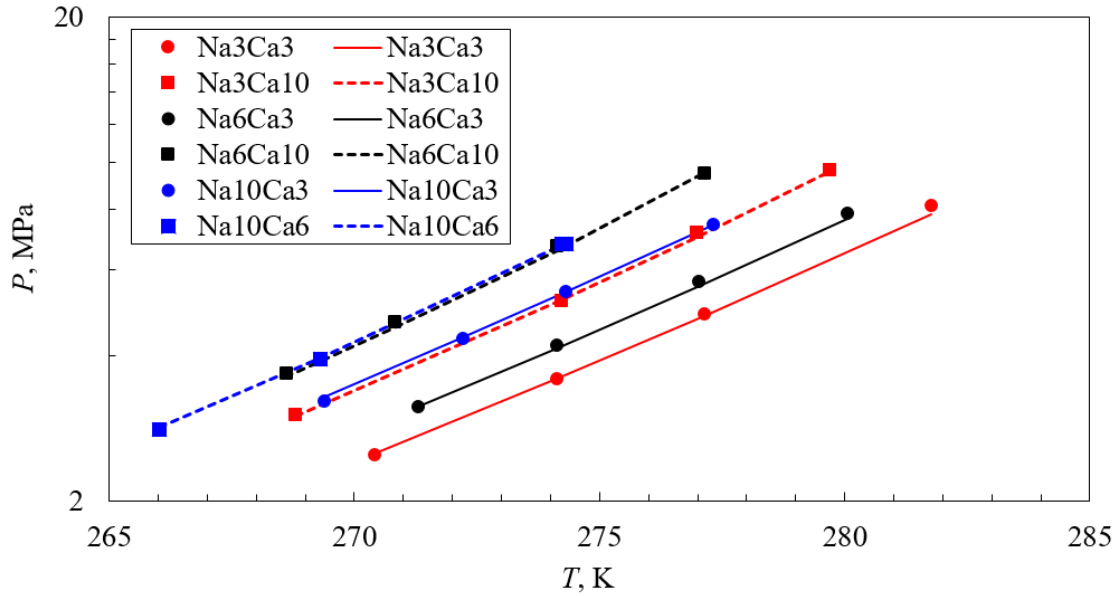


Fig. 5-9 Collected and calculated phase boundary of CH₄ hydrate formed in the mixed NaCl-CaCl₂ solutions

(Symbols and curves represent the collected data points and the calculated results respectively; Na3Ca3 means the concentration of NaCl and CaCl₂ are both 3 wt%)

5.2.3 Phase boundary of CH₄-CO₂ and CH₄-C₂H₆ hydrates in single-electrolyte solutions

The newly developed model is applied to calculate the phase boundary of binary CH₄-CO₂ hydrates and binary CH₄-C₂H₆ hydrates in this section. A total of 58 data points are collected, in which 47 data points are for the CH₄-CO₂ hydrates and the rest 11 points are for the CH₄-C₂H₆ hydrates. The electrolyte concentrations of these collected data range from 3.5 to 23 wt% and the temperature ranges from 261.9 to 295.1 K, as shown in Table 5-6.

Table 5-6 Phase boundary of binary hydrates formed in single-electrolyte solutions

Gas	Electrolytes	CH ₄ , mol%	C _{ele} , wt%	No. of Data	T range, K	AARD, %	Data source	
CH ₄ - CO ₂	NaCl	80	5	4	271.6-282.0	3.1	Dholabhai et al., 1994	
			10	4	268.5-279.0	3.2		
			15	5	264.8-277.2	2.5		
			20	4	261.9-274.3	4.4		
	21	3.5	5	286.1-292.4	4.8	Zheng et al., 2020b		
	29	5	5	287.0-295.1	6.0			
	KCl	80	80	5	4	271.4-282.0	0.9	Dholabhai et al., 1994
				10	4	269.2-279.0	2.6	
				15	4	267.0-277.1	0.3	
				10	4	268.6-279.1	3.4	
CaCl ₂			15	4	266.7-276.9	6.8		
CH ₄ - C ₂ H ₆	NaCl	74.7	12	6	292.4-307.4	2.4	Hu et al., 2018	
			23	5	282.3-296.7	4.4		

Note: C_{ele} denotes the concentration of electrolytes.

The phase boundary of the binary CH₄-CO₂ hydrates formed in NaCl solutions are presented in Fig. 5-10. The deviations of the calculated results from the collected data points are within 5% for most scenarios and the overall AARD of these 27 data points are 4.0%. It is suggested that the developed model is reliable not only at low pressure (below 10 MPa), but also at high-pressure conditions.

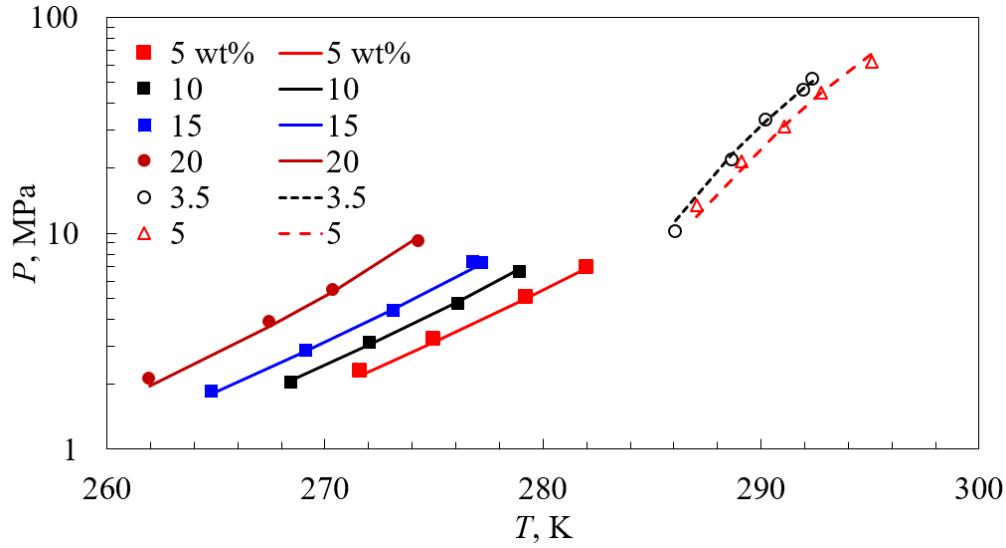


Fig. 5-10 Collected and calculated phase boundary of binary CH₄-CO₂ hydrate formed in NaCl solutions

(Symbols and curves represent the collected data points and the calculated results respectively; numbers are NaCl concentrations in wt%; data of filled symbols are measured by Dholabhai et al. (1994), those of empty symbols are by Zheng et al. (2020a))

The phase boundary of the binary CH₄-CO₂ hydrates formed in KCl and CaCl₂ solutions as well as the binary CH₄-C₂H₆ hydrates formed in NaCl solutions are illustrated in Fig. 5-11. The deviations of the calculated phase boundary of binary CH₄-CO₂ hydrates formed in KCl solutions from the measured ones are very small, with the overall AARD of 1.2%. The difference between the calculated and measure phase boundary of the binary CH₄-CO₂ hydrates formed in CaCl₂ solutions is relatively large, with the overall AARD of 5.1%, which is consistent with the conclusions in section 5.2.1.

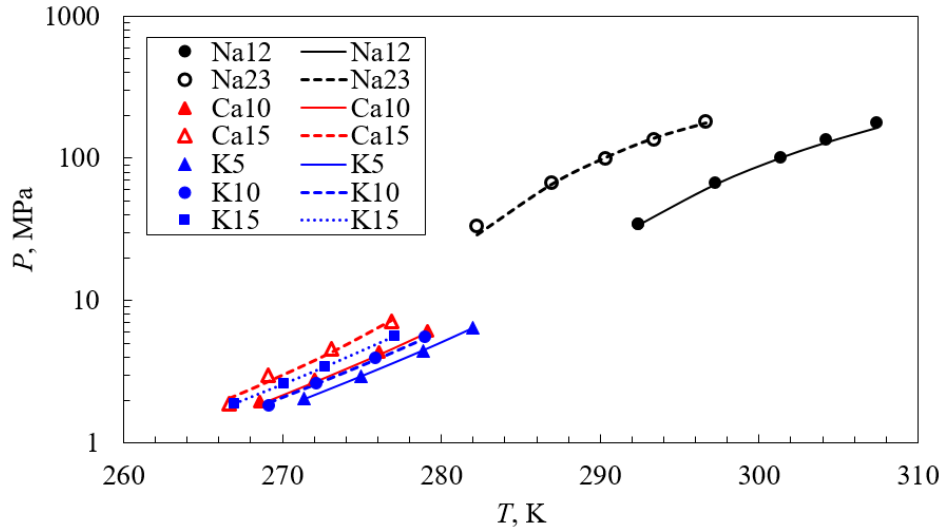


Fig. 5-11 Collected and calculated phase boundary of $\text{CH}_4\text{-C}_2\text{H}_6$ and $\text{CH}_4\text{-CO}_2$ hydrates formed in NaCl, KCl, and CaCl_2 solutions

(Symbols and curves represent the collected data points and the calculated results respectively; Na12 denotes the concentration of NaCl is 12 wt%; black symbols represent $\text{CH}_4\text{-C}_2\text{H}_6$ hydrates and others are for $\text{CH}_4\text{-CO}_2$ hydrates)

5.2.4 Phase boundary of $\text{CH}_4\text{-CO}_2$ and $\text{CH}_4\text{-C}_2\text{H}_6$ hydrates in mixed electrolyte solutions

The performance of the developed model is further evaluated by calculating the phase boundary of binary hydrates formed in mixed electrolyte solutions. A total of 31 measure hydrate phase boundary data points have been collected in this section, with 26 data points for the binary $\text{CH}_4\text{-CO}_2$ hydrates and the rest 5 for the binary $\text{CH}_4\text{-C}_2\text{H}_6$ hydrates. The temperature range of these collected data points are 265.1-286.0 K and the overall electrolyte concentration range of 11.09-15 wt%. The deviations of the calculated results from the collected data points are quantified using Eq. 4-13, as shown with AARD in Table 5-7.

Table 5-7 Phase boundary of binary hydrates formed in single-electrolyte solutions

Gas	Electrolytes	CH ₄ , mol%	C _{ele} , wt%	No. of Data	T range, K	AARD, %	Data source
	NaCl-KCl	80	[5, 10]	5	265.1-281.3	2.5	
		50	[10, 5]	5	265.8-275.5	2.2	
CH ₄ - CO ₂	NaCl-CaCl ₂		[5, 10]	4	265.5-276.7	6.6	Dholabhai et al., 1994
		80	[10, 5]	4	265.5-278.7	7.2	
	NaCl-KCl- CaCl ₂	80	[6, 5, 4]	4	265.5-278.3	2.0	
		50		4	266.0-275.5	0.7	
CH ₄ - C ₂ H ₆	NaCl-MgCl ₂	96	[5, 6.09]	5	278.8-286.0	4.0	Atik et al., 2006

Note: C_{ele} denotes the concentration of electrolytes.

The phase boundary of the binary CH₄-CO₂ hydrates and the binary CH₄-C₂H₆ hydrates formed in mixed electrolytes are presented in Fig. 5-12. The AARD of the binary CH₄-CO₂ hydrates formed in mixed NaCl-KCl, NaCl-CaCl₂, and NaCl-KCl-CaCl₂ solutions are 2.3, 6.9, and 1.3%, respectively. The AARD of the binary CH₄-C₂H₆ hydrates formed in mixed NaCl-MgCl₂ solutions is 4%. These deviations are acceptable given the fact that no cross-verification of the collected data points are available. It is suggested that the developed model is reliable in predicting the phase boundary of binary hydrates formed in mixed electrolyte solutions.

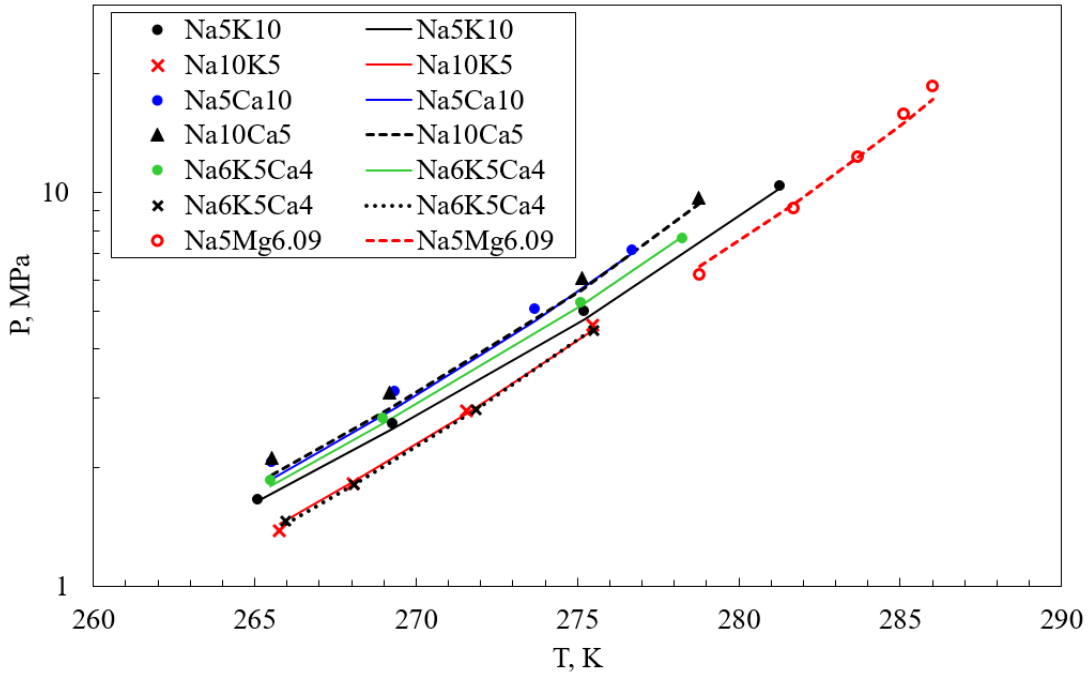


Fig. 5-12 Collected and calculated phase boundary of $\text{CH}_4\text{-C}_2\text{H}_6$ and $\text{CH}_4\text{-CO}_2$ hydrates formed in mixed-electrolyte solutions

(Symbols and curves represent the collected data points and the calculated results respectively; Na5K10 denotes that the electrolyte concentration of this scenario is 5 wt% NaCl and 10 wt% KCl; Empty circle denotes binary $\text{CH}_4\text{-C}_2\text{H}_6$ hydrates and others are for $\text{CH}_4\text{-CO}_2$ hydrates)

5.2.5 Phase boundary of hydrates in pure water

The developed model is able to predict hydrate formation in pure water when the concentrations of electrolytes are set as 0. In this section, the calculated and collected phase boundary of single CH_4 (i.e., 100 mol%) and the binary $\text{CH}_4\text{-CO}_2$ hydrates formed in pure water are compared with the database established in Chapter 3. A total of 314 data points have been compared in Fig. 5-13, with 213 data points for pure CH_4 hydrates and the rest 101 points for the binary $\text{CH}_4\text{-CO}_2$ hydrates. The deviations of the calculated results from the collected data points are evaluated using Eq. 4-13. The deviations for most scenarios are below 5%. For example, the AARD of 2.0, 3.8,

3.5, and 1.6% are obtained respectively for the binary CH₄-CO₂ hydrates with CH₄ composition of 90, 80, 70, and 60 mol%. The overall AARD of pure CH₄ hydrates is 2.7% and that of the binary CH₄-CO₂ hydrates is 3.8%. This indicates that the developed model is also capable of predicting the phase boundary of hydrates formed in pure water.

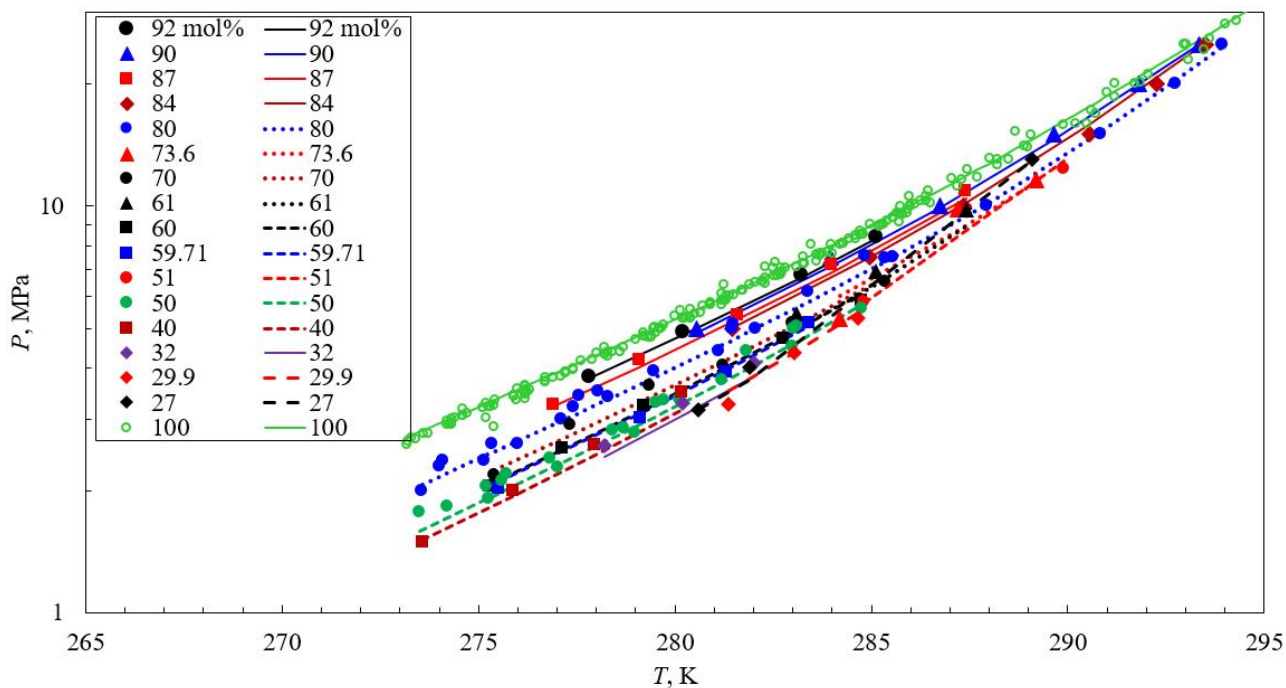


Fig. 5-13 Collected and calculated phase boundary of CH₄-CO₂ hydrates formed in pure water (Symbols represent collected data points, curves denote calculated results, numbers are the composition of CH₄ in mol%)

Overall, a total of 734 data points have been used in this work to evaluate the performance of the newly developed model in predicting the phase boundary of pure and binary hydrates formed in single and mixed electrolyte solutions as well as in pure water, among which 276 data points are for pure CH₄ hydrates formed in single NaCl, KCl, MgCl₂, and CaCl₂ solutions, 55 data points

for CH₄ hydrates formed in mixed electrolyte solutions, 58 data points for the binary CH₄-CO₂ and binary CH₄-C₂H₆ hydrates formed in single electrolyte solutions, 31 data points for the binary hydrates formed in mixed electrolyte solutions, and 314 data points for hydrate formed in pure water. The overall AARD of all these 734 data points is 3.4%, which proves that the new model developed in this work is reliable to predict the phase boundary of hydrates formed in pure water and electrolyte solutions.

5.3 Summary

In this chapter, a new thermodynamic model has been proposed to determine the phase boundary of gas hydrates by using the vdW-P model for the hydrate phase and a unified EoS for the non-hydrate phases. In the vdW-P model, the Kihara parameters of C₂H₆ are optimized by fitting against the phase boundary of pure C₂H₆ hydrates formed in pure water using particle swarm optimization method. In the unified EoS model, a mPR EoS is applied to describe the interactions between water, gas, and uncharged ions, a simplified explicit MSA term for the long-range Coulombic forces, and Born terms for the discharging-charging processes. The values of all the ion-associated parameters are selected from literature without regression. The reliability of the newly developed model has been evaluated by comparing with 734 measured phase boundary data points of pure and binary CH₄, C₂H₆, and CO₂ hydrates formed in single- and mixed-NaCl, KCl, MgCl₂, and CaCl₂ solutions as well as in the pure water.

It has been found that the phase boundary pressure of both pure and binary hydrates increases with the concentration of electrolytes for both single- and mixed-electrolyte solutions. The deviations between the calculated and measured phase boundary data points of CH₄ hydrates are 3.9, 3.1, 3.8, and 5.0% respectively for those formed in NaCl, KCl, MgCl₂, and CaCl₂ solutions.

It is noted that the deviations of predictions for 2-1 electrolyte (i.e., MgCl_2 and CaCl_2) solutions are relatively large than that for the 1-1 electrolyte (NaCl and KCl) solutions. This trend is also observed in the binary $\text{CH}_4\text{-CO}_2$ hydrates formed in KCl and CaCl_2 solutions, which lead to an AARD of 1.2 and 3.3%, respectively. Despite the relatively large deviations for the 2-1 electrolyte solutions, the framework applied in this modeling work is still believed reliable since all the ion-associated parameters used in this work are from literature instead of regression.

The reliability of the newly developed model is also proved by comparing with the collected phase boundary data of hydrates formed in mixed electrolyte solutions and in pure water. For example, the AARD of CH_4 hydrates formed in mixed NaCl-KCl and NaCl-CaCl_2 solutions are 4.2 and 1.1%, respectively. The overall AARD of the binary $\text{CH}_4\text{-C}_2\text{H}_6$ and $\text{CH}_4\text{-CO}_2$ hydrates in the mixed electrolytes solutions is 3.4% and that of hydrates formed in pure water is 3.0%.

CHAPTER 6 INSIGHTS INTO THE STABILITY OF CH₄-C₂H₆/CO₂ HYDRATES USING MOLECULAR DYNAMIC SIMULATION

In this section, the classical MD simulator LAMMPS (Large-Scale Atomic/Molecular Massively Parallel Simulator) is employed, which is open-source software distributed by the Sandia National Laboratories, a U.S. national lab of the Department of Energy (Plimpton, 1995). As aforementioned, the MD simulation enables us to describe the position evolution of each atom in the simulation box at each time step regulated by the pre-determined intermolecular potential function. The open-source visualization software of VMD (i.e., Visual Molecular Dynamics) is used for visualization (William et al., 1996).

Numerous intermolecular potential models have been proposed for water molecules, e.g., SPC, TIP3P, and TIP4P (Jorgensen et al., 1983; Yonezawa, 2013). SPC and TIP3P potential functions are three-site models. TIP4P model inserts a fictitious massless and negatively charged site (i.e., M site). More advanced water potential functions have been developed, e.g., TIP4P/Ice and TIP4P-Ew to improve the model performance in various fields. In addition, various coarse-grained models, e.g., mW and mTIP4P/2005 are being investigated to reduce the computational cost (Liu et al., 2014). Even though the coarse-grained models are advantageous in computational efficiency, they may lead to a compromise in structural properties (Lu et al., 2014). The reliability of the simulation results depends on the pre-defined potential functions exerted on each molecule. Ding et al. (2007) compared the radial distribution function (RDF) of water cage and guest molecules using SPC, SPC/E, and TIP4P water potential functions and found that these three potential models yielded similar results. Similar hydrate structural features resulted from SPC and SPC/E models were also observed by Chialvo et al. (2002). However, an increase in the system's

density was noticed when the SPC/E model is used due to the larger dipole moment of this model. Also, the TIP5P model led to an increase in the configurational energy compared to the SPC model, which was attributed to the fact that the TIP5P model was more favorable to the formation of hydrogen bonds. The TIP4P/2005 water model generates phase boundary of hydrate with higher deviation than TIP4P/ICE (Jin and Coasne, 2017). The TIP4P/Ice model results in a reasonable phase boundary value while the TIP4P/2005 and TIP4P water models underestimate the phase boundary condition (Conda and Vega, 2010). Duan and Zhang (2006) suggested that the SPC/E potential function of water molecules could predict the PVT properties accurately at high-pressure conditions, e.g., 5 GPa.

The influence of potential function adopted for the guest molecules has also been explored (English and MacElroy, 2003; Waldron et al., 2016). It was revealed that the size parameters had a great impact on the resulted energy parameters when the atomic Lennard-Jones (i.e., LJ) potential function was employed for CH₄ and CO₂. When the multi-site molecular potential functions, e.g., five-site and three-site were applied for these two guest molecules, the effect of the size parameters was much less significant. Also, the guest asymmetry has been found to greatly affect the configuration of hydrate cages (Chialvo et al., 2002). Zhang and Duan (2005) compared various force field models of CO₂, e.g., MSM, EPM2 and proposed an optimized CO₂ potential function which can reproduce the experimental observations such as the saturated liquid density and vapor pressure.

6.1 Structure of Hydrate Cages

6.1.1 sI hydrate structure

As aforementioned, a unit sI hydrate cell is made of two 5¹² cages and six 5¹²6² cages. In sI structure, the 5¹² cages are connected through their vertices instead of face sharing. The unit cell

of sI hydrates consists of 46 water molecules and $Pm3n$ space group symmetry, which can be regarded as a cubic lattice with an average lattice parameter around 12.03 Å. The Cartesian coordinates of the atoms in water cages of the unit sI and sII hydrate cells reported by Takeuchi et al. (2013) are employed as the initial configurations of the hydrate cages, where the positions of oxygen atoms in water cages were determined using X-ray diffraction experiments and those of hydrogen atoms were decided by following three criteria, i.e., the ice rule, the lowest potential energy, and the net-zero dipole moment. These configurations have been adopted in MD simulation of gas hydrates in the literature (Cladek et al., 2018; 2019). In this work, $3\times 3\times 3$ unit cells of both sI and sII structures are adopted. We can use unit cells for MD simulation because it was found that there was no dissociation preference of small or large cages in a unit cell, i.e., the small and large cages dissociate simultaneously and the gas composition in the small and large hydrate cages remains constant (Gupta et al., 2007; Rovetto, 2007). Also, using unit cells of gas hydrates can eliminate the boundary edge effect (Martos-Villa et al., 2013).

The normal view of a $3\times 3\times 3$ unit cell of sI $\text{CH}_4\text{-C}_2\text{H}_6$ hydrates is demonstrated in Fig. 6-1, where the gas molecules are inserted randomly into the cage center (Zheng et al., 2021).

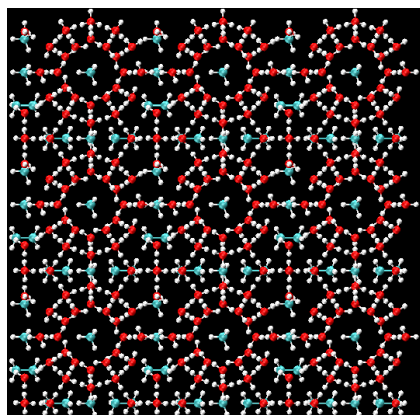


Fig. 6-1 Configuration of the $3\times 3\times 3$ sI hydrate cages of $\text{CH}_4\text{-C}_2\text{H}_6$ hydrates in this work
(The red, white, and green balls represent oxygen, hydrogen, and carbon atoms, respectively)

6.1.2 sII hydrate structure

The cubic sII hydrate unit cell consists of 136 water molecules and $Fd3m$ space group symmetry. The lattice parameter of the unit cell of sII hydrates is 17.31 Å. The normal view of a $3\times 3\times 3$ unit cell of sII CH₄-C₂H₆ hydrates from different perspectives are demonstrated in Fig. 6-2, where the gas molecules are inserted randomly into the center of hydrate cages.

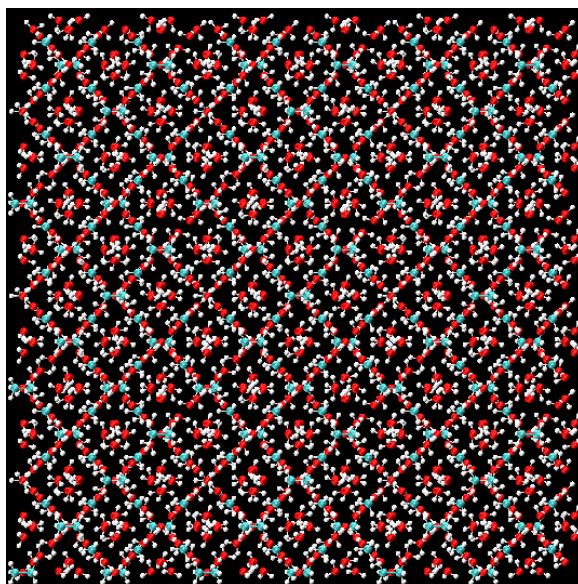


Fig. 6-2 Configuration of the $3\times 3\times 3$ sII hydrate cages of CH₄-C₂H₆ hydrates in this work
(The red, white, and green balls represent oxygen, hydrogen, and carbon atoms, respectively)

6.2 MD Simulation

6.2.1 Potential models

The potential functions are used in the Lammmps package to calculate the interactions between various molecules. The potential models are essential in MD simulation because they not only impact the reliability of the simulation results but also affect the computational costs due to the fact that they are supposed to capture the interaction forces of each molecule and will be

implemented at each iteration. Numerous potential models have been proposed for water molecules, e.g., SPC, TIP2, TIP4P, and TIP5P (Jorgensen et al., 1983). Coarse-grained models, e.g., mW and mTIP4P/2005 are being investigated to reduce the computational cost. The simulation results may be greatly impacted by the potential models selected for water molecules. For instance, it was found that SPC and SPC/E models of water molecules generated similar radial distribution function results for CH₄ and CO₂ hydrates but SPC/E model led to higher system density due to the larger dipole moment in this model (Chialvo et al., 2002).

In this work, the TIP4P-Ew model is applied for the H₂O molecules (Horn et al., 2004), which combines the TIP4P model and the Ewald techniques for the long-range interaction and can generate structure properties in agreement with experimental data. For CH₄ and C₂H₆ molecules, the Optimized Potentials for Liquid Simulations All-Atom (i.e., OPLS-aa) force field is used (Kaminski et al., 1994). An optimized potential function proposed by Zhang and Duan (2005) is employed for the CO₂ molecules. The associated parameters of these potential functions are summarized in Table 6-1.

Table 6-1 Parameters and potential function in the MD simulation

Molecules	Atom	Mass, g/mol	Charges, eV	E , kcal/mol	σ , Å	l , Å ^a
H ₂ O	H	1.008	0.5242	0	0	O-H: 0.9572
	O	15.9994	-	0.16275	3.16435	O-M: 0.1250
	M	-	-1.0484	-	-	
CH ₄	C	12.011	-0.24	0.066	3.500	C-H: 1.090
	H	1.008	+0.06	0	0	
C ₂ H ₆	C	12.011	-0.18	0.066	3.500	C-H: 1.090
	H	1.008	+0.06	0	0	C-C: 1.529
CO ₂	C	12.011	+0.5888	0.05728	2.7918	C-O: 1.163
	O	15.9994	-0.2944	0.16414	3.0	

^a bond length

The formulas of the abovementioned intermolecular potential can be summarized in Eq. 6-1 (Zhang and Duan, 2005).

$$U(1,2) = \sum_{i \in \{1\}} \sum_{j \in \{1\}} 4E_{ij} \left[\left(\frac{\sigma_{ij}}{r_{ij}} \right)^{12} - \left(\frac{\sigma_{ij}}{r_{ij}} \right)^6 \right] + \sum_{i \in \{1\}} \sum_{j \in \{1\}} \frac{q_i q_j}{r_{ij}} \quad (6-1)$$

where the first term represents the short-range interaction and the second term denotes the Coulombic interaction. E_{ij} is the well depth in the LJ potential curve, i.e., the maximum attractive energy; σ_{ij} denotes the distance of two atoms where the potential energy equals zero; r_{ij} is the separation distance between the two atoms; q_i represents the partial charge designated on the center of atom i . The Lorentz-Berthelot combination rules are used for cross interactions, as shown in Eqs. 6-2 and 6-3.

$$E_{ij} = \sqrt{E_i E_j} \quad (6-2)$$

$$\sigma_{ij} = \frac{\sigma_i + \sigma_j}{2} \quad (6-3)$$

6.2.2 Simulation procedures

The simulation procedure in this work is similar to that applied by Cladek et al. (2018; 2019) who utilized LAMMPS to investigate the interaction between guests and hosts of CH₄-CO₂ hydrates at low temperatures. The flowchart of the simulation procedure is illustrated in Fig. 6-3. The first step is to initialize the position of water molecules forming the hydrate cages. The initial position and orientation of the water molecules of both sI and sII hydrates are those demonstrated in Fig. 6-1 and Fig. 6-2, respectively. The periodic boundary condition is applied in all the simulation

models. The second step is to fill the hydrate cage with guest molecules, according to the pre-defined cage occupancy ratio. It is noted that the gas molecules are inserted into the center of the specified hydrate cages randomly. The third step is to specify the potential models for water and gas molecules, as demonstrated in Table 6-1. The next step, i.e., the fourth one is to use the NPT ensemble to obtain the equilibrium lattice parameter in the defined simulation box and the equilibrium state is reached when the volume of the ensemble reaches constant. It is found that 6000 fs is long enough to reach a satisfactory equilibrium state in the NPT ensemble in this work with a time step of 0.5 fs. In the fifth step, an NVT ensemble will be applied to observe the evolution of the system in terms of the interaction energy and the structure. The time step of the simulation is 0.5 fs and the total simulation time of NVT ensemble simulation is 5×10^4 fs. When the simulation is terminated, the following parameters are used to analyze the stability of hydrates and the influencing factors: *i*) Radial distribution function (i.e., RDF), which is a measure of the probability of finding a pair of molecules at a specific distance. *ii*) Mean square displacement (i.e., MSD), a measure of average distance that molecules travel during simulation, which has been widely used to demonstrate the relative stability of hydrate structure (Martos-Villa et al., 2013). *iii*) Rotation angle, to trace the rotational motion of the gas and water molecules; *iv*) potential energy between water and gas molecules, to quantify the interaction of various gas species with the water cages.

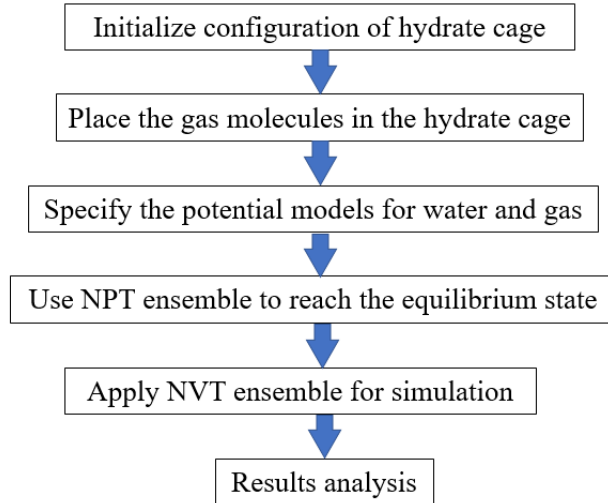


Fig. 6-3 Flowchart of the MD simulation in this work

6.2.3 Simulation scenarios

In this section, 12 scenarios are designed to investigate the stability of $\text{CH}_4\text{-C}_2\text{H}_6$ hydrates and the influence of pressure, gas composition, and CO_2 , as listed in Table 6-2. The temperature in all these scenarios is 274.2 K. In Scenarios #1 and #2, the composition of CH_4 and C_2H_6 is 90 and 10 mol%, which represents a stable sII structure according to the theoretical models developed in Chapter 4 and 5. The gas composition (20 mol% CH_4 and 80 mol% C_2H_6 in Scenarios #3 and #4) corresponds to the stable sI structure hydrates based on the thermodynamic calculation. In the Scenarios #5 through #8, 20 mol% CO_2 is added into the Scenarios #1 and #2, respectively. More CO_2 of 50 mol% is mixed with the $\text{CH}_4\text{-C}_2\text{H}_6$ mixtures in Scenarios #9 through #12. Two different pressures are applied in each gas composition scenario, both of which are above the phase boundary pressure. For instance, 2.0 MPa is employed in Scenario #1 and 5.0 MPa in Scenario #2, with the former one close to the phase boundary and the latter one far above the phase boundary pressure.

Table 6-2 Designed scenarios with various gas composition and pressure conditions

Scenarios No.	CH ₄ , mol%	C ₂ H ₆ , mol%	CO ₂ , mol%	<i>P</i> , MPa
#1	90	10	-	2.0
#2				5.0
#3	20	80	-	1.0
#4				5.0
#5	90×0.8	10×0.8	20	2.0
#6				5.0
#7	90×0.5	10×0.5	50	2.0
#8				5.0
#9	20×0.8	80×0.8	20	1.0
#10				5.0
#11	20×0.5	80×0.5	50	1.0
#12				5.0

The cage occupancy changes with pressure and gas composition conditions. In this work, the cage occupancy ratio of gas molecules in the small and large cages of sI and sII hydrates are determined using the developed theoretical models in Chapter 4, which represents a more realistic cage occupancy mode. It is noted that both sI and sII are simulated for Scenarios #1 through #4 to explore the structure change mechanisms of the CH₄-C₂H₆ hydrates with gas composition. For the hydrates in Scenarios #5 through #12, the sI structure is more stable according to the theoretical calculation. This is in consistent with the schematic diagram in Fig. 2-8 where the hydrate structure change point corresponds to a gas mixture containing around 73 mol% CH₄ and 27 mol% C₂H₆. As aforementioned, the stable structure of CH₄-C₂H₆ hydrates mainly depends on two factors. The first one is the occupancy preference of gas molecules in the small and large hydrate cages. The second one is the ratio of small and large cages in various hydrate structures. According to previous

research, CO₂ molecules prefer large cages to small cages. For the CH₄-C₂H₆-CO₂ mixture, CO₂ would compete with the C₂H₆ molecules for the large hydrate cages. Therefore, the sI structure, which can provide a higher ratio of large cages is more favorable for the CH₄-C₂H₆-CO₂ hydrates designed in Table 6-2. The cage occupancy ratio of each gas species in the 12 designed scenarios in Table 6-2 is presented in Table 6-3.

Table 6-3 The occupancy ratio of various gas components in the small and large cages of sI and sII hydrates

Scenarios	sI						sII					
	5 ¹² (2)			5 ¹² 6 ² (6)			5 ¹² (16)			5 ¹² 6 ⁴ (8)		
	C1	C2	CO ₂	C1	C2	CO ₂	C1	C2	CO ₂	C1	C2	CO ₂
#1	0.88	0	-	0.43	0.54	-	0.87	0	-	0.08	0.91	-
#2	0.94	0	-	0.49	0.50	-	0.94	0	-	0.09	0.90	-
#3	0.46	0	-	0.02	0.97	-	0.44	0	-	0	0.99	-
#4	0.89	0	-	0.08	0.92	-	0.88	0	-	0.01	0.99	-
#5	0.79	0	0.08	0.31	0.38	0.29						
#6	0.86	0	0.07	0.35	0.35	0.29						
#7	0.60	0	0.24	0.16	0.20	0.62						
#8	0.69	0	0.22	0.19	0.18	0.62						
#9	0.34	0	0.16	0.02	0.88	0.08						
#10	0.77	0	0.11	0.07	0.81	0.11						
#11	0.19	0	0.35	0.02	0.70	0.27						
#12	0.58	0	0.30	0.06	0.61	0.32						

Note: C1 and C2 represents CH₄ and C₂H₆, respectively.

The cage occupancy of different scenarios is plotted to clearly demonstrate the impact of pressure and gas composition. The impact of pressure on the cage occupancy of CH₄ molecules in the large and small cages in the sI and sII structures are illustrated in Fig. 6-4, where the gas composition and pressure conditions correspond to the scenarios listed in Table 6-2. It can be seen that CH₄ molecules prefer occupying the small cages in both sI and sII structure hydrates at the designed pressure and gas composition conditions. Also, the cage occupancy of the CH₄ molecules in all the cages increases with pressure, and the increasing trend is more obvious when the composition of CH₄ is lower. For the binary CH₄-C₂H₆ hydrates, the occupancy of CH₄ in the large cages of the sI hydrates increases significantly with the composition of CH₄, as demonstrated in Fig. 6-4 (a) and Fig. 6-4 (b). When CO₂ is added in Fig. 6-4 (a) through (f), the occupancy of CH₄ in the sI hydrates declines, due to the decrease in the partial pressure of CH₄ components.

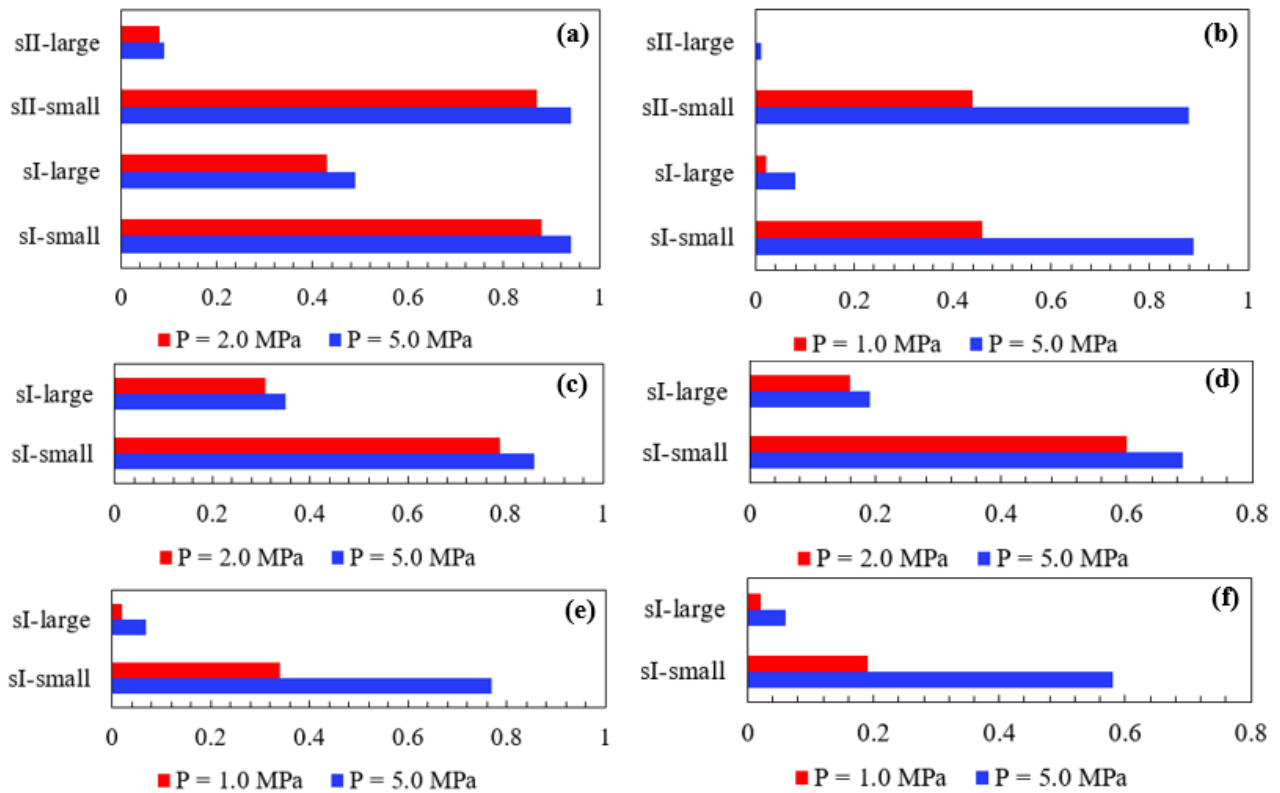


Fig. 6-4 Cage occupancy of CH₄ molecules in the small and large cages

Note: the gas composition in the above scenarios: (a) 90 mol% CH₄-10 mol% C₂H₆; (b) 20 mol% CH₄-80 mol% C₂H₆; (c) 72 mol% CH₄-8 mol% C₂H₆-20 mol% CO₂; (d) 45 mol% CH₄-5 mol% C₂H₆-50 mol% CO₂; (e) 16 mol% CH₄-64 mol% C₂H₆-20 mol% CO₂; (f) 10 mol% CH₄-40 mol% C₂H₆-50 mol% CO₂.

The occupancy ratio of C₂H₆ molecules in hydrate cages are presented in Fig. 6-5, where we can see the C₂H₆ molecules only enter the large cages of sI and sII hydrates. Contrary to the CH₄ molecules, the occupancy ratio of the C₂H₆ molecules declines with the increase in pressure. This is because the large cages will be partially occupied by the CH₄ molecules at high-pressure conditions. For the binary CH₄-C₂H₆ hydrates, the cage occupancy of C₂H₆ molecules in sII hydrates is larger than that in the sI hydrates, due to the higher ratio of small cages in sII hydrates so that the competition between CH₄ and C₂H₆ molecules for the large cages in sII is less strong. Overall, the cage occupancy of C₂H₆ molecules increases with its concentration in the gas mixture.

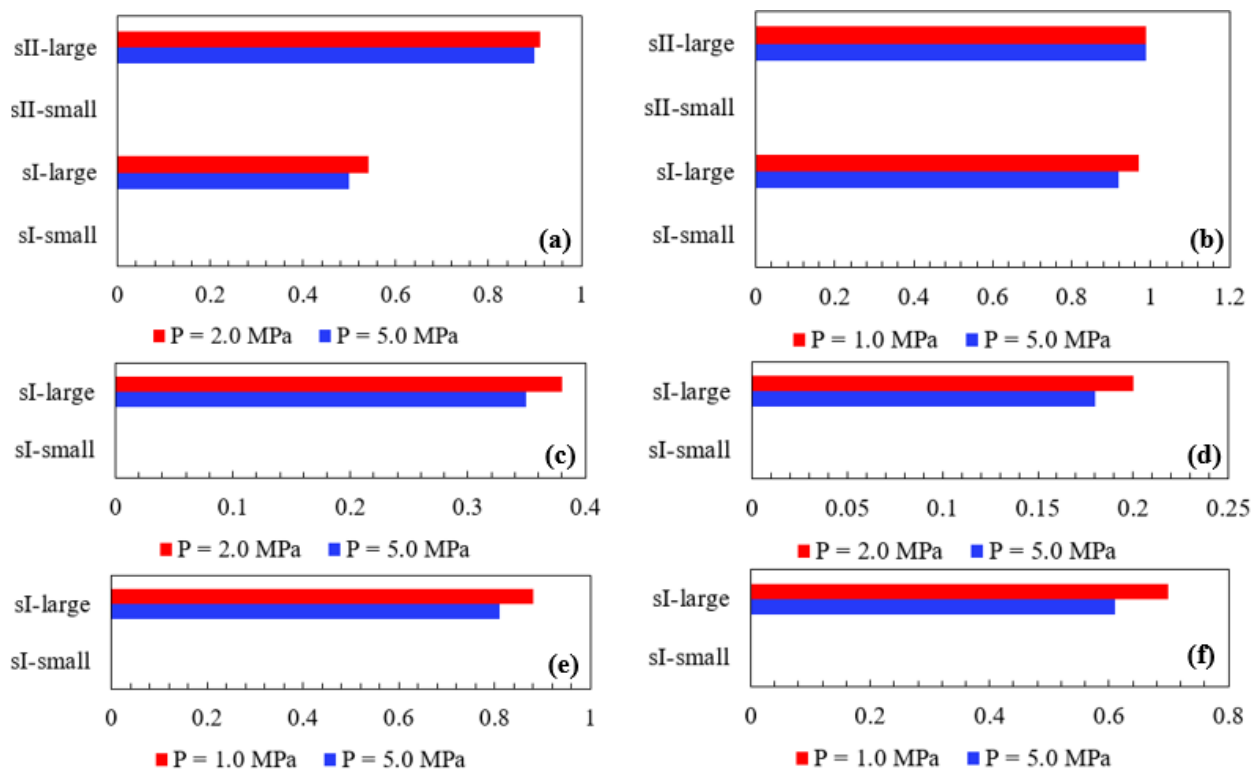


Fig. 6-5 Cage occupancy of C₂H₆ molecules in the small and large cages

Note: the gas composition in the above scenarios: (a) 90 mol% CH₄-10 mol% C₂H₆; (b) 20 mol% CH₄-80 mol% C₂H₆; (c) 72 mol% CH₄-8 mol% C₂H₆-20 mol% CO₂; (d) 45 mol% CH₄-5 mol% C₂H₆-50 mol% CO₂; (e) 16 mol% CH₄-64 mol% C₂H₆-20 mol% CO₂; (f) 10 mol% CH₄-40 mol% C₂H₆-50 mol% CO₂.

The cage occupancy of CO₂ molecules in the sI hydrates at various pressure and gas composition conditions are demonstrated in Fig. 6-6. It is seen that in the scenarios with higher CH₄ concentration, the occupancy of CO₂ molecules in the large cages is higher than that in the small cages, due to the higher stability of CH₄ molecules in the small cages than CO₂, and the cage occupancy ratio of CO₂ is slightly dependent on the pressure. However, the cage occupancy of CO₂ molecules is greatly dependent on the pressure when the concentration of C₂H₆ is higher than CH₄. In the large cages, the occupancy ratio of CO₂ increases with pressure, whereas that in the small cages declines with pressure. Overall, the cage occupancy of CO₂ molecules rises with the CO₂ concentration in the gas mixture.

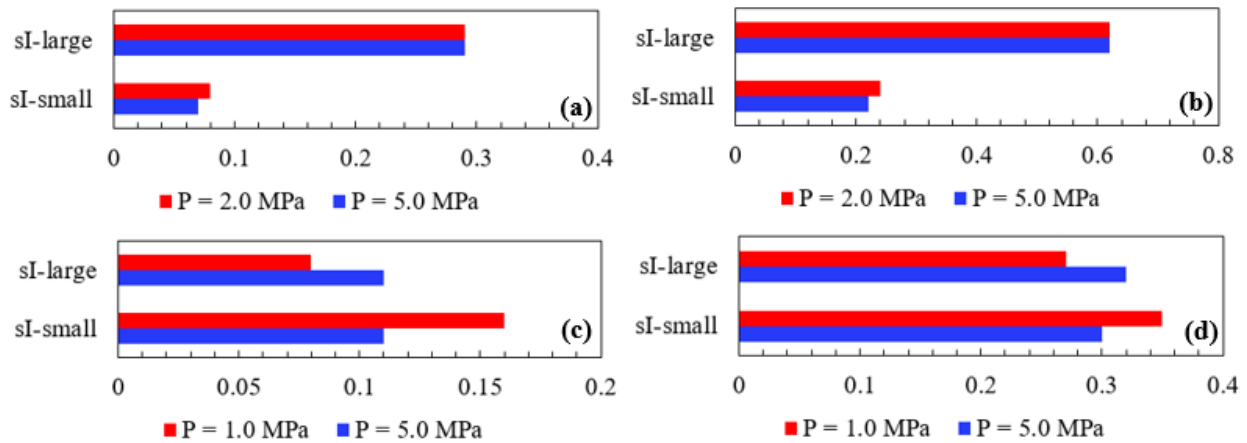


Fig. 6-6 Cage occupancy of CO₂ molecules in the small and large cages of sI hydrates

Note: the gas composition in the above scenarios: (a) 72 mol% CH₄-8 mol% C₂H₆-20 mol% CO₂; (b) 45 mol% CH₄-5 mol% C₂H₆-50 mol% CO₂; (c) 16 mol% CH₄-64 mol% C₂H₆-20 mol% CO₂; (d) 10 mol% CH₄-40 mol% C₂H₆-50 mol% CO₂.

6.3 MD Simulation Results

6.3.1 Stability of CH₄-C₂H₆ hydrates in sI and sII structures

The configurations of the sI and sII CH₄-C₂H₆ hydrates at the end of the simulation in Scenario #1 are demonstrated in Fig. 6-7. It is noted that the water and gas molecules deviate from the initial positions as shown in Fig. 6-1 and Fig. 6-2, but the water molecules still keep the cage structure. This is because the simulation conditions are inside the hydrate phase boundary, i.e., the pressure is above the phase boundary pressure and the temperature is lower than the phase boundary temperature. Therefore, either the sI or the sII hydrates are dissociated. The stability of a hydrate structure can be evaluated by analyzing the translational, rotational, and vibrational motions of the cage water molecules. In this work, the vibrational motion of gas and water molecules can be ignored because all the molecules are set as fixed rigid models. Therefore, only the translational and rotational motions are employed in the evaluation of stability of various gas hydrates.

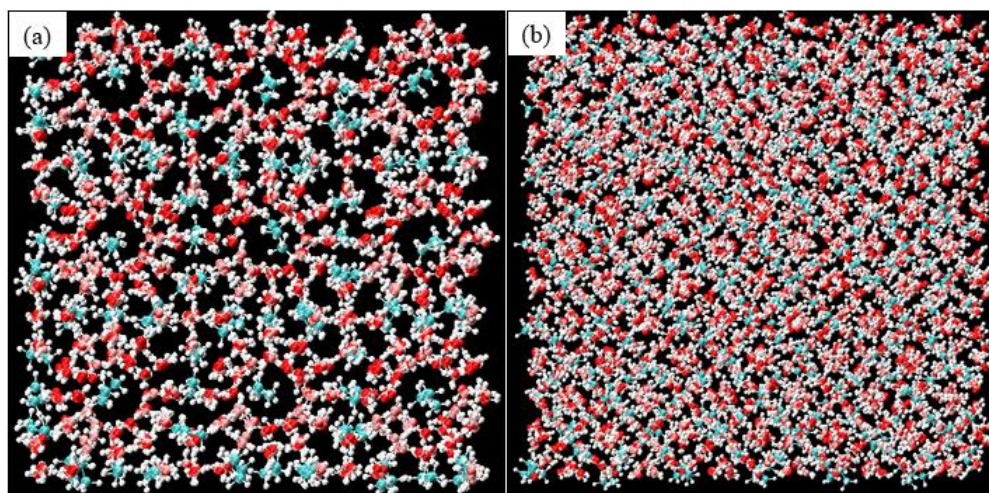


Fig. 6-7 Configuration of sI and sII hydrates at the end of simulation of the Scenario #1 (a-sI, b-sII)

The mean square displacement (MSD) is used to quantify the translational motion of H₂O molecules forming the hydrate cages. The MSD of H₂O molecules in the sI and sII hydrates of the Scenarios #1 and #3 is presented in Fig. 6-8. It is demonstrated that the MSD curves of Scenarios #1 and #3 have a similar frequency in both sI and sII hydrates. As shown in Fig. 6-8(a), the MSD of the H₂O molecules in the sI structure of Scenario #3 (i.e., 0.195 Å² on average) is smaller than that of Scenario #1 (i.e., 0.210 Å² on average), which indicates that the sI hydrates in Scenario #3 are more stable than these in Scenario #1. On the contrary, the MSD of H₂O molecules in the sII structure has a larger amplitude in Scenario #3 (i.e., 0.260 Å² on average) than that in Scenario #1 (i.e., 0.255 Å² on average). This suggests that the hydrates of Scenario #1 are more stable than those of Scenario #3 in sII structure. It is noted that the MSD of the H₂O molecules in sII structure is larger than that in sI structure on average, due to the larger number of large hydrate cages in sII structure than that in the sI structure.

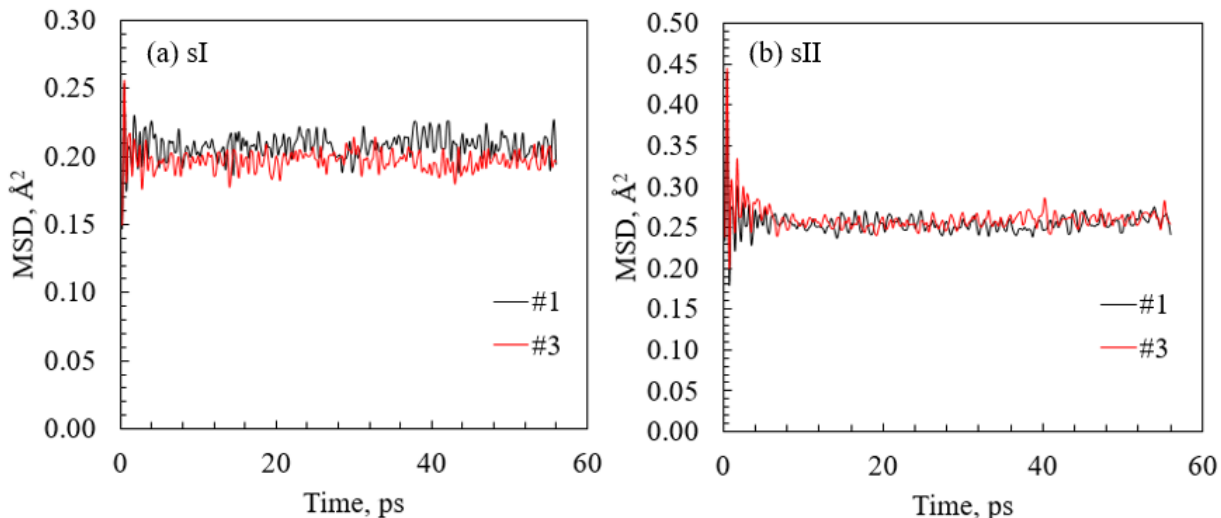


Fig. 6-8 MSD of H₂O molecules in the sI and sII hydrates of the Scenarios #1 and #3

When the pressure is elevated to 5.0 MPa, i.e., in Scenarios #2 and #4, the MSD of H₂O molecules in sI and sII is illustrated in Fig. 6-9. Similarly, the amplitude of the MSD curve for Scenarios #2 (i.e., 0.205 Å² on average) is higher than that for Scenarios #4 (i.e., 0.200 Å² on average) in the sI structure. While in the sII structure, the MSD amplitude of hydrates in Scenarios #2 (i.e., 0.245 Å² on average) is lower than that in Scenarios #4 (i.e., 0.264 Å² on average). Therefore, the MSD results indicate that the hydrates in Scenarios #2 are more stable in sII structure than those in Scenarios #4, and in sI structure, the stability of hydrates in Scenarios #4 is higher than that in Scenarios #2.

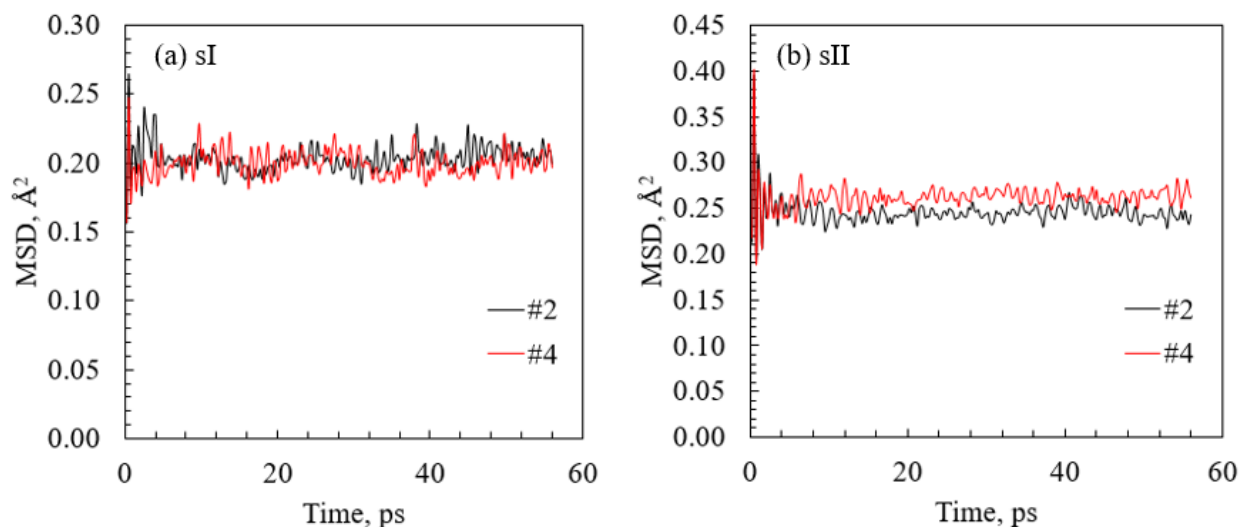


Fig. 6-9 MSD of H₂O molecules in the sI and sII hydrates of the Scenarios #2 and #4

The rotation angle serves as an indicator of the rotational motion of gas and water molecules in the hydrate cage. The variation of rotation angle of two random H₂O molecules and two CH₄ molecules in the sI hydrates of Scenario #1 are demonstrated in Fig. 6-10. It is shown that the rotational motion of individual molecules is different. Generally, the H₂O molecules rotate more

frequently than the CH₄ molecules and the amplitude of CH₄ rotation is significantly higher than the H₂O molecules. For instance, the amplitude of the two CH₄ molecules ranges from 0.2 to 2.9 radians and the largest amplitude of the two H₂O molecules is less than 1.0 radian. Also, the various H₂O molecules have various amplitudes. For instance, the amplitude of the second H₂O molecule in Fig. 6-10 is larger than the first one. In this work, the rotation of molecules of the same species is quantified using the average value, e.g., the average radians of all the H₂O molecules at various times in the sI hydrates serve as the rotational motion of H₂O in the sI hydrates.

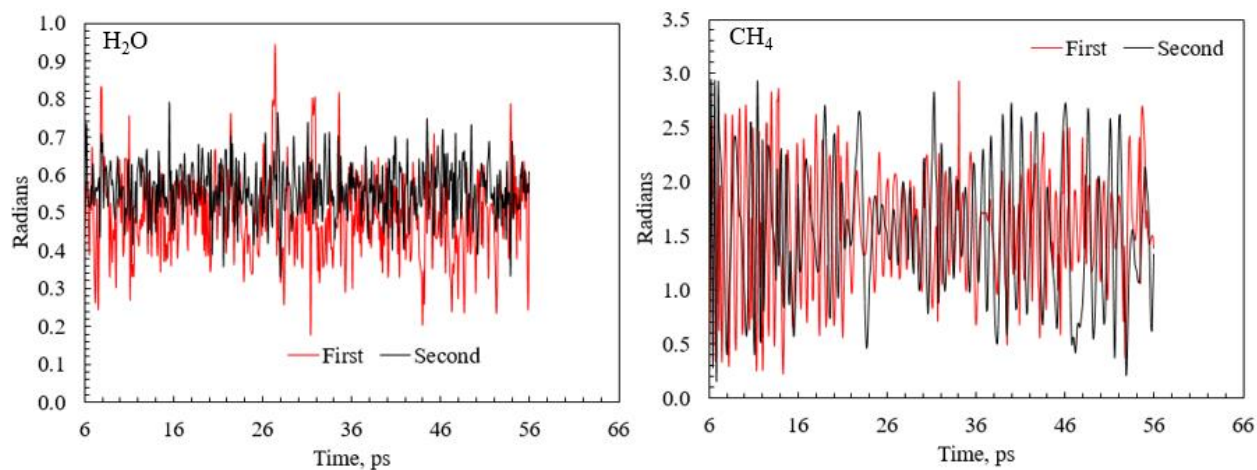


Fig. 6-10 Rotation of two random H₂O and two CH₄ molecules in the sI hydrates in Scenario #1

The variation of the average rotation angle of the H₂O molecules in sI and sII hydrates of Scenarios #1 and #3 is illustrated in Fig. 6-11. It is illustrated that in the sI structure, the H₂O molecules have a higher rotational motion in Scenario #1 (with an average rotation angle of 0.936 radians) than these in the Scenario #3 (with an average rotation angle of 0.928 radians), which indicates that the hydrate cages are more stable in Scenario #3 in the sI structure than those in Scenario #1. While in sII structure, the rotational motion of the H₂O molecules in Scenario #3

(with an average rotation angle of 0.826 radians) is higher than that in Scenario #1 (with an average rotation angle of 0.824 radians). Therefore, the hydrate cages in Scenario #1 are more stable in sII structure than that those in Scenario #1.

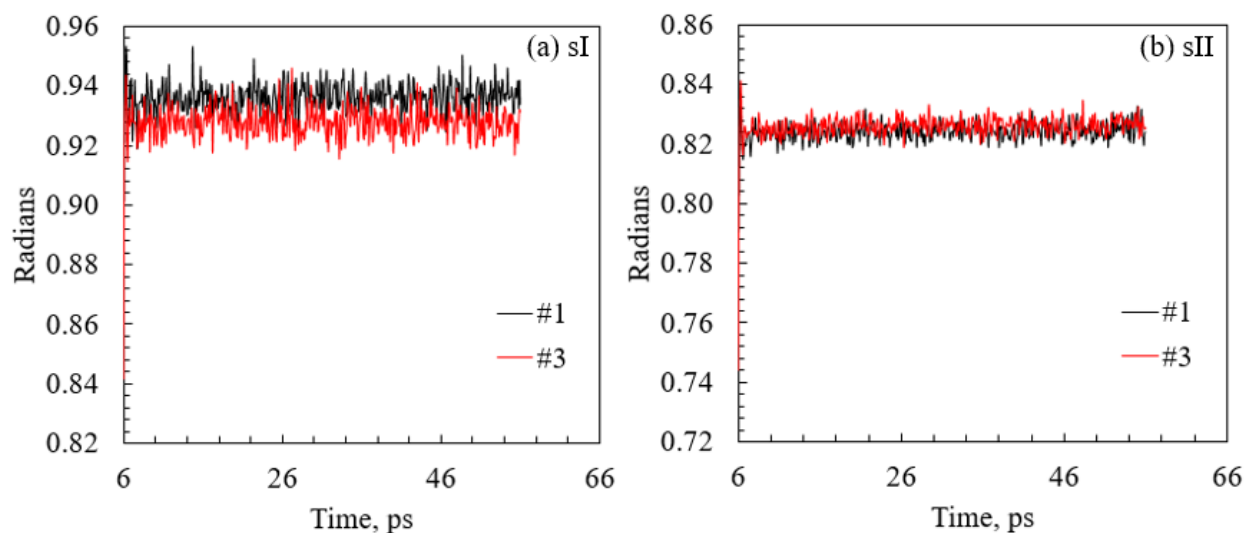


Fig. 6-11 Rotational motion of H₂O molecules in the sI and sII hydrates of the Scenarios #1 and #3

The rotational motion of the H₂O molecules in Scenarios #2 and #4 is compared in Fig. 6-12. It is observed that in sI structure, the rotation angle of H₂O molecules in Scenario #2 (i.e., 0.930 radians) is larger than that in Scenario #4 (i.e., 0.925 radians). The rotation angle of H₂O molecules in Scenario #2 (i.e., 0.820 radians) is similar to that in Scenario #4 (i.e., 0.819 radians) if the sII structure hydrates are formed. Therefore, it can be concluded that the hydrate cages in Scenario #4 are more stable in sI structure than that those in Scenario #2 and they have a similar rotational motion in sII structure.

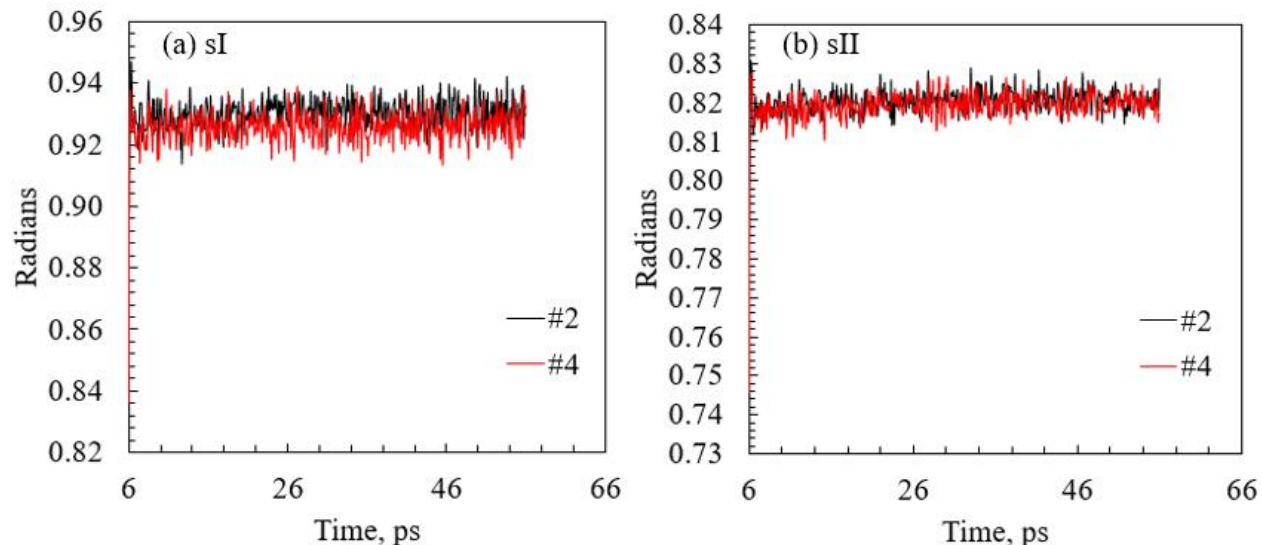


Fig. 6-12 Rotational motion of H₂O molecules in the sI and sII hydrates of the Scenarios #2 and #4

The radial distribution function (i.e., RDF) is also used to evaluate the structure of hydrate cages of various scenarios in the two hydrate structures. The RDF curves are truncated at a distance of 10 Å. The RDF of the O-O pairs in the H₂O molecules in Scenarios #1 and #3 are illustrated in Fig. 6-13. The first which is also the highest peak in the RDF curves in Fig. 6-13 shows up at the O-O distance of 2.725 Å. This means that the closest H₂O molecules in the sI and sII hydrates are separated 2.725 Å away from each other. The second peak appears at the O-O distance of 4.495 Å, which indicates the tetrahedral hydrogen bonding structures of H₂O molecules in gas hydrates (Geng et al., 2009). The rest peaks, i.e., at the O-O distance of 6.395 and 8.675 Å correspond to the O-O pairs in a higher distance. It can be observed that the difference between the two RDF curves in Fig. 6-13(a) is not significant. This is because the simulation conditions are inside the hydrate phase boundary. The hydrates are not dissociated and therefore, the hydrate cages are not greatly distorted. However, with a closer observation, it can be seen that the RDF peaks of Scenario

#1 are lower in sI than the those of Scenario #3, which indicates that the sI hydrate structure is more stable in Scenario #3 than in Scenario #1. On the contrary, the comparison of the RDF peaks in sII structure suggests that the hydrate cages in Scenario #1 is more stable.

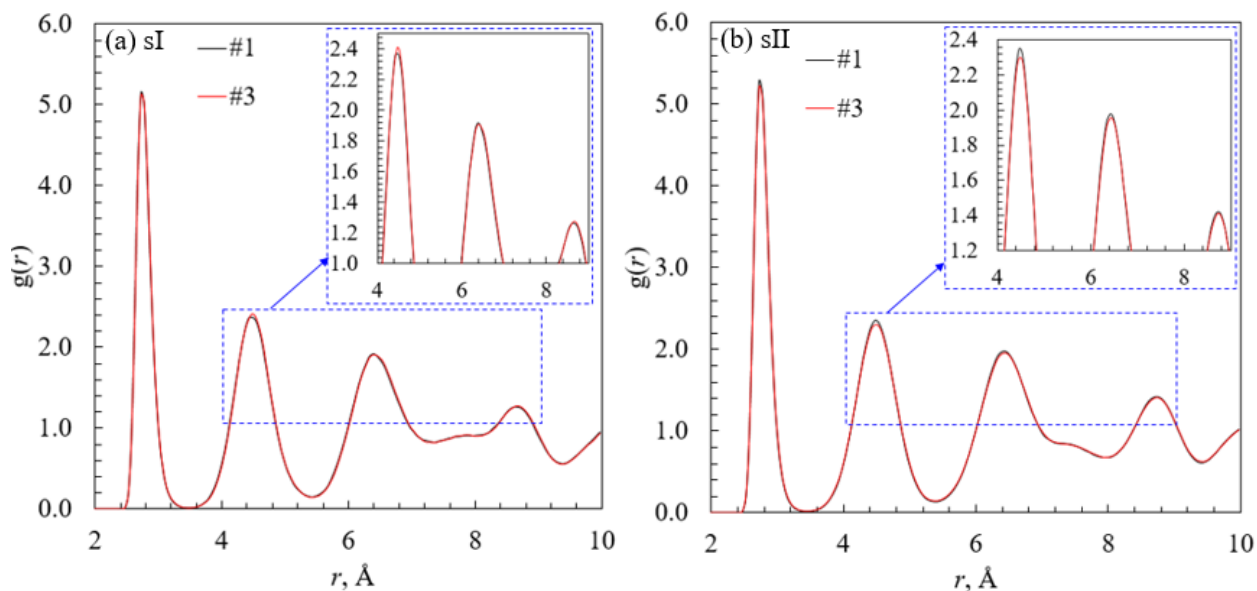


Fig. 6-13 RDF of O-O in H₂O molecules in the sI and sII hydrates of the Scenarios #1 and #3

The RDF curves of O-O pairs in the H₂O molecules in Scenarios #2 and #4 are compared in Fig. 6-14. Similarly, it is shown that the peaks of the RDF curves of Scenario #4 is sharper in the sI structure, which means that the hydrate cages in Scenario #4 is more stable in sI structure than those in Scenario #2. On the contrary, the RDF curves of sII hydrates are more stable in Scenario #2 than Scenario #4.

In summary, it can be concluded from the analysis of the MSD, rotation angle, and the RDF of H₂O molecules that the gas hydrates in Scenarios #1 and 2 are more stable in sII structure and for the hydrates in Scenarios #3 and 4 are more stabilized in sI structure. This conclusion is in

consistent with the theoretical calculation and experimental observation as discussed in Section 2.3.

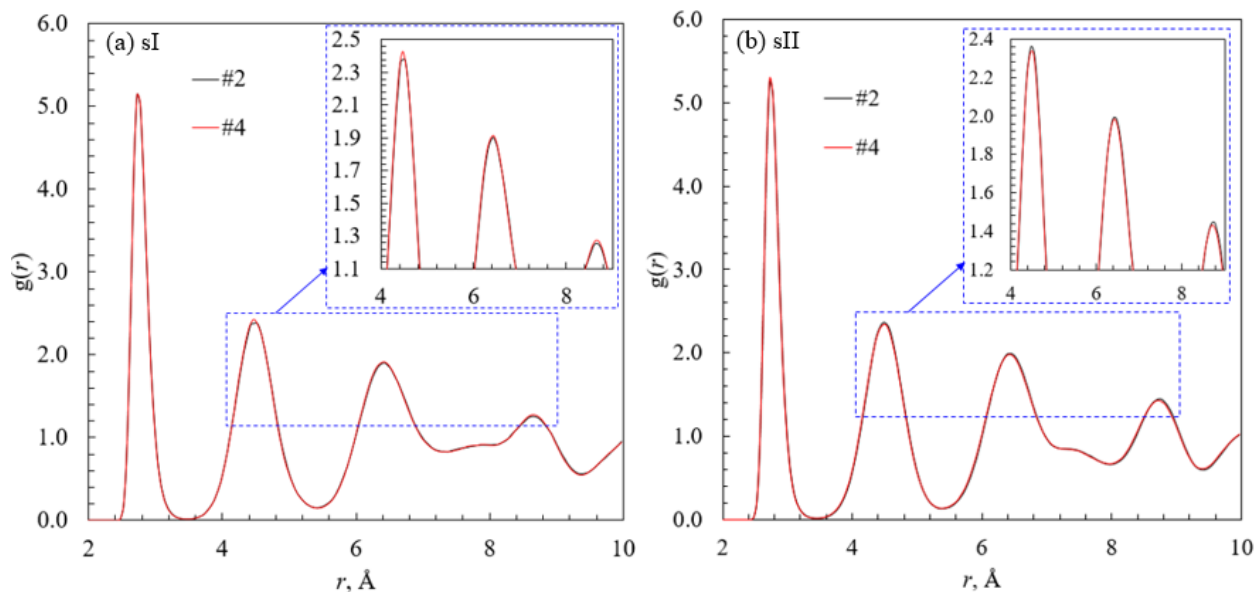


Fig. 6-14 RDF of O-O in H₂O molecules in the sI and sII hydrates of the Scenarios #2 and #4

6.3.2 Stability of CH₄-C₂H₆-CO₂ hydrates with various gas compositions

The rotational and translational motion of water and gas molecules in the sI hydrates in Scenarios #5 & #7 (with the CH₄:C₂H₆ mole ratio of 9:1) and Scenarios #9 & #11 (with the CH₄:C₂H₆ mole ratio of 1:4) are examined to analyze the impact of CO₂ on hydrate stability and also the interaction between various gas species.

The rotation angle, MSD, and RDF of the H₂O molecules of the CH₄-C₂H₆-CO₂ hydrates in Scenarios #5 and #7 are compared in Fig. 6-15. The pressure of these two scenarios is the same and the gas composition can be found in Table 6-2. It is observed that both the rotational and translational motions of the H₂O molecules become more active when the composition of CO₂

increases from 20 mol% in Scenario #5 to 50 mol% in Scenario #7, indicating that the hydrate cages become less stable when the CO₂ composition increases from 20 to 50 mol%. It also can be seen from the RDF curves in Fig. 6-15(c) that the H₂O molecules become slightly less ordered when the composition of CO₂ increases, which is another evidence that the stability of hydrate cages decreases with the increase in CO₂ composition.

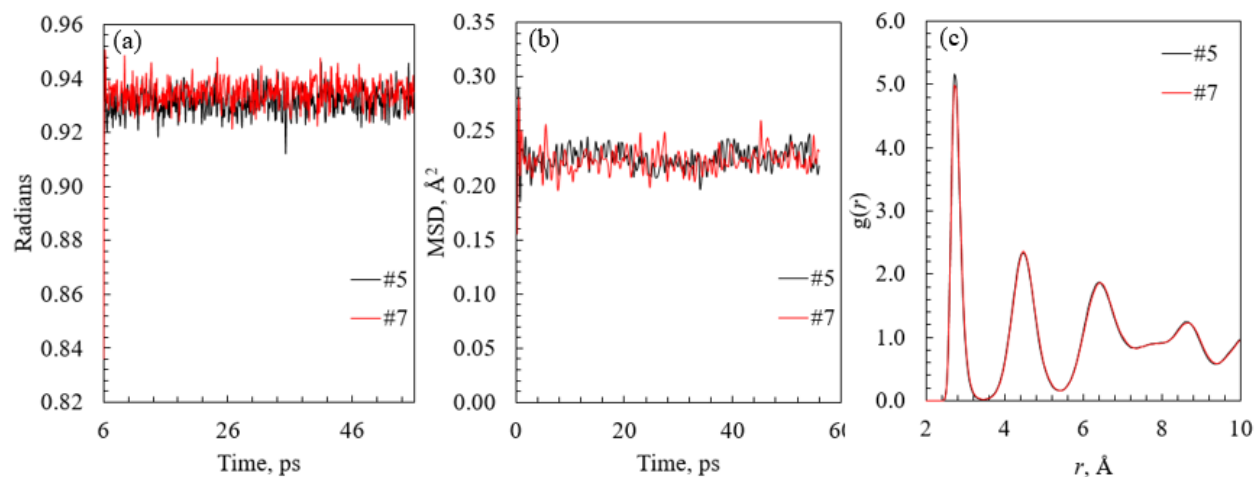


Fig. 6-15 Rotation angle (a), MSD (b), and RDF (c) of H₂O molecules in Scenarios #5 and #7

The evolution of rotation angle and MSD of the CH₄ molecules, as well as the RDF of C-O pair, i.e., the carbon atoms in CH₄ molecules and the oxygen in cage H₂O are compared at various CO₂ compositions in Scenarios #5 and #7, as shown in Fig. 6-16. It can be seen that the rotational motion of CH₄ molecules in Scenario #7 is similar to that in Scenario #5 as shown in Fig. 6-16(a). However, the translational motion, i.e., MSD is significantly reduced when the CO₂ composition is increased. In addition, the RDF peak of the C-O pair in Scenario #7 is narrower than that in Scenario #5 and the amplitude is also larger, which suggests that CH₄ molecules are more ordered in the hydrate cages in Scenario #7. Therefore, it can be concluded that the motion of CH₄ molecules in the hydrate cages becomes less freely as the composition of CO₂ rises.

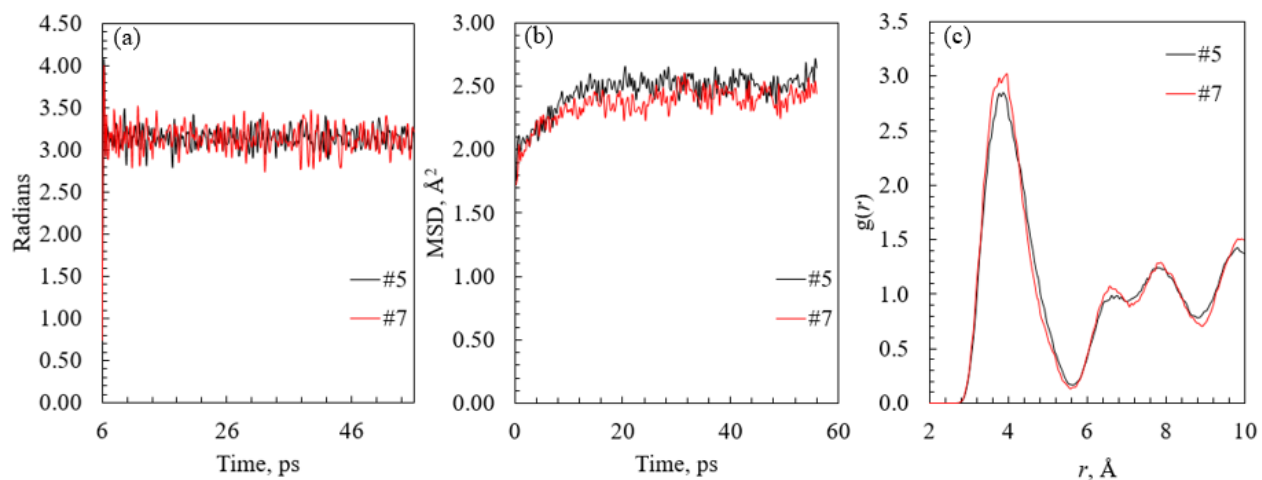


Fig. 6-16 Rotation angle (a), MSD (b), and RDF (c) of CH₄ molecules in Scenarios #5 and #7

The impact of CO₂ addition on the rotational and translational motions of C₂H₆ molecules in the hydrate cages is depicted in Fig. 6-17. It is obvious that the average rotation angle and the MSD of C₂H₆ molecules in Scenario #7 is larger. Also, the C₂H₆ molecules in Scenario #7 is less ordered compared with that in Scenario #5, as illustrated in the RDF curves of the C-O pairs (C in C₂H₆, O in H₂O). Therefore, the C₂H₆ molecules move more freely as CO₂ concentration increases from 20 mol% to 50 mol%.

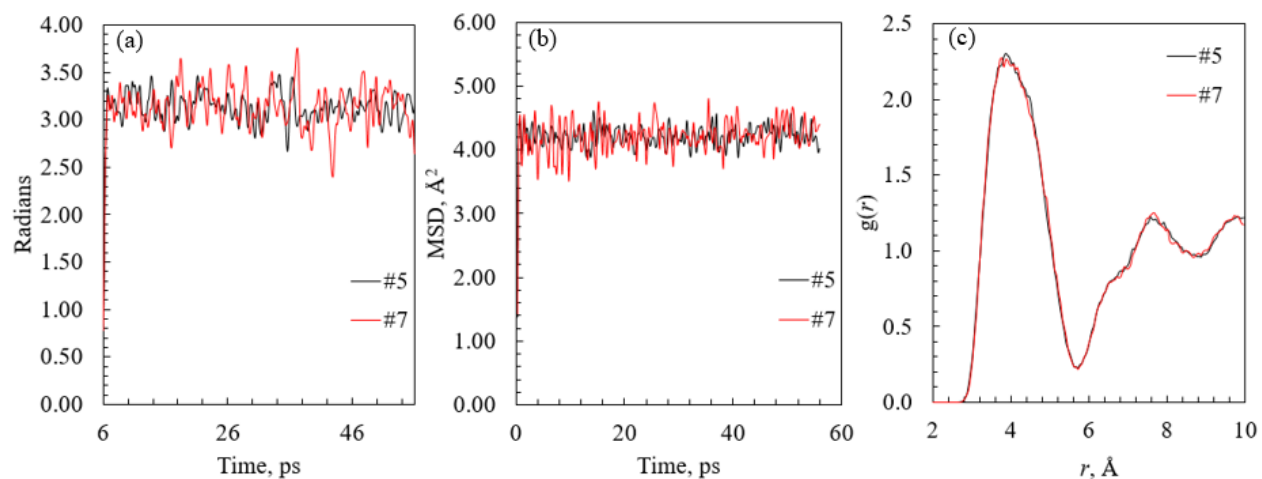


Fig. 6-17 Rotation angle (a), MSD (b), and RDF (c) of C₂H₆ molecules in Scenarios #5 and #7

The motion of CO₂ is also analyzed in Fig. 6-18. It is shown that the rotational and translational motion of CO₂ molecules become less active with the increase in CO₂ composition. The RDF curves of the C-O pairs (C in CO₂ and O in H₂O) in Fig. 6-18(c) show that the CO₂ molecules are more ordered in Scenario #7. Therefore, the motion of CO₂ grows more restricted as more CO₂ is added.

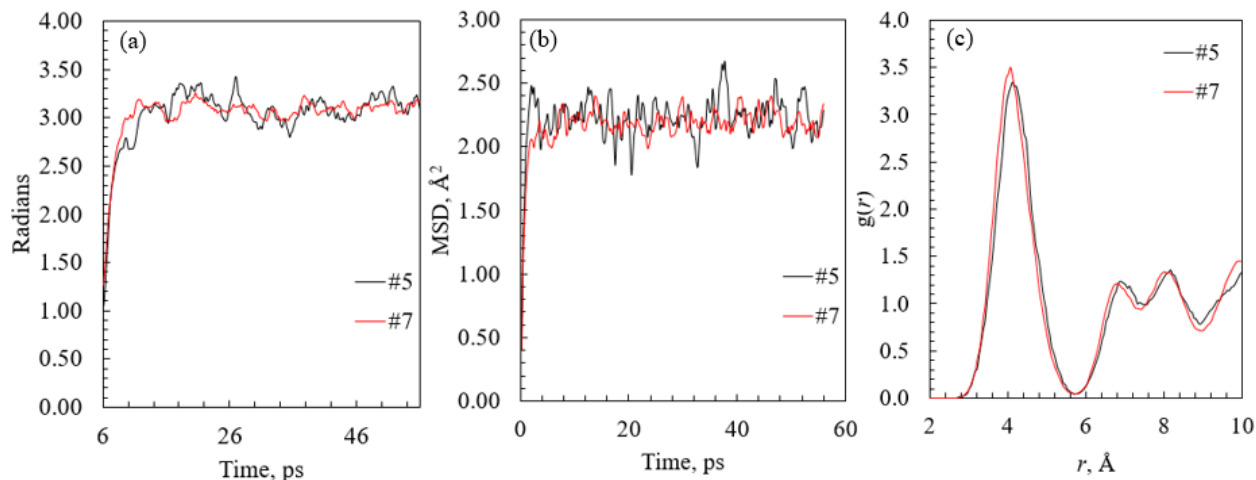


Fig. 6-18 Rotation angle (a), MSD (b), and RDF (c) of CO₂ molecules in Scenarios #5 and #7

When more C₂H₆ than CH₄ molecules exist in the gas mixture, i.e., with the mole ratio of CH₄ to C₂H₆ at 1:4 in Scenarios #9 and #11, the rotational and translational motion of water and gas molecules are investigated in this section. The pressure in these two scenarios are the same and the gas compositions are described in Table 6-2.

The rotation angle, MSD, and RDF of H₂O molecules in Scenarios #9 and #11 are illustrated in Fig. 6-19. It is obvious that the motion of H₂O molecules becomes more active with the increase in CO₂ concentration, as shown by the rotational and translational motion of H₂O molecules, as

well as the more ordered configuration of H₂O molecules in the RDF curves. Therefore, the hydrate cages are more stable when the concentration of CO₂ is lower, i.e., 20 mol%.

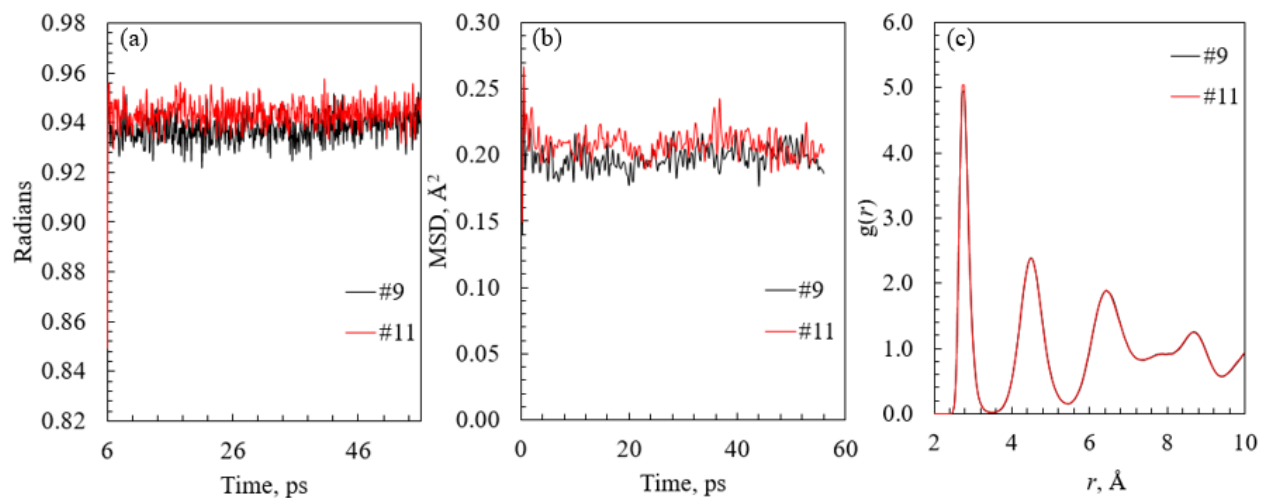


Fig. 6-19 Rotation angle (a), MSD (b), and RDF (c) of H₂O molecules in Scenarios #9 and #11

The rotational motion of CH₄ in the hydrate cages are similar in Scenarios #9 and #11, as demonstrated in Fig. 6-20(a). The MSD curves in these two scenarios are also close in the late stage. In the RDF curves, it is observed that the CH₄ molecules in Scenario #11 are more ordered than those in Scenario #9. Therefore, it can be concluded that the motion CH₄ molecules is slightly restricted when the concentration of CO₂ is increased from 20 to 50 mol%. However, compared with the variation of CH₄ motion due to CO₂ addition in Scenarios #5 and #7, the change of CH₄ motion in Scenarios #9 and #11 is less significant. This may be attributed to the lower concentration of CH₄ in the gas mixture in Scenarios #9 and #11.

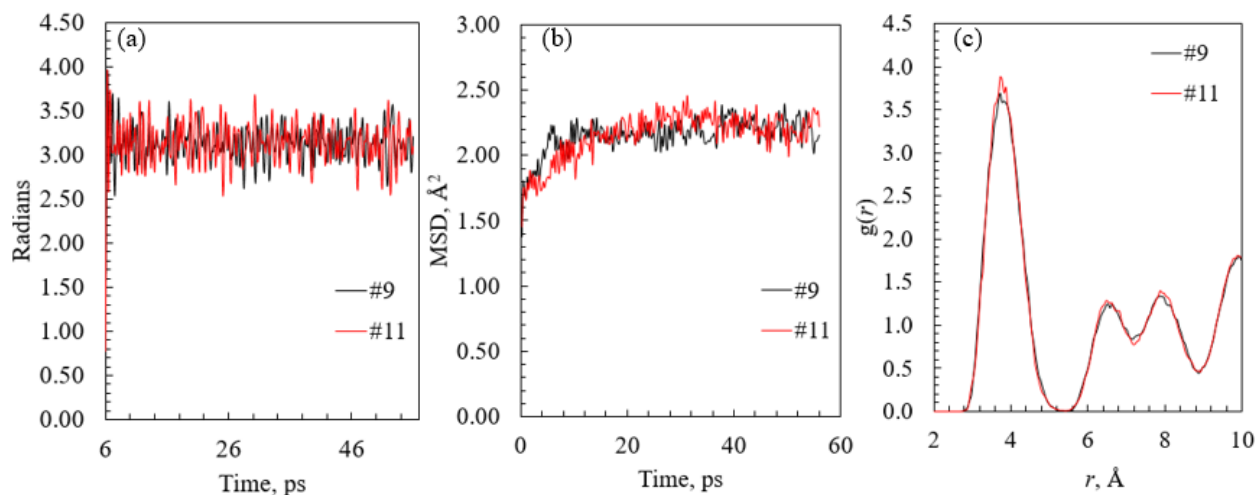


Fig. 6-20 Rotation angle (a), MSD (b), and RDF (c) of CH₄ molecules in Scenarios #9 and #11

The rotational and translational motions of C₂H₆ molecules in Scenarios #9 and #11 are described in Fig. 6-21. It is evident that the average rotation angle decreases slightly as more CO₂ is added, and the MSD does not show a significant difference. In the RDF curves of C-O pairs, it is observed that the C₂H₆ molecules are slightly more ordered in Scenario #11. By comparing the change of the motion of C₂H₆ molecules due to the addition of CO₂ in Fig. 6-17 and Fig. 6-21, it is found that the impact of CO₂ on C₂H₆ motion is less significant when the concentration of C₂H₆ is smaller. This is a result of the competing effect of CO₂ and C₂H₆ molecules for the large hydrate cages. The competition between CO₂ and C₂H₆ molecules for the large hydrate cages is obvious in Fig. 6-6. When the concentration of C₂H₆ is low, e.g., in Fig. 6-6(a) and (b), the occupancy ratio of CO₂ increases by around 0.32 in the large cages when the concentration of CO₂ changes from 20 to 50 mol%. However, the cage occupancy of CO₂ increases only by 0.20 in the large cages from Scenario #9 to #11 where the C₂H₆ concentration is high. The preference of CO₂ in the large hydrate cages is also observed in the literature (Geng et al., 2009; Nohra et al., 2012).

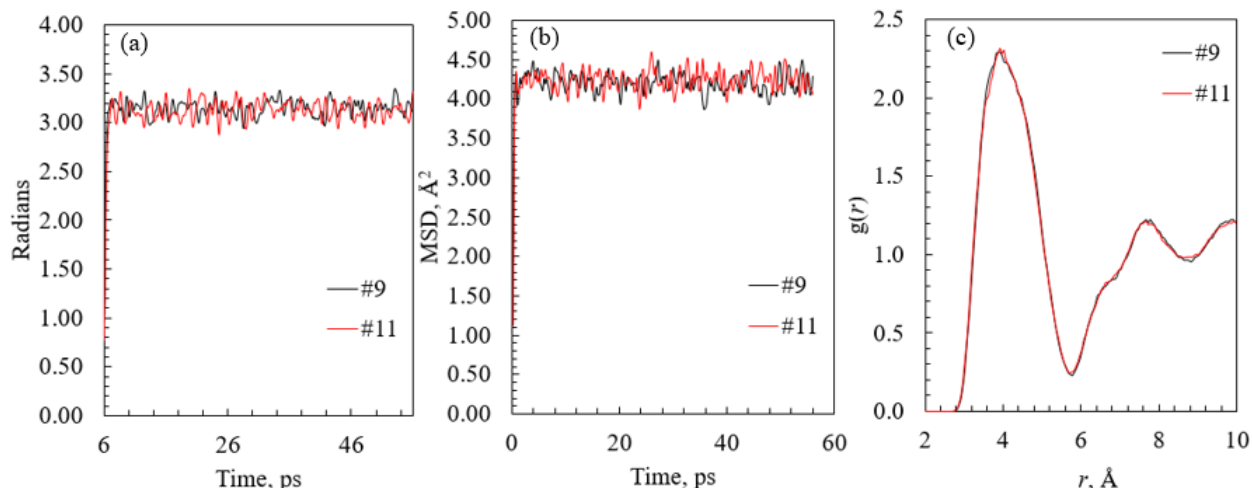


Fig. 6-21 Rotation angle (a), MSD (b), and RDF (c) of C_2H_6 molecules in Scenarios #9 and #11

The motion of CO_2 molecules in the hydrate cages of Scenarios #9 and #11 are examined in Fig. 6-22. It is shown that the average rotation angle of CO_2 molecules in Scenario #11 is slightly larger than that in Scenario #9. The MSD of CO_2 molecules is also higher in Scenario #11. The broader RDF peaks of CO_2 in Scenario #11 suggest that the CO_2 molecules are less ordered in the hydrate cages. Therefore, it can be concluded that the CO_2 molecules can move more freely when the concentration of CO_2 is higher.

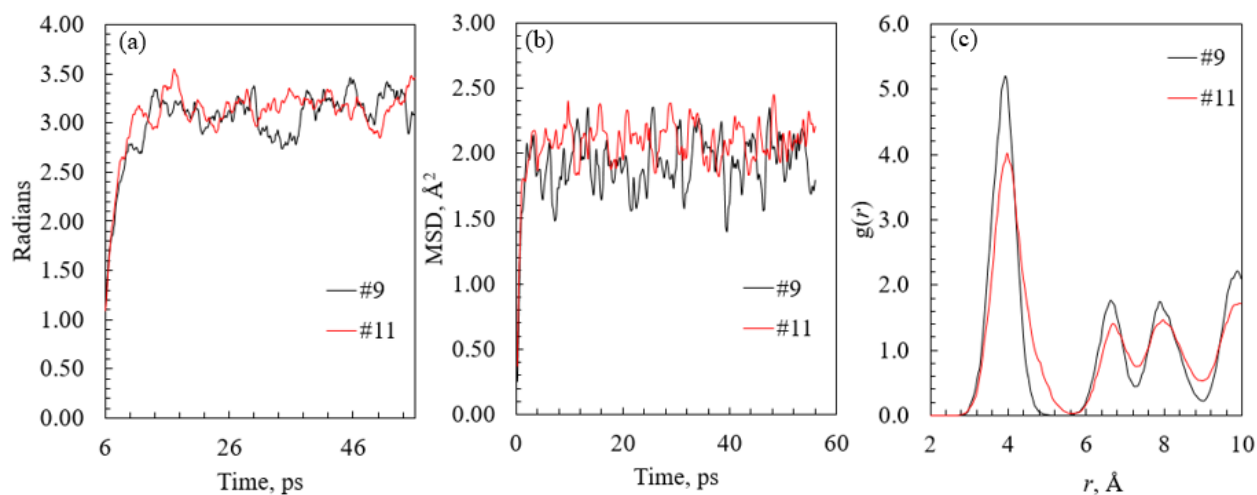


Fig. 6-22 Rotation angle (a), MSD (b), and RDF (c) of CO_2 molecules in Scenarios #9 and #11

It is worth noting that the frequency of both the rotational and translational motion of various gas species are significantly different. Specifically, the frequency of CH₄ is higher than C₂H₆, both of which are significantly larger than CO₂ molecules. This is a result of the interactions between gas and water molecules, which can be reflected by the potential energy between gas and water molecules, as presented in Fig. 6-23. Note that the value illustrated in Fig. 6-23 is averaged on the number of molecules of each species. It is shown that potential energy between H₂O molecules is the lowest due to the hydrogen bonds. The potential energy between gas and water pairs is larger than that between water molecules, and increases in the following order: CO₂-H₂O < C₂H₆-H₂O < CH₄-H₂O, which is consistent with the rotational and translational motion frequency of gas molecules in the hydrate cages.

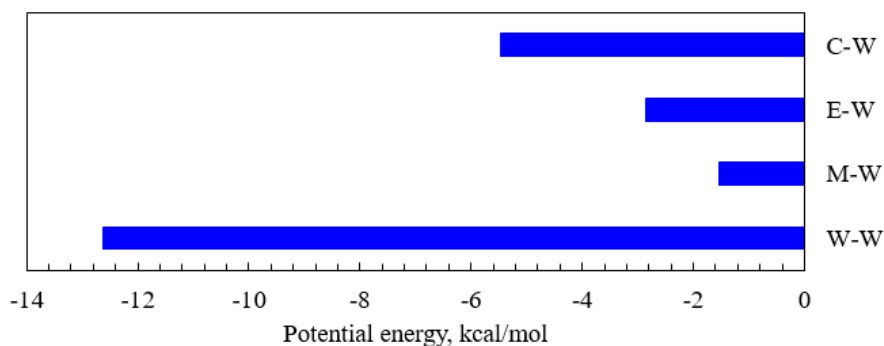


Fig. 6-23 Potential energy of between water and gas molecules

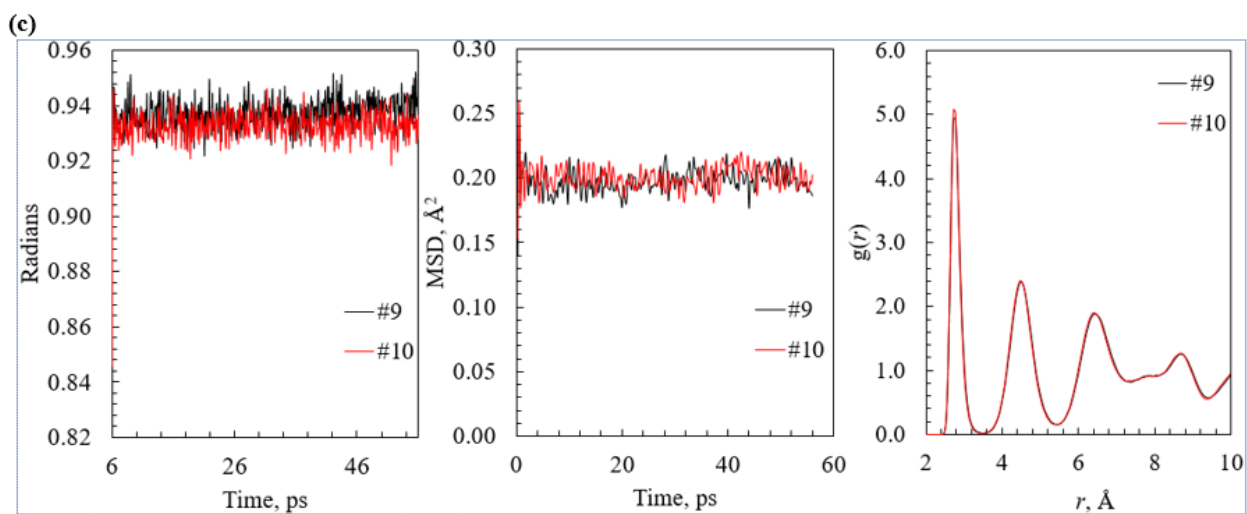
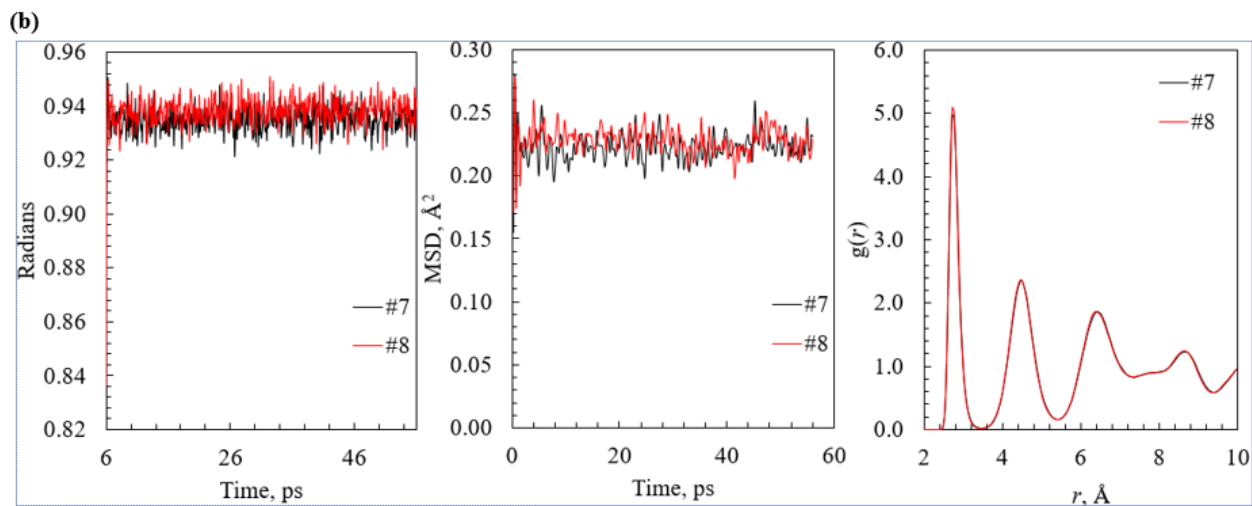
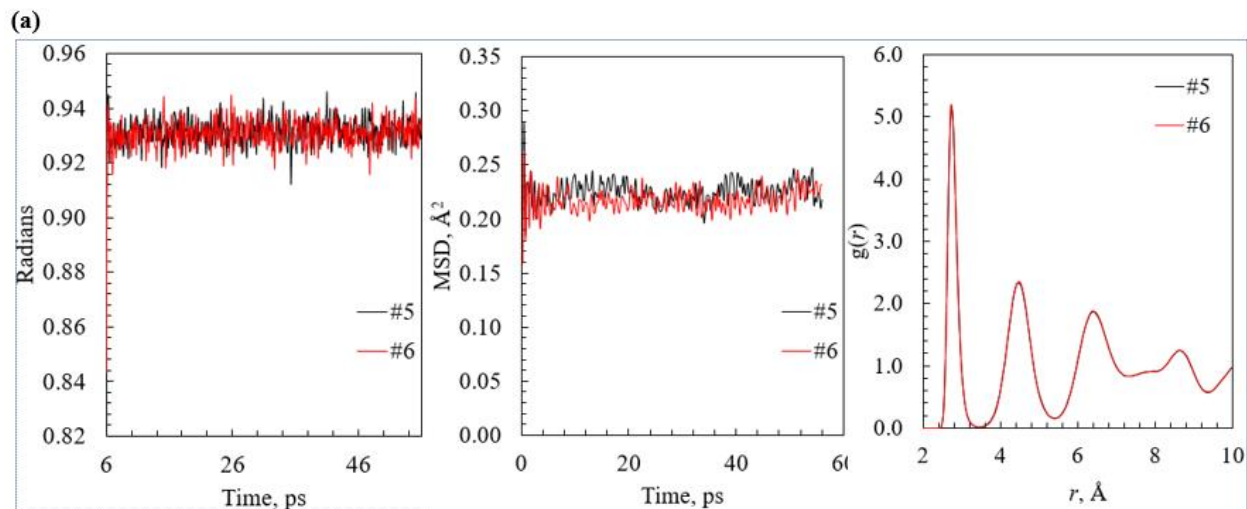
(C, E, M, W represent CO₂, C₂H₆, CH₄, and H₂O molecules, respectively)

6.3.3 Stability of CH₄-C₂H₆-CO₂ hydrates at various pressures

The influence of pressure on the stability of CH₄-C₂H₆-CO₂ hydrates with various gas compositions scenarios, i.e., Scenarios #5 (with the composition of CH₄, C₂H₆, and CO₂ at 72,

8, and 20 mol%, respectively), #7 (with the composition of CH₄, C₂H₆, and CO₂ at 45, 5, and 50 mol%, respectively), #9
 (with the composition of CH₄, C₂H₆, and CO₂ at 16, 64, and 20 mol%, respectively), #11 (with the composition of CH₄, C₂H₆, and CO₂ at 10, 40, and 50 mol%, respectively) are explored in this section.

The rotation angle, MSD, and RDF of the H₂O molecules in the sI hydrate cages of Scenarios #5 through #12 are compared in Fig. 6-24. It can be seen in Fig. 6-24(a) that the rotational motion of the H₂O molecules in these two scenarios are similar, with the average rotation angle around 0.935 radians. However, the MSD curves indicate that the translational motion of H₂O molecules is less active. Also, the H₂O molecules are more orderly distributed as shown by the sharper peaks in the RDF curves. Therefore, it is suggested that when the composition of CH₄, C₂H₆, and CO₂ are 72, 8, and 20 mol%, the stability of the sI hydrate cages demonstrates a slight increase when the pressure increases from 2.0 to 5.0 MPa. The effect of pressure on the gas hydrates in Scenarios #7 and #8 are shown in Fig. 6-24(b), where we can see the average rotation angle and MSD of H₂O molecules are elevated as the pressure increases from 2.0 to 5.0 MPa. Hence, the stability of gas hydrates in Scenarios #7 and #8 is reduced with the pressure rising. Similarly, it is observed that the stability of gas hydrate in Scenarios #9 and #10 is enhanced and that in Scenarios #11 and #12 is decreased. It is noted that the amplitude and frequency of the rotation angle and MSD curves of H₂O molecules in Fig. 6-24(a)-(d) do not show significant differences.



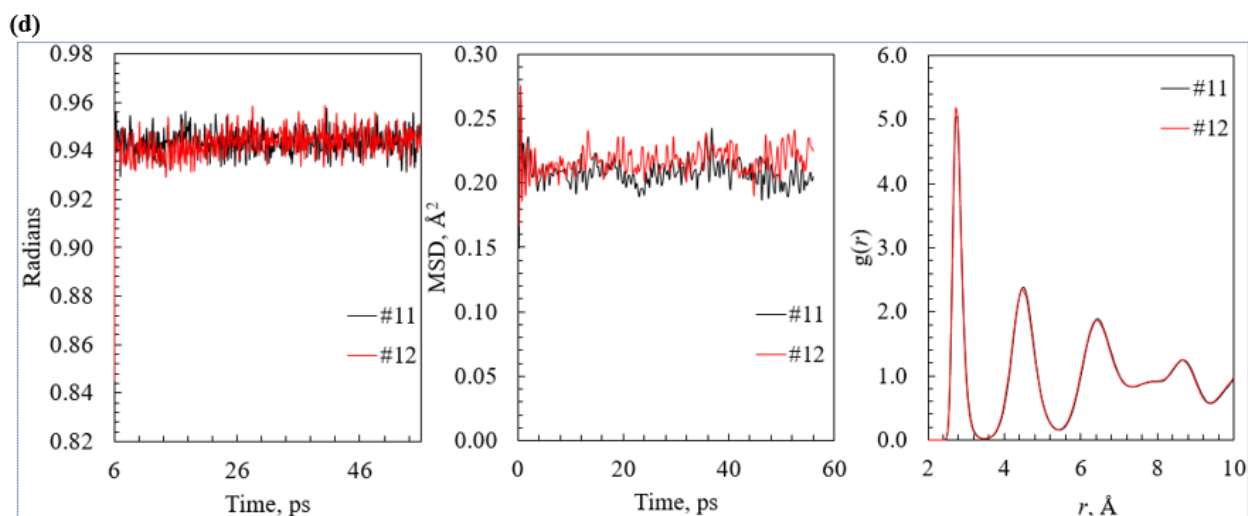
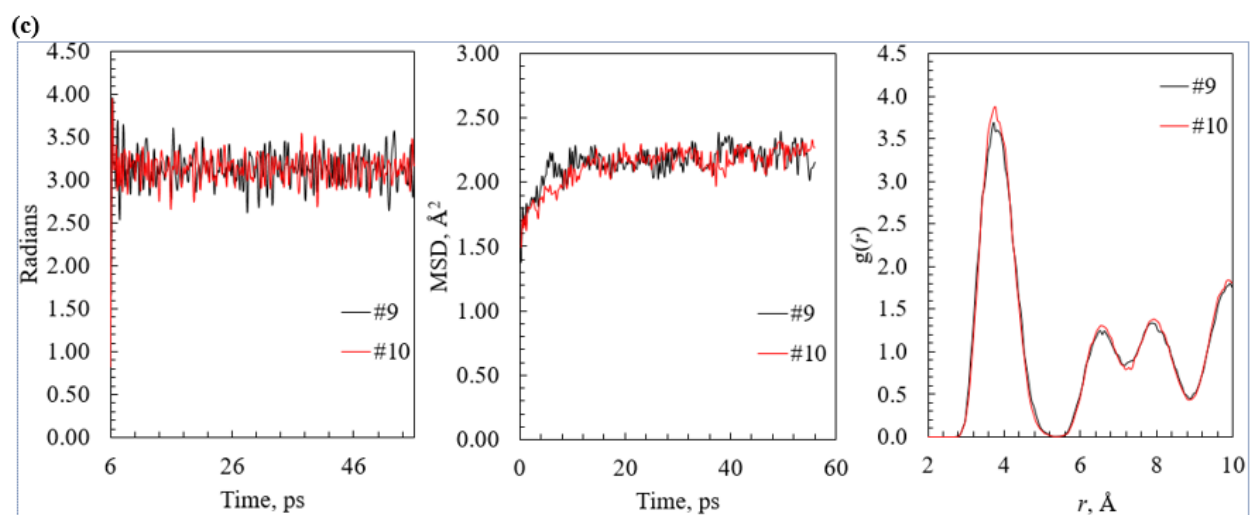
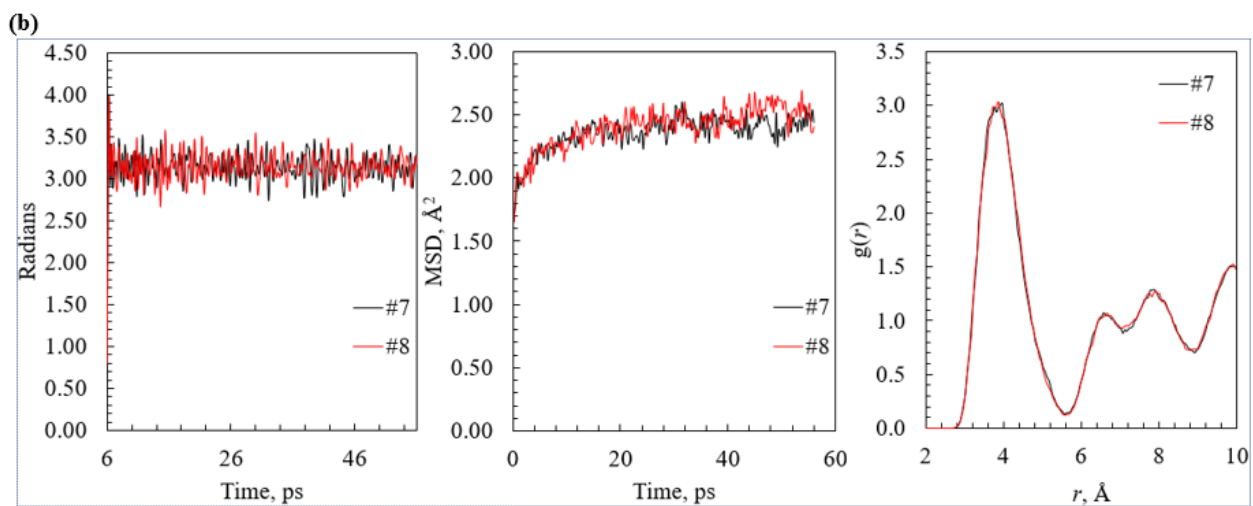
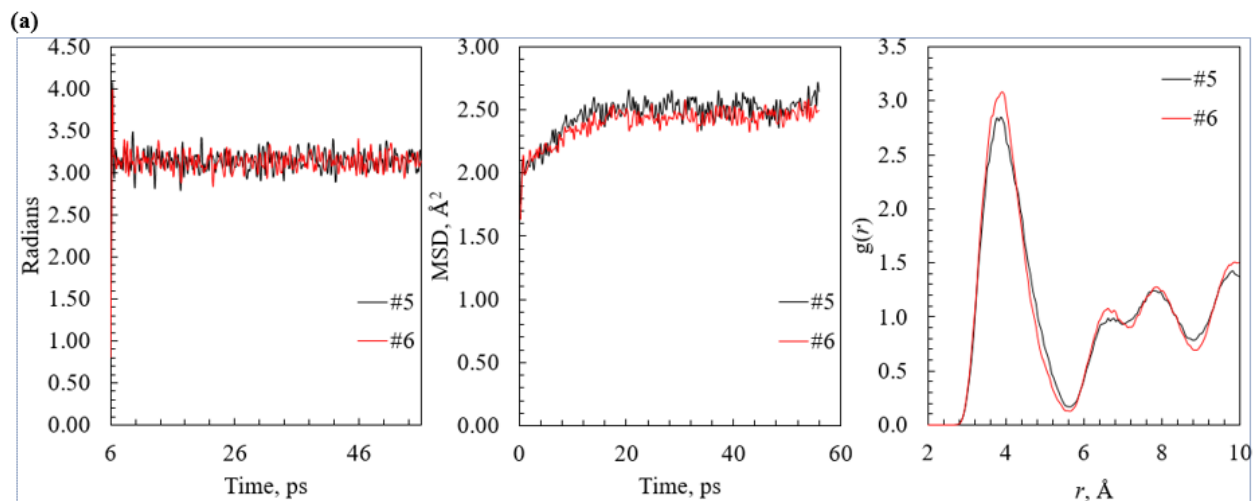


Fig. 6-24 Rotation angle, MSD, and RDF of H₂O molecules in Scenarios #5 (a), #7 (b), #9
 (c), #11 (d)

The effect of pressure on the rotational and translational motions of the CH₄ molecules in various scenarios can be observed in Fig. 6-25. It is shown that the rotation of CH₄ molecules in Scenarios #5 and #6 are similar but the MSD curve demonstrates a declining trend as pressure increase. Also, the CH₄ molecules in the sI hydrate cages get more ordered, which means that the motion of CH₄ molecules in the hydrate cages is restricted with an increase in pressure. In Scenarios #7, #9
, #11, the concentration of CH₄ is less than that in Scenarios #5 and #6. It can be seen that the effect of pressure on the motion of CH₄ molecules become more and more negligible as the concentration of CH₄ decreases. For instance, when the concentration of CH₄ is 10 mol% in Scenarios #11 and #12, the average rotation angle, MSD, and the RDF curves are alike in these two scenarios. It is interesting to find that even though the average rotation angle in various scenarios is similar, the amplitude of the fluctuation in these rotation angle curves is different. In general, the fluctuation amplitude of the rotation curves increases as the concentration of CH₄ decreases, which may be a result of the interaction between CH₄ and CO₂.



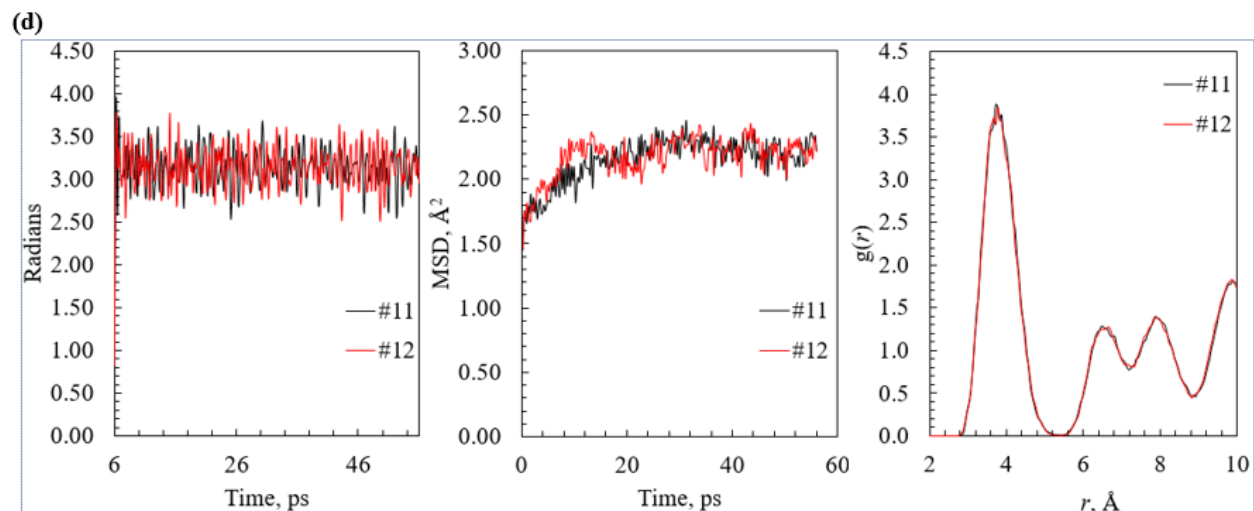
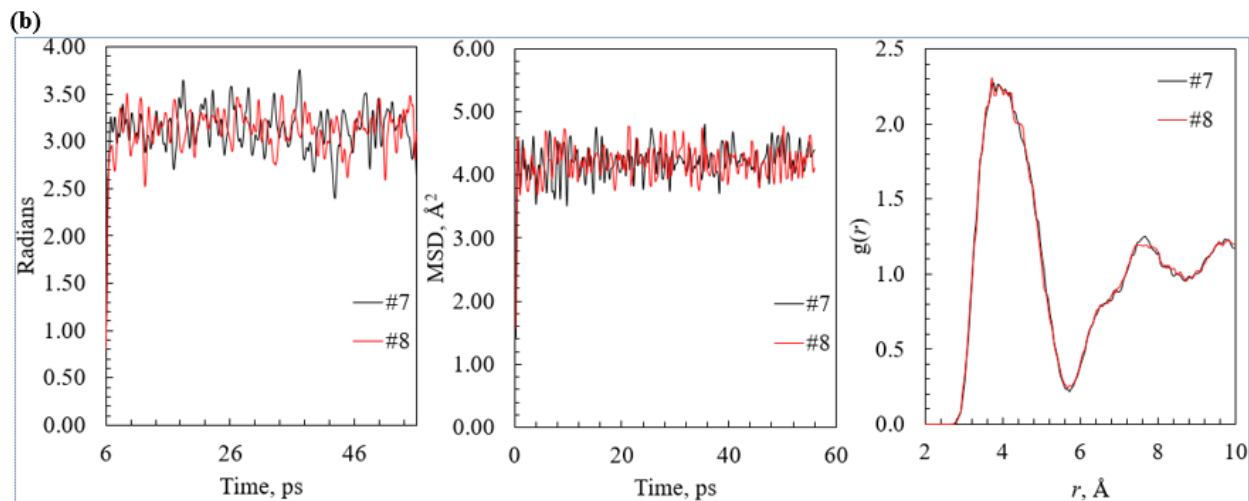
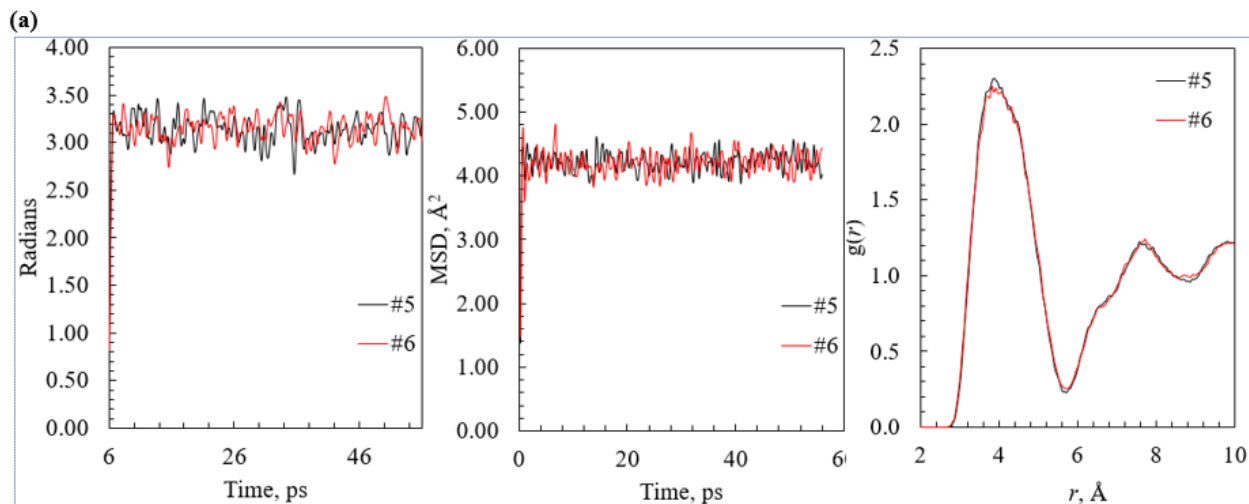


Fig. 6-25 Rotation angle, MSD, and RDF of CH₄ molecules in Scenarios #5 (a), #7 (b), #9
 (c), #11 (d)

The change of C₂H₆ molecule motion due to pressure increase is presented in Fig. 6-26. It is demonstrated that the average rotation angle and MSD of C₂H₆ molecules in the scenario pairs are similar. The less sharp peak in the RDF curve of Scenario #6 indicates that the C₂H₆ molecules become less ordered in the sI hydrate cages as pressure increases. When the composition of C₂H₆ is decreased to 5 mol% in Scenarios #7 and #8, the amplitude of the rotation angle curve is smaller as the pressure increases. The variation of MSD and RDF curve is negligible. However, the fluctuation amplitude of both the rotation angle and MSD curves are higher when the composition of C₂H₆ gets lower. In Scenarios #9 and #10, the composition of C₂H₆ is elevated to 64 mol%, the rotational and translational motion of C₂H₆ in the hydrate cages hardly varies with the pressure, as shown in Fig. 6-26(c). In Scenarios #11 and #12 where the composition of C₂H₆ is 40 mol%, the amplitude of the fluctuation of both the rotation angle and the MSD curves are higher than the scenarios where the C₂H₆ composition is 64 mol%. Also, the average rotation angle gets slightly

larger when the pressure is higher. Furthermore, the RDF curves suggest that the C_2H_6 molecules grow less ordered with the increase in pressure.



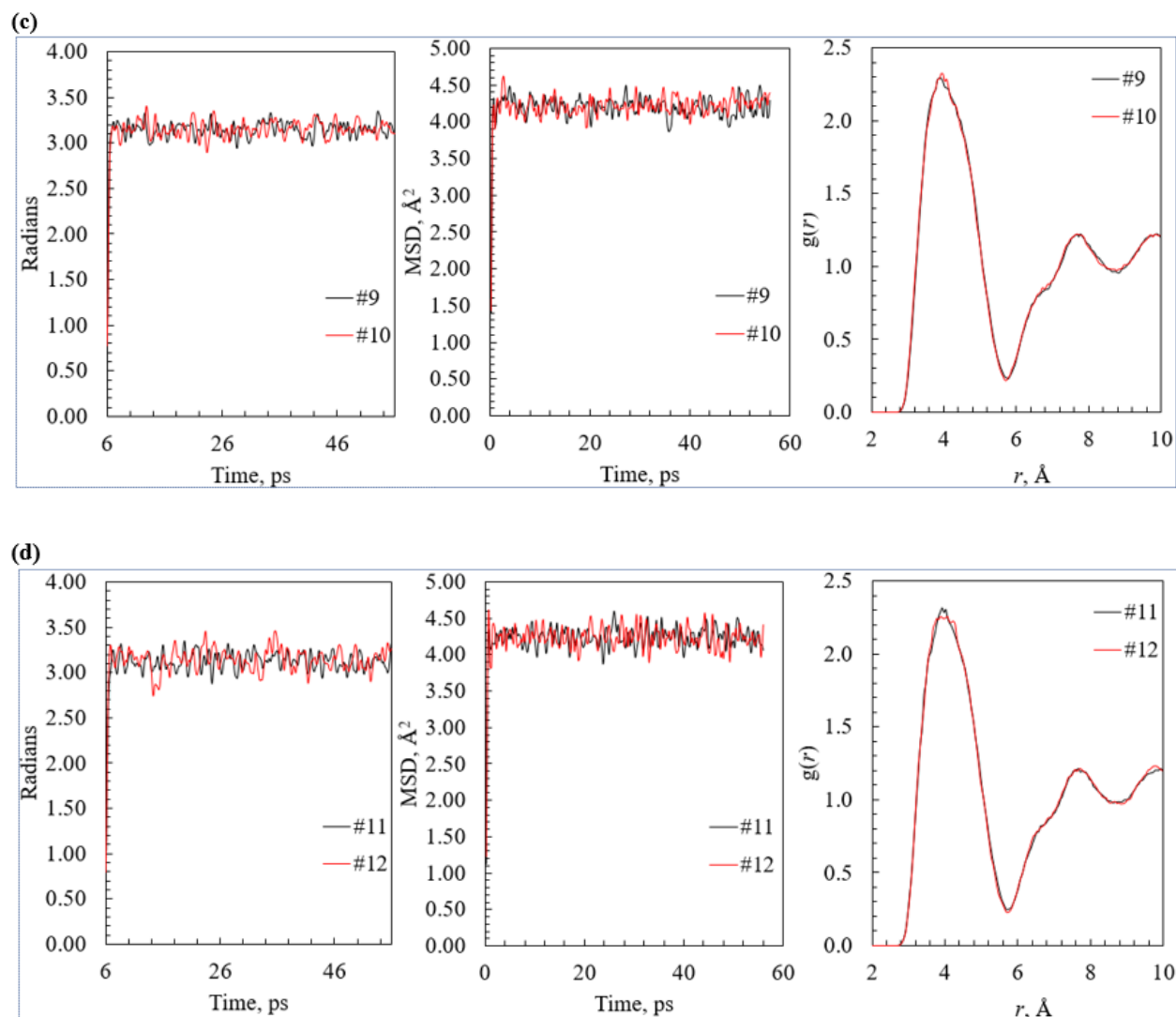
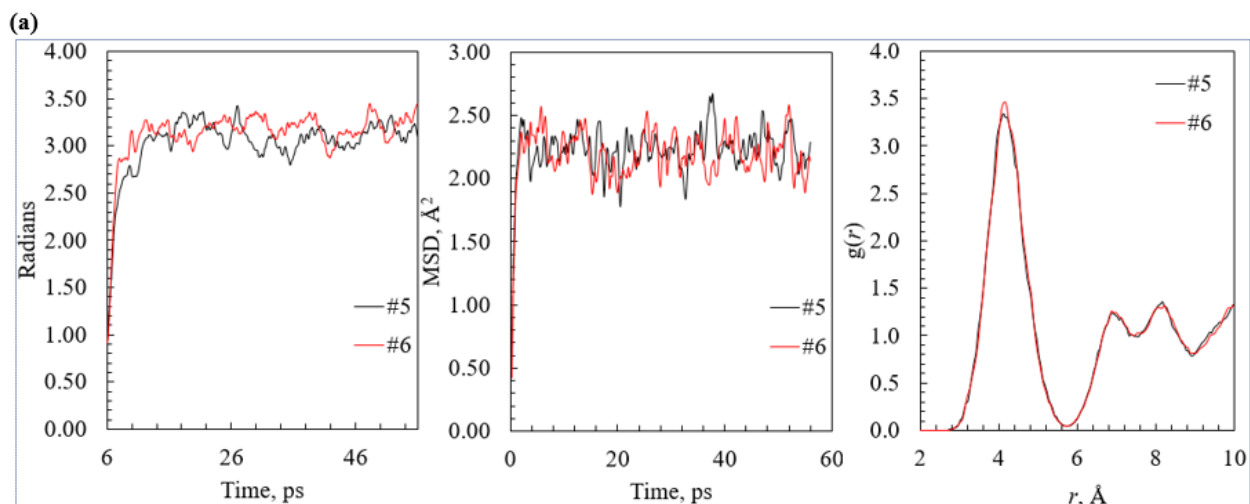


Fig. 6-26 Rotation angle, MSD, and RDF of C_2H_6 molecules in Scenarios #5 (a), #7 (b), #9
 (c), #11 (d)

The influence of pressure on the motion of CO_2 molecules in Scenarios #5 through #12 is shown in Fig. 6-27. It is shown in Fig. 6-27(a) that both the average rotation angle and MSD of CO_2 molecules are similar for the two scenarios. The CO_2 molecules in the hydrate cages get slightly more ordered as pressure increases. In Fig. 6-27(b), both the average rotation angle and MSD grow larger as pressure increases. The RDF curve shifts slightly to a larger C-O distance,

due to the lower occupancy ratio of CO₂ molecules in the small cages at higher pressure, as shown in Fig. 6-6. In Fig. 6-27(c), it is shown that the average rotation angle and MSD get larger when the pressure is elevated. The RDF curve not only becomes broader but also shifts to a larger C-O distance, which means the CO₂ molecules are less ordered in Scenario #10 due to the higher occupancy of CO₂ molecules in the large cages with the increase of pressure. Therefore, the CO₂ molecules move more freely when the pressure is higher in the scenarios where the composition of CH₄, C₂H₆, and CO₂ at 16, 64, and 20 mol%, respectively. In Fig. 6-27(d), it can be observed that with the increase in pressure, the average rotation angle decreases, and the MSD increases. Similar to Scenarios #9 and #10, the RDF curve in Scenario #12 becomes broader and shifted to right due the higher occupancy of CO₂ molecules in the large cages.



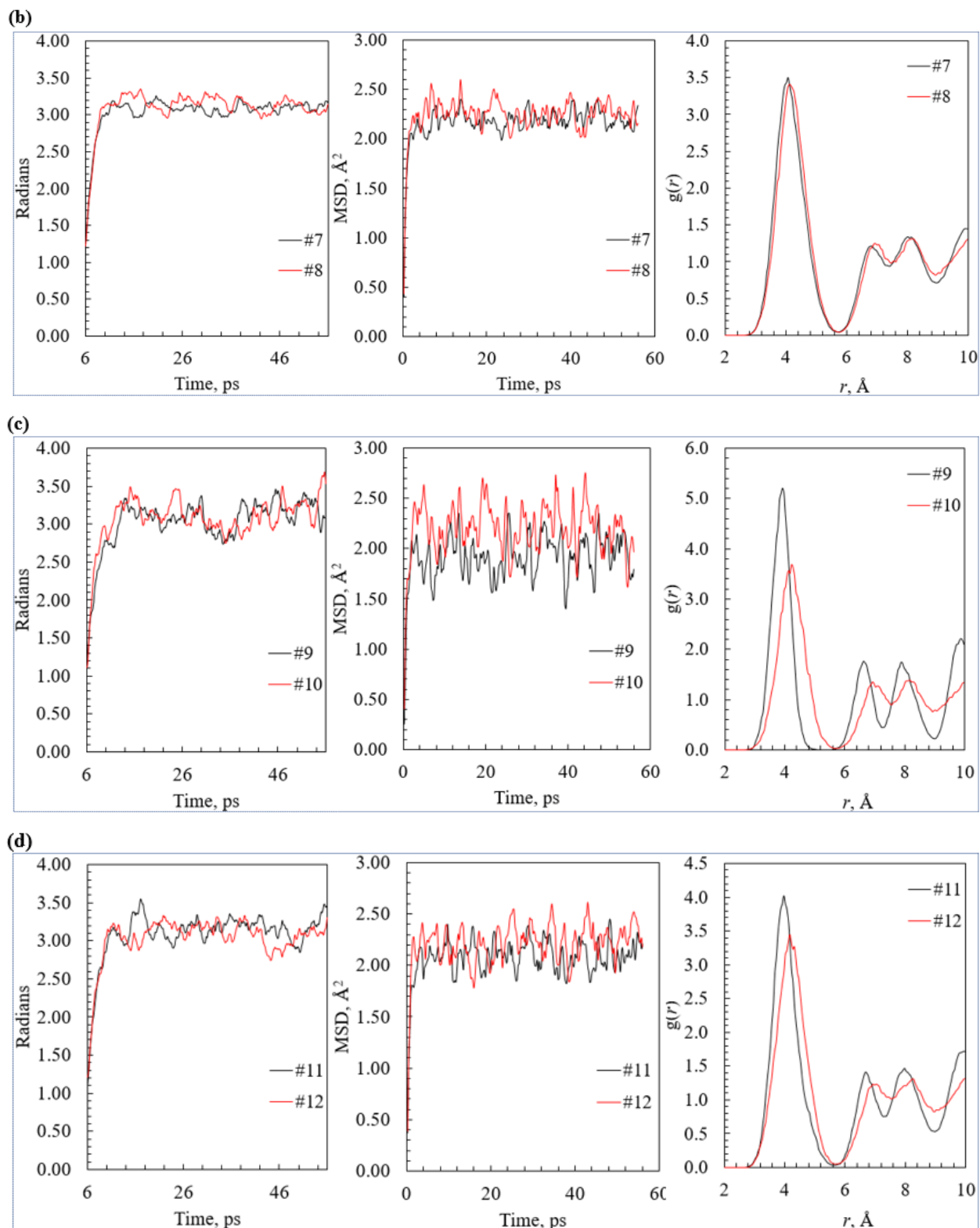


Fig. 6-27 Rotation angle, MSD, and RDF of CO₂ molecules in Scenarios #5 (a), #7 (b), #9
 (c), #11 (d)

6.4 Summary

In this chapter, the MD simulation approach has been adopted to examine the stability of CH₄-C₂H₆ hydrates and the influence of gas composition and pressure on the stability of CH₄-C₂H₆-CO₂ hydrates. The TIP4P-Ew force field is applied for the H₂O molecules, the OPLS-aa model for the CH₄ and C₂H₆ molecules, and a reparameterized potential model for CO₂ molecules. For the simulation models of both the sI and sII structure hydrates, a simulation box containing 3×3×3 unit cells is used and the periodic boundary condition is adopted. A total of twelve scenarios are designed. The first four scenarios are aimed at evaluating the relative stability of CH₄-C₂H₆ hydrates with various gas compositions in the sI and sII hydrates. The rest eight cases are used to examine the effect of gas composition and pressure on the cage stability and motion of gas molecules in the hydrate cage. In each simulation, the cage occupancy of each gas species in the small and large hydrate cages are determined using the theoretical models developed in Chapter 4.

The average rotation angle and MSD of H₂O molecules, as well as the RDF of O-O pairs in the H₂O molecules are applied to evaluate the stability of CH₄-C₂H₆ hydrates with two different gas compositions. It is found that for the simulation using sI structure, the hydrates formed by CH₄-C₂H₆ mixtures with a composition of 20-80 mol% are more stable, i.e., with a smaller MSD, average rotation angle, and more orderly distributed H₂O molecules in the hydrate cages. Whereas in the sII structure, the hydrates formed by CH₄-C₂H₆ with a composition of 90-10 mol% are more stabilized. This conclusion is in consistent with the theoretical calculation and also the experimental observations that at 274.2 K, the sI hydrates is more stable when the CH₄ composition of the CH₄-C₂H₆ mixtures is below 73 mol%, whereas if the CH₄ composition is above 73 mol%, the sII structure hydrates tend to be formed.

For the scenarios of CH₄-C₂H₆-CO₂ hydrates, two CO₂ compositions are designed, i.e., 20 and 50 mol%, which result in stable sI hydrates as indicated by the theoretical models. This is reasonable based on a preliminary observation that the CO₂ molecules prefer the large cages to the small cages. The effect of gas composition is analyzed by comparing Scenarios #5 where the CH₄-C₂H₆ composition ratio is 9:1 and Scenarios #9 where the CH₄-C₂H₆ composition ratio is 1:4. It is observed that the hydrate stability decreases when the CO₂ composition increases. When the composition of CH₄ is higher, i.e., in Scenarios #5, the addition of CO₂ will restrict the motion of CH₄ molecules. However, in Scenarios #9 with a lower CH₄ concentration, the CO₂ has little impact on the motion of CH₄ molecules. On the contrary, the added CO₂ enhances the free motion of C₂H₆ and this effect becomes less significant when the concentration of C₂H₆ is increased due to the stronger competition of C₂H₆ and CO₂ for the larger hydrate cages when the concentration is lower. For the motion of CO₂ itself, its motion is more restricted when more CO₂ is added in Scenarios #5 where the concentration of CH₄ is high. While in Scenarios #9, CO₂ molecules can move more freely as the concentration of CO₂ is increased. The fluctuation frequency of the MSD and the rotation angle curves of the water and gas molecules can be explained by the potential energy between water-water and gas-water pairs.

The impact of pressure on the hydrate cage stability is also evaluated at various gas composition conditions. It is found that the stability of hydrate cages is slightly enhanced with an increase in pressure for the gas compositions in Scenarios #5 and #9, i.e., with a CO₂ concentration of 20 mol%. Whereas for the scenarios with a CO₂ concentration of 50 mol%, the hydrate cages get less stable when the pressure is increased. The impact of pressure on the motion of CH₄ molecules depends on the CH₄ concentration. At high concentrations, the motion of CH₄ molecules is slightly restricted with the increase in pressure. The pressure effect on CH₄ motion becomes

negligible as the concentration of CH₄ decreases. However, the amplitude of the fluctuation in the rotation angle curves is smaller when the CH₄ concentration is higher, due to the interaction between CH₄ and CO₂ molecules. When the C₂H₆ concentration is high, e.g., 64 mol% the impact of pressure is negligible. When the concentration of C₂H₆ is lower, e.g., 40 mol%, the motion of C₂H₆ gets more freely. As the C₂H₆ concentration decreases further, the impact of pressure on the average rotation angle and MSD is negligible, but the fluctuation amplitude of both the rotation angle and MSD curves are larger.

CHAPTER 7 CONCLUSIONS AND RECOMMENDATIONS FOR FUTURE WORK

7.1 Conclusions

The contributions of this work are summarized as follows:

A database of the measured phase boundary of CH₄, C₂H₆, CO₂, and binary CH₄-C₂H₆ and CH₄-CO₂ hydrates formed in the bulk pure H₂O phase and NaCl solutions is established. This new database is significant in providing not only a benchmark to evaluate the reliability of the developed theoretical models, but also a guide for future experimental work on the hydrate phase boundary measurement.

A high-pressure PVT equipment is designed with working pressure up to 70 MPa to measure the phase boundary of gas hydrates. The phase boundary of CH₄-CO₂ hydrates formed in NaCl solutions is measured, with phase boundary pressure up to 61.99 MPa and the temperature to 295.09 K. These data points are significant to fill the blank of the database of CH₄-CO₂ hydrate phase boundary in NaCl solutions under high-pressure and high-temperature conditions, which is practical in industrial applications. The morphology and growth behavior of hydrate film formed at the water-gas interfaces in the PVT cell is also observed.

A review of the reference properties in the theoretical models of hydrate phase boundary is performed and a set of reference properties determined through ab initio calculation is applied in this work. Three theoretical models are developed in this work to predict the phase boundary of gas hydrates. The first model is a standard one using the original PR EoS for the gas-rich phases and the Henry's law combined with the Poynting correction for the gas solubility in the aqueous

phase. In the second model, a single modified PR EoS is applied to calculate the aqueous and gas-rich phases. In these two models, the effect of electrolytes on the hydrate phase boundary is determined by employing the Pitzer model. The first two theoretical models are also termed as separate models because different models are used for non-hydrate phases, i.e., gas-rich phase, aqueous phase, and dissolved electrolytes. In the third model, a unified EoS is proposed to account for these non-hydrate phases, i.e., an mPR EoS is applied to describe the interactions between water, gas, and uncharged ions, a simplified explicit MSA term for the long-range Coulombic forces, and Born terms for the discharging-charging processes. The vdW-P model is applied in all these three models for the hydrate phase.

The MD simulation is applied to explore the stability of CH₄-C₂H₆ hydrates in the sI and sII structures with various gas compositions, i.e., four scenarios with a CH₄ composition of 90 and 20 mol%, respectively. The effect of CO₂ and pressure on the cage stability and motion of gas molecules are also observed for the CH₄-C₂H₆-CO₂ hydrates by using eight scenarios. These observations provide insights into the mechanisms behind the structure change of CH₄-C₂H₆ hydrates and also the change of interactions between gas molecules as the gas composition and pressure change.

The major findings and conclusions of this research can be summarized below:

When the CH₄-CO₂ hydrates are formed in the NaCl solutions, the roughness of the water-gas interface is greatly increased at the initial stage of hydrate formation in the PVT cell due to the appearance of fine pillars. Two hypotheses are proposed to explain the fine pillars formed at the water-gas interface, i.e., the non-equilibrium state of gas and water phases and the non-uniform

lateral growth of hydrates at the interface. However, the water-gas interface becomes smoother with time because of the thickness growth of the hydrate film.

The established database and the measure phase boundary of CH₄-CO₂ hydrates in Chapter 3 are used to evaluate the reliability of the first separate model developed in Chapter 4. The overall AARD of the 984 data points using the first theoretical model is 5.0%. The data points of the binary CH₄-C₂H₆ and CH₄-CO₂ hydrates formed in the pure water and NaCl solution are employed to quantify the reliability of the second model. The overall AARD of the 187 data points of the binary hydrates is 5.2%.

It is observed that the two models can capture the general trend that the phase boundary pressure of CH₄, C₂H₆, CO₂, and binary CH₄-C₂H₆ and CH₄-CO₂ hydrates increase with the temperature and the concentration of NaCl solutions. Also, the phase boundary pressure of the binary CH₄-C₂H₆ and CH₄-CO₂ hydrates increase with the concentration of CH₄ in the feed gas. It is worth noting that the two theoretical models are capable of detecting the sII structure formed by the binary CH₄-C₂H₆ hydrates. The structure of the binary CH₄-C₂H₆ hydrates is influenced not only by the gas composition, but the temperature and temperature as well.

The reliability of the newly developed unified EoS has been evaluated by comparing with 734 measured phase boundary data points of pure and binary CH₄, C₂H₆, and CO₂ hydrates formed in single- and mixed-NaCl, KCl, MgCl₂, and CaCl₂ solutions as well as in the pure water. It is noted that the deviations of predictions for 2-1 electrolyte (i.e., MgCl₂ and CaCl₂) solutions are relatively large than that for the 1-1 electrolyte (NaCl and KCl) solutions. The overall AARD of these 734 data points predicted by this newly developed model is 3.4%, which proves the capability of the newly developed model in predicting the phase boundary of hydrates in multi-component systems.

The average rotation angle, MSD, and RDF of H₂O molecules are applied to evaluate the stability of CH₄-C₂H₆ hydrates in sI and sII structure hydrates. It is found that for the simulation using sI structure, the hydrates formed by CH₄-C₂H₆ mixtures with a composition of 20-80 mol% are more stable than those with a CH₄-C₂H₆ composition of 90-10 mol%. Whereas in the sII structure, the hydrates formed by CH₄-C₂H₆ with a composition of 90-10 mol% are more stabilized. This conclusion is consistent with the theoretical calculation and also the experimental observations.

Scenarios with two CO₂ compositions are designed, i.e., 20 and 50 mol%, which result in stable sI structure CH₄-C₂H₆-CO₂ hydrates as indicated by the theoretical models. This is reasonable based on a preliminary observation that the CO₂ molecules prefer the large cages to the small cages. It is observed that the hydrate stability decreases when the CO₂ composition increases. When the composition of CH₄ is higher than C₂H₆, the addition of CO₂ will restrict the motion of CH₄ molecules. However, in scenarios with a lower CH₄ concentration, the CO₂ has little impact on the motion of CH₄ molecules. On the contrary, the added CO₂ enhances the free motion of C₂H₆ and this effect becomes less significant when the concentration of C₂H₆ is increased due to the stronger competition of C₂H₆ for the larger hydrate cages when the concentration is lower. The motion of CO₂ is slightly restricted when more CO₂ is added in scenarios with a higher concentration of CH₄. In scenarios with a lower concentration of CH₄, CO₂ molecules can move more freely as the concentration of CO₂ is increased. The fluctuation frequency of the MSD and the rotation angle curves of the water and gas molecules can be explained by the potential energy between water-water and gas-water pairs.

The stability of hydrate cages is slightly enhanced as the pressure increases in scenarios with a CO₂ concentration of 20 mol%. Whereas for the scenarios with a CO₂ concentration of 50 mol%,

the hydrate cages get less stable when the pressure is elevated. The impact of pressure on the motion of CH₄ molecules depends on the CH₄ concentration. At high concentrations, the motion of CH₄ molecules is slightly restricted with the increase in pressure. The pressure effect on CH₄ motion becomes negligible as the concentration of CH₄ decreases. However, the amplitude of the fluctuation in the rotation angle curves is smaller when the CH₄ concentration is higher, due to the interaction between CH₄ and CO₂ molecules. When the C₂H₆ concentration is high, e.g., 64 mol% the impact of pressure is negligible. When the concentration of C₂H₆ is lower, e.g., 40 mol%, the motion of C₂H₆ gets more freely. As the C₂H₆ concentration decreases further, the impact of pressure on the average rotation angle and MSD is negligible, but the fluctuation amplitude of both the rotation angle and MSD curves are larger. Similarly, the effect of pressure on CO₂ also depends on the gas composition. In scenarios with a CO₂ concentration of 20 mol%, the motion of CO₂ molecules is slightly restricted when the CH₄-C₂H₆ concentration ratio is 9:1, whereas CO₂ moves more freely when the CH₄-C₂H₆ concentration ratio is 2:8.

7.2 Recommendations for Future Work

Based on the collected database, more experimental phase boundary data points of the binary CH₄-C₂H₆ hydrates and the ternary CH₄-C₂H₆-CO₂ hydrates formed in electrolyte solutions are needed. For example, only two groups of phase boundary data points of the binary CH₄-C₂H₆ hydrates formed in NaCl solutions are available in the literature, with the CH₄ concentration of 74.7 mol% as shown in Table 3-4. This gas composition is very close to the structure change point. Hence, the data points of the binary CH₄-C₂H₆ hydrates with a composition away from the structure change point are necessary for us to better understand the stability mechanisms of the CH₄-C₂H₆ hydrates in the presence of ions. As for the ternary CH₄-C₂H₆-CO₂ hydrates, the phase boundary

data points are scarce not only for those formed in electrolyte solutions but also in pure water. The measured phase boundary data points of the ternary $\text{CH}_4\text{-C}_2\text{H}_6\text{-CO}_2$ hydrates will provide us a macroscopic perspective to investigate the interactions among the gas, water, and ions, e.g., the competing effect of CO_2 for the small and large cages with the CH_4 and C_2H_6 hydrate, respectively.

The morphology of gas hydrates is essential to analyze the interfacial phenomena of hydrate particles. Apart from the electrolytes, e.g., NaCl adopted in this work, many chemical additives will have a significant impact on the nucleation and growth of gas hydrates, which further determine the morphology of the surface of hydrate particles. The potential candidates of those chemical additives include the hydrate inhibitors, e.g., PVCap and hydrate promoters, e.g., SDS and THF . Also, the observations of hydrate morphology at different scales and dynamic conditions are also very important.

The reference properties in the theoretical models of hydrate phase boundary need further investigation. It is illustrated that the new reference properties applied in this work are different from those in the literature but the models developed are still capable of predicting the hydrate phase boundary within reasonable deviation if the Kihara parameters are optimized accordingly. However, the effect of reference properties on the microscopic properties, e.g., cage occupancy of gas molecules in the hydrate cages is not clear, which is significant to provide a consistent modeling framework of hydrate phase behavior at various pressure and gas composition conditions.

MD simulation is an effective tool to analyze the stability of gas hydrates at various gas composition and pressure conditions. The temperature is crucial for the rotational, vibrational, and translational motion of gas and water molecules. The stability of $\text{CH}_4\text{-C}_2\text{H}_6$ and $\text{CH}_4\text{-C}_2\text{H}_6\text{-CO}_2$ hydrates at a higher temperature, i.e., higher than 274.2 K should be investigated. Also, the gas

and water molecules in this work are modeled as fixed rigid molecules. The vibrational motion of the gas and water molecules on the hydrate stability may be included in future work. Also, the kinetic effect of hydrate nucleation on the structure stability of CH₄-C₂H₆ and CH₄-C₂H₆-CO₂ hydrates should be investigated.

REFERENCES

- Aasen, A., Hammer, M., Skaugen, G., Jakobsen, J.P., and Wilhelmsen, Ø. Thermodynamic models to accurately describe the PVT_{xy}-behavior of water/carbon dioxide mixtures. *Fluid Phase Equilibria*. 2017, 442, 125-139.
- Adamova, T.P., Subbotin, O.S., Pomeransky, A.A., and Belosludov, V.R. Modeling of phase transition sI- sII in binary gas hydrates of methane and ethane in dependence on composition of gas phase. *Computational Materials Science*., 2010, 49, 4, S317-S321.
- Adisasmito, S., Frank, III R.J., and Sloan, E.D. Hydrates of carbon dioxide and methane mixtures. *Journal of Chemical & Engineering Data*. 1991, 36, 1, 68-71.
- Adisasmito, S. and Sloan, E.D. Hydrates of hydrocarbon gases containing carbon dioxide. *Journal of Chemical & Engineering Data*. 1992, 37, 3, 343-349.
- Ahmed, S., Ferrando, N., de Hemptinne, J.C., Simonin, J.P., Bernard, O., and Baudouin, O. Modeling of mixed-solvent electrolyte systems. *Fluid Phase Equilibria*. 2018, 459, 138-157.
- Aman, Z.M., Dieker, L.E., Aspenes, G., Sum, A.K., Sloan, E.D., and Koh, C.A. Influence of model oil with surfactants and amphiphilic polymers on cyclopentane hydrate adhesion forces. *Energy & Fuels*. 2010, 24, 10, 5441-5445.
- Aman, Z.M., Joshi, S.E., Sloan, E.D., Sum, A.K., and Koh, C.A. Micromechanical cohesion force measurements to determine cyclopentane hydrate interfacial properties. *Journal of Colloid and Interface Science*. 2012, 376, 1, 283-288.
- Aman, Z.M. and Koh, C.A. Interfacial phenomena in gas hydrate systems. *Chemical Society Reviews*. 2016, 45, 6, 1678-1690.

- Anderson, B. Molecular modeling of hydrate-clathrates via ab initio, cell potential, and dynamic methods. Ph.D. Thesis, Department of Chemical Engineering, Massachusetts Institute of Technology, USA, 2005.
- Anderson, B., Boswell, R., Collett, T.S., Farrell, H., Ohtsuki, S., White, M., and Zyrianova, M. Review of the findings of the ignik Sikumi CO₂-CH₄ gas hydrate exchange field trial. In Proceedings of the 8th international conference on gas hydrates (ICGH8), 17, 2014.
- Atik, Z., Windmeier, C. and Oellrich, L.R. Experimental gas hydrate dissociation pressures for pure methane in aqueous solutions of MgCl₂ and CaCl₂ and for a (methane+ ethane) gas mixture in an aqueous solution of (NaCl+ MgCl₂). Journal of Chemical & Engineering Data. 2006, 51, 5, 1862-1867.
- Atik, Z., Windmeier, C., and Oellrich, L.R. Experimental and theoretical study on gas hydrate phase equilibria in seawater. Journal of Chemical & Engineering Data. 2010, 55, 2, 804-807.
- Avlonitis, D. The determination of Kihara potential parameters from gas hydrate data. Chemical Engineering Science. 1994, 49, 8, 1161-1173.
- Babu, P., Nambiar, A., He, T., Karimi, I.A., Lee, J.D., Englezos, P., and Linga, P. A review of clathrate hydrate based desalination to strengthen energy-water nexus. ACS Sustainable Chemistry & Engineering. 2018, 6, 7, 8093-8107.
- Ballard, A.L. and Sloan, E.D. Structural transitions in methane+ ethane gas hydrates—Part II: Modeling beyond incipient conditions. Chemical Engineering Science. 2000, 55, 23, 5773-5782.
- Ballard, A.L. and Sloan, E.D. The next generation of hydrate prediction: I. Hydrate standard states and incorporation of spectroscopy. Fluid Phase Equilibria. 2002, 194, 371-383.

- Barnes, B.C. and Sum, A.K. Advances in molecular simulations of clathrate hydrates. *Current Opinion in Chemical Engineering*. 2013, 2, 2, 184-190.
- Becke, P., Kessel, D., and Rahimian, I. Influence of liquid hydrocarbons on gas hydrate equilibrium. In *European Petroleum Conference*. Society of Petroleum Engineers. 1992.
- Belandria, V., Mohammadi, A.H., and Richon, D. Phase equilibria of clathrate hydrates of methane+ carbon dioxide: New experimental data and predictions. *Fluid Phase Equilibria*. 2010, 296, 1, 60-65.
- Beltrán, J.G. and Servio, P. Equilibrium studies for the system methane+ carbon dioxide+ neohexane+ water. *Journal of Chemical & Engineering Data*. 2008, 53, 8, 1745-1749.
- Bi, Y., Yang, T., and Guo, K. Determination of the upper-quadruple-phase equilibrium region for carbon dioxide and methane mixed gas hydrates. *Journal of Petroleum Science and Engineering*. 2013, 101, 62-67.
- Bishnoi, P.R. and Natarajan, V. Formation and decomposition of gas hydrates. *Fluid Phase Equilibria*. 1996, 117, 1-2, 168-177.
- Boswell, R., Schoderbek, D., Collett, T.S., Ohtsuki, S., White, M., and Anderson, B.J. The Ignik Sikumi field experiment, Alaska North Slope: Design, operations, and implications for CO₂-CH₄ exchange in gas hydrate reservoirs. *Energy & Fuels*. 2016, 31, 1, 140-153.
- Braeuer, A., Hankel, R.F., Mehnert, M.K., Schuster, J.J., and Will, S. A Raman technique applicable for the analysis of the working principle of promoters and inhibitors of gas hydrate formation. *Journal of Raman Spectroscopy*. 2015, 46, 11, 1145-1149.
- Brooks, J.M., Cox, H.B., Bryant, W.R., Kennicutt II, M.C., Mann, R.G., and McDonald, T.J. Association of gas hydrates and oil seepage in the Gulf of Mexico. *Organic Geochemistry*. 1986, 10, 1-3, 221-234.

- Burshears, M., O'brien, T.J., and Malone, R.D, January. A multi-phase, multi-dimensional, variable composition simulation of gas production from a conventional gas reservoir in contact with hydrates. In SPE Unconventional Gas Technology Symposium. Society of Petroleum Engineers, 1986.
- Cai, J., Tao, Y.Q., von Solms, N., Xu, C.G., Chen, Z.Y., and Li, X.S. Experimental studies on hydrogen hydrate with tetrahydrofuran by differential scanning calorimeter and in-situ Raman. *Applied Energy*. 2019, 243, 1-9.
- Cai, J., Xia, Y., Lu, C., Bian, H., and Zou, S. Creeping microstructure and fractal permeability model of natural gas hydrate reservoir. *Marine and Petroleum Geology*. 2020, 115, 104282.
- Cao, Z. Modeling of gas hydrates from first principles. Ph.D. Thesis, Department of Chemical Engineering, Massachusetts Institute of Technology, USA, 2002.
- Cao, Z., Tester, J.W., and Trout, B.L. Sensitivity analysis of hydrate thermodynamic reference properties using experimental data and ab initio methods. *The Journal of Physical Chemistry B*. 2002, 106, 31, 7681-7687.
- Castellini, D.G., Dickens, G.R., Snyder, G.T., and Ruppel, C.D. Barium cycling in shallow sediment above active mud volcanoes in the Gulf of Mexico. *Chemical Geology*. 2006, 226, 1-2, 1-30.
- Cha, M., Hu, Y., and Sum, A.K. Methane hydrate phase equilibria for systems containing NaCl, KCl, and NH₄Cl. *Fluid Phase Equilibria*. 2016, 413, 2-9.
- Chapoy, A., Burgass, R., Tohidi, B., Austell, J.M., and Eickhoff, C. Effect of common impurities on the phase behavior of carbon-dioxide-rich systems: Minimizing the risk of hydrate formation and two-phase flow. *SPE Journal*. 2011, 16, 4, 921-930.

- Chapoy, A., Burgass, R., Tohidi, B., and Alsiyabi, I. Hydrate and phase behavior modeling in CO₂-rich pipelines. *Journal of Chemical & Engineering Data*. 2014, 60, 2, 447-453.
- Chialvo, A.A., Houssa, M., and Cummings, P.T. Molecular dynamics study of the structure and thermophysical properties of model sI clathrate hydrates. *The Journal of Physical Chemistry B*. 2002, 106, 2, 442-451.
- Chen, G.J. and Guo, T.M. Thermodynamic modeling of hydrate formation based on new concepts. *Fluid Phase Equilibria*. 1996, 122, 1-2, 43-65.
- Chen, L.T., Li, N., Sun, C.Y., Chen, G.J., Koh, C.A., and Sun, B.J. Hydrate formation in sediments from free gas using a one-dimensional visual simulator. *Fuel*. 2017, 197, 298-309.
- Child, W.C. Thermodynamic functions for metastable ice structures I and II. *The Journal of Physical Chemistry*. 1964, 68, 7, 1834-1838.
- Chong, Z.R., Yang, S.H.B., Babu, P., Linga, P., and Li, X.S. Review of natural gas hydrates as an energy resource: Prospects and challenges. *Applied Energy*. 2016, 162, 1633-1652.
- Chou, I.M., Sharma, A., Burruss, R.C., Shu, J., Mao, H.K., Hemley, R.J., Goncharov, A.F., Stern, L.A., and Kirby, S.H. Transformations in methane hydrates. *Proceedings of the National Academy of Sciences*. 2000, 97, 25, 13484-13487.
- Cladek, B.R., Everett, S.M., McDonnell, M.T., Tucker, M.G., Keffer, D.J., and Rawn, C.J. Guest–host interactions in mixed CH₄-CO₂ hydrates: Insights from molecular dynamics simulations. *The Journal of Physical Chemistry C*. 2018, 122, 34, 19575-19583.
- Cladek, B.R., Everett, S.M., McDonnell, M.T., Tucker, M.G., Keffer, D.J., and Rawn, C.J. Molecular rotational dynamics in mixed CH₄-CO₂ hydrates: Insights from molecular dynamics simulations. *The Journal of Physical Chemistry C*. 2019, 123, 43, 26251-26262.

- Clarke, M.A. and Bishnoi, P.R. Development of an implicit least squares optimisation scheme for the determination of Kihara potential parameters using gas hydrate equilibrium data. *Fluid Phase Equilibria*. 2003, 211, 1, 51-60.
- Clerc, M. and Kennedy, J. The particle swarm-explosion, stability, and convergence in a multidimensional complex space. *IEEE transactions on Evolutionary Computation*. 2002, 6, 1, 58-73.
- Collett, T.S., Bird, K.J., Kvenvolden, K.A., and Magoon, L.B. Geologic interrelations relative to gas hydrates within the North Slope of Alaska (NO. 88-389). US Geological Survey, 1988.
- Colwell, F., Matsumoto, R., and Reed, D. A review of the gas hydrates, geology, and biology of the Nankai Trough. *Chemical Geology*. 2004, 205, 3-4, 391-404.
- Conde, M.M. and Vega, C. Determining the three-phase coexistence line in methane hydrates using computer simulations. *The Journal of Chemical Physics*. 2010, 133, 6, 064507.
- Courtial, X., Ferrando, N., de Hemptinne, J.C., and Mougín, P. Electrolyte CPA equation of state for very high temperature and pressure reservoir and basin applications. *Geochimica et Cosmochimica Acta*. 2014, 142, 1-14.
- De Menezes, D.É.S., Sum, A.K., Desmedt, A., de Alcântara Pessôa Filho, P., and Fuentes, M.D.R. Coexistence of sI and sII in methane-propane hydrate former systems at high pressures. *Chemical Engineering Science*. 2019, 208, 115149.
- De Roo, J.L., Peters, C.J., Lichtenthaler, R.N., and Diepen, G.A. Occurrence of methane hydrate in saturated and unsaturated solutions of sodium chloride and water in dependence of temperature and pressure. *AIChE Journal*. 1983, 29, 4, 651-657.
- Deaton, W.M. and Frost, E.M. Gas hydrates and their relation to the operation of natural gas pipe lines. US Bureau of Mines Monograph 8, 1946.

- Debenedetti, P.G. and Sarupria, S. Hydrate molecular ballet. *Science*. 2009, 326, 5956, 1070-1071.
- Dec, S.F., Bowler, K.E., Stadterman, L.L., Koh, C.A., and Sloan, E.D. NMR study of methane+ethane structure I hydrate decomposition. *The Journal of Physical Chemistry A*. 2007, 111, 20, 4297-4303.
- Dharmawardhana, P.B., Parrish, W.R., and Sloan, E.D. Experimental thermodynamic parameters for the prediction of natural gas hydrate dissociation conditions. *Industrial & Engineering Chemistry Fundamentals*. 1980, 19, 4, 410-414.
- Dholabhai, P.D., Englezos, P., Kalogerakis, N., and Bishnoi, P.R. Equilibrium conditions for methane hydrate formation in aqueous mixed electrolyte solutions. *The Canadian Journal of Chemical Engineering*. 1991, 69, 3, 800-805.
- Dholabhai, P.D., Kalogerakis, N., and Bishnoi, P.R. Equilibrium conditions for carbon dioxide hydrate formation in aqueous electrolyte solutions. *Journal of Chemical & Engineering Data*. 1993, 38, 4, 650-654.
- Dholabhai, P.D. and Bishnoi, P.R. Hydrate equilibrium conditions in aqueous electrolyte solutions: mixtures of methane and carbon dioxide. *Journal of Chemical & Engineering Data*. 1994, 39, 1, 191-194.
- Ding, L.Y., Geng, C.Y., Zhao, Y.H., and Wen, H. Molecular dynamics simulation on the dissociation process of methane hydrates. *Molecular Simulation*. 2007, 33, 12, 1005-1016.
- Duan, Z. and Zhang, Z. Equation of state of the H₂O, CO₂, and H₂O-CO₂ systems up to 10 GPa and 2573.15 K: Molecular dynamics simulations with ab initio potential surface. *Geochimica Et Cosmochimica Acta*. 2006, 70, 9, 2311-2324.
- Dyadin, Y.A., Aladko, E.Y., and Larionov, E.G. Decomposition of methane hydrates up to 15 kbar. *Mendeleev Communications*. 1997, 7, 1, 34-35.

- Englezos, P. Computation of the incipient equilibrium carbon dioxide hydrate formation conditions in aqueous electrolyte solutions. *Industrial & Engineering Chemistry Research*. 1992, 31, 9, 2232-2237.
- Englezos, P. and Bishnoi, P.R. Experimental study on the equilibrium ethane hydrate formation conditions in aqueous electrolyte solutions. *Industrial & Engineering Chemistry Research*. 1991, 30, 7, 1655-1659.
- Englezos, P. and Bishnoi, P.R. Prediction of gas hydrate formation conditions in aqueous electrolyte solutions. *AIChE Journal*. 1988, 34, 10, 1718-1721.
- English, N.J. and MacElroy, J.M.D. Structural and dynamical properties of methane clathrate hydrates. *Journal of Computational Chemistry*. 2003, 24, 13, 1569-1581.
- Erfan-Niya, H., Modarress, H., and Zaminpayma, E. Molecular dynamics study on the structure I clathrate-hydrate of methane+ ethane mixture. *Energy Conversion and Management*. 2011, 52, 1, 523-531.
- Fan, S.S. and Guo, T.M. Hydrate formation of CO₂-rich binary and quaternary gas mixtures in aqueous sodium chloride solutions. *Journal of Chemical & Engineering Data*. 1999, 44, 4, 829-832.
- Fan, S.S., Chen, G.J., Ma, Q.L., and Guo, T.M. Experimental and modeling studies on the hydrate formation of CO₂ and CO₂-rich gas mixtures. *Chemical Engineering Journal*. 2000, 78, 2-3, 173-178.
- Fan, S.S., Liang, D.Q., and Guo, K.H. Hydrate equilibrium conditions for cyclopentane and a quaternary cyclopentane-rich mixture. *Journal of Chemical & Engineering Data*. 2001, 46, 4, 930-932.

- Fleyfel, F. and Devlin, J.P. Carbon dioxide clathrate hydrate epitaxial growth: Spectroscopic evidence for formation of the simple type-II carbon dioxide hydrate. *The Journal of Physical Chemistry*. 1991, 95, 9, 3811-3815.
- Freer, E.M., Selim, M.S., and Sloan, E.D. Methane hydrate film growth kinetics. *Fluid Phase Equilibria*. 2001, 185, 1-2, 65-75.
- Fu, B. and Aharon, P. Sources of hydrocarbon-rich fluids advecting on the seafloor in the northern Gulf of Mexico. *Gulf Coast Association of Geological Societies Transactions*. 1998, 48, 1, 73-81.
- Fu, X., Cueto-Felgueroso, L., and Juanes, R. Nonequilibrium thermodynamics of hydrate growth on a gas-liquid interface. *Physical Review Letters*. 2018, 120, 14, 144501-1-6.
- Fürst, W. and Renon, H. Representation of excess properties of electrolyte solutions using a new equation of state. *AIChE Journal*. 1993, 39, 2, 335-343.
- Galloway, T.J., Ruska, W., Chappellear, P.S., and Kobayashi, R. Experimental measurement of hydrate numbers for methane and ethane and comparison with theoretical values. *Industrial & Engineering Chemistry Fundamentals*. 1970, 9, 2, 237-243.
- Gambelli, A.M., Castellani, B., Nicolini, A., and Rossi, F. Gas hydrate formation as a strategy for CH₄/CO₂ separation: Experimental study on gaseous mixtures produced via Sabatier reaction. *Journal of Natural Gas Science and Engineering*. 2019, 71, 102985.
- Geng, C.Y., Wen, H., and Zhou, H. Molecular simulation of the potential of methane reoccupation during the replacement of methane hydrate by CO₂. *The Journal of Physical Chemistry A*. 2009, 113, 18, 5463-5469.
- Goel, N. In situ methane hydrate dissociation with carbon dioxide sequestration: Current knowledge and issues. *Journal of Petroleum Science and Engineering*. 2006, 51, 3-4, 169-184.

- Guo, G.J., Zhang, Y.G., and Liu, H. Effect of methane adsorption on the lifetime of a dodecahedral water cluster immersed in liquid water: A molecular dynamics study on the hydrate nucleation mechanisms. *The Journal of Physical Chemistry C*. 2007, 111, 6, 2595-2606.
- Guo, G.J., Li, M., Zhang, Y.G., and Wu, C.H. Why can water cages adsorb aqueous methane? A potential of mean force calculation on hydrate nucleation mechanisms. *Physical Chemistry Chemical Physics*. 2009, 11, 44, 10427-10437.
- Guo, G.J., Zhang, Y.G., Liu, C.J., and Li, K.H. Using the face-saturated incomplete cage analysis to quantify the cage compositions and cage linking structures of amorphous phase hydrates. *Physical Chemistry Chemical Physics*. 2011, 13, 25, 12048-12057.
- Gupta, A., Dec, S.F., Koh, C.A., and Sloan, E.D. NMR investigation of methane hydrate dissociation. *The Journal of Physical Chemistry C*. 2007, 111, 5, 2341-2346.
- Haghighi, H., Chapoy, A., and Tohidi, B. Methane and water phase equilibria in the presence of single and mixed electrolyte solutions using the cubic-plus-association equation of state. *Oil & Gas Science and Technology-Revue de l'IFP*. 2009, 64, 2, 141-54.
- Haghtalab, A. and Mazloumi, S.H. Electrolyte cubic square-well equation of state for computation of the solubility CO₂ and H₂S in aqueous MDEA solutions. *Industrial & Engineering Chemistry Research*. 2010, 49, 13, 6221-6230.
- Hammerschmidt, E.G. Formation of gas hydrates in natural gas transmission lines. *Industrial & Engineering Chemistry*. 1934, 26, 8, 851-855.
- Handa, Y.P. and Tse, J.S. Thermodynamic properties of empty lattices of structure I and structure II clathrate hydrates. *The Journal of Physical Chemistry*. 1986, 90, 22, 5917-5921.
- Haugen, K.B., Firoozabadi, A., and Sun, L. Efficient and robust three-phase split computations. *AIChE Journal*. 2011, 57, 9, 2555-2565.

- He, Z., Gupta, K.M., Linga, P., and Jiang, J. Molecular insights into the nucleation and growth of CH₄ and CO₂ mixed hydrates from microsecond simulations. *The Journal of Physical Chemistry C*. 2016, 120, 44, 25225-25236.
- Hendriks, E.M., Edmonds, B., Moorwood, R.A.S., and Szczepanski, R. Hydrate structure stability in simple and mixed hydrates. *Fluid Phase Equilibria*. 1996, 117, 1-2, 193-200.
- Hester, K.C. and Sloan, E.D. sII structural transitions from binary mixtures of simple sI formers. *International Journal of Thermophysics*. 2005, 26, 1, 95-106.
- Hirai, H., Kondo, T., Hasegawa, M., Yagi, T., Yamamoto, Y., Komai, T., Nagashima, K., Sakashita, M., Fujihisa, H., and Aoki, K. Methane hydrate behavior under high pressure. *The Journal of Physical Chemistry B*. 2000, 104, 7, 1429-1433.
- Holder, G.D. and Grigoriou, G.C. Hydrate dissociation pressures of (methane+ ethane+ water) existence of a locus of minimum pressures. *The Journal of Chemical Thermodynamics*. 1980, 12, 11, 1093-1104.
- Holder, G.D., Corbin, G., and Papadopoulos, K.D. Thermodynamic and molecular properties of gas hydrates from mixtures containing methane, argon, and krypton. *Industrial & Engineering Chemistry Fundamentals*. 1980, 19, 3, 282-286.
- Holder, G.D. and Hand, J.H. Multiple-phase equilibria in hydrates from methane, ethane, propane and water mixtures. *AIChE Journal*. 1982, 28, 3, 440-447.
- Holder, G.D., Malekar, S.T., and Sloan, E.D. Determination of hydrate thermodynamic reference properties from experimental hydrate composition data. *Industrial & Engineering Chemistry Fundamentals*. 1984, 23, 1, 123-126.
- Holder, G.D., Zetts, S.P., and Pradhan, N. Phase behavior in systems containing clathrate hydrates: A review. *Reviews in Chemical Engineering*. 1988, 5, 1-4, 1-70.

- Horn, H.W., Swope, W.C., Pitner, J.W., Madura, J.D., Dick, T.J., Hura, G.L. and Head-Gordon, T. Development of an improved four-site water model for biomolecular simulations: TIP4P-Ew. *The Journal of Chemical Physics*. 2004, 120, 20, 9665-9678.
- Hu, Y., Makogon, T.Y., Karanjkar, P., Lee, K.H., Lee, B.R., and Sum, A.K. Gas hydrates phase equilibria and formation from high concentration NaCl brines up to 200 MPa. *Journal of Chemical & Engineering Data*. 2017, 62, 6, 1910-1918.
- Hu, Y., Makogon, T.Y., Karanjkar, P., Lee, K.H., Lee, B.R., and Sum, A.K. Gas hydrates phase equilibria for structure I and II hydrates with chloride salts at high salt concentrations and up to 200 MPa. *The Journal of Chemical Thermodynamics*. 2018, 117, 27-32.
- Humphrey, W., Dalke, A., and Schulten, K. VMD: visual molecular dynamics. *Journal of Molecular Graphics*. 1996, 14, 1, 33-38.
- Inchekel, R., de Hemptinne, J.C., and Fürst, W. The simultaneous representation of dielectric constant, volume and activity coefficients using an electrolyte equation of state. *Fluid Phase Equilibria*. 2008, 271, 1-2, 19-27.
- Inkong, K., Veluswamy, H.P., Rangsunvigit, P., Kulprathipanja, S., and Linga, P. Innovative approach to enhance the methane hydrate formation at near-ambient temperature and moderate pressure for gas storage applications. *Industrial & Engineering Chemistry Research*. 2019, 58, 49, 22178-22192.
- Jager, M.D. and Sloan, E.D. The effect of pressure on methane hydration in pure water and sodium chloride solutions. *Fluid Phase Equilibria*. 2001, 185, 1-2, 89-99.
- Jager, M.D., Ballard, A.L., and Sloan, E.D. The next generation of hydrate prediction: II. Dedicated aqueous phase fugacity model for hydrate prediction. *Fluid Phase Equilibria*. 2003, 211, 1, 85-107.

- Jhaveri, J. and Robinson, D.B. Hydrates in the methane - nitrogen system. *The Canadian Journal of Chemical Engineering*. 1965, 43, 2, 75-78.
- Jia, B., Tsau, J.S., and Barati, R. Role of molecular diffusion in heterogeneous, naturally fractured shale reservoirs during CO₂ huff-n-puff. *Journal of Petroleum Science and Engineering*. 2018, 164, 31-42.
- Jia, B., Tsau, J.S., and Barati, R. A review of the current progress of CO₂ injection EOR and carbon storage in shale oil reservoirs. *Fuel*. 2019a, 236, 404-427.
- Jia, B., Tsau, J.S., and Barati, R. Measurement of CO₂ diffusion coefficient in the oil-saturated porous media. *Journal of Petroleum Science and Engineering*. 2019b, 181, 106189.
- Jin, G. and Donohue, M.D. An equation of state for electrolyte solutions. 1. Aqueous systems containing strong electrolytes. *Industrial & Engineering Chemistry Research*. 1988, 27, 6, 1073-1084.
- Jin, D. and Coasne, B. Molecular simulation of the phase diagram of methane hydrate: free energy calculations, direct coexistence method, and hyperparallel tempering. *Langmuir*. 2017, 33, 42, 11217-11230.
- John, V.T., Papadopoulos, K.D., and Holder, G.D. A generalized model for predicting equilibrium conditions for gas hydrates. *AIChE Journal*. 1985, 31, 2, 252-259.
- Jorgensen, W.L., Chandrasekhar, J., Madura, J.D., Impey, R.W., and Klein, M.L. Comparison of simple potential functions for simulating liquid water. *The Journal of Chemical Physics*. 1983, 79, 2, 926-935.
- Kamari, A., Hashemi, H., Babaei, S., Mohammadi, A.H., and Ramjugernath, D. Phase stability conditions of carbon dioxide and methane clathrate hydrates in the presence of KBr, CaBr₂,

- MgCl₂, HCOONa, and HCOOK aqueous solutions: Experimental measurements and thermodynamic modelling. *The Journal of Chemical Thermodynamics*. 2017, 115, 307-317.
- Kaminski, G., Duffy, E.M., Matsui, T., and Jorgensen, W.L. Free energies of hydration and pure liquid properties of hydrocarbons from the OPLS all-atom model. *The Journal of Physical Chemistry*. 1994, 98, 49, 13077-13082.
- Kang, S.P., Chun, M.K., and Lee, H. Phase equilibria of methane and carbon dioxide hydrates in the aqueous MgCl₂ solutions. *Fluid Phase Equilibria*. 1998, 147, 1-2, 229-238.
- Kang, S.P., Lee, H., and Ryu, B.J. Enthalpies of dissociation of clathrate hydrates of carbon dioxide, nitrogen, (carbon dioxide+ nitrogen), and (carbon dioxide+ nitrogen+ tetrahydrofuran). *The Journal of Chemical Thermodynamics*. 2001, 33, 5, 513-521.
- Kastanidis, P., Romanos, G.E., Michalis, V.K., Economou, I.G., Stubos, A.K., and Tsimpanogiannis, I.N. Development of a novel experimental apparatus for hydrate equilibrium measurements. *Fluid Phase Equilibria*. 2016, 424, 152-161.
- Kastanidis, P., Romanos, G.E., Stubos, A.K., Economou, I.G., and Tsimpanogiannis, I.N. Two- and three-phase equilibrium experimental measurements for the ternary CH₄+ CO₂+ H₂O mixture. *Fluid Phase Equilibria*. 2017, 451, 96-105.
- Kastanidis, P., Tsimpanogiannis, I.N., Romanos, G.E., Stubos, A.K., and Economou, I.G. Recent advances in experimental measurements of mixed-gas three-phase hydrate equilibria for gas mixture separation and energy-related applications. *Journal of Chemical & Engineering Data*. 2019, 64, 12, 4991-5016.
- Kastner, M., Claypool, G., and Robertson, G. Geochemical constraints on the origin of the pore fluids and gas hydrate distribution at Atwater Valley and Keathley Canyon, northern Gulf of Mexico. *Marine and Petroleum Geology*. 2008, 25, 9, 860-872.

Katz, D.L. Prediction of conditions for hydrate formation in natural gases. Transactions of the AIME. 1945, 160, 1, 140-149.

Kennett, J.P., Cannariato, K.G., Hendy, I.L., and Behl, R.J. Methane hydrates in quaternary climate change: The clathrate gun hypothesis. American Geophysical Union, 2003.

Khan, M.N., Warriar, P., Peters, C.J., and Koh, C.A. Review of vapor-liquid equilibria of gas hydrate formers and phase equilibria of hydrates. Journal of Natural Gas Science and Engineering. 2016, 35, 1388-1404.

Kharrat, M. and Dalmazzone, D. Experimental determination of stability conditions of methane hydrate in aqueous calcium chloride solutions using high pressure differential scanning calorimetry. The Journal of Chemical Thermodynamics. 2003, 35, 9, 1489-1505.

Khurana, M., Yin, Z., and Linga, P. A review of clathrate hydrate nucleation. ACS Sustainable Chemistry & Engineering. 2017, 5, 12, 11176-11203.

Kishimoto, M., Iijima, S., and Ohmura, R. Crystal growth of clathrate hydrate at the interface between seawater and hydrophobic-guest liquid: Effect of elevated salt concentration. Industrial & Engineering Chemistry Research. 2012, 51, 14, 5224-5229.

Klauda, J.B. and Sandler, S.I. Phase behavior of clathrate hydrates: a model for single and multiple gas component hydrates. Chemical Engineering Science. 2003, 58, 1, 27-41.

Kontogeorgis, G.M., Maribo-Mogensen, B., and Thomsen, K. The Debye-Hückel theory and its importance in modeling electrolyte solutions. Fluid Phase Equilibria. 2018, 462, 130-152.

Kobayashi, R. and Katz, D. Methane hydrate at high pressure. Journal of Petroleum Technology. 1949, 1, 3, 66-70.

Koh, C.A. and Sloan, E.D. Natural gas hydrates: Recent advances and challenges in energy and environmental applications. AIChE Journal. 2007, 53, 7, 1636-1643.

- Kvenvolden, K.A. A review of the geochemistry of methane in natural gas hydrate. *Organic Geochemistry*. 1995, 23, 11-12, 997-1008.
- Lafond, P.G., Olcott, K.A., Sloan, E.D., Koh, C.A., and Sum, A.K. Measurements of methane hydrate equilibrium in systems inhibited with NaCl and methanol. *The Journal of Chemical Thermodynamics*. 2012, 48, 1-6.
- Larson, S.D. Phase studies of the two-component carbon dioxide-water system, involving the carbon dioxide hydrate. Ph.D. Thesis, Department of Chemistry, University of Illinois, USA, 1955.
- Lee, S.Y. and Holder, G.D. Model for gas hydrate equilibria using a variable reference chemical potential: Part 1. *AIChE Journal*. 2002, 48, 1, 161-167.
- Lee, J.H., Kim, S.H., Kang, J.W., and Lee, C.S. Modeling gas hydrate-containing phase equilibria for carbon dioxide-rich mixtures using an equation of state. *Fluid Phase Equilibria*. 2016, 409, 136-149.
- Lehmkuhler, F., Paulus, M., Sternemann, C., Lietz, D., Venturini, F., Gutt, C., and Tolan, M. The carbon dioxide– water interface at conditions of gas hydrate formation. *Journal of the American Chemical Society*. 2009, 131, 2, 585-589.
- Legoix, L., Ruffine, L., Donval, J.P., and Haeckel, M. Phase equilibria of the CH₄-CO₂ binary and the CH₄-CO₂-H₂O ternary mixtures in the presence of a CO₂-rich liquid phase. *Energies*. 2017, 10, 12, 2034.
- Li, S.L., Sun, C.Y., Liu, B., Li, Z.Y., Chen, G.J., and Sum, A.K. New observations and insights into the morphology and growth kinetics of hydrate films. *Scientific Reports*. 2014, 4, 4129-1-6.

- Li, S., Xu, X., Zheng, R., Chen, Y., and Hou, J. Experimental investigation on dissociation driving force of methane hydrate in porous media. *Fuel*. 2015a, 160, 117-122.
- Li, S., Zheng, R., Xu, X., and Chen, Y. Dissociation of methane hydrate by hot brine. *Petroleum Science and Technology*. 2015b, 33, 6, 671-677.
- Li, S., Zheng, R., Xu, X., and Hou, J. Energy efficiency analysis of hydrate dissociation by thermal stimulation. *Journal of Natural Gas Science and Engineering*. 2016a, 30, 148-155.
- Li, S., Zheng, R., Xu, X., and Hou, J. Natural gas hydrate dissociation by hot brine injection. *Petroleum Science and Technology*. 2016b, 34, 5, 422-428.
- Li, S., Zheng, R., Wang, Y. Numerical simulation on the perforation optimization of Class 2 hydrate reservoirs. Presented at the 9th International Conference on Gas Hydrates. Denver, CO, June 25-30, 2017.
- Li, S., Li, S., Zheng, R., Li, Q., and Pang, W. Strategies for gas production from Class 2 hydrate accumulations by depressurization. *Fuel*. 2020, 286, 119380.
- Li, X. and Yang, D. Determination of mutual solubility between CO₂ and water by using the Peng-Robinson equation of state with modified alpha function and binary interaction parameter. *Industrial & Engineering Chemistry Research*. 2013, 52, 38, 13829-13838.
- Li, Z. and Firoozabadi, A. Initialization of phase fractions in Rachford-Rice equations for robust and efficient three-phase split calculation. *Fluid Phase Equilibria*. 2012, 332, 21-27.
- Liao, J., Mei, D.H., Yang, J.T., and Guo, T.M. Prediction of gas hydrate formation conditions in aqueous solutions containing electrolytes and (electrolytes+ methanol). *Industrial & Engineering Chemistry Research*. 1999, 38, 4, 1700-1705.
- Lin, Y., Thomsen, K., and de Hemptinne, J.C. Multicomponent equations of state for electrolytes. *AIChE Journal*. 2007, 53, 4, 989-1005.

- Liu, Y., Zhao, J., and Xu, J. Dissociation mechanism of carbon dioxide hydrate by molecular dynamic simulation and ab initio calculation. *Computational and Theoretical Chemistry*. 2012, 991, 165-173.
- Liu, J., Yan, Y., Liu, H., Xu, J., Zhang, J., and Chen, G. Understanding effect of structure and stability on transformation of CH₄ hydrate to CO₂ hydrate. *Chemical Physics Letters*. 2016, 648, 75-80.
- Liu, S. Molecular dynamics study of the nucleation of CH₄/C₂H₆ binary hydrate. Ph.D dissertation, Colorado School of Mines, 2017.
- Liu, Z., Li, H., Chen, L., and Sun, B. A new model of and insight into hydrate film lateral growth along the gas–liquid interface considering natural convection heat transfer. *Energy & Fuels*. 2018, 32, 2, 2053-2063.
- Lu, H., Matsumoto, R., Tsuji, Y., and Oda, H. Anion plays a more important role than cation in affecting gas hydrate stability in electrolyte solution?—A recognition from experimental results. *Fluid Phase Equilibria*. 2001, 178, 1-2, 225-232.
- Lu, J., Qiu, Y., Baron, R., and Molinero, V. Coarse-graining of TIP4P/2005, TIP4P-Ew, SPC/E, and TIP3P to monatomic anisotropic water models using relative entropy minimization. *Journal of Chemical Theory and Computation*. 2014, 10, 9, 4104-4120.
- Maekawa, T. Equilibrium conditions of gas hydrate from mixtures of methane and ethane and outline of experimental apparatus for gas hydrate synthesis in porous sediment. *Bull. Geol. Surv. Japan*. 1998, 49, 501-507.
- Maekawa, T. Equilibrium conditions for gas hydrates of methane and ethane mixtures in pure water and sodium chloride solution. *Geochemical Journal*. 2001, 35, 1, 59-66.

- Maekawa, T. and Imai, N. Equilibrium conditions of methane and ethane hydrates in aqueous electrolyte solutions. *Annals of the New York Academy of Sciences*. 2000, 912, 1, 932-939.
- Maekawa, T., Itoh, S., Sakata, S., Igari, S.I., and Imai, N. Pressure and temperature conditions for methane hydrate dissociation in sodium chloride solutions. *Geochemical Journal*. 1995, 29, 5, 325-329.
- Makogon, Y.F. and Omelchenko, R.Y. Commercial gas production from Messoyakha deposit in hydrate conditions. *Journal of Natural Gas Science and Engineering*. 2013, 11, 1-6.
- Majid, A.A., Wu, D.T., and Koh, C.A. New in situ measurements of the viscosity of gas clathrate hydrate slurries formed from model water-in-oil emulsions. *Langmuir*. 2017, 33, 42, 11436-11445.
- Maribo-Mogensen, B. Development of an Electrolyte CPA Equation of state for Applications in the Petroleum and Chemical Industries. (Doctoral dissertation, Technical University of Denmark), 2014.
- Marshall, D.R., Saito, S., and Kobayashi, R. Hydrates at high pressures: Part I. Methane - water, argon - water, and nitrogen - water systems. *AIChE Journal*. 1964, 10, 2, 202-205.
- Martos-Villa, R., Francisco-Márquez, M., Mata, M.P., and Sainz-Díaz, C.I. Crystal structure, stability and spectroscopic properties of methane and CO₂ hydrates. *Journal of Molecular Graphics and Modelling*. 2013, 44, 253-265.
- Masoudi, R., Arjmandi, M., and Tohidi, B. Extension of Valderrama-Patel-Teja equation of state to modelling single and mixed electrolyte solutions. *Chemical Engineering Science*. 2003, 58, 9, 1743-1749.
- McKoy, V. and Sinanoğlu, O. Theory of dissociation pressures of some gas hydrates. *The Journal of Chemical Physics*. 1963, 38, 12, 2946-2956.

- McLeod Jr, H.O. and Campbell, J.M. Natural gas hydrates at pressures to 10,000 psia. *Journal of Petroleum Technology*. 1961, 13, 6, 590-594.
- Mehta, A.P. and Sloan, E.D. A thermodynamic model for structure - H hydrates. *AIChE Journal*. 1994, 40, 2, 312-320.
- Mei, D.H., Liao, J., Yang, J.T., and Guo, T.M. Experimental and modeling studies on the hydrate formation of a methane+ nitrogen gas mixture in the presence of aqueous electrolyte solutions. *Industrial & Engineering Chemistry Research*. 1996, 35, 11, 4342-4347.
- Meragawi, S., Diamantonis, N.I., Tsimpanogiannis, I.N., and Economou, I.G. Hydrate-fluid phase equilibria modeling using PC-SAFT and Peng-Robinson equations of state. *Fluid Phase Equilibria*. 2016, 413, 209-219.
- Milkov, A.V. and Sassen, R. Preliminary assessment of resources and economic potential of individual gas hydrate accumulations in the Gulf of Mexico continental slope. *Marine and Petroleum Geology*. 2003, 20, 2, 111-128.
- Mohammadi, A.H., Anderson, R., and Tohidi, B. Carbon monoxide clathrate hydrates: Equilibrium data and thermodynamic modeling. *AIChE Journal*. 2005, 51, 10, 2825-2833.
- Mohammadi, A.H., Afzal, W., and Richon, D. Gas hydrates of methane, ethane, propane, and carbon dioxide in the presence of single NaCl, KCl, and CaCl₂ aqueous solutions: Experimental measurements and predictions of dissociation conditions. *The Journal of Chemical Thermodynamics*, 2008, 40, 12, 1693-1697.
- Mohammadi, A.H., Kraouti, I., and Richon, D. Methane hydrate phase equilibrium in the presence of NaBr, KBr, CaBr₂, K₂CO₃, and MgCl₂ aqueous solutions: Experimental measurements and predictions of dissociation conditions. *The Journal of Chemical Thermodynamics*. 2009, 41, 6, 779-782.

- Mohammadi, A.H., Eslamimanesh, A., and Richon, D. Semi-clathrate hydrate phase equilibrium measurements for the CO₂+ H₂/CH₄+ tetra-n-butylammonium bromide aqueous solution system. *Chemical Engineering Science*. 2013, 94, 284-290.
- Mooijer-Van Den Heuvel, M.M., Witteman, R., and Peters, C.J. Phase behaviour of gas hydrates of carbon dioxide in the presence of tetrahydropyran, cyclobutanone, cyclohexane and methylcyclohexane. *Fluid Phase Equilibria*. 2001, 182, 1-2, 97-110.
- Moon, C., Taylor, P.C., and Rodger, P.M. Molecular dynamics study of gas hydrate formation. *Journal of the American Chemical Society*. 2003, 125, 16, 4706-4707.
- Moortgat, J., Li, Z., and Firoozabadi, A. Three-phase compositional modeling of CO₂ injection by higher-order finite element methods with CPA equation of state for aqueous phase. *Water Resources Research*. 2012, 48, W12511.
- Mori, Y.H. Clathrate hydrate formation at the interface between liquid CO₂ and water phases—a review of rival models characterizing “hydrate films”. *Energy Conversion and Management*. 1998, 39, 15, 1537-1557.
- Mortezazadeh, E. and Rasaei, M.R. A robust procedure for three-phase equilibrium calculations of water-hydrocarbon systems using cubic equations of state. *Fluid Phase Equilibria*. 2017, 450, 160-174.
- Munck, J., Skjold-Jørgensen, S., and Rasmussen, P. Computations of the formation of gas hydrates. *Chemical Engineering Science*. 1988, 43, 10, 2661-2672.
- Nakamura, T., Makino, T., Sugahara, T., and Ohgaki, K. Stability boundaries of gas hydrates helped by methane—structure-H hydrates of methylcyclohexane and cis-1, 2-dimethylcyclohexane. *Chemical Engineering Science*. 2003, 58, 2, 269-273.

- Nakano, S., Moritoki, M., and Ohgaki, K. High-pressure phase equilibrium and Raman microprobe spectroscopic studies on the CO₂ hydrate system. *Journal of Chemical & Engineering Data*. 1998, 43, 5, 807-810.
- Nakano, S., Moritoki, M., and Ohgaki, K. High-pressure phase equilibrium and Raman microprobe spectroscopic studies on the methane hydrate system. *Journal of Chemical & Engineering Data*. 1999, 44, 2, 254-257.
- Nasrifar, K. and Moshfeghian, M. Computation of equilibrium hydrate formation temperature for CO₂ and hydrocarbon gases containing CO₂ in the presence of an alcohol, electrolytes and their mixtures. *Journal of Petroleum Science and Engineering*. 2000, 26, 1-4, 143-150.
- Nazari, M., Asadi, M.B., and Zendehboudi, S. A new efficient algorithm to determine three-phase equilibrium conditions in the presence of aqueous phase: Phase stability and computational cost. *Fluid Phase Equilibria*. 2019, 486, 139-158.
- Ng, H.J. and Robinson, D.B. Hydrate formation in systems containing methane, ethane, propane, carbon dioxide or hydrogen sulfide in the presence of methanol. *Fluid Phase Equilibria*. 1985, 21, 1-2, 145-155.
- Nohra, M., Woo, T.K., Alavi, S., and Ripmeester, J.A. Molecular dynamics Gibbs free energy calculations for CO₂ capture and storage in structure I clathrate hydrates in the presence of SO₂, CH₄, N₂, and H₂S impurities. *The Journal of Chemical Thermodynamics*. 2012, 44, 1, 5-12.
- Ohgaki, K., Makihara, Y., and Takano, K. Formation of CO₂ hydrate in pure and sea waters. *Journal of Chemical Engineering of Japan*. 1993, 26, 5, 558-564.

- Ohgaki, K., Takano, K., Sangawa, H., Matsubara, T., and Nakano, S. Methane exploitation by carbon dioxide from gas hydrates-phase equilibria for CO₂-CH₄ mixed hydrate system. *Journal of Chemical Engineering of Japan*. 1996, 29, 3, 478-483.
- Ohmura, R., Matsuda, S., Uchida, T., Ebinuma, T., and Narita, H. Clathrate hydrate crystal growth in liquid water saturated with a guest substance: observations in a methane+ water system. *Crystal Growth & Design*. 2005, 5, 3, 953-957.
- Ohno, H., Strobel, T.A., Dec, S.F., Sloan, E.D., and Koh, C.A. Raman studies of methane– ethane hydrate metastability. *The Journal of Physical Chemistry A*. 2009, 113, 9, 1711-1716.
- Osfouri, S., Azin, R., Gholami, R., and Izadpanah, A.A. Modeling hydrate formation conditions in the presence of electrolytes and polar inhibitor solutions. *The Journal of Chemical Thermodynamics*. 2015, 89, 251-263.
- Østergaard, K.K., Anderson, R., Llamedo, M., and Tohidi, B. Hydrate phase equilibria in porous media: Effect of pore size and salinity. *Terra Nova*. 2002, 14, 5, 307-312.
- Parrish, W.R. and Prausnitz, J.M. Dissociation pressures of gas hydrates formed by gas mixtures. *Industrial & Engineering Chemistry Process Design and Development*. 1972, 11, 1, 6-35.
- Partoon, B., Sabil, K.M., Roslan, H., Lal, B., and Keong, L.K. Impact of acetone on phase boundary of methane and carbon dioxide mixed hydrates. *Fluid Phase Equilibria*. 2016, 412, 51-56.
- Peng, D.Y. and Robinson, D.B. A new two-constant equation of state. *Industrial & Engineering Chemistry Fundamentals*. 1976, 15, 1, 59-64.
- Peng, B.Z., Dandekar, A., Sun, C.Y., Luo, H., Ma, Q.L., Pang, W.X., and Chen, G.J. Hydrate film growth on the surface of a gas bubble suspended in water. *The Journal of Physical Chemistry B*. 2007, 111, 43, 12485-12493.

- Pietrass, T., Gaede, H.C., Bifone, A., Pines, A., and Ripmeester, J.A. Monitoring xenon clathrate hydrate formation on ice surfaces with optically enhanced ^{129}Xe NMR. *Journal of the American Chemical Society*. 1995, 117, 28, 7520-7525.
- Pitzer, K.S. and Mayorga, G. Thermodynamics of electrolytes. II. activity and osmotic coefficients for strong electrolytes with one or both ions univalent. *The Journal of Physical Chemistry*. 1973, 77, 19, 2300-2308.
- Plimpton, S. Fast parallel algorithms for short-range molecular dynamics. *Journal of Computational Physics*. 1995, 117, 1, 1-19.
- Porz, L.O., Clarke, M.A., and Oellrich, L.R. Experimental investigation of methane hydrates equilibrium condition in the presence of KNO_3 , MgSO_4 , and CuSO_4 . *Journal of Chemical & Engineering Data*. 2009, 55, 1, 262-266.
- Qi, Y.X. and Zhang, H. MD simulation of $\text{CO}_2\text{-CH}_4$ mixed hydrate on crystal structure and stability. *Advanced Materials Research*. 2011, 181, 310-315.
- Qiu, L., Wang, Y., Jiao, Q., Wang, H., and Reitz, R.D. Development of a thermodynamically consistent, robust and efficient phase equilibrium solver and its validations. *Fuel*. 2014, 115, 1-16.
- Radhakrishnan, R. and Trout, B.L. A new approach for studying nucleation phenomena using molecular simulations: application to CO_2 hydrate clathrates. *The Journal of chemical physics*. 2002, 117, 4, 1786-1796.
- Ricaurte, M., Torr , J.P., Asbai, A., Broseta, D., and Dicharry, C. Experimental data, modeling, and correlation of carbon dioxide solubility in aqueous solutions containing low concentrations of clathrate hydrate promoters: Application to $\text{CO}_2\text{-CH}_4$ gas mixtures. *Industrial & Engineering Chemistry Research*. 2012, 51, 7, 3157-3169.

- Ripmeester, J.A. Hydrate research - from correlations to a knowledge - based discipline: The importance of structure. *Annals of the New York Academy of Sciences.*, 2000, 912, 1, 1-16.
- Robinson, D.B. and Mehta, B.R. Hydrates in the propane-carbon dioxide-water system. *Journal of Canadian Petroleum Technology.* 1971, 10, 1, 33-35.
- Ross, M.J. and Toczylkin, L.S. Hydrate dissociation pressures for methane or ethane in the presence of aqueous solutions of triethylene glycol. *Journal of Chemical & Engineering Data.* 1992, 37, 4, 488-491.
- Rovetto, L.J., Bowler, K.E., Stadterman, L.L., Dec, S.F., Koh, C.A., and Sloan, E.D. Dissociation studies of CH₄-C₂H₆ and CH₄-CO₂ binary gas hydrates. *Fluid Phase Equilibria.* 2007, 261, 1-2, 407-413.
- Rowland, D., Königsberger, E., Hefter, G., and May, P.M. Aqueous electrolyte solution modelling: Some limitations of the Pitzer equations. *Applied Geochemistry.* 2015, 55, 170-183.
- Sabil, K.M., Nasir, Q., Partoon, B., and Seman, A.A. Measurement of H-LW-V and dissociation enthalpy of carbon dioxide rich synthetic natural gas mixtures. *Journal of Chemical & Engineering Data.* 2014, 59, 11, 3502-3509.
- Sadeq, D., Iglauer, S., Lebedev, M., Smith, C., and Barifcani, A. Experimental determination of hydrate phase equilibrium for different gas mixtures containing methane, carbon dioxide and nitrogen with motor current measurements. *Journal of Natural Gas Science and Engineering.* 2017, 38, 59-73.
- Saito, K., Kishimoto, M., Tanaka, R., and Ohmura, R. Crystal growth of clathrate hydrate at the interface between hydrocarbon gas mixture and liquid water. *Crystal Growth & Design.* 2011, 11, 1, 295-301.

- Sakemoto, R., Sakamoto, H., Shiraiwa, K., Ohmura, R., and Uchida, T. Clathrate hydrate crystal growth at the seawater/hydrophobic-guest-liquid interface. *Crystal Growth & Design*. 2010, 10, 3, 1296-1300.
- Sandler, S.I. *Chemical, biochemical, and engineering thermodynamics*, 5th Edition. John Wiley & Sons, 2017.
- Sassen, R. and MacDonald, I.R. Thermogenic gas hydrates, Gulf of Mexico continental slope. In *Preprints of Symposia-Division of Fuel Chemistry American Chemical Society*. 1997, 42, 1, 472-474.
- Sassen, R., MacDonald, I.R., Guinasso, N.L., Joye, S., Requejo, A.G., Sweet, S.T., Alcalá-Herrera, J., DeFreitas, D.A., and Schink, D.R. Bacterial methane oxidation in sea-floor gas hydrate: Significance to life in extreme environments. *Geology*. 1998, 26, 9, 851-854.
- Sassen, R., Joye, S., Sweet, S.T., DeFreitas, D.A., Milkov, A.V., and MacDonald, I.R. Thermogenic gas hydrates and hydrocarbon gases in complex chemosynthetic communities, Gulf of Mexico continental slope. *Organic Geochemistry*. 1999, 30, 7, 485-497.
- Sassen, R., Sweet, S.T., Milkov, A.V., DeFreitas, D.A., and Kennicutt, M.C. Thermogenic vent gas and gas hydrate in the Gulf of Mexico slope: Is gas hydrate decomposition significant?. *Geology*. 2001a, 29, 2, 107-110.
- Sassen, R., Losh, S.L., Cathles III, L., Roberts, H.H., Whelan, J.K., Milkov, A.V., Sweet, S.T., and DeFreitas, D.A. Massive vein-filling gas hydrate: Relation to ongoing gas migration from the deep subsurface in the Gulf of Mexico. *Marine and Petroleum Geology*. 2001b, 18, 5, 551-560.

- Schicks, J.M. and Ripmeester, J.A. The coexistence of two different methane hydrate phases under moderate pressure and temperature conditions: Kinetic versus thermodynamic products. *Angewandte Chemie International Edition*. 2004, 43, 25, 3310-3313.
- Schicks, J.M. and Luzzi-Helbing, M. Cage occupancy and structural changes during hydrate formation from initial stages to resulting hydrate phase. *Spectrochimica Acta Part A: Molecular and Biomolecular Spectroscopy*. 2013, 115, 528-536.
- Selam, M.A., Economou, I.G., and Castier, M. A thermodynamic model for strong aqueous electrolytes based on the eSAFT-VR Mie equation of state. *Fluid Phase Equilibria*. 2018, 464, 47-63.
- Seo, Y.T., Kang, S.P., Lee, H., Lee, C.S., and Sung, W.M. Hydrate phase equilibria for gas mixtures containing carbon dioxide: a proof-of-concept to carbon dioxide recovery from multicomponent gas stream. *Korean Journal of Chemical Engineering*. 2000, 17, 6, 659-667.
- Seo, Y.T., Lee, H., and Yoon, J.H. Hydrate phase equilibria of the carbon dioxide, methane, and water system. *Journal of Chemical & Engineering Data*, 2001, 46, 2, 381-384.
- Servio, P. and Englezos, P. Measurement of dissolved methane in water in equilibrium with its hydrate. *Journal of Chemical & Engineering Data*. 2002, 47, 1, 87-90.
- Servio, P. and Englezos, P. Morphology of methane and carbon dioxide hydrates formed from water droplets. *AIChE Journal*. 2003, 49, 1, 269-276.
- Servio, P., Lagers, F., Peters, C., and Englezos, P. Gas hydrate phase equilibrium in the system methane-carbon dioxide-neohexane and water. *Fluid Phase Equilibria*. 1999, 158, 795-800.
- Shahnazar, S. and Hasan, N. Gas hydrate formation condition: Review on experimental and modeling approaches. *Fluid Phase Equilibria*. 2014, 379, 72-85.

- Shedd, W., Boswell, R., Frye, M., Godfriaux, P., and Kramer, K. Occurrence and nature of “bottom simulating reflectors” in the northern Gulf of Mexico. *Marine and Petroleum Geology*. 2012, 34, 1, 31-40.
- Sloan, E.D. and Koh, C. *Clathrate hydrates of natural gases*. CRC Press, 2007.
- Song, Y., Wang, S., Jiang, L., Zhang, Y., and Yang, M. Hydrate phase equilibrium for CH₄ - CO₂ - H₂O system in porous media. *The Canadian Journal of Chemical Engineering*. 2016, 94, 8, 1592-1598.
- Søreide, I. and Whitson, C.H. Peng-Robinson predictions for hydrocarbons, CO₂, N₂, and H₂S with pure water and NaCl brine. *Fluid Phase Equilibria*. 1992, 77, 217-240.
- Sparks, K.A., Tester, J.W., Cao, Z., and Trout, B.L. Configurational properties of water clathrates: Monte Carlo and multidimensional integration versus the Lennard-Jones and Devonshire approximation. *The Journal of Physical Chemistry B*. 1999, 103, 30, 6300-6308.
- Stackelberg, M.V. and Müller, H.R. On the structure of gas hydrates. *The Journal of Chemical Physics*. 1951, 19, 10, 1319-1320.
- Staykova, D.K., Kuhs, W.F., Salamatin, A.N., and Hansen, T. Formation of porous gas hydrates from ice powders: diffraction experiments and multistage model. *The Journal of Physical Chemistry B*. 2003, 107, 37, 10299-10311.
- Subramanian, S., Kini, R.A., Dec, S.F., and Sloan, E.D. Evidence of structure II hydrate formation from methane+ ethane mixtures. *Chemical Engineering Science*. 2000a, 55, 11, 1981-1999.
- Subramanian, S., Ballard, A.L., Kini, R.A., Dec, S.F. and Sloan, E.D. Structural transitions in methane+ ethane gas hydrates—Part I: Upper transition point and applications. *Chemical Engineering Science*. 2000b, 55, 23, 5763-5771.

- Sugaya, M. and Mori, Y.H. Behavior of clathrate hydrate formation at the boundary of liquid water and a fluorocarbon in liquid or vapor state. *Chemical Engineering Science*. 1996, 51, 13, 3505-3517.
- Sun, C.Y., Chen, G.J., Ma, C.F., Huang, Q., Luo, H., and Li, Q.P. The growth kinetics of hydrate film on the surface of gas bubble suspended in water or aqueous surfactant solution. *Journal of Crystal Growth*. 2007, 306, 2, 491-499.
- Sun, X., Nanchary, N., and Mohanty, K.K. 1-D modeling of hydrate depressurization in porous media. *Transport in Porous Media*. 2005, 58, 3, 315-338.
- Takeuchi, F., Hiratsuka, M., Ohmura, R., Alavi, S., Sum, A.K., and Yasuoka, K. Water proton configurations in structures I, II, and H clathrate hydrate unit cells. *The Journal of Chemical Physics*. 2013, 138, 12, 124504.
- Takeya, S., Kamata, Y., Uchida, T., Nagao, J., Ebinuma, T., Narita, H., Hori, A., and Hondoh, T. Coexistence of structure I and II hydrates formed from a mixture of methane and ethane gases. *Canadian Journal of Physics*. 2003, 81, 1-2, 479-484.
- Tanaka, R., Sakemoto, R., and Ohmura, R. Crystal growth of clathrate hydrates formed at the interface of liquid water and gaseous methane, ethane, or propane: Variations in crystal morphology. *Crystal Growth and Design*. 2009, 9, 5, 2529-2536.
- Thakore, J.L. and Holder, G.D. Solid vapor azeotropes in hydrate-forming systems. *Industrial & Engineering Chemistry Research*. 1987, 26, 3, 462-469.
- Tohidi, B., Danesh, A., Todd, A.C., and Burgass, R.W. Hydrate-free zone for synthetic and real reservoir fluids in the presence of saline water. *Chemical Engineering Science*. 1997, 52, 19, 3257-3263.

- Tohidi, B., Burgass, R.W., Danesh, A., Østergaard, K.K. and Todd, A.C. Improving the accuracy of gas hydrate dissociation point measurements. *Annals of the New York Academy of Sciences*. 2000, 912, 1, 924-931.
- Uchida, T., Takeya, S., Kamata, Y., Ikeda, I.Y., Nagao, J., Ebinuma, T., Narita, H., Zatsepina, O., and Buffett, B.A. Spectroscopic observations and thermodynamic calculations on clathrate hydrates of mixed gas containing methane and ethane: Determination of structure, composition and cage occupancy. *The Journal of Physical Chemistry B*. 2002, 106, 48, 12426-12431.
- Uchida, T., Takeya, S., Chuvilin, E.M., Ohmura, R., Nagao, J., Yakushev, V.S., Istomin, V.A., Minagawa, H., Ebinuma, T., and Narita, H. Decomposition of methane hydrates in sand, sandstone, clays, and glass beads. *Journal of Geophysical Research: Solid Earth*. 2004, 109, B05206.
- Unruh, C.H. and Katz, D.L. Gas hydrates of carbon dioxide-methane mixtures. *Journal of Petroleum Technology*. 1949, 1, 4, 83-86.
- Van Denderen, M., Ineke, E., and Golombok, M. CO₂ removal from contaminated natural gas mixtures by hydrate formation. *Industrial & Engineering Chemistry Research*. 2009, 48, 12, 5802-5807.
- Van der Waals, J.H. and Platteeuw, J.C. Clathrate solutions. *Advances in Chemical Physics*. 1958, 2, 1-57.
- Vatamanu, J. and Kusalik, P.G. Unusual crystalline and polycrystalline structures in methane hydrates. *Journal of the American Chemical Society*. 2006, 128, 49, 15588-15589.

- Velaga, S.C. and Anderson, B.J. Carbon dioxide hydrate phase equilibrium and cage occupancy calculations using ab initio intermolecular potentials. *The Journal of Physical Chemistry B*. 2013, 118, 2, 577-589.
- Verma, V.K. Gas hydrates from liquid hydrocarbon-water systems. Ph.D. Thesis, Department of Chemical Engineering, University of Michigan, USA, 1974.
- Verrett, J., Posteraro, D., and Servio, P. Surfactant effects on methane solubility and mole fraction during hydrate growth. *Chemical Engineering Science*. 2012, 84, 80-84.
- Vlahakis, J.G., Chen, H.S., Suwandi, M.S., and Barduhn, A.J. The growth rate of ice crystals: Properties of carbon dioxide hydrates, A Review of properties of 51 gas hydrates. Research and Development Report 830, prepared for US Department of the Interior, 1972.
- Waldron, C.J., Lauricella, M., and English, N.J. Structural and dynamical properties of methane clathrate hydrates from molecular dynamics: Comparison of atomistic and more coarse-grained potential models. *Fluid Phase Equilibria*. 2016, 413, 235-241.
- Walsh, M.R., Koh, C.A., Sloan, E.D., Sum, A.K., and Wu, D.T. Microsecond simulations of spontaneous methane hydrate nucleation and growth. *Science*. 2009, 326, 5956, 1095-1098.
- Wang, W., Wang, X., Li, Y., Liu, S., Yao, S., and Song, G. Study on the characteristics of natural gas hydrate crystal structures during decomposition process. *Fuel*. 2020, 271, 117537.
- Ward, Z.T., Deering, C.E., Marriott, R.A., Sum, A.K., Sloan, E.D., and Koh, C.A. Phase equilibrium data and model comparisons for H₂S hydrates. *Journal of Chemical & Engineering Data*. 2014, 60, 2, 403-408.
- White, C.M., Smith, D.H., Jones, K.L., Goodman, A.L., Jikich, S.A., LaCount, R.B., DuBose, S.B., Ozdemir, E., Morsi, B.I., and Schroeder, K.T. Sequestration of carbon dioxide in coal with enhanced coalbed methane recovery a review. *Energy & Fuels*. 2005, 19, 3, 659-724.

- Whitson, C.H. and Brulé, M.R. Phase behavior (Vol. 20). Richardson, TX: Henry L. Doherty Memorial Fund of AIME, Society of Petroleum Engineers, 2000.
- Wilcox, W.I., Carson, D.B., and Katz, D.L. Natural gas hydrates. *Industrial & Engineering Chemistry*. 1941, 33, 5, 662-665.
- William, H., Andrew, D., and Klaus, S. VMD: Visual molecular dynamics. *Journal of molecular graphics*. 1996, 14, 1, 33-38.
- Wilson, D.T., Barnes, B.C., Wu, D.T., and Sum, A.K. Molecular dynamics simulations of the formation of ethane clathrate hydrates. *Fluid Phase Equilibria*. 2016, 413, 229-234.
- Wu, J. and Prausnitz, J.M. Phase equilibria for systems containing hydrocarbons, water, and salt: An extended Peng-Robinson equation of state. *Industrial & Engineering Chemistry Research*. 1998, 37, 5, 1634-1643.
- Xu, H., Khan, M.N., Peters, C.J., Sloan, E.D., and Koh, C.A. Hydrate-based desalination using cyclopentane hydrates at atmospheric pressure. *Journal of Chemical & Engineering Data*. 2018, 63, 4, 1081-1087.
- Xu, L., Wang, X., Liu, L., and Yang, M. First-principles investigation on the structural stability of methane and ethane clathrate hydrates. *Computational and Theoretical Chemistry*. 2011, 977, 1-3, 209-212.
- Yang, T., Chen, G.J., Yan, W., and Guo, T.M. Extension of the Wong-Sandler mixing rule to the three-parameter Patel-Teja equation of state: Application up to the near-critical region. *Chemical Engineering Journal*. 1997, 67, 1, 27-36.
- Yonezawa, Y. Electrostatic properties of water models evaluated by a long-range potential based solely on the Wolf charge-neutral condition. *Chemical Physics Letters*. 2013, 556, 308-314.

- Yousif, M.H., Li, P.M., Selim, M.S., and Sloan, E.D. Depressurization of natural gas hydrates in Berea sandstone cores. *Journal of Inclusion Phenomena and Molecular Recognition in Chemistry*. 1990, 8, 1-2, 71-88.
- Yu, L.C., Charlton, T.B., Aman, Z.M., Wu, D.T., and Koh, C.A. Hydrate Growth on Methane Gas Bubbles in the Presence of Salt. *Langmuir*, 2020, 36, 84-95.
- Zatsepina, O.Y. and Pooladi-Darvish, M. Storage of CO₂ as hydrate in depleted gas reservoirs. *SPE Reservoir Evaluation & Engineering*. 2012, 15, 1, 98-108.
- Zele, S.R., Lee, S.Y., and Holder, G.D. A theory of lattice distortion in gas hydrates. *The Journal of Physical Chemistry B*. 1999, 103, 46, 10250-10257.
- Zha, L., Liang, D.Q., and Li, D.L. Phase equilibria of CO₂ hydrate in NaCl-MgCl₂ aqueous solutions. *The Journal of Chemical Thermodynamics*. 2012, 55, 110-114.
- Zhang, Z. and Duan, Z. An optimized molecular potential for carbon dioxide. *The Journal of Chemical Physics*. 2005, 122, 21, 214507.
- Zhang, Z., Liu, C.J., Walsh, M.R., and Guo, G.J. Effects of ensembles on methane hydrate nucleation kinetics. *Physical Chemistry Chemical Physics*. 2016, 18, 23, 15602-15608.
- Zhao, J., Yu, T., Song, Y., Liu, D., Liu, W., Liu, Y., Yang, M., Ruan, X., and Li, Y. Numerical simulation of gas production from hydrate deposits using a single vertical well by depressurization in the Qilian Mountain permafrost, Qinghai-Tibet Plateau, China. *Energy*. 2013, 52, 308-319.
- Zheng, R., Li, S., Li, Q., and Hao, Y. Using similarity theory to design natural gas hydrate experimental model. *Journal of Natural Gas Science and Engineering*. 2015, 22, 421-427.

- Zheng, R., Li, S., and Liu, J. Investigation on the boundaries among different controlling mechanisms of hydrate exploitation. Presented at the 9th International Conference on Gas Hydrates. Denver, CO, June 25-30, 2017.
- Zheng, R., Li, S., Li, Q., and Li, X. Study on the relations between controlling mechanisms and dissociation front of gas hydrate reservoirs. *Applied Energy*. 2018a, 215, 405-415.
- Zheng, R., Li, S., and Li, X. Sensitivity analysis of hydrate dissociation front conditioned to depressurization and wellbore heating. *Marine and Petroleum Geology*. 2018b, 91, 631-638.
- Zheng, R., Li, S., Li, X., and Negahban, S. Multi-Scale Analyses on the Advance of Dissociation Front in Gas Hydrate Reservoirs. Presented at AGU Fall Meeting. San Francisco, CA, Dec. 9-13, 2019.
- Zheng, R., Fan, Z., Li, X., and Negahban, S. Phase behavior of high-pressure CH₄-CO₂ hydrates in NaCl solutions. *Fuel*. 2020a, 280, 118549.
- Zheng, R., Fan, Z., Li, X., and Negahban, S. Phase boundary of CH₄, CO₂, and binary CH₄-CO₂ hydrates formed in NaCl solutions. *Journal of Chemical Thermodynamics*. 2020b, 154, 106333.
- Zheng, R., Li, X., and Negahban, S. Phase boundary of gas hydrates in single and mixed electrolyte solutions: Using a novel unified equation of state. *Journal of Molecular Liquids*. 2020c. (Under review)
- Zheng, R., Li, X., and Negahban, S. Molecular-level insights into the structure stability of CH₄-C₂H₆ hydrates. *Chemical Engineering Science*. 2021. (Under review)
- Zhong, X., Pu, H., Zhou, Y., and Zhao, J.X. Comparative study on the static adsorption behavior of zwitterionic surfactants on minerals in middle Bakken formation. *Energy & Fuels*. 2019, 33, 2, 1007-1015.

Zuo, Y.X. and Guo, T.M. Extension of the Patel-Teja equation of state to the prediction of the solubility of natural gas in formation water. *Chemical Engineering Science*. 1991, 46, 12, 3251-3258.

Zuo, Y.X. and Stenby, E.H. Prediction of gas hydrate formation conditions in aqueous solutions of single and mixed electrolytes. *SPE Journal*. 1997, 2, 4, 406-416.